



MAGNETO-STRUCTURAL CORRELATIONS AND THE ROLE OF DISORDER IN FRUSTRATED MAGNETS

JENNIFER NADINE GRAHAM

A thesis submitted to
the University of Birmingham
for the degree of
DOCTOR OF PHILOSOPHY

School of Chemistry
College of Engineering and Physical Sciences
University of Birmingham
June 2023

ABSTRACT

This thesis is an experimental study that explores the role correlated disorder plays in the ground state selection of quantum magnetic materials. Whilst magnetic materials with conventional long-range magnetic orderings give rise to magnetic Bragg peaks that can be understood through average structure methods, the unconventional correlated short-range orderings of quantum magnetic materials give rise to broad diffuse features that rely on local structure methods for their elucidation. One of the most powerful local structure methods is reverse Monte Carlo analysis, which has been employed extensively throughout this thesis.

In the first chapter, a discussion surrounding the complexities of realising different quantum magnetic models in real materials is presented. This chapter also includes an overview of the experimental methods used in this thesis, from both an average and local structure perspective, a formalism that is employed throughout the results chapters.

Chapter 2 explores the structural and magnetic evolution of two samples of the $S = 1$ cubic spinel, ZnV_2O_4 , one prepared via a conventional solid-state sintering synthesis route and the other via a novel, rapid microwave assisted method. The microwave sample was found to be highly crystalline and remained in the cubic symmetry down to 4 K, whereas strain caused the sintered sample to undergo a tetragonal distortion below 35 K. This leads both samples to unique magnetic ground states that were explored with magnetic susceptibility measurements and diffuse neutron scattering.

Chapter 3 presents LiYbO_2 as the first experimental realisation of a spiral spin liquid ground state in a distorted diamond structure. Comprehensive neutron scattering measurements have been conducted and analysed using state-of-the-art reverse Monte Carlo analysis, allowing for the experimental signature of the spiral spin liquid—a continuous ring of mag-

netic diffuse scattering—to be reconstructed.

Chapter 4 involves a neutron scattering study on a quasi-two-dimensional layered honeycomb material, $\text{Mn}_{0.5}\text{Fe}_{0.5}\text{PS}_3$, which was found to have a spin glass ground state. Measurements of a single-crystal confirmed the model used to calculate the spin correlations was correct, which could be understood through considering differences in the ordered magnetic structures of the parent compounds.

Finally, in Chapter 5, the conclusions and outlook of this thesis are presented, with a focus on how disorder can be used to an advantage in future materials design, and how reverse Monte Carlo methodologies are developing in order to characterise more complex partially ordered quantum materials.

ACKNOWLEDGMENTS

Firstly, I would like to thank my supervisors Dr Lucy Clark and Dr Andrew Wildes for all the help and guidance over the last few years. To Lucy, thank you for giving me the confidence to do a PhD and move to France, I don't think I would've believed you at the start of my Masters year if you said this is where I'd end up. To Andrew, thank you for being my personal cheerleader throughout the years and always being ready for a chat, I will miss your desk-bombing antics.

This thesis would not have been possible without all the instrument scientists who have gone above and beyond the call of duty with helping me with my experiments, particularly those measured through pandemic time; Dr Clemens Ritter (D20 and D2B), Dr Emmanuelle Suard (D2B), Dr Pascal Manuel (WISH), Dr Dominic Fortes (HRPD) and Dr Giorgia Confalonieri (ID22). I am grateful to the other scientists who have helped me with my research, particularly Dr Navid Qureshi and Dr Juan Rodriguez-Carvajal (ILL) for the magnetism and Fullprof tutorials, Dr Joya Cooley (UCSB) for preparing the microwave sample of ZnV_2O_4 , Dr Manila Songvilay (Institut Néel) for all attempts at measuring the susceptibility of ZnV_2O_4 and Dr Matthew Coak (Birmingham) for making my first two weeks as a PhD student so memorable on the PS_3 D7 experiment. A special thanks goes to Dr Ross Stewart, who although was not an official supervisor I see as my science uncle for the many hours we've spent discussing ZnV_2O_4 .

I would also like to thank my examiners; Prof. Andrew Goodwin and Dr Phoebe Allan, aswell as Dr Zoe Schnepf, for taking the time out of their busy schedules to be the examiners for my thesis.

At this point, I would like to acknowledge the University of Liverpool, University

of Birmingham and ILL Graduate School for funding my PhD, as well as the Science and Technology Facilities Council for funding beam time.

I have been very lucky to meet many young scientists over the past few years, some I hope are friends for life. Thank you to all members of the Clark group, past and present. A particular shout out goes to Aly and Kate, some of our beam time trips were the best times of my PhD (not least because I always crushed you at Dobble and Exploding Kittens) and our weekly fika's! I would also like to thank all the friends I've made in Grenoble who have made it so easy to live away from home in such strange times, in particular, Maddie, Mo, Bettina, Arianna and Rasmus. Maddie, I don't think I'll ever find a better office mate, or one that will let me put such fabulous party decorations everywhere! I would also like to thank my two best friends back home, Alice and Ursula for all of our chats and little adventures when we actually get to see each other!

Finally, I would like to thank my family for all their support and love throughout my life.

Contents

	Page
1 Introduction	1
1.1 Magnetic Ground States	3
1.1.1 DC Magnetic Susceptibility	4
1.1.2 Quantum Magnetic Ground States	6
1.2 A Recipe for Quantum Magnetic Materials	8
1.2.1 Moments Approaching the Quantum Limit, $S \leq 1$	8
1.2.2 Lower Dimensions	14
1.2.3 Increase Competition	15
1.2.4 Chemical Disorder	17
1.3 Understanding Order: Average Structure Methods	20
1.3.1 Scattering Experiments	21
1.3.2 Interactions with Matter	22
1.3.3 Order and Diffraction	26
1.4 Understanding Disorder: Local Structure Methods	30
1.4.1 Disorder and Diffraction	31
1.4.2 Reverse Monte Carlo SPINVERT Analysis	37
1.4.3 Spin Correlations	41
1.4.4 Pair Distribution Function Analysis	42
1.5 Characterising Real Quantum Materials	46
1.5.1 Quantum Spin Liquid (QSL)	46

1.5.2	Spin Glass	48
1.5.3	Spin Ice	50
1.6	Aims of Thesis	51
2	Understanding Synthesis-Driven Structure-Property Relationships in	
	ZnV₂O₄	53
2.1	Introduction	53
2.2	Experimental Methods	61
2.2.1	Synthesis	61
2.2.2	Powder Neutron Diffraction	62
2.2.3	Powder X-ray Diffraction	64
2.2.4	Total X-ray Scattering	65
2.2.5	Magnetometry	66
2.3	Results and Discussion	66
2.3.1	Average Chemical Structure	66
2.3.2	Local Chemical Structure	79
2.3.3	Magnetic Susceptibility	83
2.3.4	Magnetic Diffuse Scattering	89
2.3.5	Discussion	96
2.4	Conclusions and Outlook	98
2.5	Appendix	102
3	Experimental Evidence for the Spiral Spin Liquid in LiYbO₂	115
3.1	Introduction	115
3.2	Experimental Methods	121
3.2.1	Synthesis	121
3.2.2	Neutron Powder Diffraction	122
3.2.3	Diffuse Scattering	122
3.3	Results and Discussion	123

3.3.1	Average Chemical Structure	123
3.3.2	Magnetic Structure	123
3.3.3	Single-Crystal Simulations	135
3.3.4	Spin Correlations	136
3.3.5	Discussion	140
3.4	Conclusions and Outlook	144
3.5	Appendix	146
4	Local Chemical and Magnetic Order in the Two-Dimensional Spin Glass,	
	$\text{Mn}_{0.5}\text{Fe}_{0.5}\text{PS}_3$	151
4.1	Introduction	151
4.2	Experimental Methods	156
4.2.1	Synthesis	156
4.2.2	Neutron Powder Diffraction	157
4.2.3	Magnetometry	157
4.2.4	Diffuse Scattering	157
4.3	Results and Discussion	158
4.3.1	Average Chemical Structure	158
4.3.2	Magnetic Susceptibility	160
4.3.3	Magnetic Diffuse Scattering	162
4.3.4	Spin Correlations	167
4.3.5	Discussion	170
4.4	Conclusions and Outlook	173
5	Conclusions and Outlook	177

Chapter One

Introduction

The fundamental building block of all magnetic materials is the unpaired electron, whose intrinsic spin produces a tiny atomic magnetic moment that can interact with other moments to form different types of magnetic ground states. Moments can range from being randomly orientated and having little interaction at high temperatures (paramagnets) to forming a long-range ordered arrangement upon cooling. This long-range order can be relatively simple, as in the case of ferromagnets or antiferromagnets [1], to complex helical [2–4] and cycloidal [5–7] orderings, but the principle remains the same; a periodic, repeating unit of moments can describe the magnetic structure in its entirety.

Sometimes though, long-range magnetic order wants to develop but is prevented [8, 9]. Such materials are of huge theoretical and experimental interest as they have exotic, often short-range ordered magnetic ground states, that may have applications in high-temperature superconductivity [10–12], multiferroics [13–15] and quantum technologies [16–18]. The central ingredient that prevents magnetic order is a perplexing phenomenon known as magnetic frustration [8, 9, 19]. In its simplest terms, magnetic frustration is the result of the magnetic moments being unable to arrange themselves in the most energetically favourable configuration which forces the system to make some compromises. There are many reasons why a system may be, or has the potential to become, frustrated.

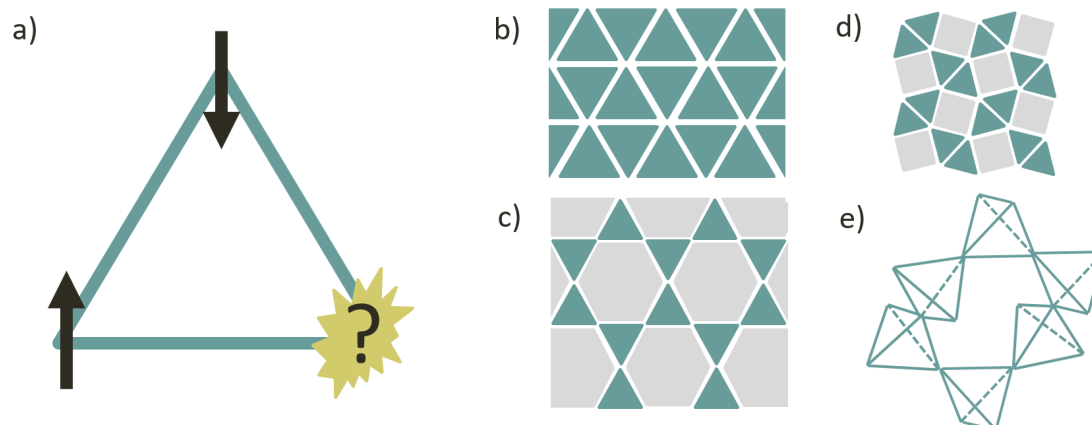


Figure 1.1: a) The geometry of a magnetic lattice can cause an effect known as magnetic frustration where moments are unable to align in the most energetically favourable arrangement. Geometric frustration can arise in many lattice types, including in two-dimensions, b) edge-sharing [20–22], c) corner sharing (kagomé) [23–25] and d) snub square lattices [26, 27], and e) three-dimensional corner sharing tetrahedra that form pyrochlore networks [28–30].

For example, frustration may be caused by the geometry of the magnetic lattice. Geometric frustration can be easily visualised by trying to simultaneously arrange all the moments on the corners of an equilateral triangle to align in an antiferromagnetic arrangement with Ising anisotropy. As Fig. 1.1a) shows, only two of the moments can simultaneously align antiparallel to each other, with the third left with no choice but to align parallel with one of its neighbours. The antiferromagnetic condition is now broken, and the resulting effect is known as magnetic frustration. In just one single triangle, there are six unique but energetically equivalent ways to arrange the moments. Repeated across the whole magnetic lattice (Fig. 1.1b)-e)), this frustration effect is therefore amplified creating a huge degeneracy of ground states which are all energetically the same. The choice of which magnetic ground state to enter is thus a delicate balance of energetics and is often susceptible to the small defects and disorder that exist in real materials [8, 19]. Understanding this relationship between disorder and the magnetic ground state is the main aim of this thesis.

1.1 Magnetic Ground States

There are an abundance of possible magnetic ground states, with varying degrees of magnetic order (Figure 1.2). An intuitive way to think about these magnetic orderings is to compare them to states of matter. At high-temperatures, the randomly arranged and non-interacting moments are analogous to the particles in an ideal gas. But if a material is cooled sufficiently,

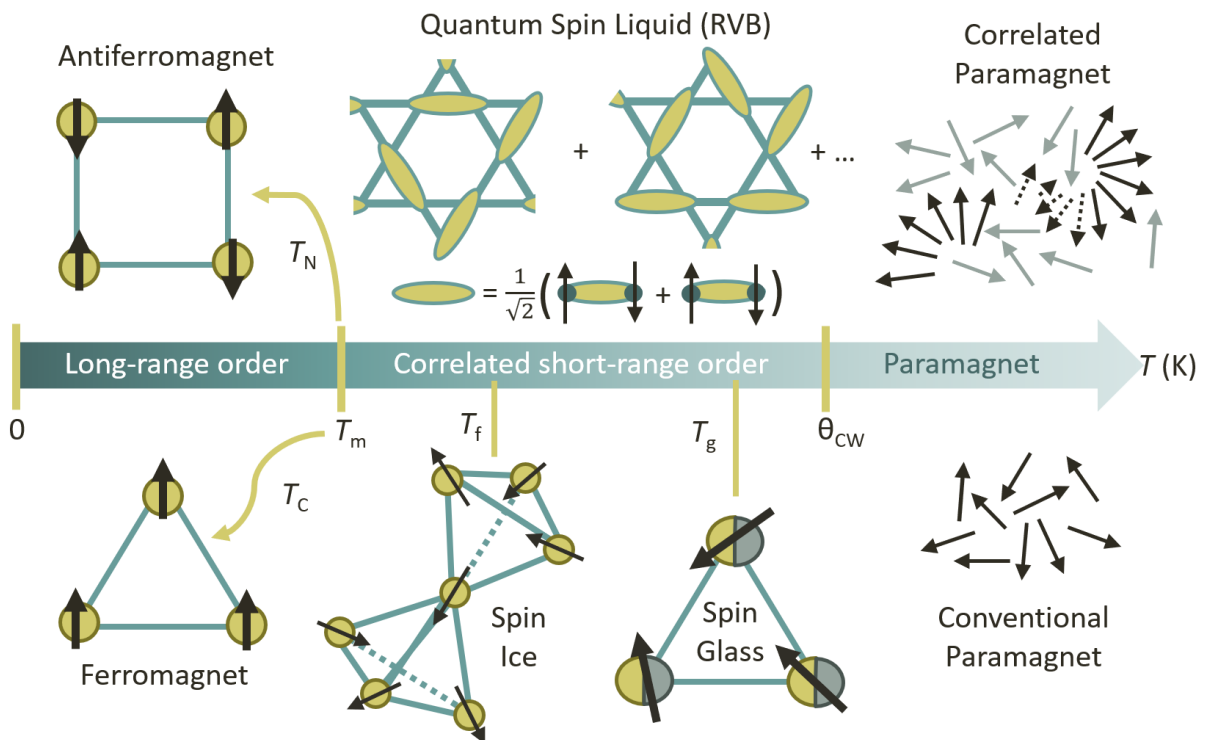


Figure 1.2: A selection of possible magnetic ground states. Many materials at high-temperatures with unpaired electrons are paramagnets, where the moments are non-interacting and randomly fluctuating. Continued cooling causes the system to pass a magnetic ordering temperature, T_m where it becomes energetically favourable for moments to form a regular, periodic arrangement, such as (anti)ferromagnets. The magnetic ground states most interesting to this thesis are the correlated short-range ordered states, the quantum spin liquid, spin glass and correlated paramagnet. These ground states are usually highly quantum entangled and complex, leading to a wide variety of physical phenomena.

most will pass through their magnetic transition, T_m and the moments will become ordered. Conventional magnetic orderings, such as ferromagnets and antiferromagnets, typically have long-ranged interactions across a regular arrangement of moments, and thus are comparable to the periodic arrangement of atoms, ions or molecules in solids in condensed matter. The transition from paramagnet to long-range magnetic order can usually be detected through DC magnetic susceptibility measurements—an essential characterisation tool for magnetic materials [31, 32].

1.1.1 DC Magnetic Susceptibility

Magnetic susceptibility is commonly measured by a SQUID (Superconducting QUantum Interference Device) magnetometer. The SQUID consists of two superconductors separated by a thin insulating layer forming two parallel Josephson junctions. In a direct current (DC) measurement, a fixed magnetic field is applied as the sample is moved through a set of parallel superconducting detection coils. From Faraday’s law, a change in flux induces an output voltage as a function of the samples position. This change in flux is also proportional to the magnet moment, and hence, the magnetisation, \mathbf{M} ($= \sum \mu/V$, where μ is the magnetic moment and V is the volume of the sample), of the sample. For a DC measurement, the magnetic susceptibility, χ , is assumed to be inversely proportional to the applied field, \mathbf{H} ($\approx B/\mu_0$, where μ_0 is the permeability of free space), such that

$$\mathbf{M} = \chi\mathbf{H} \tag{1.1}$$

Magnetic susceptibility measurements are usually displayed as a function of temperature, and provide information on the average strength of magnetic interactions within the system (Curie-Weiss constant, θ_{CW}), and the temperature, T_m , at which long-range order develops, through discontinuities or anomalies in the susceptibility curve (Fig. 1.3) [32]. Typically, θ_{CW} is positive for ferromagnets and negative for antiferromagnets, and in conventional magnetic materials it is expected that T_m will be comparable in magnitude to θ_{CW} .

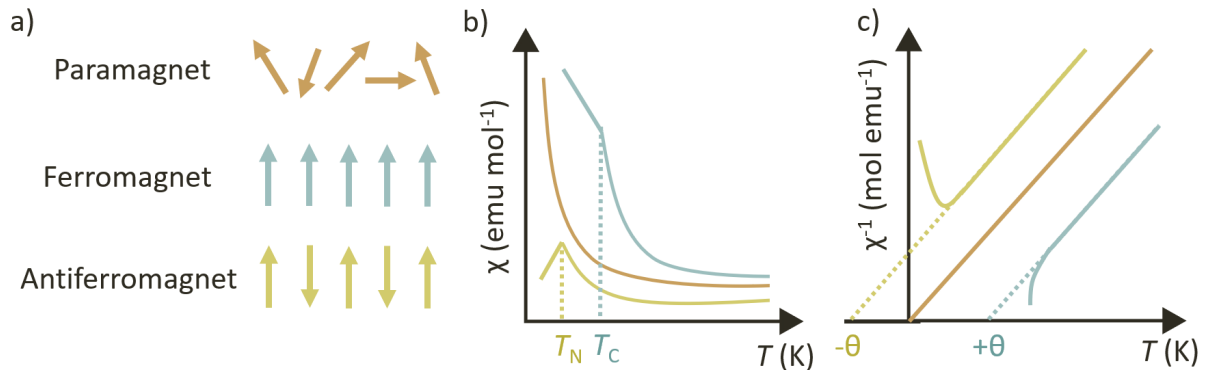


Figure 1.3: The way in which individual magnetic moments align and interact give rise to different types of magnetic order, each with their own experimental signatures. a) Moments are randomly aligned in paramagnets and align (anti)parallel in (anti)ferromagnets resulting in long-range magnetic order. Characteristic b) susceptibility, χ and c) inverse susceptibility, χ^{-1} curves. The Curie-Weiss temperatures, θ_{CW} can be estimated through a Curie-Weiss fit of the linear part of the data at high-temperatures, with θ_{CW} being defined as the intercept with the x -axis.

These quantities can be derived through a Curie-Weiss fit of the data,

$$\chi = \frac{C}{T_m - \theta_{CW}} (+\chi_0) \quad (1.2)$$

where C is the Curie constant which is a material dependent property that relates susceptibility and temperature. Crucially, determining C is an experimental means to establish the atomic magnetic moment of the magnetic species present, using the conversion, $\mu_{\text{eff}} \approx 2.83\sqrt{C}$ and $\mu_{\text{eff}} \approx 797.8\sqrt{C}$ for for data in cgs and SI units, respectively [31]. For this law to be valid, the data need to be modelled in the paramagnetic region. This paramagnetic region is usually defined from the point in the inverse susceptibility where the data become linear as a function of temperature. For some materials, an additional term is added to the Curie-Weiss law, χ_0 , to account for a materials inherent diamagnetic contribution [33]. Diamagnetism (repulsion of a substance to a magnetic field) is a temperature independent property that affects all atoms or compounds. χ_0 corrections can be calculated from tabulated values and are always negative.

1.1.2 Quantum Magnetic Ground States

For many magnetic materials, the system has clear features in the susceptibility which can be attributed to the onset of conventional long-range order. But for quantum magnetic materials, T_m is not necessarily commensurate with θ_{CW} , and this can open up a region between the solid and gas phases for the corresponding "liquid" magnet (Fig. 1.2). Unlike paramagnets and conventional long-range ordered magnetic phases, the liquid phase is much more difficult to define, and even harder to experimentally realise.

At the opposite end of the spectrum to conventional long-range magnet order is the ultimate quantum magnetic ground state, the quantum spin liquid (QSL). A QSL is a magnetic ground state that is theorised to remain dynamic and highly correlated, even at absolute zero [8]. Whilst theoretically attainable, experimentally achieving a QSL ground state is arduous. For it is often the same defects and disorder that prevent long-range order from forming, that also prevent the elusive QSL ground state from being stabilised. Consequently, a lot of quantum magnetic materials do order but have unconventional, short-ranged correlations between their magnetic moments. These materials are still a worthwhile pursuit as the variety and versatility of correlated short-range ordered magnetic ground states are vast and there is still a lot to learn about their underlying physics (Fig. 1.2).

Below I will outline a selection of unconventional quantum magnetic ground states, some of which will be encountered in the results chapters of this thesis. Later in Section 1.5, I will explore the relationships between these quantum magnetic ground states with external parameters like chemical structure or disorder, and their experimental signatures with a few key examples.

- **Quantum Spin Liquid**

Quantum spin liquids (QSLs) are complex magnetic ground states that support dynamic fluctuations down to the lowest temperatures. A popular theory of QSLs was

proposed by Anderson in 1973 in which unpaired spins dimerise to form short-range entangled $S = 0$ singlets [34]. These singlets can form a static arrangement on the lattice, which is known as a valence bond solid or crystal (VBS or VBC). The VBS and VBC are not considered QSL states due to the symmetry breaking associated with the ordering of spin dimers. Alternatively, if the singlets resonate from bond to bond, effectively creating a superposition of singlets across the lattice, then this resonating valence bond (RVB, Fig. 1.2) model is considered highly frustrated and dynamic, which may generate a QSL ground state [34–36].

- **Spin Glass**

A disruption to the magnetic lattice, for example, an impurity or site-mixing, can induce a classical phase transition, T_f , on a frustrated system. This is known as a spin glass [37]. A spin glass ground state involves the co-operative freezing of moments into random positions across the magnetic lattice. Distinct from an (anti)ferromagnet, the static moments fail to adopt a periodic arrangement that can be described by a simple model.

- **Spin Ice**

The ferromagnetic arrangement of moments across corner-sharing tetrahedra, like in a pyrochlore lattice, is geometrically frustrated when the local anisotropic axis points into the centres of the tetrahedra. The lowest energy configuration this system may take is to have two spins pointing in and two pointing out of the tetrahedra, creating four low energy in-out interactions and two high energy in-in and out-out interactions. This is known as a spin ice [38, 39]. So called because of its similarity to the arrangement of hydrogen atoms in water ice, this highly correlated magnetic ground state lacks the breaking of symmetry expected at low temperatures leading to unique excitations and properties, with magnetic monopoles as an example [40].

1.2 A Recipe for Quantum Magnetic Materials

There is no perfect recipe for a quantum magnet, but there are certain ingredients that can enhance the quantum fluctuations and competition between exchange interactions of the system, making the stabilisation of an exotic magnetic ground state more likely.

1.2.1 Moments Approaching the Quantum Limit, $S \leq 1$

The first case is to select candidate systems where the magnetic moment is as close to the quantum limit, $S = \frac{1}{2}$, as possible. The magnetic ground states most alluring to experimentalists and theorists are those which have a dynamic magnetic ground state, such as the quantum spin liquid. In order to evade long-range magnetic order to realise a quantum spin liquid ground state, it is thus favourable to increase the quantum fluctuations of the system, which are felt most strongly for small spin systems. The total (or effective) spin of a system is a combination of the number of unpaired electrons, the applicability of Hund's rules, and how the moments interact with each other and their environment. These are several important concepts that I will introduce with a full description available in the following Refs. [31, 41, 42].

1.2.1.1 S or J : A Quantum Introduction to Magnetism

Each individual electron has an inherent spin angular momentum which is described by the quantum number, $s = \frac{1}{2}$. The total spin of a system, \mathbf{S} (quantum number, S) is the vector sum of all the unpaired electrons in the system, $\mathbf{S} = \sum s$, and can be related to the magnetic moment, $\boldsymbol{\mu}$:

$$\boldsymbol{\mu} = -g\mathbf{S}\mu_B \tag{1.3}$$

where g is the Landé g -factor, a dimensionless constant that is ion specific. The quantity, μ_B (Bohr magneton) is one of the most important quantities in atomic magnetism, representing the magnetic moment of a ground-state electron in hydrogen. Owing to the small magnitude of the magnetic moment size, magnetic moments of other ions are commonly expressed as multiples of μ_B

$$\mu_B = \frac{e\hbar}{2m_e} = 9.274 \times 10^{-24} \text{ JT}^{-1} \quad (1.4)$$

where e is the charge of the electron, \hbar is the reduced Planck's constant, and m_e is the mass of the electron. In addition to this spin angular momentum, which is purely quantum in origin, there are three other quantum numbers needed to describe atomic magnetism, which each have a classical counterpart. Firstly, the principle quantum number, n , describes the relative energy of each orbital and is only allowed to take integer values greater than zero ($n = 1, 2, \dots$). Secondly, the orbital angular momentum quantum number, ℓ , describes the shape of each orbital and may take integer values up to $n - 1$ ($\ell = 0, 1, \dots, (n - 1)$). For atoms with more than one electron, the orbital energy is dependent on both n and ℓ . Thirdly, the orientation of the orbital can be described by the magnetic quantum number, m_ℓ . This can be thought of as a projection of the total orbital angular momentum along a specific axis and can take $2\ell + 1$ values between $-\ell$ and $+\ell$. Spin can also take $2s + 1$ values between $-s$ and $+s$, with a single electron therefore having two possible spin states, $m_s = \pm\frac{1}{2}$, so called spin up and down states for positive and negative values, respectively. The Heisenberg uncertainty principle states it is only possible to measure two quantities simultaneously and precisely, in this case, the magnitude of the angular momentum, and its projection along a single axis of an electron. For the total orbital, L and spin, S angular momentum, these quantities are given by:

$$|L| = \sqrt{L(L + 1)}\hbar \quad \text{and} \quad |S| = \sqrt{S(S + 1)}\hbar \quad (1.5)$$

$$L_z = M_l\hbar \quad \text{and} \quad S_z = M_s\hbar \quad (1.6)$$

Depending on how many electrons are occupying a sub-shell there are different ways that the electrons may be arranged, with different L and S accordingly. A more appropriate

measure of the system may be reached by considering spin-orbit interactions, with the total angular momentum, $\mathbf{J} = \mathbf{L} \pm \mathbf{S}$ (quantum number, J). The values of S , L and J are calculated for an electronic ground state of an isolated atom or ion using Hund's rules of maximum multiplicity. First S , then L is maximised. Finally, if the sub-shell is less than half-filled then $J = |L - S|$, and $J = L + S$, otherwise. The magnetic moment can therefore be expressed as:

$$\mu_{\text{eff}} = g\sqrt{J(J+1)}\mu_{\text{B}} \quad \text{with} \quad g = \frac{3}{2} + \frac{S(S+1) - L(L+1)}{2J(J+1)} \quad (1.7)$$

The applicability of Hund's rules largely depends on the size of the ion, and consequently which interaction term dominates, spin-orbit coupling or the interaction with the crystal field. Spin-orbit coupling interactions scale with a Z^4 dependence ($Z =$ atomic number), and is, therefore, much stronger in heavier atoms and ions. The heavy $4f$ and $5f$ sub-shells of rare-earth ions are also orbitally contracted, and therefore have a much weaker interaction with the crystal field. This combination of factors mean that for rare-earth ions, spin-orbit coupling dominates and Hund's third rule is valid.

1.2.1.2 Transition-Metals, Orbital Quenching and the Effect of the Crystal Field

In contrast, the more extended $3d$ and $4d$ sub-shells of transition-metals feel a much stronger coupling to the crystal field than with spin-orbit interactions. In effect the crystal field takes into account that metal ions are not free, but instead interact with a local environment that may perturb their energy levels. The local environment of the crystal is considered as the interaction that arises from the overlap of orbitals between the metal ion and the surrounding ligands.

In the absence of a crystal field, a transition-metal ion has five degenerate energy levels, each describing a different orbital. These orbitals point in different directions in space, and, for the octahedral case, are divided into two groups: (1) t_{2g} orbitals which point between the x , y and z axes (d_{xy} , d_{yz} and d_{xz}), and (2) e_g orbitals which point along the

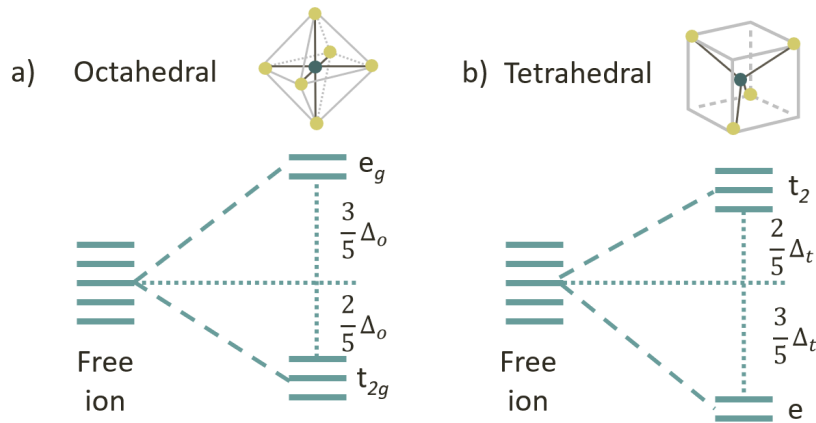


Figure 1.4: A free ion may split with the introduction of a crystal field. The way the energy levels split is dependent on orientation of the orbitals with respect to the crystal field environment, for example in a) octahedral and b) tetrahedral environments. The total energy of the orbitals is given by Δ , which splits proportionally depending on the environment.

axes (d_{z^2} and $d_{x^2-y^2}$). The crystal field can be considered as a uniform negative sphere of charge surrounding a positively charged metal ion. In reality, these metal ions are connected to ligands via symmetry, and the ligands can be thought of as pulling all the negative charge of the sphere towards them creating distinct spots of negative charge in space. The way that the orbitals of the metal align with respect to these charge spots causes electrostatic repulsion and attraction and therefore can change the energy of the orbitals. A common type of symmetry is the octahedral environment as pictured in Fig. 1.4a), which is encountered in Chapter 2 as the V^{3+} ions are co-ordinated to six oxygen atoms in the cubic spinel structure of ZnV_2O_4 . Here, it can be seen that this environment results in the raising of the e_g orbitals and lowering of the t_{2g} orbitals, which alleviates some of the degeneracy of the system. Another common case is the tetrahedral environment, shown in Fig. 1.4b).

As interactions with the crystal field dominate, Hund's rules are not valid for transition-metal ions which led to consistent discrepancies between the experimentally measured moment and the theoretical prediction from Eq. 1.7 [31]. Instead, it was found that transition-

metal systems under the influence of the crystal field were choosing a magnetic ground state such that $L = 0$, an effect known as orbital quenching. In this case, the magnetic moment is better described by considering spin-only contributions.

$$\mu_{\text{eff}} = 2\sqrt{S(S+1)}\mu_{\text{B}} \quad (1.8)$$

In real materials, the orbital component of the moment may not fully be quenched. It can depend on a number of factors, such as the crystal field environment, the arrangement of electrons in the orbitals, and whether there is remaining degeneracy in the t_{2g} or e_g set (for octahedral environments). The effects of orbital quenching to some degree will be applied in Chapters 2 and 4.

1.2.1.3 Jahn-Teller Distortions

Though the crystal field goes part of the way to lifting the degeneracy of the system, for many materials it does not go far enough. Therefore, sometimes it is energetically favourable for an octahedron, for example, to spontaneously distort as the increased elastic energy is balanced by the saving in electronic energy. This is known as a Jahn-Teller distortion [31]. An example is shown in Fig. 1.5, which is specific to the case of the V^{3+} ions in ZnV_2O_4 in Chapter 2, and shows the respective raising and lowering of orbital energies via a compression or elongation along the tetragonal c -axis.

This behaviour is often observed within cubic spinels, whose A - and B -site cations are connected via a geometrically frustrated diamond and pyrochlore sub-lattice, respectively. The presence of a Jahn-Teller distortion in cubic spinels often leads away from a dynamic spin liquid ground state by triggering what is commonly referred to as an order-by-disorder transition [43]. In such a case, a single long-range ordered ground state is selected by the collective fluctuations in the system combined with the spontaneous breaking of symmetry following the Jahn-Teller distortion. This has been a significant issue within the search for

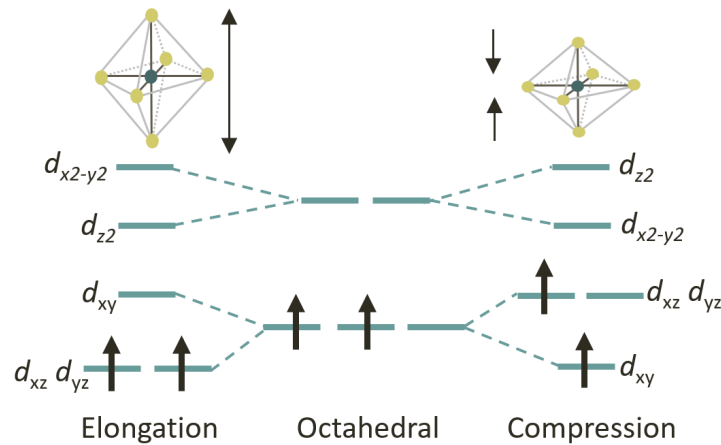


Figure 1.5: Jahn-Teller distortion for a V^{3+} ion in an octahedral environment has two potential ground states depending on the system undergoing an elongation or a compression along the tetragonal c -axis.

the spiral spin liquid ground state [44–46]. However, as I will show in Chapter 3, in conjunction with a recent theoretical study [46], a spiral spin liquid is achievable in a tetragonally elongated structure.

Another consideration following the splitting of orbitals by either the crystal field or a Jahn-Teller distortion, is how to fill the now non-degenerate energy levels [31]. In the octahedral example, the lower energy t_{2g} orbitals will begin filling first before the e_g orbitals. The energy cost of putting two electrons in a single orbital is known as the pairing energy. If the crystal field energy is lower than the pairing energy then orbitals will all be filled singularly before becoming doubly occupied. This is known as a high-spin configuration. Contrastingly, if the crystal field energy is higher than the pairing energy then electrons will doubly occupy the lowest energy orbitals before filling orbitals at higher energies. This is known as a low-spin configuration. This theory is particularly important for understanding susceptibility data of $Mn_{0.5}Fe_{0.5}PS_3$ in Chapter 4.

1.2.1.4 Kramers Theorem

Finally, in some special cases, a system with a large J or S , can map onto a smaller J_{eff} or S_{eff} state through the application of Kramers theorem [31, 47]. Kramers theorem states that if a system has an odd number of unpaired electrons, then in the absence of a magnetic field, at least two-fold degeneracy of states must remain. The pairs of states are known as Kramers doublets and are time conjugate (Heisenberg uncertainty principle applies [41]). For some systems, the energy required to populate a higher energy doublet is so high that the system chooses to populate the lowest lying states in their entirety first, effectively producing lower spin systems.

An example is found in the study of LiYbO_2 in Chapter 3, where the Yb^{3+} ions with an electron configuration of $4f^{13}$ can be regarded as a Kramers ion. The moment arising from this Yb^{3+} ion should have $J = \frac{7}{2}$, but in fact, inelastic neutron scattering revealed that the four Kramers doublets split and that the lowest energy crystal electric field (CEF) transition is high enough from the ground state Kramers doublet for the system to map onto an effective, $J_{\text{eff}} = \frac{1}{2}$ state at low temperatures [46]. This can be very useful as it means that when measuring at low temperatures in experiments, only the ground state interactions are probed. This system, therefore, is a good candidate for exotic magnetic ground states as its moment size can be considered as quantum.

1.2.2 Lower Dimensions

Secondly, confining the magnetic lattice to one or two-dimensions will experimentally increase the quantum fluctuations of the system which in turn suppresses long-range magnetic order. Low-dimensional magnetic systems have been of theoretical and experimental interest for years, however until relatively recently, conventional magnetic order was thought not to exist in two-dimensional systems due to the Mermin-Wagner theorem [48–51]. Recently it has

been shown that there is a huge amount of exotic magnetism existing in low-dimensions, and theoretically, these systems are preferable as they are often easier to solve, and in some cases, exactly solve [52, 53]. Systems which combine low-dimensionality and interesting magnetism include layered compounds with van der Waals gaps [54, 55] such as the transition-metal thiophosphates, MPS_3 (explored in Chapter 4) [56–59], transition-metal halides like CrI_3 [60–62], and ternary iron-based tellurides such as Fe_3GeTe_2 [63–66]. For materials with covalent bonding between adjacent layers, increasing the separation of magnetic layers with non-magnetic ions in compounds like $YbMgGaO_4$ [20, 67, 68], or adding organic linkers to form MOF structures [25, 69, 70], has the potential to produce the same effect, by effectively suppressing the interlayer exchange between the magnetic planes.

1.2.3 Increase Competition

Finally, increasing the competition of exchange interactions between moments ensures a highly frustrated system. Earlier, I introduced the concept of geometric frustration but there are many materials with non-triangular based geometries that also exhibit magnetic frustration.

An example is the square lattice where the moments can easily align in a conventional ferromagnetic or antiferromagnetic arrangement [71–74]. Figure 1.6a) shows that in the J_1 - J_2 square-planar Heisenberg model, there are several magnetic ground states that are possible depending on the ratio of exchange interactions. For example, when $J_1 \gg J_2$, a conventional Néel antiferromagnetic ground state exists, or conversely when $J_2 \gg J_1$, a conventional columnar order is present. However, when the ratio of exchange interactions is between $0.4 \leq J_2/J_1 \leq 0.6$, then the interactions become frustrated and may lead to exotic magnetic ground states such as the quantum spin liquid (QSL) and valence bond crystal (VBC).

An example of a potential mechanism to mediate this magnetic exchange is superex-

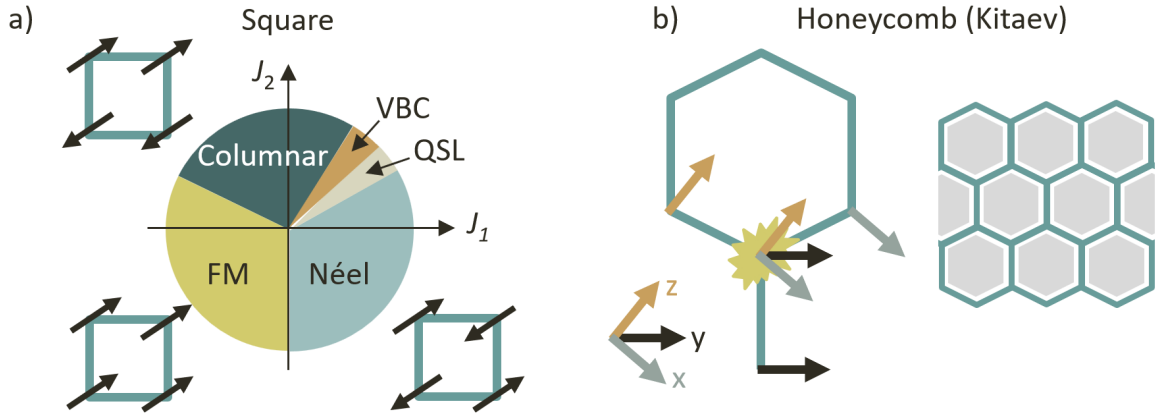


Figure 1.6: Different ways to generate magnetic frustration. a) The phase diagram of the J_1 - J_2 square-planar Heisenberg model includes frustrated quantum spin liquid (QSL) and valence bond crystal (VBC) as well as more conventional ordered states. b) The Kitaev model comprises of directionally dependent Ising spins on a honeycomb.

change as shown in Fig. 1.7 [75, 76]. In superexchange it is the overlap of the partially filled orbitals of metal ions (M) with the occupied orbitals of a non-magnetic mediator, for example, an oxygen ion (O^{2-}) that transfers the exchange. It is predicted that the M-O-M bond will mediate antiferromagnetic and ferromagnetic exchanges when the M-O-M bond angle is close to 180° and 90° , respectively. In real materials, superexchange pathways can be very complex, but for this work are particularly important in the discussion of diamond geometries in Chapter 3 [45, 77, 78].

Though not explored in this thesis, one area that is becoming increasingly prevalent is to engineer magnetic frustration via strong spin-orbit interactions, with the Kitaev model on a honeycomb lattice being a prime example [52, 53]. In the Kitaev model, moments are described as non-interacting Majorana fermions—where the particle and antiparticle are the same—with highly anisotropic couplings between the neighbours. On the honeycomb lattice, the moments form pairs of directionally dependent Ising spins, with each pair acting along a different crystallographic axis as seen in Fig. 1.6b). Since a single Ising moment

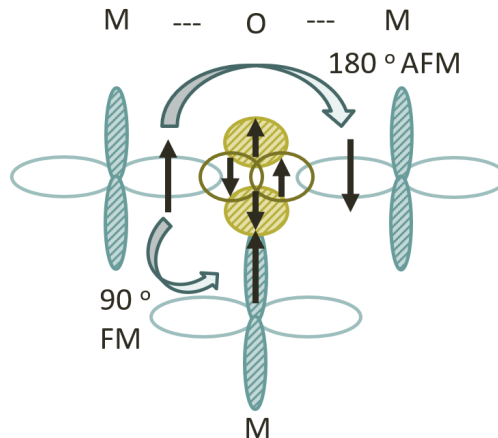


Figure 1.7: Superexchange is an example of an exchange interaction that can contribute to magnetic frustration. Superexchange pathways are mediated by non-magnetic ligands, such as oxygen. The geometry dictates if an ferromagnetic or antiferromagnetic arrangement is preferred.

can not spin in three directions simultaneously (up, right and in), the system becomes frustrated. The Kitaev model was particularly striking as it was the first exactly solvable spin liquid model presented, however, experimentally the search has largely focused only on two candidate systems, α - RuCl_3 [79–81] and $A_2\text{IrO}_3$ ($A = \text{Li}, \text{Na}$) [82–86], which are both highly susceptible to stacking faults and thus neither show this elusive magnetic ground state.

1.2.4 Chemical Disorder

As discussed, quantum magnetic ground states can be realised across a variety of different lattice types. These models often assume that the chemical structure is perfect, but in reality this is rarely the case. All real materials will have some degree of chemical disorder, and regardless of whether this disorder affects the magnetic or non-magnetic atoms or ions, the influence that this disorder can have on the magnetic ground state selection can be substantial [39, 67, 87]. Chemical disorder is associated with the physical arrangement of

atoms or ions away from their ideal positions, and can typically be grouped into three broad categories:

1. Compositional disorder which occurs when the stoichiometry of the system is different to what is expected.
2. Positional disorder where there is a translational error in the symmetry or when thermal energy distorts the structure.
3. Amorphous structures where there is a complete lack of periodicity in the structure.

1.2.4.1 Compositional Disorder

Compositional disorder occurs from the non-regular placement of two or more atomic species on a crystalline lattice. Compositional disorder can be induced from mixing ions of a similar charge and radius, like in the QSL candidate, YbMgGaO_4 , where on average there is a 50 % occupancy of Mg^{2+} and Ga^{3+} ions on the triangular bipyramid layers, but locally a completely random distribution throughout the non-magnetic lattice [68, 88, 89]. Additionally, instead of substituting similar components, compositional disorder is also found when components are removed from the system, whether that is intentional as in the production of vacancies for semiconductor applications [90], or accidental in the case of off-stoichiometries. A material that does not have the correct stoichiometry is often the result of the synthetic procedure, as particularly volatile reactants are hard to contain within the reaction. This may be overcome by changing the firing temperature, rate, time or changing the atmosphere and containing the sample within a vacuumed tube if necessary. As will be explored later in this thesis, the degree to which the sample is off-stoichiometry can be incredibly minimal and still have a profound effect on the magnetic ground state [39].

1.2.4.2 Positional disorder

Positional disorder is an effect that no real material can escape: thermal energy within the system causes individual atoms to vibrate off their average site positions. This can usually be accounted for in average-structure models with thermal parameters like the isotropic displacement parameters, B_{iso} . Substantial correlated positional disorder has however been found to have applications in ferroelectricity [91, 92], and be responsible for some exotic correlated states, like charge- and spin ices [93, 94]. Also grouped with positional disorder are materials where there is a translational error in the repetition of the crystalline lattice, for example, stacking faults. α - RuCl_3 is a Kitaev QSL candidate, and as described earlier, the Kitaev model considers the anisotropic interactions of moments across a two-dimensional honeycomb lattice [52, 53]. However, stacking faults in α - RuCl_3 , cause an interlayer exchange to occur between adjacent honeycomb planes, and so the system cannot be considered as two-dimensional, meaning the Kitaev state is not realised [80, 81]. Additionally, positional disorder can occur when there is strain present within the crystal. Strain is defined as the ratio between the change in length of a material with regards to its original length. Strain in materials is often observed in diffraction measurements as an overall broadening of peaks and drop in their intensity, and manipulating strain effects has become popular to try and tune certain magnetic and electric properties [95, 96].

1.2.4.3 Amorphous Structures

Finally, materials that lack a long-range ordered chemical structure are said to be amorphous. This means all of the average structure methods will not be useful in exploring materials as there is no average structure to probe. It is here that local structure determination, through diffuse and total scattering methods, come into their own. Many examples of materials with amorphous structures exist in nature and synthetic form, but the effects such disorder can have on quantum magnetic materials are not as successively characterised, due to the

complexities of the underlying chemical structure. Recently, materials with unconventional periodicity have been investigated on an unusual frustrated system composed from Truchet tiling on a MOF network [97], and in the spin glass phase of quasicrystalline compound, $\text{Ce}_3\text{Au}_{13}\text{Ge}_4$ [98].

1.3 Understanding Order: Average Structure Methods

The first step to understanding complex quantum magnetic materials is to measure the average or bulk properties of the material. Whilst magnetic susceptibility measurements can determine the magnetic ordering temperatures and an estimate for the strength of the interactions, they are not able to tell us the precise way the moments order. Neutron scattering experiments on the other hand, are an ideal tool to determine a material's magnetic structure as neutrons also have an inherent magnetic moment that can interact with unpaired electrons in the sample via the dipole-dipole interaction. Scattering from neutrons works due to the de Broglie relationship, that a particle can be considered as a wave and vice versa. This opens up the possibility to use other experimental probes such as X-rays and electrons in scattering experiments. The results of a scattering experiment are diverse depending on the setup of the instrument and probe used. For example, the elastic scattering produced from neutrons, X-rays or electrons can be used in a diffraction experiment to understand a material's chemical or magnetic structure. Though not utilised in this thesis, inelastic scattering occurs when there is a change in energy of the probe following its interaction with the sample, and may reveal information on the dynamics of the system. Diffraction techniques are a cornerstone method for materials characterisation and therefore essential to this thesis. In this section I will outline the fundamental concepts of average structure determination using X-ray and neutron powder diffraction needed to interpret the results presented in the results chapters, with a full description of the theory found in the following Refs. [99–101].

1.3.1 Scattering Experiments

Scattering experiments are typically divided into two classes, constant wavelength and time-of-flight (TOF).

1.3.1.1 Constant Wavelength

Constant wavelength diffraction measurements from neutron reactor sources like the Institut Laue-Langevin (ILL) or X-ray synchrotron facilities like the ESRF, involve selecting a single wavelength of a white beam using a monochromator. The wavelength chosen is similar to the interplanar spacing of a crystal, which allows for constructive interference to occur through the application of Bragg's law. The sample, usually contained in a cylindrical sample can or borosilicate capillary, diffracts the monochromised incident beam over a wide 2θ angular range. The detectors are either moved as a function of 2θ or on certain instruments, a large array of detector banks covering a wide angular range are used to capture all the scattering at the same time. More commonly scattering data are expressed as a function of the scattering vector, \mathbf{Q} , which can be related to the incident, \mathbf{k}_i and final, \mathbf{k}_f wavevectors of the probe by $\mathbf{Q} = \mathbf{k}_f - \mathbf{k}_i$. One of the most useful consequences of a constant wavelength setup is that the integration window (area over which scattering is measured) is exactly known. This is important, as in a diffraction measurement, the integration is only performed over the elastic line, but sometimes due to the excitations in the system, there is significant intensity outside the experimental window. Therefore, knowing how much of the data is visible within the diffraction pattern can help determine if the static approximation is valid and if the resultant analysis is likely to be physical or not.

This thesis has included many constant wavelength diffraction measurements for average structure determination including laboratory X-ray diffraction characterisation, synchrotron X-ray (ID22 at ESRF) and neutron diffraction (D20 and D2B at the ILL).

1.3.1.2 Time-of-Flight (TOF)

In contrast, time-of-flight measurements are performed at spallation sources such as the ISIS Neutron and Muon Source, where the neutron beam is produced from accelerating a pulsed beam of protons in a synchrotron. The proton beam is then collided with a heavy metal target, for example tungsten, which produces short packages of neutrons with a range of wavelengths within each pulse. The diffraction pattern is measured by fixing the scattering angle and measuring the time it takes for the neutrons to travel from the source to the detector, which is where the term time-of-flight comes from. The wavelength of the neutron is given by

$$\lambda = \frac{ht}{m_n L} \quad (1.9)$$

where h is Planck's constant, t is the neutron time-of-flight (μs), m_n is the neutron mass (kg) and L is the total flight path (distance from source to detector, m).

This thesis includes TOF measurements on the HRPD and WISH diffractometers, which are optimised for high-resolution powder diffraction and magnetic structure determination, respectively.

1.3.2 Interactions with Matter

In a powder diffraction experiment it is the intensity, I_{hkl} of the scattering that is measured. The intensity is proportional to the structure factor of the sample, F_{hkl} , squared.

$$F_{hkl} = \sum_j f_j \exp[2\pi i(hx_j + ky_j + lz_j)] \quad (1.10)$$

The exponential in this equation tells us where the diffraction is occurring from (the positions of the atoms in the unit cell, x_j, y_j and z_j , and the lattice plane of interest, h, k and l) and f_j , known as the scattering factor, tells us what the scattering species is and how it scatters. f_j therefore has different dependencies for neutrons and X-rays:

1.3.2.1 X-rays: $f_j = f(Q)$

The interaction between X-rays and the electron cloud of a material is mediated by the electromagnetic interaction. This is known as the atomic form factor, $f(Q)$. Because the scattering occurs from the number of orbital electrons, the magnitude of the signal is proportional to the atomic number, Z . $f(Q)$ has a form factor dependence, meaning the scattering power of all atoms decreases as a function of Q , which is due to the spatial distribution of the electrons acting across a similar length scale as the X-ray wavelength. Due to these dependencies, X-rays are very useful for studying heavier elements at low angles, but struggle to distinguish neighbouring atoms on the periodic table and low mass elements, such as oxygen.

1.3.2.2 Neutrons (nuclear): $f_j = -b$

The interactions between neutrons and the nuclear (crystallographic) structure is mediated by the strong nuclear force by the neutron scattering length, b . Unlike the X-ray case, b does not have a form factor dependence because the nucleus size, and the interaction length scale with the neutrons, are much smaller than the wavelength of thermal neutrons. The origin of b is thought to arise from the orientation of nuclear spins within the nucleus of an atom. This is important as neutrons can be used to distinguish between different isotopes of the same element. The size and magnitude of b is erratic across the periodic table, and this contrast can be useful for identifying elements close together (or isotopes), that would not be resolvable with X-rays. Unlike X-ray atomic form factors, the sign of b can be positive or negative, which depends on if the incident and outgoing waves are in or (180°) out of phase.

The nuclear scattering, $I_{\text{nuc}}(\mathbf{Q})$, is the sum of two terms (Fig. 1.8):

$$I_{\text{nuc}}(\mathbf{Q}) = I_{\text{coh}}(\mathbf{Q}) + I_{\text{incoh}}(\mathbf{Q}) \quad (1.11)$$

In the static approximation, $I_{\text{coh}}(\mathbf{Q})$ is the coherent scattering intensity, which concerns the

scattering from all atomic sites and is a function of the average scattering length, $b_{\text{coh}} \equiv \bar{b}$. Physically $I_{\text{coh}}(\mathbf{Q})$ can provide information on the crystallographic structure in diffraction (Bragg peaks) and correlated motions or collective excitations (eg. phonons and magnons) in inelastic scattering. In contrast, $I_{\text{incoh}}(\mathbf{Q})$, is the incoherent signal which arises from the deviations in the neutron scattering length from the mean value

$$I_{\text{incoh}}(\mathbf{Q}) = \frac{1}{N} \sum_i \left(\bar{b}_i^2 - \bar{b}_i^2 \right) \quad (1.12)$$

where \bar{b}_i^2 and \bar{b}_i^2 represent that the neutron scattering lengths have been averaged over all atoms of the same element and isotope, i . $I_{\text{incoh}}(\mathbf{Q})$ is related to the probability of self-scattering effects for a given element or isotope. Incoherent scattering typically adds a featureless background that contains no information about the crystal structure.

1.3.2.3 Neutrons (magnetic): $f_j = f_{\text{M}}(Q)$

Owing to the fact that neutrons have a magnetic moment, there is a second interaction type, this time between a neutrons magnetic moment and the electrons in the material via the dipole-dipole interaction. Similarly to the X-ray atomic form factor, the magnetic scattering of neutrons is subject to a form factor dependence, $f_{\text{M}}(Q)$. However, typically, the fall off in Q is more pronounced for magnetic neutron scattering as it is only the outermost electrons in the sub-shells involved in the interaction. This means that magnetic intensity is most distinctly seen at low Q . The magnetic form factor is also ion specific due to the different way the electrons can be arranged in the sub-shells. Magnetic form factors are obtained from the Fourier transform of the magnetisation distribution of a single magnetic ion [99]. Usually an analytical approximation, $\langle j_0(s) \rangle$ is used to estimate this form factor

$$f_{\text{M}}(Q) \approx \langle j_0(s) \rangle = A \exp(-as^2) + B \exp(-bs^2) + C \exp(-cs^2) + D \quad (1.13)$$

where $s = \sin\theta/\lambda$ (\AA) and the co-efficients are tabulated in the International Tables of Crystallography, Volume C [102]. For rare-earth ions where $L \neq 0$, it may be necessary to

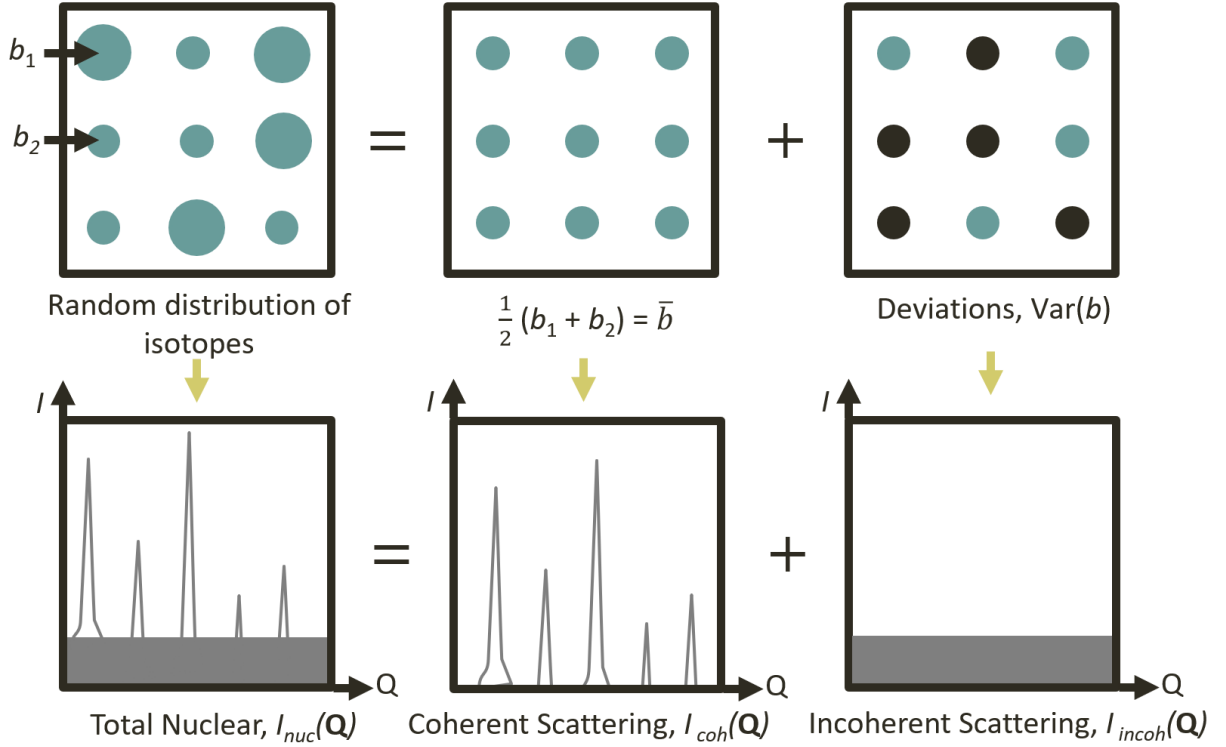


Figure 1.8: Schematic illustrating the origin of coherent and incoherent neutron scattering in a system with two different scattering lengths, b_1 and b_2 . The coherent scattering gives the Bragg peaks and arises from the average neutron scattering length, $b_{\text{coh}} \equiv \bar{b}$. Incoherent scattering arises from the deviation of the neutron scattering from the mean, $b_{\text{incoh}} \equiv \bar{b}^2 - \bar{b}^2$. Both contribute to the total nuclear scattering.

calculate the form factor to higher orders (j_2 , j_4 and j_6). $f_M(Q)$ can be converted into the elastic differential magnetic cross-section of a paramagnet via

$$\frac{d\sigma}{d\Omega} = \frac{2}{3}(\gamma r_0)^2 \left\{ \frac{1}{2} g f_M(Q) \right\}^2 S(S+1) \text{ barns/ster.} \quad (1.14)$$

where $\gamma = 1.9132$ is the gyromagnetic ratio of a neutron, r_0 is the classical radius of an electron and g is the Landé g -factor [103]. A magnetic material in its paramagnetic regime should show only a dependence according to Eq. 1.14, however experimentally for quantum materials this is rarely the case. In all of the results chapters the magnetic form factor is calculated and compared to the data to check if at high temperatures the paramagnetic phase has been reached.

1.3.3 Order and Diffraction

A well ordered, periodic crystal culminates in a series of Bragg peaks in diffraction patterns that are as unique as a fingerprint. The peak position gives information on the size and symmetry of the unit cell. The peak intensity reveals which atoms are contained within the unit cell and where they are. Finally, the peak shape is a convolution of the instrument resolution and the size and strain effects on the crystal. Integrated powder diffraction data can be analysed via a variety of techniques, most commonly Rietveld refinement [104], which matches a model to the data by a least squares process. Due to powder averaging and the integrated intensity being proportional to the structure factor, F_{hkl} of the sample squared, structure determination is often not possible in powder diffraction experiments only phase identification and structure refinement of known (or similar) substances. To determine the crystal structure without any prior model, single-crystal diffraction is usually required.

1.3.3.1 Average Chemical Structure Determination with Rietveld Refinement

Rietveld refinement is a process where a least squares refinement is carried out until the best fit between the observed powder diffraction pattern and the model is reached. One of the most important considerations during a Rietveld refinement is that it is a "whole" pattern approach which means that all the peaks are fit simultaneously and all contribute to the overall quality of the fit. This is important, as fitting the details of the main phase will not make physical sense if there is significant intensity from unaccounted for peaks of impurities or contributions from the sample environment in the data. There are typically two quality of fit parameters quoted in this thesis, χ^2 , and the weighted R -factor, R_{wp} (%)

$$\chi^2 = \sum_i \left(\frac{y_{\text{obs},i} - y_{\text{cal},i}}{\sigma_i} \right)^2 \quad R_{\text{wp}} = 100 \left[\frac{\sum_{i=1,n} w_i |y_{\text{obs},i} - y_{\text{cal},i}|^2}{\sum_{i=1,n} w_i y_{\text{obs},i}^2} \right]^{\frac{1}{2}} \quad (1.15)$$

where $y_{\text{obs},i}$ and $y_{\text{cal},i}$ are the observed and calculated values for the i^{th} atom, respectively, σ_i is the standard deviation, and w_i is the weighting factor. Rietveld refinement can be

analysed using a number of softwares, such as `Fullprof` [105], `Mag2Pow` [106] and `GSAS` [107]. I will outline the steps to a Rietveld refinement below [104].

1. Firstly a model is selected. Usually this comes in the form of a crystallographic information file (CIF) from the ICSD or single-crystal data from in-house characterisation. The model contains information on the space group symmetry, and where and how many atoms there are in the unit cell. If no previously determined structure or single-crystal is available, an alternative method to phase identification of a powder sample is to index the peaks followed by a Le Bail fit. This follows similar steps to Rietveld refinement, however the unit cell in this case is considered as empty. Realistically, the only information obtainable from a Le Bail fit is if the unit cell has the right space group and size.
2. The first step in a refinement is to get a reasonable guess of the scale of the pattern and background. Background points are normally selected manually and then fit with a polynomial function, for example, the Chebyshev function.
3. Next, the lattice parameters, a , b and c , and angles, α , β and γ are refined according to the symmetry of the space group. Usually this makes a large difference to the quality of the fit.
4. Then the peak shape. Peak shapes from diffractometers are rarely simple Gaussians, therefore a convolution of different shapes and asymmetries are required. Common peak shapes used in this thesis are Thompson-Cox Hastings (TCH) pseudo-Voigt profile with axial divergence [108, 109] for synchrotron X-ray and constant wavelength neutron, and convolution pseudo-Voigt [110] for time-of-flight (TOF) neutron.

The parameters used to fit peak shape are not often quoted in publications, however, understanding peak shape can reveal very important information on the average size, strain and behaviour of the crystal. In order to produce these physical values the instrument resolution needs to be well defined first. This can be achieved by measuring an

instrument standard, such as Si for ID22 and $\text{Na}_2\text{Ca}_3\text{Al}_2\text{F}_{14}$ for WISH, and performing a very comprehensive refinement. The results are then contained within an instrument resolution file (IRF) which essentially deconvolutes the sample and instrumental broadening. The FWHM of the Gaussian (H_G) and Lorentzian (H_L) components of the TCH pseudo-Voigt profile with axial divergence are given by [108, 109, 111]:

$$\begin{aligned} H_G^2 &= (U + (1 - \zeta)^2 D_{ST}^2(\alpha_D)) \tan^2\theta + V \tan\theta + W + \frac{I_G}{\cos^2\theta} \\ H_L &= (X + \zeta D_{ST}(\alpha_D)) \tan\theta + \frac{[Y + F(\alpha_Z)]}{\cos\theta} \end{aligned} \quad (1.16)$$

If using an IRF then V and W are set to zero for the sample, and the rest of the parameters have physical meaning in terms of strain (U, α_D, X) and size (Y, I_G, α_D). $D_{ST}(\alpha_D)$ and $F(\alpha_Z)$ are functions that describe the strain model and ζ is a mixing co-efficient for Lorentzian contributions to the strain. This theory has been used in the strain analysis of the ZnV_2O_4 samples in Chapter 2. `Fullprof` outputs two quantities, the apparent size (\AA), which can be considered as the coherent domain size (or volume) of the sample and the maximum strain, e (dimensionless, $\times 10^{-4}$) which is described by the Stokes and Wilson formalism [111]

$$e = \frac{\Delta d}{d} = \frac{\eta}{4} = \frac{\beta_D(2\theta)}{4 \tan\theta}; e = \frac{\beta_D}{2s} \quad (1.17)$$

where, η is the apparent strain, β_D is the breadth of the line profile due to strain and $s = 2 \sin\theta = 1/d$.

5. At this point, if there are any impurities or sample environment peaks, additional phases are added and refined in a similar way.
6. Returning to the main phase, the atomic co-ordinates of atoms not in special positions, and the isotropic thermal parameters, B_{iso} ($= 8\pi^2 U_{\text{iso}}$) are refined. B_{iso} accounts for that even in an average structure model, atoms are not completely stationary due to the thermal energy of the system. Though not present in this thesis, sometimes the distribution of thermal energy can be particularly distorted and anisotropic B_{iso} parameters may be necessary.

7. Finally, in some special cases, a correction to account for the powder sample not being perfectly isotropic is required. This is known as preferred orientation, and is often applied using a spherical harmonics function. This was used in Chapter 4 for $\text{Mn}_{0.5}\text{Fe}_{0.5}\text{PS}_3$ whose van der Waals layers slide over each other and is therefore very difficult to crush a single crystal into a perfect isotropic powder. However, as I will highlight in Chapter 3, caution should be taken as preferred orientation can completely change the distribution in peak intensities, which in this case, altered the previous physical interpretation of the material considerably.

1.3.3.2 Average Magnetic Structure Determination

In addition to the Bragg peaks produced from the chemical structure, the presence of an ordered magnetic structure can add additional peaks or intensity to a diffraction pattern. In these experiments, typically two measurements are required (1) at a high-temperature whilst the system is in its paramagnetic regime where no ordered magnetic intensity is expected, and (2) at a low-temperature, once the material has undergone its transition to a magnetically ordered phase. The intensities of magnetic Bragg peaks are proportional to the moment squared, and have a form factor dependence as given by $f_M(Q)$. Therefore, for the low spin systems explored in this thesis, the intensities of these magnetic Bragg peaks are often very weak in comparison to the average chemical peaks, and so isolating the magnetic intensity via temperature subtraction is essential. The positions of the magnetic Bragg peaks will depend on the propagation vector, \mathbf{k} , a vector quantity that relates the magnetic structure to the chemical structure. \mathbf{k} is known as commensurate if this relationship between the magnetic unit cell is a simple multiple of the chemical unit cell, and incommensurate otherwise. The identification of \mathbf{k} can be found by peak indexing on programs like `K-search` in `Fullprof` [105].

The full determination of a magnetic structure is completed using representational

analysis. Here, the little group G_k is defined, which contains information on the symmetry operations of the space group that involve a translation of the unit cell whilst preserving \mathbf{k} . The possible magnetic structures must be compatible with all the symmetry operators of G_k . These are known as irreducible representations, Γ_k , and are used to build the magnetic space group. Since representational analysis is complex, this process is usually aided by programs such as `BasIreps` in `Fullprof` [105] and `Mag2Po1` [106].

The different magnetic structures are then tried via trial and error against the data in a process similar to Rietveld refinement. Usually a refinement of the chemical structure is completed beforehand and the refined scale factor kept constant as the magnetic refinement is begun. This is to allow the moment size to be determined. Depending on the structure, other refinable parameters are the propagation vector (particularly if the structure is incommensurate), and the phasing of moments between different magnetic sites. This process was used to determine the incommensurate helical structure of LiYbO_2 in Chapter 3.

1.4 Understanding Disorder: Local Structure Methods

But not everything can be understood with an average structure model. The different types of disorder that were outlined earlier can lead to new features beyond the Bragg peak appearing in the scattering data. In a diffraction experiment, any intensity outside the Bragg peak is regarded as diffuse scattering. Usually diffuse scattering is quite flat and weak, as it arises from the random statistical disorder in the chemical or magnetic structure. But when this disorder becomes correlated over a local length scale, the diffuse scattering becomes structured, and these broad features and shapes contain an abundance of information on the local structure of a material. Unlike average structure methods which are analysed in reciprocal space, experimental signatures arising from structured diffuse scattering are often understood through analysis in real-space. A main aim of this thesis is to understand how

correlated disorder impacts the chemical and magnetic ground state selection of quantum materials. This section will therefore highlight the main techniques and analysis methods used in this thesis, diffuse neutron scattering, reverse Monte Carlo analysis on SPINVERT and pair-distribution function analysis.

1.4.1 Disorder and Diffraction

A simple way to understand how to identify different types of disorder experimentally is to think about how certain defects change the shape of Bragg peaks in diffraction measurements. In a perfect crystalline material, Bragg peaks would be infinitely sharp and narrow, with the width and shape determined only by the instrument resolution. But of course, the defects and disorder that inevitably exist in real materials, can distort the Bragg peaks and the type of distortion gives clues as to what is causing it. In a diffraction experiment the scattering is assumed to be completely elastic, and so if intensity is missing from a Bragg peak then this missing intensity must manifest somewhere else in the diffraction pattern. For example, if a material was particularly strained (positional disorder) then there may be a drop in intensity and broadening of the peaks. An example of the effect of strain on peak shape can be found in Chapter 2. Alternatively, if there was atomic site disorder (compositional disorder) then there may be a change in intensity of the Bragg peaks compared to what is expected. In this case, when planning experiments, its particularly useful to think about the atoms that may be disordered, as different experimental probes will give different results. This is highlighted in Chapter 4, as short-range chemical disorder would not be resolvable with X-rays due to manganese and iron being neighbours on the periodic table, but is resolvable through neutron scattering due to their contrasting neutron scattering lengths. Furthermore, asymmetric features become common in materials with stacking faults (positional disorder) or when the dimensionality of the system is lowered. This is also highlighted in Chapter 4 through Warren shape analysis of a key quasi-two-dimensional magnetic peak [103]. These

are all examples of disorder that act across relatively long length scales, and can often be accounted for with average structure models.

But when disorder acts on a short-ranged length scale, features outside the Bragg peak begin to appear. These features are often broad in Q and weak in intensity, and this makes physical sense, as instead of scattering from a structure that is well defined, the scattering is now occurring from something that has lots of variation. This is known as diffuse scattering and refers to anything outside of the Bragg peak. Structured diffuse scattering is the result of correlated disorder within a material. This is a key difference. Broad peaks, bumps and features appear when the disorder is correlated. If the disorder is truly random then the diffuse scattering will be flat, as all of these tiny distortions cancel each other out. It is the correlations that give the shape to the structured diffuse scattering, and understanding these correlations, why they arise and how they interact, is the main focus of this work.

1.4.1.1 Measuring Diffuse Scattering on D7

Because the scattering of structured diffuse features stem from correlated short-range disorder, the intensity of these features are very weak in comparison to average Bragg features. Consequently, diffuse scattering is often overlooked in the analysis of diffraction data, as it can easily be mistaken for a lumpy or poorly measured background. However, by considering these diffuse features, a lot of information about the materials local structure can be obtained. One of the best instruments to measure diffuse scattering data on is the D7 diffractometer at the ILL [112, 113]. A characteristic that makes D7 particularly suited to the study of diffuse features is its use of polarisation analysis—a technique which separates the total scattering into component parts so that diffuse features are more easily visible [112–116]. An example data set measured on D7 is shown in Fig. 1.9. In a conventional diffraction experiment, only the total scattering (dark blue) would be accessible. Figure 1.9, taken from Chapter 4 is a particularly nice example of a D7 measurement since there is clearly lots of

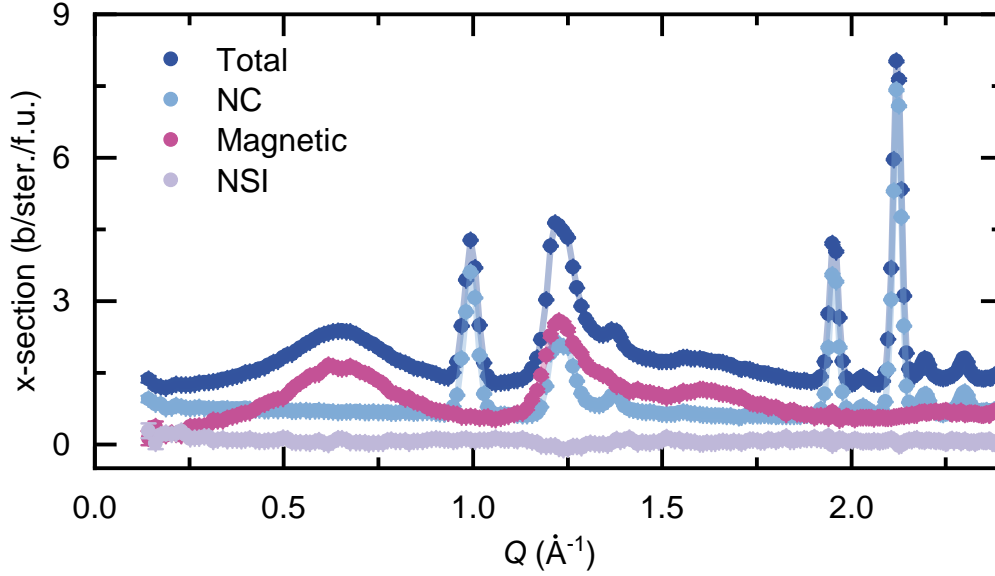


Figure 1.9: Example data from D7 showing the breakdown of the total scattering (blue) into different contributions to the scattering; nuclear coherent (NC), magnetic and nuclear-spin-incoherent (NSI) shown in light blue, pink and lilac respectively.

diffuse structure within the total scattering. But from the total scattering alone, it would be difficult to assign the features as originating from the chemical or magnetic structures, therefore introducing the need for polarisation analysis.

On D7 (Fig. 1.10) [112, 113], cold neutrons are first monochromated by a pyrolytic graphite monochromator with wavelengths 3.1 Å, 4.8 Å or 5.7 Å. In this thesis, all D7 experiments used a 4.8 Å wavelength, accessing a reciprocal space range of $0.15 \leq Q \leq 2.5 \text{ \AA}^{-1}$ and integration window of $-20 \leq \Delta E < 3.5 \text{ meV}$. The beam of neutrons is then polarised by a supermirror of alternating magnetic and non-magnetic Co/Ti layers that are magnetically saturated in the vertical (z) direction [117]. The beam polarisation is preserved by applying a small "guide field" ($\approx 10^{-3} \text{ T}$) along the z -direction. The neutrons then pass through a Mezei spin-flipper—a coil which non-adiabatically changes the direction of the polarised beam—which is therefore off when measuring non-spin-flip (NSF, initial and final spin states are the same) cross-sections and on when measuring spin-flip (SF, initial and

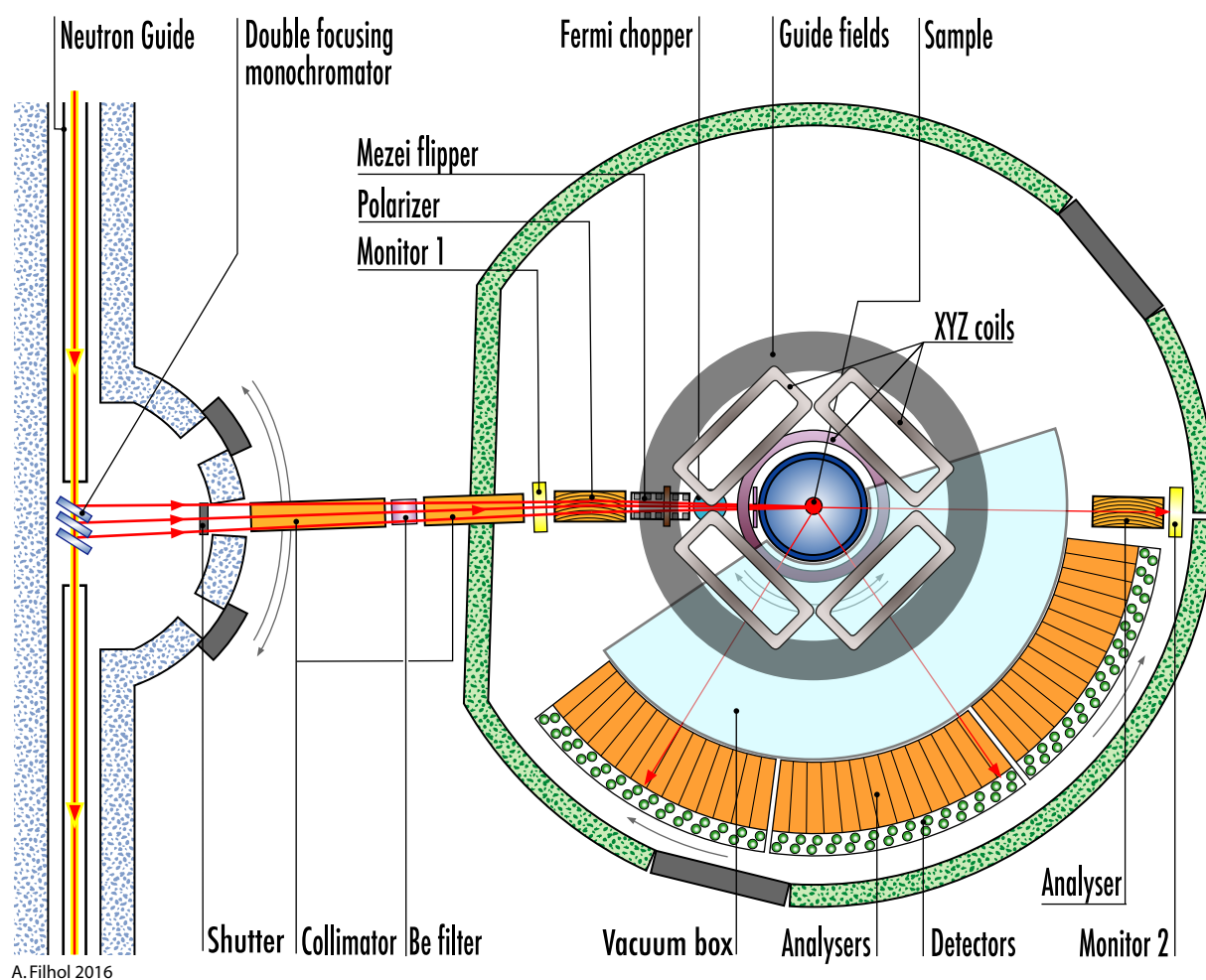


Figure 1.10: Schematic of the diffuse scattering diffractometer, D7 at the ILL [112, 113].

final spin states are different) cross-sections [116]. Next, the neutrons are rotated into the x , y , or z directions using one orthogonal pair and two quadropolar Helmholtz coils near the sample position. After scattering from the sample, the neutrons are analysed by a second set of supermirrors in their final spin state (NSF or SF) over a wide angular range (132°) using three multi-analyser detector banks.

This polarisation process and measurement of the initial and final spin states of the neutrons, means that the total scattering can be split further via polarisation analysis. The mathematics behind polarisation analysis can be found in Refs. [114–116] but is governed by three general rules:

1. Nuclear coherent (NC) and isotope incoherent (ii) scattering is entirely NSF
2. Spin-incoherent scattering is 1/3 NSF and 2/3 SF
3. Components of magnetisation; $\mathbf{M}_\perp \parallel \mathbf{P}_i$ is NSF, and $\mathbf{M}_\perp \perp \mathbf{P}_i$ is SF, where \mathbf{P}_i is the polarisation of the beam along a defined axis.

As a consequence, the cross-section can be separated into its component parts whilst remaining sensitive to the direction of magnetic moments. The D7 data in this thesis were measured according to the xyz -polarisation analysis method, which measures the ratio of SF:NSF moments along the three orthogonal x , y and z -axes [114, 116]. The directions are chosen so that x and y are in the scattering plane and the sample is rotated around z in a single-crystal measurement. Following the data reduction, the total scattering is split into the three parts shown in Fig. 1.9. The nuclear coherent, NC (light blue) and magnetic (pink) are the contributions arising from the chemical and magnetic structures of the material, respectively. Diffuse and average structure scattering can occur in both the NC and magnetic contributions, but the origin is now clearly distinguishable. Finally, the nuclear-spin-incoherent, NSI (lilac) gives a featureless background and arises from the nuclear-spin-incoherent scattering of the sample.

The different cross-sections are analysed separately, with the main focus in this thesis being the magnetic cross-sections and are detailed later. Nevertheless, the other cross-sections still provide important information on the sample. For example, the NC can contain important information on the local chemical structure of the sample, or generally be used to check the absolute normalisation process via Rietveld refinement on a program such as `Fullprof` [105]. Placing the data on an absolute intensity scale, with units b/ster./f.u., is important for this work as the magnetic moment size can be determined in the later reverse Monte Carlo analysis. D7 data are normalised to an absolute intensity scale through the measurement of several careful calibration standards.

- Firstly, the measurement of an empty and cadmium filled sample can is used to estimate the instrumental background.
- Then, an amorphous SiO₂ standard is used to correct for polarisation inefficiencies as it shows only nuclear coherent scattering (SF intensity would be zero if the polarisation was perfect) and has only diffuse scattering, so a liquid-like structure factor is observable in all detector banks at once.
- Finally, a vanadium standard is measured to normalise the detector efficiencies, because the scattering from V is flat in Q .
- The data are then normalised to the incoherent scattering from the vanadium standard. All of these corrections and data reduction were performed using the LAMP software at the ILL [118].

This process can then be checked by performing a Rietveld refinement, where a scale factor is determined which is related to the absolute intensity via the following equation:

$$I_{\text{expt}} = sI_{\text{abs}} \quad \text{where} \quad s = \text{FPScale} \times \frac{2\pi^2NV}{45\lambda^3} \quad (1.18)$$

where I_{expt} and I_{abs} are the experimental and absolute intensities, FPScale is the scale factor produced from a Rietveld refinement on `Fullprof`, N is the number of atoms per unit cell (can be substituted for N_{mag} , number of magnetic atoms per unit cell to convert to b/ster./spin), V is the volume of the cell in \AA^3 and λ is the wavelength in \AA . If the absolute normalisation on D7 is correct then $s = 1 \pm 0.1$. This conversion can also be used to convert arbitrary scattering counts to absolute units, like for the analysis of D20 data in Chapter 2. A similar procedure can be used to convert TOF data to absolute units, which was used in Chapter 2 for the WISH data

$$s_{\text{TOF}} = \text{FPScale} \times \frac{4\pi NV \sin\theta}{\text{dtt1}} \quad (1.19)$$

where dtt1 ($\mu \text{\AA}^{-1}$) is an instrument parameter that relates d -spacing to TOF. Additionally, the NSI can be used to check the separation of the cross-sections has worked correctly, as it

is expected that the NSI be flat and equal to the nuclear-spin incoherent cross-section of the sample.

To summarise, diffuse scattering gives information of the correlated short-range order within a material. Diffuse features are very weak and broad in comparison to average Bragg features meaning they are often overlooked in the analysis of diffraction data. However by using polarisation analysis on an instrument such as D7, diffuse features can be more easily accessible as the data is split into the chemical and magnetic cross-sections. In this thesis, D7 has been used to study both ZnV_2O_4 samples in Chapter 2, LiYbO_2 in Chapter 3 and powder and single-crystal samples of $\text{Mn}_{0.5}\text{Fe}_{0.5}\text{PS}_3$ in Chapter 4.

1.4.2 Reverse Monte Carlo SPINVERT Analysis

Powder diffuse magnetic scattering data were analysed using reverse Monte Carlo (RMC) methods on the program SPINVERT [119–121]. Usually, SPINVERT analysis works best on data containing only diffuse magnetic scattering data that has been isolated via polarisation analysis. However, it is possible to use temperature subtracted data (Chapter 2) and with a recent version of SPINVERT model magnetic Bragg peaks and diffuse scattering simultaneously (Chapter 3) [121].

SPINVERT follows conventional RMC processes, which are briefly outlined here. Firstly, a box is defined with the positions of the magnetic sites, which is then used to generate a supercell. It is best to use periodic boundary conditions to avoid edge effects, and this particular question is explored in more detail in Chapter 3. A classical spin vector with a random orientation is assigned to each of the sites and a sum of the squared residuals is calculated:

$$\chi^2 = W \sum_Q \left[\frac{I_{\text{calc}}(Q) - I_{\text{expt}}(Q)}{\sigma(Q)} \right]^2 \quad (1.20)$$

where $I(Q)$ is the powder-averaged magnetic scattering intensity for calculated and experi-

mental values, $\sigma(Q)$ is the experimental uncertainty and W is an empirical weighting factor. One spin is then randomly chosen and its orientation is changed depending on the anisotropy set by the user. After the move, χ^2 is recalculated with this new configuration of spins and compared to the previous result. If $\chi_{\text{new}}^2 < \chi_{\text{old}}^2$ then the move is accepted and the process continues from there. If $\chi_{\text{new}}^2 > \chi_{\text{old}}^2$ then the move is accepted with a probability according to W . This process is repeated until convergence, where no improvement in χ^2 is found as the difference between the data and residuals has been minimised, or the maximum number of moves is reached. Though specific to the data set being analysed a good rule of thumb is to aim for a configuration that produces an acceptance ratio starting around 50 % and finishing at around 85 %.

Since RMC methods are model independent, **SPINVERT** will always find the most disordered configuration of moments that will fit the data. Consequently, choosing the correct parameters to begin a RMC calculation is essential to obtaining physical results. An example is shown from Chapter 4 in Fig. 1.11 where the spin dimension of the moments is changed between 1 (Ising), 2 (XY) and 3 (Heisenberg) rotational degrees of freedom. Figure 1.11a) shows the fit to the powder data from **SPINVERT**, where each model is relatively similar. The peak intensity at $Q = 1.2 \text{ \AA}^{-1}$ is best fit by the Ising model but it is not definitively the correct answer. It can therefore be beneficial to reconstruct the expected single-crystal scattering planes via fast Fourier transforms on a program such as **SCATTY** [122]. Conclusive confirmation of the model comes by comparing the **SPINVERT** simulation to a measured single-crystal (Chapter 4, Fig. 4.8). The reconstructions of the magnetic scattering are shown in Figs. 1.11b) - g) and show stark differences between the models. For example scattering in the $(0 k l)$ plane should show strong Bragg rods at $(0 2 0)$. However, for c) XY and d) Heisenberg moments there is additional vertical intensity between $(0 \bar{1} 0)$ and $(0 1 0)$ which is not observed in the measured single-crystal. Additionally, in the $(h k \frac{-h}{3})$ plane, f) shows only very weak, smudged intensity at magnetic Bragg positions, and g) has the weaker Bragg spots missing. Therefore, the model that most accurately reproduces the

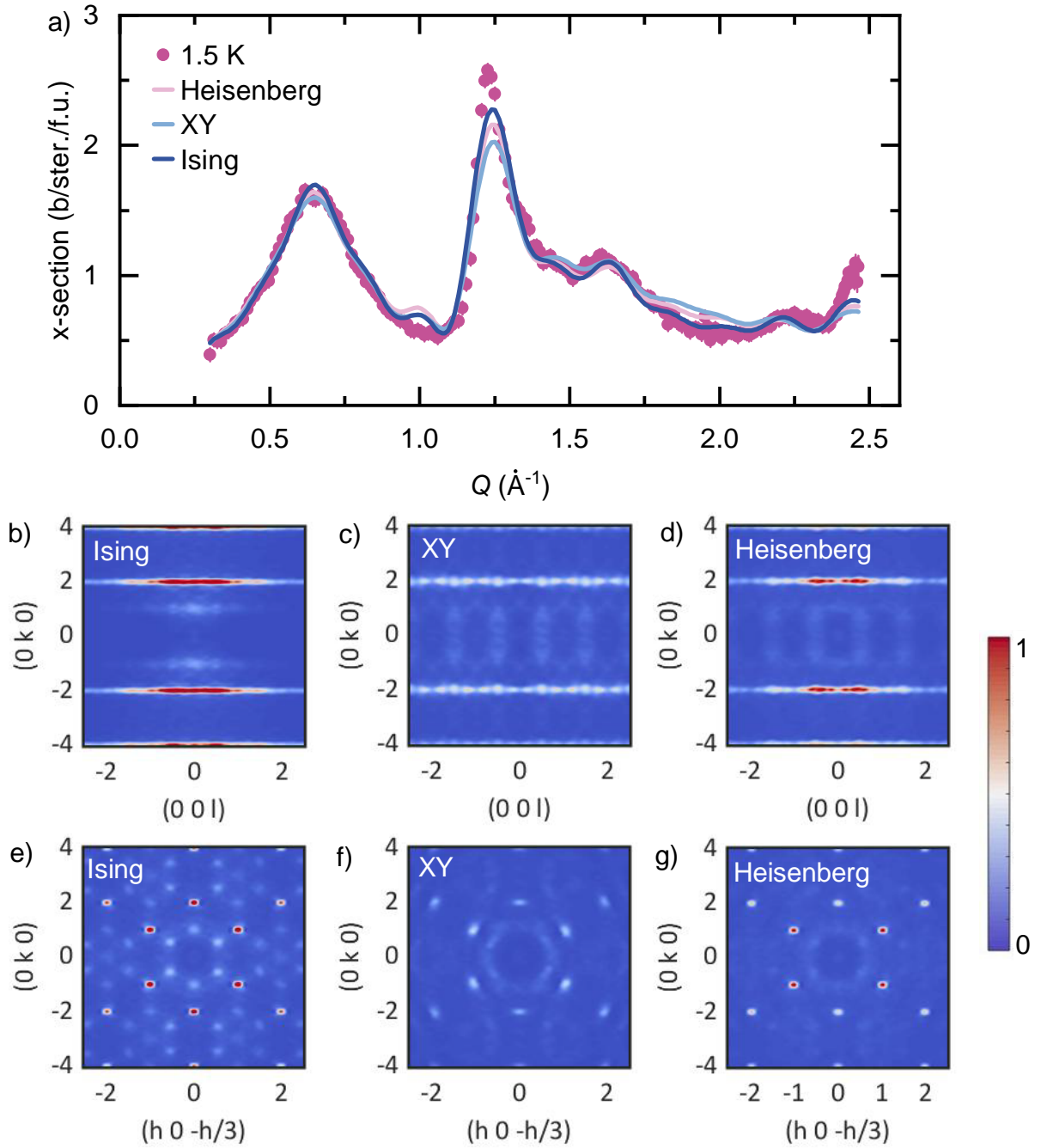


Figure 1.11: Effect of changing spin dimensionality in SPINVERT on the a) powder fit and b - g SCATTY single crystal reconstructions of $\text{Mn}_{0.5}\text{Fe}_{0.5}\text{PS}_3$ (Chapter 4). Reconstructions in the b - d) $(0 k l)$ plane and e - f) $(h k -\frac{h}{3})$ plane. Intensity of data have been normalised as given by the colour bar.

single-crystal scattering data is the Ising model described in the main text in Chapter 4, and was confirmed through the reconstruction of the single-crystal scattering planes.

Similarly, other simulation conditions need to be optimised in order to produce physical results. These conditions include the supercell size, which determines how many atoms are included in the box and the boundary conditions of the calculation. Practically, simulations work best when the box is approximately cubic as spin correlations are calculated radially from the centre, and therefore needs to be large enough to calculate spin correlations over a sufficient range but not too large that the statistical noise of the data is fitted. The weight, W , is an empirical factor that is loosely related to the Debye-Waller factor and used to determine the acceptance ratio of bad moves ($\chi_{\text{new}}^2 > \chi_{\text{old}}^2$). If the weight is too small then the RMC calculation tends to accept too many bad moves and underfit the data. If the weight is too large then the data are overfit, picking up every small bump and statistical noise in the data. Finally, calculations need to be repeated multiple times from a new seed to ensure convergence and average out statistical noise. The number of runs needed is dependent on the quality of the data and magnitude of the diffuse features.

For data collected on D7, a scaling factor is determined during the refinement. The scale factor is classically related to the size of the effective magnetic moment, μ_{eff} via Eq.1.21

$$\mu_{\text{eff}}^2 = \text{scale} = g^2 S(S + 1) \mu_{\text{B}}^2 \quad (1.21)$$

where g is the Landé g-factor and S is the total spin for the system. For data measured within the paramagnetic regime, this can be cross-checked with the moment measured from magnetic susceptibility to ensure that the full intensity of magnetic scattering is being captured within the integration window of D7. For the diffuse scattering data collected on WISH/D20 in Chapter 2 that were temperature subtracted, the scale needs to be fixed at the expected classical moment size squared.

1.4.3 Spin Correlations

Ultimately, the measurements and subsequent analysis of diffuse magnetic scattering data are probing the emergent correlations between pairs of moments throughout the magnetic structure. Understanding these correlations therefore provides an indication of the length scales over which different types of orderings exist, and their interactions with each other. Following on from the RMC fits from SPINVERT, the radial spin-spin correlations can be calculated, $\langle \mathbf{S}(0) \cdot \mathbf{S}(r) \rangle$ by SPINCORREL [119, 120].

$$\langle \mathbf{S}(0) \cdot \mathbf{S}(r) \rangle = \frac{1}{N} \sum_{i=1}^N \sum_{j=1}^{Z_i(r)} \frac{\mathbf{S}_i \cdot \mathbf{S}_j}{\langle Z_i(r) \rangle} \quad (1.22)$$

where \mathbf{S}_i is a spin vector, N is the number of spins within the supercell and $\langle Z_i(r) \rangle$ is the average number of spins that coordinate to a central spin, i at distance, r . The spin correlation function, $\langle \mathbf{S}(0) \cdot \mathbf{S}(r) \rangle$ is normalised to be equal to $+1$ if all neighbours at an equivalent r are ferromagnetically coupled and -1 if all neighbours are antiferromagnetically coupled. The correlations are calculated radially, so are averaged throughout every pair of atoms at an equivalent distance across the supercell and over multiple runs to remove statistical noise. An example is shown in Fig. 1.12a) for a configuration where one spin-up moment is interacting simultaneously between three moment pairs at an equivalent r . All neighbours are ferromagnetically coupled, therefore the $\mathbf{S} \cdot \mathbf{S}$ for each coupling is $+1$, giving the average as $\langle \mathbf{S}(0) \cdot \mathbf{S}(r) \rangle = \frac{+1+1+1}{3} = +1$, or fully ferromagnetic. Alternatively Fig. 1.12b) has two antiferromagnetic couplings ($\mathbf{S} \cdot \mathbf{S} = -1$) and one ferromagnetic coupling ($\mathbf{S} \cdot \mathbf{S} = +1$) giving a total $\langle \mathbf{S}(0) \cdot \mathbf{S}(r) \rangle = \frac{+1-1-1}{3} = -\frac{1}{3}$. Thus, equation 1.22 tells us the average magnitude of the correlation for a given distance, r .

In real materials, the $\langle \mathbf{S}(0) \cdot \mathbf{S}(r) \rangle$ is much more complex as alluded to in Fig. 1.12c). During this thesis, different methods are employed in an attempt to relate these correlations to their physical meanings within the materials. For example, it can be useful to split correlations across different high symmetry planes, or for layered compounds, to look within and between the layers. Additionally, taking the absolute magnitude of the correlations can

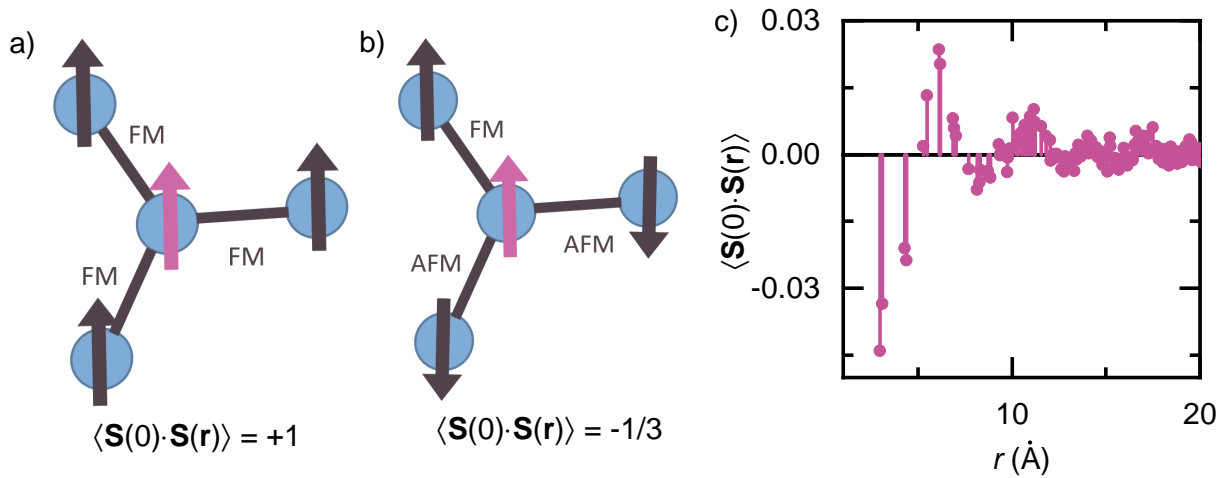


Figure 1.12: Diagram illustrating the correlation between three neighbouring moments at an equivalent distance from the central pink moment. a) If all the moments are coupled ferromagnetically (FM) then $\langle \mathbf{S}(0) \cdot \mathbf{S}(r) \rangle = 1$. b) If there are two antiferromagnetic neighbours and one ferromagnetic neighbour, then $\langle \mathbf{S}(0) \cdot \mathbf{S}(r) \rangle = -1/3$. c) Example of calculated spin correlations for a real material as a function of interatomic distance, r .

reveal new patterns that may be fit with exponential or polynomial functions, to reveal characteristic correlation lengths or strengths. Alternatively, a lot of materials with correlated disorder show a damped oscillatory dependence, where the period of the oscillation can be related to the correlation length of the material.

1.4.4 Pair Distribution Function Analysis

So far I have mostly considered the Bragg and diffuse scattering intensities separately. This works well if the distortions are small in strongly crystalline materials, but not for liquid and amorphous structures, or those approaching the nanoscale. But we must remember that Bragg and diffuse scattering exist together, and therefore analysing them together can help us understand materials structures with ever growing complexity. Such experiments

are known as total scattering experiments, and they mean just that—aiming to measure all of the scattering from all of the sample over all of reciprocal space. The most intuitive way to view these total scattering data is to take a Fourier transform of the data to produce a pair-distribution function (PDF), where the peaks are the probability of finding a pair of atoms separated by a distance r from the origin [123–125].

Experimental PDFs can be collected using X-rays, neutrons or electrons. The general steps to generating a PDF are summarised in Fig. 1.13, but for the discussion I will only use the case of X-rays. Firstly the intensity of experimental data is integrated to give a standard two-dimensional diffraction pattern, $I(2\theta)$ (Fig. 1.13a)). This is exactly the same data processing as a standard powder diffraction experiment. The data are then normalised by the scattering cross-section to produce a structure function, $S(Q)$ via Eq. 1.23 (not to be confused with structure function, F_{hkl} defined earlier).

$$S(Q) = 1 + \frac{I(Q) - \langle f_j^2(Q) \rangle}{\langle f_j(Q) \rangle^2} \quad (1.23)$$

where f_j is the scattering factor. A more conventional way of expressing $S(Q)$ is to calculate the reduced structure function, $F(Q)$ (Eq. 1.24) as the data are now transformed to physical units.

$$F(Q) = Q[S(Q) - 1] \quad (1.24)$$

As can be seen in Fig. 1.13b), these two steps act to amplify some of the small signals at high Q . Finally by taking a Fourier transform, the data are converted into the pair distribution function, $g(r)$ as shown in Fig. 1.13c) by the following equation.

$$g(r) = \frac{2}{\pi} \int_0^\infty F(Q) \sin Q(r) dQ \quad (1.25)$$

The overall success of the PDF analysis depends largely on the quality of the data collected and the data reduction, which is much more involved than a standard diffraction experiment. In the first instance, PDF data should be collected over the largest Q -range possible. The explanation for this is purely mathematical, as the integration of a Fourier

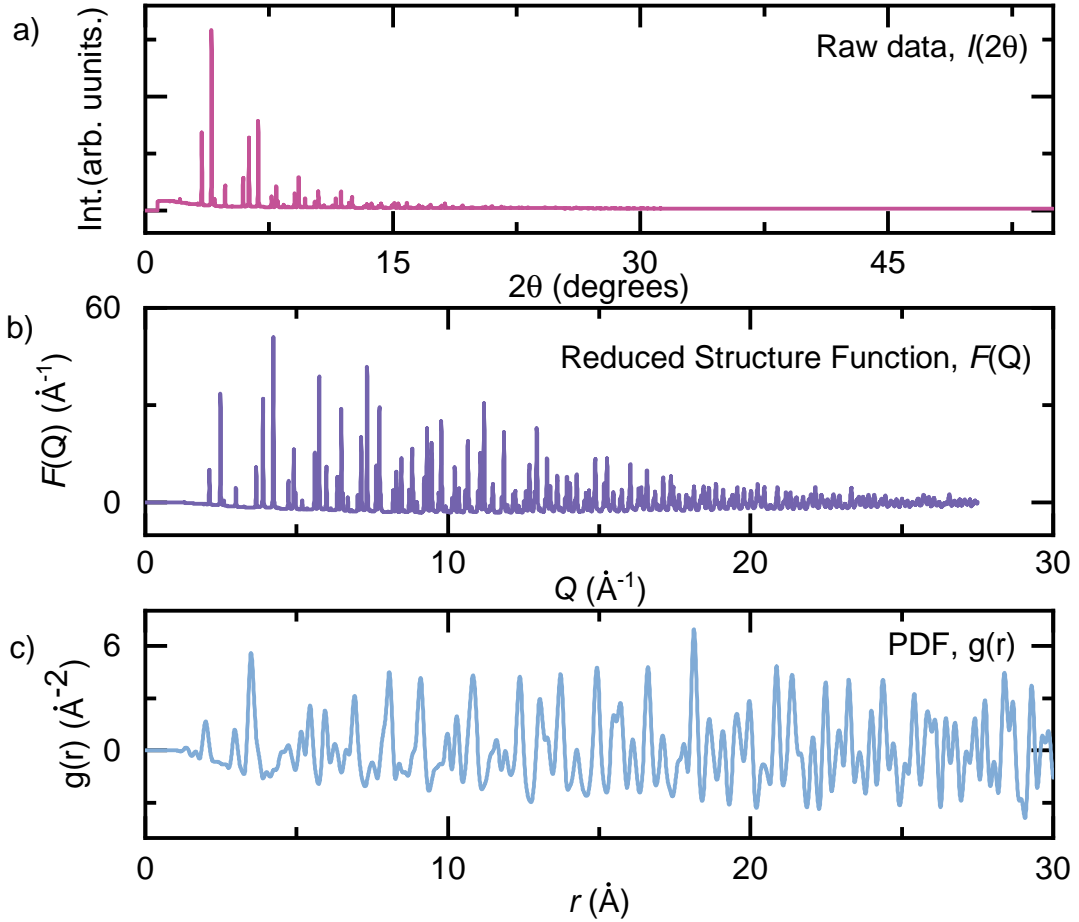


Figure 1.13: PDF data reduction involves a) measuring high quality data over a large reciprocal space range, b) normalising the data and converting into physical units, $F(Q)$ and c) taking the Fourier transform to make a pair distribution function, $g(r)$.

transform would ideally occur over infinite space (Eq. 1.25). Of course it is not possible to measure scattering over an infinite range, and this finite integration range leads to artificial peaks, known as termination ripples, in the PDF. The termination ripples can be smoothed out by a parameter, r_{poly} , which is applied during the data reduction as a polynomial correction to the data and is an approximate low- r bound of reliable g values. In order to increase the Q -range, the wavelength of the X-ray should be reduced, which does consequently lower the resolution of the diffraction data.

Careful background measurements are also required, with the measurement of an empty capillary matching closely the sample PDF temperature, time measured and diameter. Typically, the background measurement is slightly oversubtracted to account for the self-scattering and absorption that occurs during the measurement of the sample. For the case of X-rays, an additional problem is encountered by measuring out to high Q , as the atomic form factor has very low magnitude at higher angles. Therefore, synchrotron radiation is preferred, as the high intensity of X-rays ensures high quality data at all scattering angles. During the conversion of the raw data to $S(Q)$, the intensity is often divided by the atomic form factor squared, which is useful as this amplifies these small signals in the high Q region.

Analysis methods of PDF data are typically divided into two groups, big box and small box modelling. Big box modelling such as `RMCPProfile` [126] involves (reverse) Monte Carlo techniques which have a huge number of parameters and a very small number of constraints. The flexibility in these methods is very powerful for highly disordered materials but the physical interpretation can be very difficult to understand and the data can easily be overfitted. In contrast, small box methods like `PDFGui` [127] are similar in principle to Rietveld refinement, a model is chosen and its parameters refined to the data. Consequently there are only a small number of highly controllable parameters which leads to potential model bias. In this thesis, I will focus our attention on small box modelling using `PDFGui`, which was used to analyse the ZnV_2O_4 samples in Chapter 2 with data collected from ID22 at the ESRF.

The instrument resolution is specific to the range the data are fit over and must be redetermined each time. At ID22 the instrument standard was LaB_6 and parameters describing the resolution, Q_{broad} (peak broadening due to increased noise at high Q) and Q_{damp} (peak dampening due to limited Q resolution) were refined. Data are first fit over an average length scale, $\sim 50 \text{ \AA}$. The steps to the refinement are similar to Rietveld; scale, lattice parameters, atomic positions and isothermal displacement parameters (U_{iso}) are refined. This should give comparable results to the average structure refinement from Rietveld analysis,

with the exception of U_{iso} which is normally better estimated in PDF refinements due to the larger 2θ measurement range. An agreement factor, R_{wp} and χ^2 (Eq. 1.15) is calculated, but due to the complexity and number of variables in a PDF, it is not so common to quote these values. Instead it is beneficial to look for systematic differences between the refined model and data and see which atom pairs these distances relate to. If a common discrepancy is identified then the local region can be probed via the carbox method—where a small section of the PDF is analysed and the box slid along the PDF to see how different parameters evolve as a function of r . The carbox method can be very useful for identifying the breadth and degree of local disorder from the average structure.

1.5 Characterising Real Quantum Materials

This aim of this thesis is to understand how to combine these average and local structure methods to characterise real quantum materials. The ingredients to quantum magnetic materials that I outlined earlier in Section 1.2, all play an important role in selecting the magnetic ground state, with each offering unique experimental signatures. In this next section I will explore the experimental signatures of a few of the most exciting quantum magnetic ground states, their relationship with disorder, and some real life case studies which have combined these experimental methods in order to understand their materials complex ground states. This is the approach that will be followed in the experimental chapters of this thesis.

1.5.1 Quantum Spin Liquid (QSL)

Quantum spin liquids are complex magnetic ground states that remain dynamic and have correlated fluctuations, theoretically down to absolute zero. Traditionally, experimental signatures for a QSL are those which describe the absence of long-range order, for example,

the lack of a magnetic transition in magnetic susceptibility or no magnetic Bragg peaks in neutron diffraction. A common parameter quoted to gauge the size of the spin liquid regime is the frustration parameter, $f = |\theta_{\text{CW}}|/T_{\text{m}}$, with a system said to be highly frustrated if $f > 10$, and a true QSL having $f = \infty$ since $T_{\text{m}} = 0$ [9]. From this definition, it may initially be difficult to separate a QSL from a conventional paramagnet. But they are different. A QSL has a strongly correlated short-range ordered state which is induced from the quantum entanglement and superposition of the dimerised singlets in the system. The moments in paramagnets on the other hand are not strongly interacting but rather randomly fluctuating. Despite the emphasis on identification of a QSL by omission of long-range ordered features, there are a number of specific experimental signatures that are strongly associated with QSLs. For example, the continual relaxation of an antineutron in μSR measurements down to low-temperatures is a signature of the dynamic motion of the moments [128]. Furthermore, broad features and missing entropy in heat capacity, and broad continua of scattering in inelastic neutron measurements are indicative of the formation of short-range correlations, with the latter revealing information on the dynamics of the moments [9]. In a QSL, if the inelastic scattering is separated by distinct energy levels, this system is said to be gapped, as energy is required to excite the singlet ground state to the triplet excited state. This behaviour would not be observed for a paramagnet. Alternatively, if the inelastic scattering is continuous and no sharp energy excitations are required then the system is referred to as gapless [8, 129].

There have been many candidate materials considered for the QSL ground state. A notable example is YbMgGaO_4 , which was selected due to the Yb^{3+} moments having an effective spin $J_{\text{eff}} = \frac{1}{2}$, and the two-dimensional triangular magnetic sublattice combining low dimensionality and geometric frustration. Despite multiple positive indicators for the QSL ground state including no magnetic ordering down to 30 mK, and broad features in specific heat and inelastic neutron scattering, the inherent compositional disorder of the non-magnetic Mg^{2+} and Ga^{3+} ions means that determining the true nature of the magnetic

ground state remains elusive [20, 88, 89]. Another key example is the case of barlowite, which has near two-dimensional kagomé layers of $S = \frac{1}{2}$ Cu^{2+} ions, separated by an inter-site Cu^{2+} ion. Barlowite was chosen as a candidate system to overcome the problem of compositional disorder between Zn^{2+} and Cu^{2+} ions in the interstitial position of herbertsmithite, another $S = \frac{1}{2}$ kagomé mineral which has shown many QSL-like properties [23, 130, 131]. However, not only was barlowite found to form an antiferromagnetic ground state below 15 K, there was also the presence of positional disorder of Cu^{2+} ions in the inter-site position, compositional disorder of the halide ions and synthesis dependent magnetic ground states [24, 87, 131, 132]. Studies on these systems have therefore shown that finding such an exotic magnetic ground state as the QSL is not just dependent on the magnetic character, but also the structural complexities that exist in real materials.

1.5.2 Spin Glass

A spin glass ground state involves the co-operative freezing of moments into random positions across the magnetic lattice. There are many experimental signatures for a spin glass [37]. Firstly, the divergence of the field-cooled (FC) and zero-field-cooled (ZFC) DC magnetic susceptibility below the freezing temperature, T_f . This represents the strong irreversibility of the spin glass ground state, as once frozen into position, the moments are pinned to their sites, unable to move until enough energy ($T > T_f$) is added back into the system. In general there are a lack of magnetic Bragg peaks in neutron diffraction measurements due to the random orientations of the frozen moments, but diffuse features can appear. However, the defining experimental signature of a spin glass is the strong frequency dependence and dynamic response of T_f in AC susceptibility measurements.

1.5.2.1 AC Susceptibility Measurements

In contrast to DC susceptibility measurements, AC susceptibility is often referred to as the dynamic susceptibility as the measured moment is time-dependent [31]. In an AC measurement, a small alternating current (AC) drive field is superimposed on the DC field, $H = H_{\text{DC}} + H_{\text{AC}}\cos(\omega t)$. The sample is fixed into position, but the oscillating AC current invokes a change in the magnetisation, $\mathbf{M}_{\text{AC}} = d\mathbf{M}/dH$. This is proportional to the amplitude of the AC field, H_{AC} and drive frequency, ω . At low AC frequencies, the susceptibility response is very similar to a DC measurement. However, at much larger frequencies, \mathbf{M} typically lags behind the AC field leading to the measurement of two quantities, χ (magnitude of susceptibility) and ϕ (phase shift). These quantities are conventionally viewed as the real in-phase, χ' and the imaginary out-of-phase, χ'' susceptibilities that are related via

$$\begin{aligned}\chi' &= \chi \cos(\phi) & \Leftrightarrow & \chi = \sqrt{\chi'^2 + \chi''^2} \\ \chi'' &= \chi \sin(\phi) & \phi &= \arctan(\chi''/\chi')\end{aligned}\tag{1.26}$$

Physically, χ' is the change in gradient of the $\mathbf{M}(H)$ curve with respect to the applied AC field, whereas χ'' is the dissipative processes of the sample. In a spin glass, T_f presents as a cusp in χ' , and is highly frequency dependent. The observation of a cusp is particularly important as in a spin glass, a feature describing T_f is absent in specific heat measurements [37]. Additionally, at T_f a strong dynamic response is expected ($\chi'' \neq 0$), which does not occur in a conventional long-range ordered state.

Compositional disorder is often a key ingredient to form a spin glass ground state. This can be seen in studies on solid solutions like $\text{Lu}_{1-x}\text{Ca}_x\text{MnO}_3$ [133] and $\text{SrMn}_{1-x}\text{W}_x\text{O}_3$ [134] where spin glass phases were stabilised after doping ($x = 0.1 - 0.3$ calcium and $x = 0.2 - 0.4$ tungsten ions, respectively) induced site mixing on the magnetic lattices. Both were found to have the characteristic frequency dependent cusp at T_g and irreversibility in AC susceptibility measurements, no magnetic Bragg peaks in neutron diffraction and characteristic freezing patterns in μSR measurements. Alternatively, a re-entrant spin glass phase was found in

cobalt(II) co-ordination polymers [135]. A re-entrant spin glass is a peculiar magnetic ground state as these materials have an ordered antiferromagnetic state at high temperatures, which upon cooling freeze into a disordered magnetic state akin to a spin glass [37]. The authors in this work believed that this spin glass was due to the orientations and connectivity of the ligands to the cobalt, which is therefore an example of positional disorder influencing the magnetic ground state.

1.5.3 Spin Ice

Spin ice states often occur in materials with corner-sharing tetrahedra, when the ferromagnetic arrangement of moments is geometrically frustrated when the local anisotropic axis points into the centres of the tetrahedra. The defining experimental signatures of spin ice materials are "pinch-points" in diffuse neutron scattering measurements [136]. Originating from the structure factor of spin ice, bow-tie features are often observed in diffuse neutron scattering measurements, with the knots of the bow-tie commonly referred to as pinch-points. These features are interesting, as at $T = 0$ K, these pinch-points should be infinitely narrow and thus describe infinitely long-ranged interactions within the material. But the additional thermal energy at finite temperatures, along with the instrument resolution in experiments, broadens the pinch-point resulting in the characteristic scattering. These features are often observed at temperatures higher than expected and this is likely due to dipolar interactions, which are an important mechanism in stabilising spin ice states [38, 136].

Classical spin ice materials ($S > 1$), such as $\text{Dy}_2\text{Ti}_2\text{O}_7$ and $\text{Ho}_2\text{Ti}_2\text{O}_7$, were some of the first frustrated systems to be characterised [40, 136]. The fluctuations in classical spin ice states are usually driven by thermal energy and these materials showed the characteristic pinch-point scattering and even an experimental first, evidence for quasiparticle magnetic monopoles [136]. Quantum spin ice states, like $\text{Yb}_2\text{Ti}_2\text{O}_7$, have also been subject to intense scrutiny [39, 137, 138]. $\text{Yb}_2\text{Ti}_2\text{O}_7$ was an ideal spin ice candidate as it has $S_{\text{eff}} = \frac{1}{2}$ moments

across a highly frustrated pyrochlore sub-lattice. Studies on this material have shown it has a continuum of spin excitations in INS, and the absence of a magnetic transition in magnetic susceptibility measurements. However, $\text{Yb}_2\text{Ti}_2\text{O}_7$ is very prone to compositional disorder caused by different synthetic procedures and so off-stoichiometries, like site-mixing (referred to as stuffed) or oxygen deficiencies, are a common occurrence. Measurements of the nuclear coherent scattering of different samples show stark differences, which ultimately leads to a range of distinct magnetic ground states [39].

1.6 Aims of Thesis

The principal aim of this thesis is to understand the interplay of correlated disorder on the ground state selection of quantum materials. This will be achieved through synthesising inorganic materials, and detailed structural and magnetic characterisation from both an average and local perspective. Particular attention will be given to the technique of diffuse magnetic neutron scattering and the analysis of data through RMC refinements.

This thesis is structured as follows. In Chapter 2, I will investigate a commonly overlooked problem within the quantum materials community: the effect of synthesis on the magnetic ground state properties. I will use the $S = 1$ cubic spinel, ZnV_2O_4 as a case study and explore the structural and magnetic evolution of a traditionally prepared sintered sample versus a rapidly prepared microwave sample. This work shows that a high quality sample of powder ZnV_2O_4 , prepared in just 12 minutes in a microwave, has comparable physical behaviour to a single-crystal, whereas the sintered sample undergoes a structural distortion, and I explain this in the context of strain. These differences in the chemical structure lead to distinct magnetic ground states, that have been explored with magnetic susceptibility and neutron scattering measurements.

In Chapter 3, I present a comprehensive neutron study on LiYbO_2 , which I find

is the first experimental realisation of a spiral spin liquid phase on an elongated diamond lattice. This work is significant as it reveals that a highly sought-after magnetic ground state, the spiral spin liquid, is experimentally achievable in a distorted diamond lattice. I also simultaneously refine magnetic Bragg and diffuse magnetic neutron scattering features in state-of-the-art RMC SPINVERT analysis.

In Chapter 4, I explore the local chemical and magnetic structure of the spin glass, $\text{Mn}_{0.5}\text{Fe}_{0.5}\text{PS}_3$, a layered honeycomb material with a chemical structure akin to graphene. This work on one member of a topical family of van der Waals magnets highlights the importance of considering the long-range ordered magnetic structures of the parent compounds to understand the short-range structure of the mixed compound. This work includes high-resolution neutron diffraction, DC magnetic susceptibility and diffuse neutron scattering on powder and single crystal samples.

Finally, in Chapter 5, I conclude with some general observations and suggestions for future work.

Publications arising from the Thesis

- Chapter 3
Experimental Evidence for the Spiral Spin Liquid in LiYbO_2 . **J. N. Graham**, N. Qureshi, C. Ritter, P. Manuel, A. R. Wildes and L. Clark, *Physical Review Letters* **130**, 166703 (2023).
- Chapter 4
Local nuclear and magnetic order in the two-dimensional spin glass $\text{Mn}_{0.5}\text{Fe}_{0.5}\text{PS}_3$. **J. N. Graham**, M. J. Coak, S. Son, E. Suard, J.-G. Park, L. Clark and A. R. Wildes, *Physical Review Materials* **4**, 084401 (2020).

Chapter Two

Understanding Synthesis-Driven Structure-Property Relationships in ZnV_2O_4

2.1 Introduction

All scientists would agree that having a good sample is imperative to conducting a good experiment. Aside from the standard criteria of a good sample being phase pure, reliable to produce and scalable, a good sample is the one that shows the most exciting physics. But what conclusions can be drawn if the fundamental physics of the material changes from sample to sample? In chemistry, the number of possible steps and combinations of steps for each reaction are nearly infinite. Therefore, the opportunity for small defects and subtle differences in the chemical structure to arise are abundant. For materials displaying magnetic frustration in which many degenerate ground states can co-exist, all it can take is one small defect to push one ground state in favour of the rest, and thus change the way the story ends. Given the complexity of the materials being explored, and the difficulty in receiving beam time to repeat experiments at large scale facilities, the question becomes: how can we

be sure the physics reported is intrinsic to that material, and not just an individual sample?

In recent years, there has been a drive to accelerate materials discovery by targeting certain properties from first principles, and this requires a collective effort from the scientific community. Theoreticians select the best candidates through chemical screening, chemists are charged with making as many of these materials as possible and physicists characterise the few that are pure, in the hope that one will produce interesting results. Naturally, for chemists, the most important considerations in a reaction are time and effort. Traditional solid-state methods with their long sintering times at high temperatures have become routine [139]. But given the shift to a high-throughput approach and an awareness of the negative impact on the environment that these reactions typically have, new synthetic methods are necessary [140, 141]. One potential option is microwave synthesis [142]. Relatively cheap and compact, the major benefit of microwave synthesis is the reaction time, which for inorganic materials can be reduced from several days to a matter of minutes [143].

The general steps to microwave synthesis involve grinding together the reactants before pressing the powder into a pellet. Then the sample is sealed under an inert atmosphere in a quartz tube. If the reactants are not susceptible to microwaves, this tube is then placed within a crucible filled with a microwave susceptor, a material that couples to microwaves at room-temperature and is highly absorbing, such as activated charcoal [142]. The role of the susceptor is to initiate a localised heating around the reactants, so that once the reactants pass a critical temperature, they themselves become susceptible to microwaves and can couple directly. Once coupled, a process known as thermal runaway occurs, where the temperature continues to rise rapidly, and is mediated by two main heating mechanisms, dipolar polarisation and conduction loss [144–146]. It is these mechanisms that mean the reaction time can be significantly shortened. A high power cycle is used initially and once the desired temperature is reached, the power can be reduced in order to control the reaction. After the reaction is complete, the sample is left to cool naturally in the activated charcoal, then the sample is recovered and reground for analysis. This method can be applied across a range

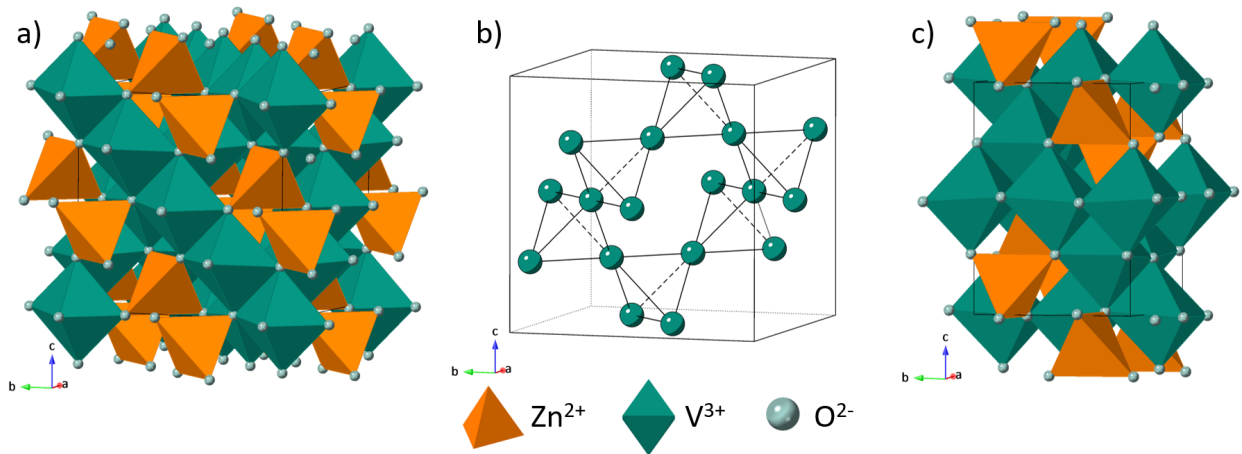


Figure 2.1: a) At high temperatures, ZnV_2O_4 adopts the $Fd\bar{3}m$ normal spinel structure where Zn^{2+} ions sit on the tetrahedrally co-ordinated A -site (orange), and V^{3+} ions occupy the octahedral B -site positions (green), oxygen atoms are shown by the light green spheres. b) Corner-sharing tetrahedra make up the vanadium pyrochlore sub-lattice. c) In many powder samples, a compression along the c -axis leads to a tetragonal $I4_1/amd$ structure at low-temperatures. In this case, the V^{3+} octahedra distort, causing the orbital degeneracy to be partially lifted [153, 155, 156].

of material classes including, but not limited to, metal oxides [147], intermetallics [148, 149] and chalcogenides [150, 151]. Critics of the technique highlight the complexity of getting the conditions "just right" and question the quality of the samples produced [152]. A general assumption is that shorter reaction time equals a less crystalline material as the sample is not given enough time to form its lowest energy periodic arrangement. Furthermore, changing the synthesis method does not guarantee the same physical properties between samples, as has been shown in numerous studies of quantum materials [39, 87, 131].

One particularly interesting material in which individual sample dependence is prominent and the chemical and magnetic ground states appear to be deeply intertwined is the $S = 1$ cubic spinel, ZnV_2O_4 . All reports state that at high temperatures ZnV_2O_4 adopts the normal cubic spinel structure, $Fd\bar{3}m$ [153, 154]. Here, the tetrahedral A -site position is

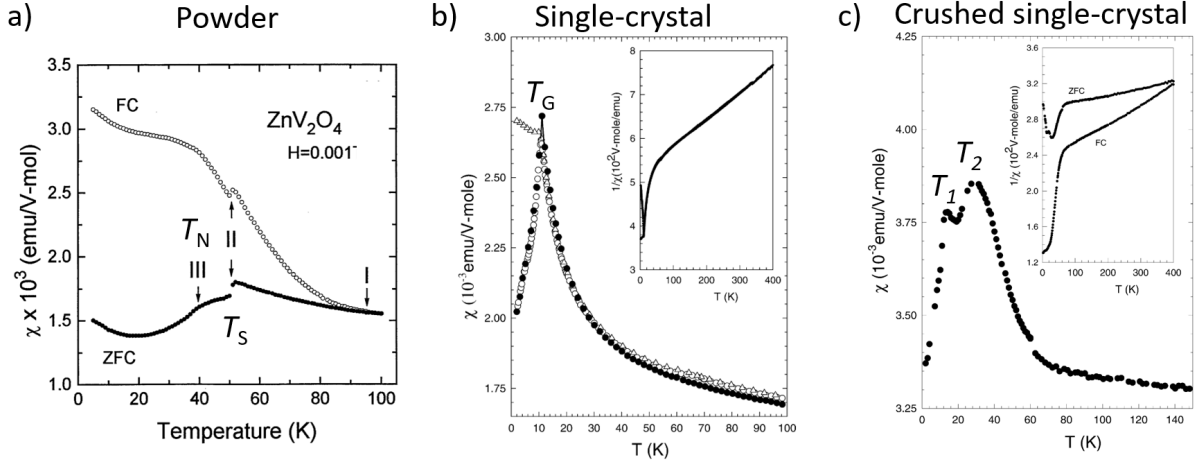


Figure 2.2: Magnetic susceptibility measurements from previous studies. a) A traditionally prepared solid-state sintered powder sample has two transitions, a discontinuity associated with the structural transition, T_S and a cusp describing the magnetic transition, T_N [155]. b) A single-crystal prepared via chemical vapour transport has one transition which may be associated with a spin glass, T_g [157]. c) Once the single-crystal is crushed two broad transitions appear.

occupied by a non-magnetic ion, such as Zn^{2+} , whilst the octahedral B -site position is occupied by magnetic V^{3+} ions, which is shown in Fig. 2.1a) by the orange and green polyhedra, respectively. ZnV_2O_4 is predicted to host an exotic magnetic ground state, as coupled with the low $S = 1$ spin state, the vanadium ions are connected via a geometrically frustrated pyrochlore sublattice (Fig. 2.1b)). This network is also subject to three-fold orbital degeneracy, originating from the $3d^2$ electron configuration of the V^{3+} ions in the octahedral crystal field (Fig. 1.4). However, this high-temperature chemical structure is the only aspect of ZnV_2O_4 agreed within the literature.

In the case of powder samples, ZnV_2O_4 usually undergoes a cubic-tetragonal Jahn-Teller distortion via a compression along the c -axis at $T_S \sim 50$ K (Fig. 2.1c)). This is evidenced by peak splitting in diffraction measurements, which has been reported to be of the order, $c/\sqrt{2}a = 0.994$ [153], and discontinuities in magnetic susceptibility data (Fig.

2.2a) labelled II) [155]. As a consequence of this structural distortion, the vanadium octahedra distort, relieving some of the geometric frustration (Fig. 1.5), and thus allows the system to settle into a long-range ordered antiferromagnetic ground state at $T_N \sim 40$ K. This is indicated by a characteristic cusp in magnetic susceptibility measurements [155], and sometimes weak antiferromagnetic Bragg peaks in neutron diffraction [153, 158]. The resulting magnetic structure has a $\mathbf{k} = (0\ 0\ 1)$ propagation vector, which is comprised of antiferromagnetic spin chains along the a - and b - axes. These spin chains are then coupled ferromagnetically along the c -axis [153, 154, 158]. The measured ordered magnetic moment, $\mu_{\text{eff}} = 0.65(1) \mu_B$ is significantly quenched from the expected moment for a $S = 1$ system of $\mu = 2.83 \mu_B$ [153]. It is theorised that this structural and magnetic behaviour is driven by the orbital degeneracy of the system. Therefore, possible orbital ordering models, in which spin-orbit couplings, along with electronic correlations, unquench the orbital moment in order to stabilise long-range order, have been proposed to explain the experimental results [159, 160].

Whilst this is the general behaviour for ZnV_2O_4 in powder form, the precise temperatures of the T_S and T_N transitions in susceptibility measurements are known to vary between samples [156, 161–163]. Additionally, large ZFC/FC splitting is observed, often at temperatures much higher than T_S and T_N , which could suggest large exchange interactions or magnetic clustering effects [155]. Furthermore, magnetic susceptibility data are found not to follow the Curie-Weiss law, leading to large and unphysical θ_{CW} [155]. Coupled with the presence of broad excitations up to at least 30 meV measured in a powder inelastic neutron scattering study [158], these results indicate that the quantum fluctuations in ZnV_2O_4 are very strong. Finally, long-range magnetic order has been confirmed only three times [153, 158, 161] with the observation of magnetic Bragg peaks in neutron diffraction, but due to their weak nature, the magnetic structure was only solvable by assuming that ZnV_2O_4 has the same magnetic structure as MgV_2O_4 [164, 165]. This combination of factors ultimately makes determining the true magnetic ground state of ZnV_2O_4 , and the mechanisms that

drive this behaviour, challenging.

Because of the complexities surrounding measuring the magnetic ground state on a powder sample of ZnV_2O_4 , an attempt was made on a single-crystal [157]. This single-crystal was grown via chemical vapour transport where powder was sealed under vacuum in a quartz tube and heated for 5 weeks at 900 °C. Whilst multiple examples of powder samples of ZnV_2O_4 exist, this single-crystal study by Ebbinghaus *et al.* is the only single-crystal of ZnV_2O_4 reported to date. The authors of this work confirmed that at high temperatures the single-crystal had the expected $Fd\bar{3}m$ cubic symmetry and that the crystal was well-ordered, stoichiometric and had no site-mixing within the resolution of the instrument. In contrast to powder studies, however, the magnetic susceptibility showed only one sharp feature at 11 K, below which the ZFC/FC measurements split, and so the authors attributed this feature to a spin glass transition (Fig. 2.2b)). For a spin glass transition to occur, they inferred that the single-crystal must remain highly frustrated and therefore cubic down to the lowest temperatures. Curiously though, when the single-crystal was crushed, two broad transitions appeared, $T_1 = 14$ K and $T_2 = 20$ K, which were attributed to the conventional antiferromagnetic (T_N) and structural (T_S) transitions that are measured in sintered powder samples of ZnV_2O_4 (Fig. 2.2c)). Ebbinghaus *et al.* concluded with two hypotheses to explain these results:

1. Single-crystals are highly strained which prevents the structural distortion from occurring. This strain is then released when the single-crystal is crushed.
2. Since the single-crystal was verified to be stoichiometric and of high-quality, sintered powder samples must have inherent structural disorder which causes the structural transition.

However, the conclusions surrounding this work are ambiguous since there are key experimental results missing from the paper. For example, no low-temperature diffraction measure-

ments exist on either the single-crystal or crushed sample to verify if the chemical structure remains in the cubic symmetry or not. Furthermore, low-temperature neutron diffraction is necessary to confirm the presence or absence of magnetic Bragg peaks which are needed for determining the nature of the magnetic ground state. Finally, the defining experimental signature for a spin glass transition is a cusp with a frequency-dependent response in AC susceptibility measurements [37]. This is required to confirm if the feature observed at $T = 11$ K in the single-crystal DC susceptibility measurements is indeed that of a spin glass.

From these previous reports it is clear that the chemical and magnetic ground states of ZnV_2O_4 are highly intertwined. Recently, it has become popular to try and capitalise on these dependencies in order to tune the magnetic properties of ZnV_2O_4 via chemical doping. This can take several different forms, but usually involves a change in the oxidation state of some of the vanadium ions ($\text{V}^{3+}/\text{V}^{4+}$) which can introduce compositional disorder into the system.

- An early example involved doping non-magnetic Li^+ ions onto the A -site [155]. LiV_2O_4 is a particularly interesting material as it was the first known report of a heavy fermionic state being found within a system with d -electrons [166–168]. Studies on a solid solution of powder samples, $\text{Li}_x\text{Zn}_{1-x}\text{V}_2\text{O}_4$, have shown that when $0.1 \leq x \leq 0.8$, the cubic-tetragonal distortion is suppressed, and only a single cusp at 10 K in magnetic susceptibility is observed. This is interpreted as a transition to a spin glass ground state [155]. The cubic symmetry was confirmed in diffraction measurements down to 8 K for the $x = 0.1$ sample only.
- Similarly, the A -site has also been doped with non-magnetic Ga^{3+} across the solid solution, $\text{Zn}_x\text{Ga}_{1-x}\text{V}_2\text{O}_4$ [156]. Unlike ZnV_2O_4 , GaV_2O_4 adopts a rhombohedral $R\bar{3}m$ structure and undergoes a charge ordering at 415 K. However, with as little as 6 % doping of Zn^{2+} ions into the structure, this charge ordering is suppressed and the crystal symmetry returns to the cubic, $Fd\bar{3}m$ at room temperature. In DC magnetic

susceptibility measurements, between $0.06 \leq x \leq 0.875$, the cubic-tetragonal structural distortion is suppressed which leads to the cusp (with varying transition temperature depending on doping) attributed to the spin glass ground state appearing.

- Finally, magnetic Ni^{2+} ions have been doped over the range $0 \leq x \leq 0.2$ in $\text{Zn}_{1-x}\text{Ni}_x\text{V}_2\text{O}_4$ [163]. Though targeting substitution of the *A*-site, Raman measurements showed extra phonon modes that were attributed to some cation disorder on both the *A*- and *B*-sites. This was likely due to the similarity in the ionic charge and radius of Ni^{2+} and V^{3+} ions. The study found that when x was as little as 0.02, the cubic-tetragonal structural distortion was suppressed and that the susceptibility had the appearance of a spin glass.

Despite these claims, all of these studies are lacking conclusive proof of the nature of the magnetic ground state, as no AC measurements or investigations into the presence of magnetic Bragg peaks are included in any of the reports [37, 155, 156, 163].

These previous experimental studies show that ZnV_2O_4 is a highly complex material where a consensus over the true nature of the chemical and magnetic ground states is still unknown. Doping ZnV_2O_4 with other ions has shown that the ground state is highly sensitive to disorder with substitutions of just a few percent being able to completely transform the chemical and magnetic properties. I now ask the question, what if the same principle applies to pure ZnV_2O_4 ? That disorder on a local scale is responsible for the different behaviours seen, and if this disorder can be parameterised, then would it be possible to select the magnetic ground state by targeting certain defects during the synthesis?

One way to test this hypothesis is to make a series of powder samples of ZnV_2O_4 via different synthetic routes and then characterise them side-by-side to allow for a direct comparison. Traditionally, powder ZnV_2O_4 is synthesised by solid-state methods in which stoichiometric quantities of ZnO , V and V_2O_3 (prepared via reducing V_2O_5 under flowing H_2 at 900 °C) are ground together. The powder is then pelletised and sealed under vacuum

to control the oxidation state of V^{3+} ions before being fired at 650-900 °C for duration's ranging from 2 days to several weeks [155, 156]. Given the involved synthesis and long sintering times, this is an ideal opportunity to test the rapid microwave synthesis method as an alternative synthetic procedure for producing quantum materials. In this chapter I will explore how synthesis affects the chemical and magnetic ground state selection of ZnV_2O_4 through a combination of average and local structure determination on two powder samples of ZnV_2O_4 . This will be achieved using high-resolution neutron and X-ray diffraction, PDF analysis, magnetic susceptibility and diffuse magnetic neutron scattering. The main aim of this chapter is to understand what drives the ground state selection in ZnV_2O_4 , both within this study and across the wider context of the literature.

2.2 Experimental Methods

2.2.1 Synthesis

Powder samples of ZnV_2O_4 were prepared via two different methods: a conventional high-temperature sintering route (sintered) and a novel rapidly prepared microwave assisted route [142]. For the sintered sample, stoichiometric quantities of ZnO (99.999%, Sigma Aldrich) and V_2O_3 (99.99%, Sigma Aldrich) were combined and ground in a ball mill with isopropanol for 24 hours. Ball milling the sample was selected to significantly reduce the firing time previously required [153, 155] and increase homogeneity between the batches. The solution was dried on a hotplate, and the resultant powder was pressed into 1 g pellets, and sealed under vacuum in quartz tubes to a pressure of 10^{-7} mbar. Although neither the reactants or product were air sensitive, sealing the tubes under vacuum was necessary to prevent unwanted oxidation of V^{3+} to V^{5+} . The sealed tubes were fired at 800 °C for 24 hours, and slowly cooled back to room temperature before being hand ground into a fine black powder. Some samples had small V_2O_3 impurities present, in these cases additional ZnO powder was

hand ground into the sample, the powders were pelletised and resealed as before, and fired for an additional 12 hours at 800 °C. The total mass of the sample was ~ 9 g.

The microwave sample was prepared by Dr. Joya Cooley in the Department of Chemistry and Biochemistry at the University of California Santa Barbara, USA. Stoichiometric quantities of ZnO (99.999%, Sigma Aldrich) and V_2O_3 (99.99%, Sigma Aldrich) were ground by hand in a mortar and pestle for 10 minutes. The resulting powder was pressed into pellets of ~ 400 mg and sealed under vacuum in a quartz tube. The tube was then placed within a crucible filled with activated charcoal [142]. The sample was then heated in a Panasonic NN-SN651B 1200 W microwave on power level 3 (360 W) for 12 minutes. After heating, the charcoal temperature was measured to be approximately 740 °C with a physical K-type thermocouple probe. The tube was left to cool naturally to room temperature, after which the sample was recovered and ground into a fine black powder. The total mass of the sample was ~ 2 g made from smaller batches. This method was reproducible within the setup at UCSB.

2.2.2 Powder Neutron Diffraction

2.2.2.1 HRPD

Time-of-flight neutron powder diffraction (NPD) data were collected on the high-resolution powder diffractometer, HRPD [169] at the ISIS Neutron and Muon Source. 2 g of the microwave sample was measured in a flat-plate vanadium-windowed sample container between 10 K and 120 K in 10 K steps. In the same configuration, 8 g of the sintered sample was measured at 10 K, 20 K, 30 K, 40 K and 100 K. Raw data can be accessed via links provided in Ref. [170].

2.2.2.2 WISH

Time-of-flight neutron powder diffraction data were collected on the long-wavelength WISH diffractometer at the ISIS Neutron and Muon Source. 1.8 g of the microwave and 5.6 g of the sintered samples were contained in cylindrical aluminium cans. Measurements were made in an orange cryostat at 1.5 K, 25 K, 50 K and 80 K. The instrumental resolution was determined via Rietveld refinement of the Na₂Ca₃Al₂F₁₄ standard. Absorption corrections were applied during the data reduction on Mantid. Data were converted to absolute units according to Eq. 1.19. Rietveld refinements of the chemical and magnetic structures were completed using the `Fullprof` program [105]. Raw data can be accessed via Ref. [171].

2.2.2.3 D20

Constant wavelength neutron powder diffraction data were collected on the high-flux D20 diffractometer [172] at the Institut Laue-Langevin. The incident wavelength was $\lambda = 1.3 \text{ \AA}$ selected by a Cu(200) monochromator, allowing the scattering to be measured over an angular range of $10 < 2\theta < 160^\circ$. 7.75 g of the sintered sample was contained in a 12 mm vanadium sample can and a liquid helium cryofurnace was used for the temperature control. Data were measured at 1.5 K, 25 K, 80 K, 150 K, 300 K, 450 K and 520 K. Refinements of the chemical structure were completed using the `Fullprof` program [105]. Data were converted to absolute units according to Eq. 1.18. Temperature subtractions were completed with 520 K defined as the paramagnetic temperature. Subtracted data were modelled using `SPINVERT` and `SPINCORREL` [119, 120]. Raw data can be accessed via links in the following Ref. [173].

2.2.2.4 D7

Diffuse neutron scattering measurements were measured on the polarised diffuse scattering diffractometer, D7 [112] the Institut Laue-Langevin. The incident neutron wavelength was $\lambda = 4.87 \text{ \AA}$, giving a reciprocal space range in both cases of $0.15 < Q < 2.5 \text{ \AA}^{-1}$. For the sintered sample, 8 g of sample was measured at 1.5 K, 25 K, 50 K and 300 K, and 2 g of the microwave sample was measured at 1.5 K only. The technique of *xyz*-polarisation analysis was used to separate out the nuclear-coherent (NC), magnetic and nuclear-spin-incoherent (NSI) contributions of the scattering. Full calibration measurements included measurements of an empty and cadmium-filled sample can to estimate the instrumental background, a quartz standard to correct for polarisation inefficiencies and a vanadium standard to normalise the detector efficiencies. Data were placed on an absolute intensity scale (with units b/ster./f.u.) by normalising to the incoherent scattering from the vanadium standard. The normalisation process was verified through Rietveld refinement of the NC cross-sections using Fullprof [105]. Due to the low sample mass of the microwave sample, background corrections had to be removed from the data reduction in order to isolate the magnetic contribution correctly. Full background subtractions were made for the sintered sample. Magnetic diffuse scattering data were analysed using RMC methods on the programs SPINVERT and SPINCORREL [119, 120]. SPINVERT calculations were repeated 10 times to average out statistical noise. Raw data can be accessed via links provided in the following references [174, 175].

2.2.3 Powder X-ray Diffraction

Powder X-ray diffraction (PXRD) data were collected on the high-resolution ID22 beamline at the European Synchrotron Radiation Facility (ESRF). Samples were packed into 1 mm borosilicate glass capillaries and attached to brass holders with grease. The samples were cooled using a helium cryostream, and thus the capillary left open to allow for proper gas

exchange. Data were collected using an Eiger 2 X CdTe 2M-W detector with nine Si(111) analyser crystals. The incident X-ray energy was 35 keV, with a calibrated wavelength, $\lambda = 0.354195 \text{ \AA}$. Calibration measurements of a Si standard were measured, and the instrument resolution determined via Rietveld analysis of this standard on Fullprof [105]. Data were measured in regular intervals of 2 K between 4 K and 55 K, 5 K steps between 60 K and 100 K and 50 K steps between 150 K and 300 K. Raw data can be accessed via links provided in Ref. [176]. Combined neutron and X-ray refinements of the chemical structural were completed using physical size and strain analysis as applied on Fullprof and outlined in the introduction using the Stokes and Wilson formalism [111].

2.2.4 Total X-ray Scattering

X-ray total scattering measurements on both samples were conducted on ID22. Samples were packed into 1 mm borosilicate glass capillaries and cooled using a helium cryostream. Data were collected using a PerkinElmer XRD1611 2D detector to access the high- Q scattering. The incident X-ray energy was 70 keV, with a calibrated wavelength, $\lambda = 0.1771189 \text{ \AA}$. A calibration standard of LaB₆ standard was measured. Refinements of the ZnV₂O₄ samples between the two ID22 data sets showed good agreement, indicating both experimental set-ups were calibrated correctly. Data were measured in regular intervals between 4 K and 300 K for the sintered sample, and 7 K and 300 K for the microwave sample. The total integrated data were averaged over multiple runs of $200 \times 0.3 \text{ s}$ exposures. Full background measurements of an empty 1 mm capillary were measured at regular intervals. PDFGETX3 was used to make the background corrections to the patterns, convert the integrated data to structure functions, $S(Q)$, and transform the data to PDFs, $g(r)$. Data were measured up to $Q = 27.5 \text{ \AA}^{-1}$, and for both samples a correction associated with the maximum frequency in $F(Q)$, $r_{\text{poly}} = 1.73$, was applied. Fits of the PDFs were conducted using PDFGUI, with the average structure refined over a 1.5 to 50 \AA range, and the local structure probed in 10 \AA

sections via the carbox method. Raw data can be accessed via links provided in Ref. [177].

2.2.5 Magnetometry

DC susceptibility measurements of both the sintered and microwave samples were conducted in on a MPMS3 SQUID magnetometer, Quantum Design at the Midlands MagLab, University of Birmingham. The powder sample was packed into a capsule, and sealed with an epoxy grease. A full zero-field cooled (ZFC) and field cooled (FC) cycle was collected at 0.01 T over a range of 2 K to 300 K. Data were collected in a variable applied magnetic field (2.5 - 25 mT) in a ZFC measurement over a temperature range of 2 K to 100 K. After each field step, the sample was warmed to 200 K to eliminate any remnant magnetism.

AC susceptibility measurements were collected by Dr Ross Stewart for both the sintered and microwave samples, and were conducted in on a MPMS3 SQUID magnetometer, Quantum Design at the Midlands MagLab, University of Birmingham. A niobium standard was used to check the calibration of the instrument. Data were measured over a range of 2 - 70 K for the applied AC driving frequencies, $\omega_{\text{AC}} = 3, 11, 33, 105, 330, 660, 990$ Hz, with an applied field, H_{AC} of 10 Oe, aside from 660 Hz ($H_{\text{AC}} = 4$ Oe) and 990 Hz ($H_{\text{AC}} = 0.5$ Oe). The measurement time and number of cycles were adjusted according to the signal strength.

2.3 Results and Discussion

2.3.1 Average Chemical Structure

To summarise the key findings from the average structure refinements, both the microwave and sintered samples adopt the normal cubic spinel structure, $Fd\bar{3}m$, at high-temperatures. From previous investigations into powder samples, it is expected that a structural distortion

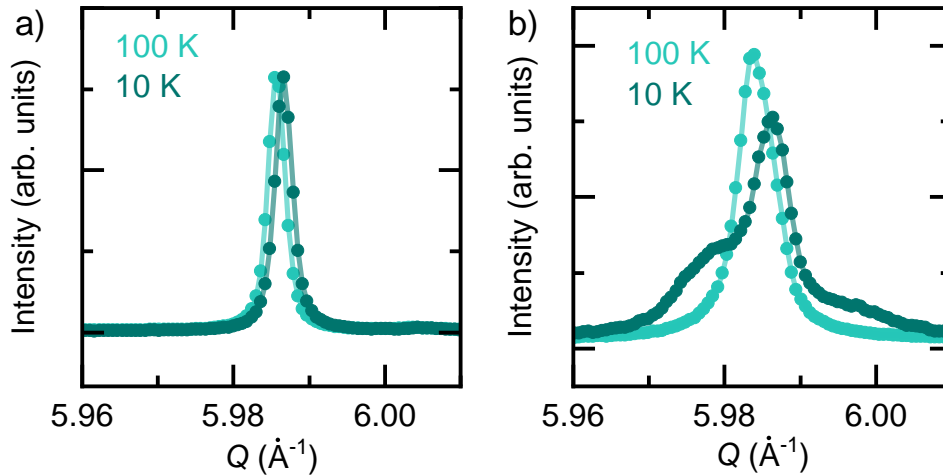


Figure 2.3: ID22 data showing the (8 0 0) reflection for the a) microwave and b) sintered samples at 100 K and 10 K. This peak should show characteristic peak splitting following the distortion, which is seen for the sintered sample but not for the microwave.

to the tetragonal $I4_1/amd$ structure occurs via a compression along the c -axis below 50 K [153, 155, 156]. This would be observable through peak splitting of the (800) reflection at $Q = 5.99 \text{\AA}^{-1}$, for example. The (800) reflection is shown in Fig. 2.3 for the a) microwave and b) sintered samples, respectively. Extraordinarily, the absence of any change in size or shape of this reflection in the microwave sample provides evidence that this sample remains in the cubic $Fd\bar{3}m$ phase down to 4 K. This is remarkable. The microwave sample is the first powder sample of ZnV_2O_4 that has been confirmed to remain in the cubic symmetry down to low temperatures. In contrast, the (800) reflection in the sintered sample shows a clear splitting below 35 K as the cubic structure undergoes a global elongation along the c -axis. This is unusual. The sintered sample is the first known ZnV_2O_4 sample to undergo an elongation as oppose to a compression along the c -axis.

Experimental evidence for this structural behaviour is detailed in the following sections. Physical size and strain analysis has been conducted on the samples using the method outlined by Stokes and Wilson [111]. Details of the combined ID22 and HRPD refinements at 100 K can found below, which were used as a normalisation basis so that all param-

eters, aside from lattice parameters and isotropic thermal parameters, B_{iso} , were fixed in subsequent refinements.

2.3.1.1 Microwave Sample

Figure 2.4 shows the combined Rietveld refinement of the cubic $Fd\bar{3}m$ model against high-resolution synchrotron X-ray data from ID22 ($R_{\text{wp}} = 15.5\%$, $\chi^2 = 37.5$) and neutron powder diffraction (NPD) data from HRPD ($R_{\text{wp}} = 13.6\%$, $\chi^2 = 2.29$) of the microwave sample at 100 K. A non-stoichiometric VO_2 impurity is present and accounts for 12 % of the total sample volume (grey tickmarks). At 10 K, the same cubic $Fd\bar{3}m$ model was used and gave comparable quality of fit parameters, $R_{\text{wp}} = 15.6\%$, $\chi^2 = 37.86$ for ID22 and $R_{\text{wp}} = 14.7\%$, $\chi^2 = 3.92$ for HRPD (Fig. 2.5). The only parameters refined between the temperatures were the lattice parameter and B_{iso} , verifying that no structural phase transition occurs in the microwave sample (Appendix Fig. 2.18). A summary of the refined structural parameters at 10 K can be found in Table 2.1. No site mixing or off-stoichiometries were resolvable within the resolution of the instruments.

Atom	Site	x	y	z	B_{iso} (\AA^2)
Zn	8a	0.125	0.125	0.125	0.295(5)
V	16d	0.5	0.5	0.5	0.236(4)
O	32e	0.26025(7)	0.26025(7)	0.26025(7)	0.40(1)

Table 2.1: Refined average chemical structure parameters for the cubic $Fd\bar{3}m$ model fitted to synchrotron and NPD data collected for the microwave sample at 10 K on ID22 and HRPD. Refined lattice parameter is $c = 8.39642(1)$ \AA .

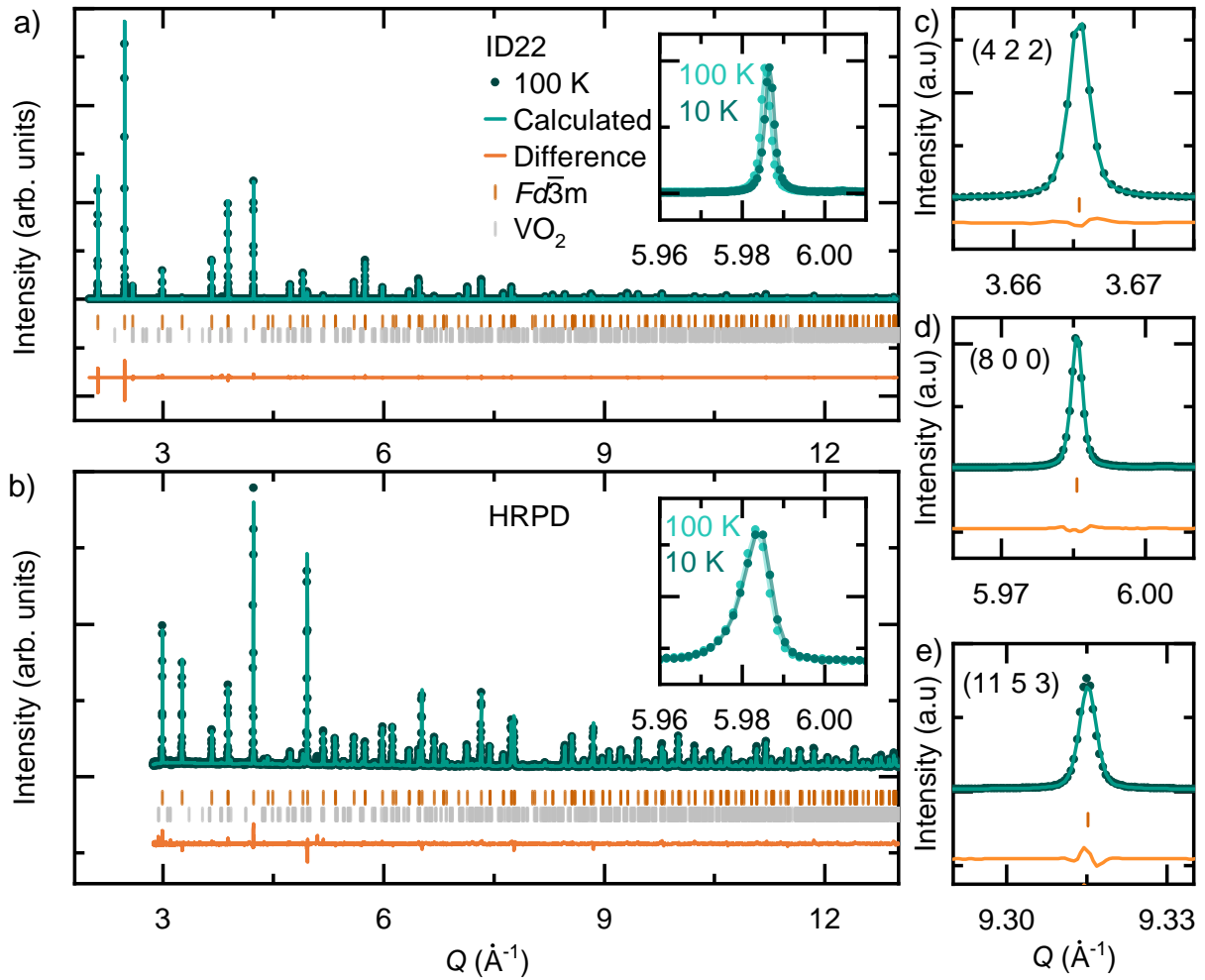


Figure 2.4: Combined Rietveld refinements of the microwave sample measured at 100 K. a) ID22, $R_{\text{wp}} = 15.5\%$, $\chi^2 = 37.5$, b) HRPD, $R_{\text{wp}} = 13.6\%$, $\chi^2 = 2.29$. The microwave sample was fit to the cubic $Fd\bar{3}m$ structure at all temperatures (orange tickmarks) and a non-stoichiometric VO_2 impurity (grey tickmarks, 12 % of total sample volume). Refined lattice parameter, $c = 8.3980(1)$ Å. Rietveld fit of three key peaks from ID22, c) (4 2 2), d) (8 0 0) and e) (11 5 3).

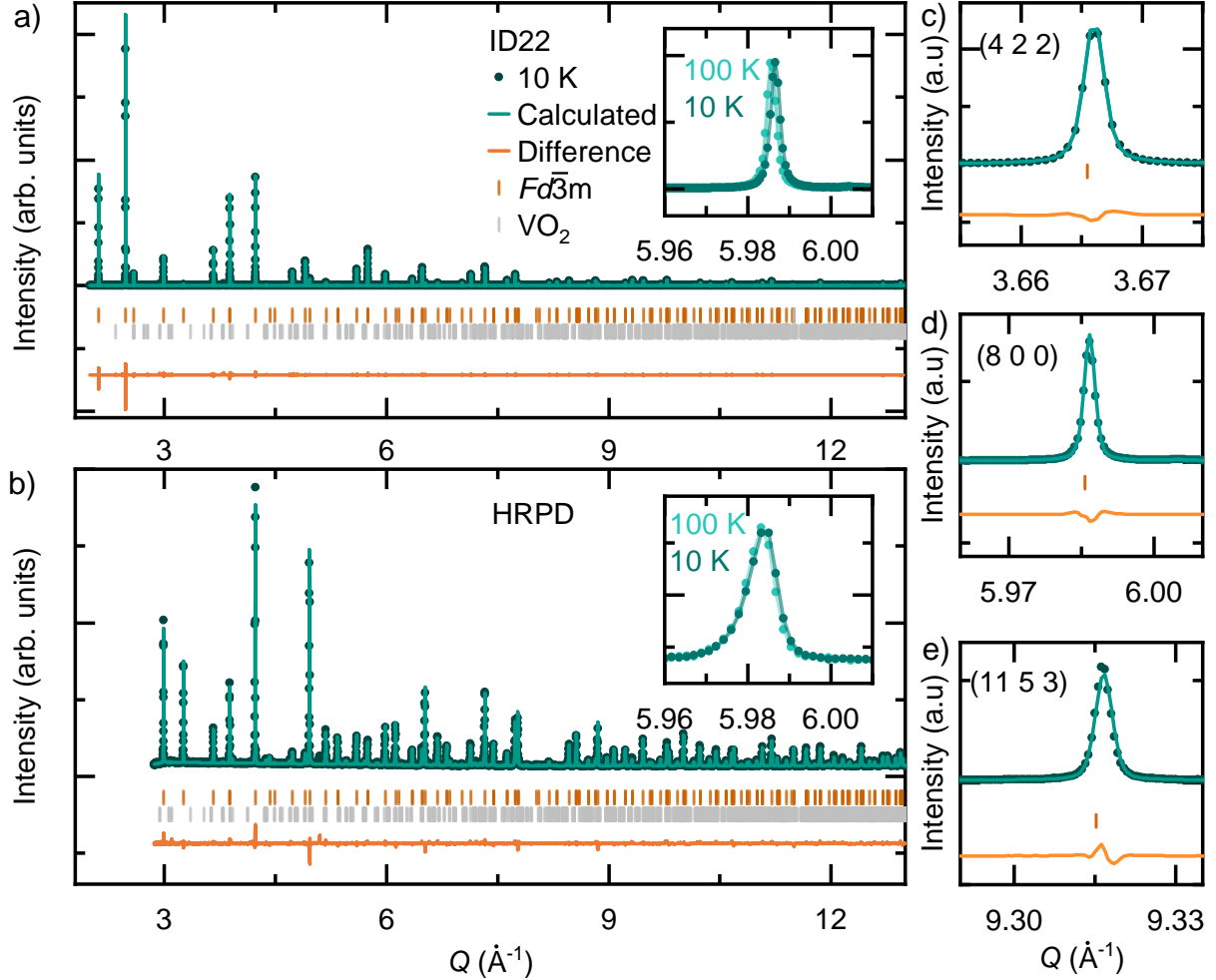


Figure 2.5: Combined Rietveld refinement of the microwave sample measured at 10 K. a) ID22, $R_{\text{wp}} = 15.6\%$, $\chi^2 = 37.86$, b) HRPD, $R_{\text{wp}} = 14.7\%$, $\chi^2 = 3.92$. The microwave sample was fit to the cubic $Fd\bar{3}m$ structure at all temperatures (orange tickmarks) and a non-stoichiometric VO_2 impurity (grey tickmarks, 12 % of total sample volume). Refined lattice parameter, $c = 8.39642(1)$ \AA . Insets on each panel show the temperature evolution of the (800) reflection for the instrument. Rietveld fit of three key peaks from ID22, c) (4 2 2), d) (8 0 0) and e) (11 5 3).

2.3.1.2 Sintered Sample: High-Temperature Cubic Phase

The sintered sample also adopts the cubic $Fd\bar{3}m$ structure at high-temperatures. However, whilst in the parent cubic phase, the Bragg peaks from the sintered sample were found to be inherently broad. With the resolution afforded by ID22, a clear shoulder can be seen on the (13 5 5) reflection (inset Fig. 2.6a)), demonstrating that a distribution of lattice parameters are present within the phase. One way to model this shoulder is to use two cubic $Fd\bar{3}m$ phases in the Rietveld analysis with different lattice parameters. Physically, this may arise from small deviations in the sample stoichiometry from the different batches that were combined during the sample preparation. All other structural parameters, such as oxygen coordinates, B_{iso} and peak widths, are coupled during the fit across the two cubic phases. The results of a combined ID22 ($R_{\text{wp}} = 10.4\%$, $\chi^2 = 20.9$) and HRPD ($R_{\text{wp}} = 11.3\%$, $\chi^2 = 2.65$) refinement are shown in the Appendix (Fig. 2.19a) and b), respectively), and fit the data very well. The refined lattice parameters were $a_1 = 8.39729(2)$ Å and $a_2 = 8.40053(1)$ Å which were split in a 0.3 : 0.7 ratio, respectively.

To return to a single cubic phase model, the weighted average of the refined lattice parameters was taken, giving the average lattice parameter, $a_{\text{ave}} = 8.400(2)$ Å. Figure 2.6 shows the combined refinement of the cubic $Fd\bar{3}m$ model where a_{ave} was fixed against data from ID22 ($R_{\text{wp}} = 12.4\%$, $\chi^2 = 22.6$) and HRPD ($R_{\text{wp}} = 13.1\%$, $\chi^2 = 3.63$) of the sintered sample at 100 K. Although, the asymmetry of the peaks is lost in this model, fixing the lattice parameter ensured that results from subsequent refinements would be comparable. A summary of the refined parameters for the sintered sample at 100 K can be found in Table 2.2. No site mixing or off-stoichiometries were resolvable within the resolution of the instruments.

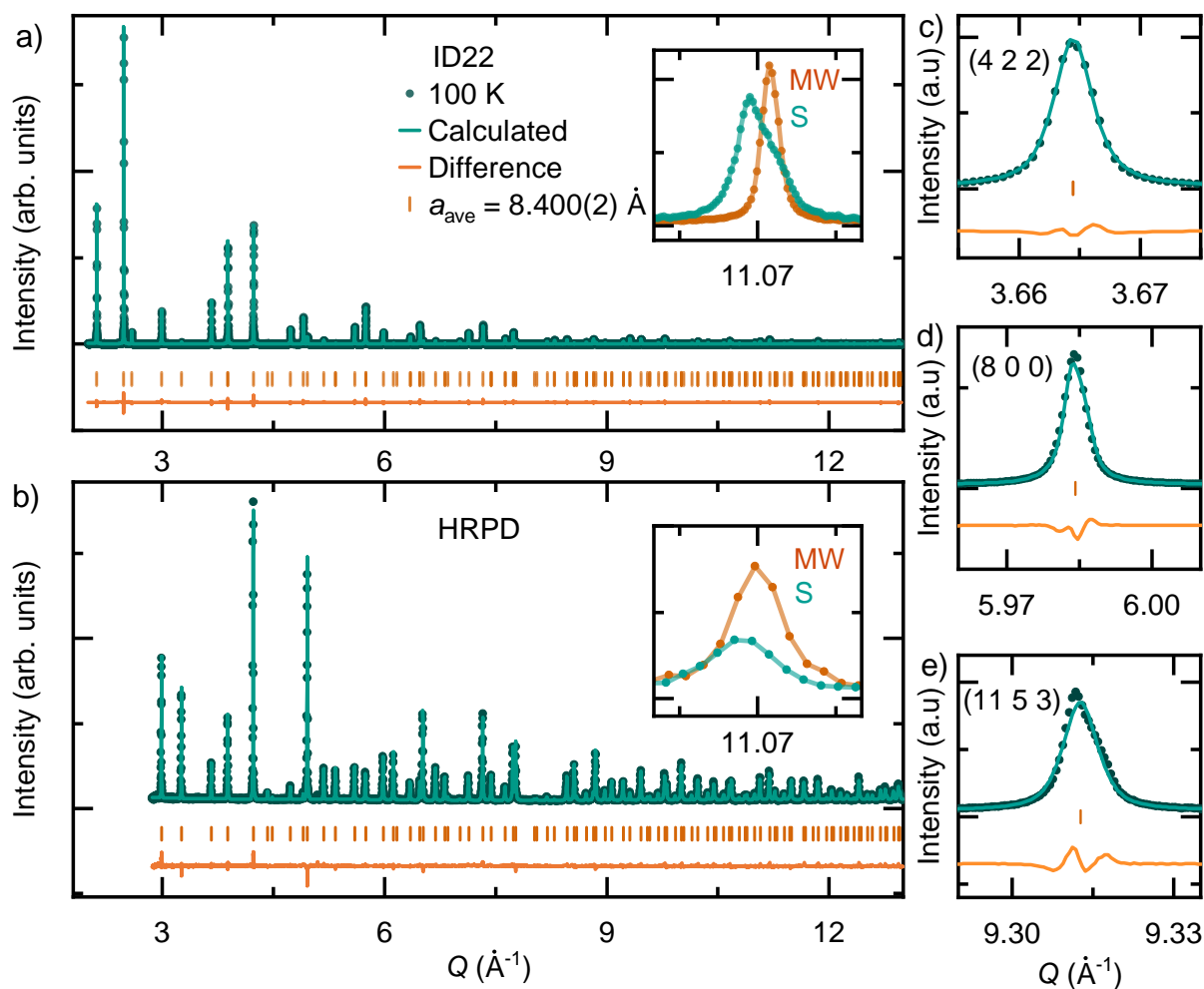


Figure 2.6: Combined Rietveld refinement of the sintered sample measured at 100 K. a) ID22, $R_{\text{wp}} = 10.4 \%$, $\chi^2 = 20.9$, b) HRPD, $R_{\text{wp}} = 11.3 \%$, $\chi^2 = 2.65$. The weighted average lattice parameter, $a_{\text{ave}} = 8.400(2) \text{ \AA}$ was fixed for this single phase refinement. Insets show the (13 5 5) reflection for the microwave (orange) and sintered (green) samples, where a clear shoulder can be seen in the sintered sample in a). Rietveld fit of three key peaks from ID22, c) (4 2 2), d) (8 0 0) and e) (11 5 3).

Atom	Site	x	y	z	B_{iso} (Å ²)
Zn	8a	0.125	0.125	0.125	0.312(4)
V	16d	0.5	0.5	0.5	0.235(4)
O	32e	0.26023(5)	0.26023(5)	0.26023(5)	0.43(1)

Table 2.2: Refined average chemical structure parameters for the cubic $Fd\bar{3}m$ model fitted to synchrotron and NPD data collected for the sintered sample at 100 K on ID22 and HRPD. Weighted average lattice parameter is $c = 8.400(2)$ Å.

2.3.1.3 Sintered Sample: Low-Temperature Distorted Phase

Below 35 K, a gradual phase transition occurs and was tracked in regular intervals on ID22 down to 4 K. At no point does the peak intensity plateau, indicating that the transition is still ongoing at 4 K. Previous studies of powder ZnV₂O₄ concluded that the experimental low-temperature structure has a compression along the tetragonal c -axis to the $I4_1/amd$ structure, with an axial compression of the order of $c/\sqrt{2}a = 0.994$ [153]. A fit of this structure was attempted in a combined ID22 and HRPD refinement at 10 K and yielded poor quality of fit parameters, $R_{\text{wp}} = 25.5$ %, $\chi^2 = 30.3$ for ID22 and $R_{\text{wp}} = 19.9$ %, $\chi^2 = 38.2$ for HRPD (Appendix Fig. 2.20). The lattice parameters refined to $a = 5.94035(1)$ Å and $c = 8.39287(2)$ Å, giving an axial compression, $c/\sqrt{2}a$ of just 0.9990. Figure 2.7 shows that on further inspection of the peaks there are additional issues. Most notably, the $(8\ 0\ 0)$ reflection at $Q = 5.99$ Å⁻¹, which clearly splits following the transition, has the intensity in the Rietveld fit inverted in comparison to the experimental data.

It is therefore clear that the sintered sample adopts a different low-temperature structure to that reported in the literature. An exhaustive search for potential lower symmetry space groups was completed using ISODISTORT [178, 179] from the parent cubic phase. In total, 10 candidates were identified, including 6 tetragonal models. Each of these structures were fit to the 10 K data, and showed that whilst the tetragonal models fit best, they were in-

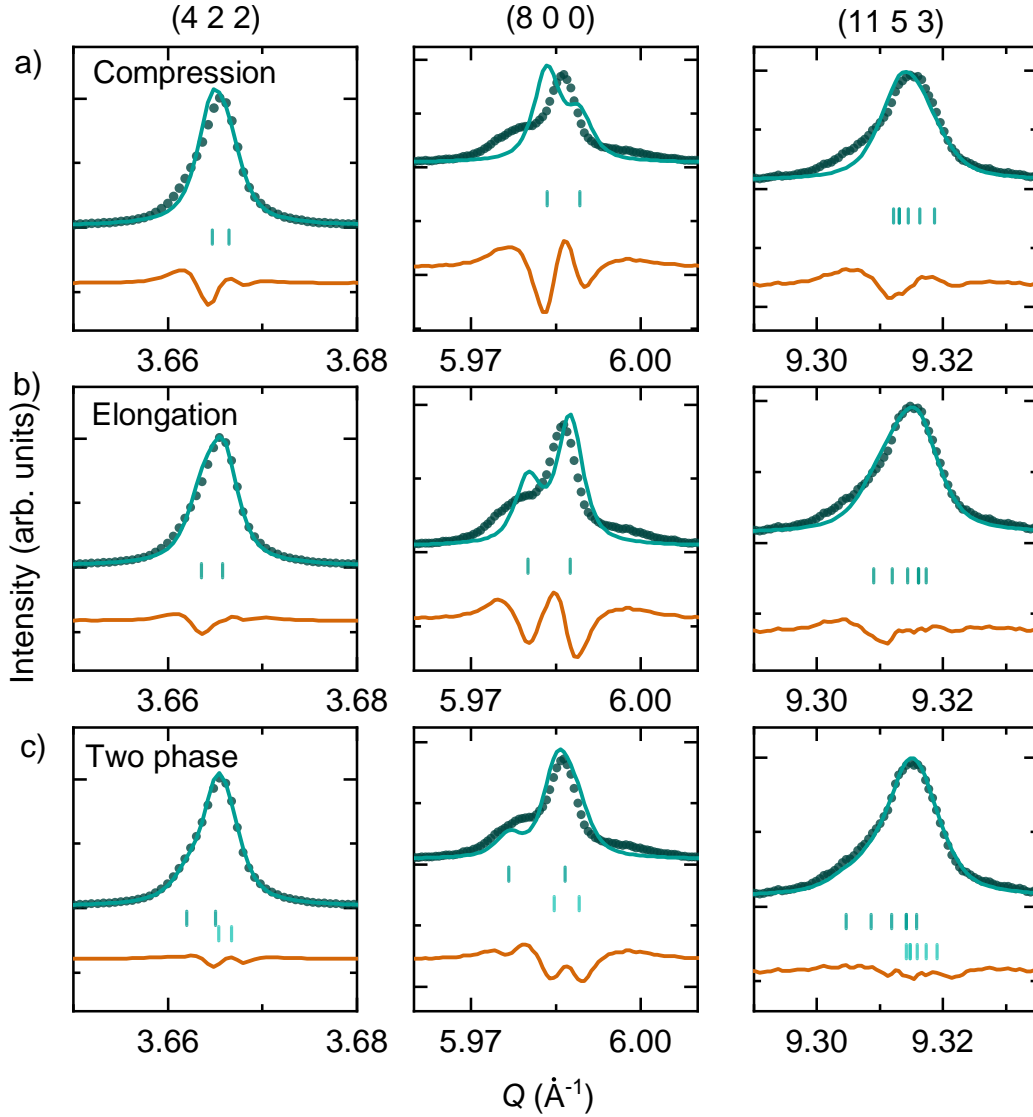


Figure 2.7: Rietveld refinement of three tetragonal models for the sintered sample across three key peaks; a) $I4_1/amd$ model with a compression along the c -axis, $c/\sqrt{2}a = 0.9990$, b) $I4_1/amd$ model with an elongation along the c -axis, $c/\sqrt{2}a = 1.0012$, and c) two tetragonal $I4_1/amd$ models giving a global elongation along the c -axis, $c/\sqrt{2}a = 1.001$, but locally a mixture of compression and elongation. Peaks shown are the (4 2 2) at $Q = 3.665 \text{ \AA}^{-1}$ in column 1, (8 0 0) at $Q = 5.99 \text{ \AA}^{-1}$ in column 2 and (11 5 3) at $Q = 9.32 \text{ \AA}^{-1}$ in column 3 from data measured at 10 K on ID22.

distinguishable from each other (Appendix Table 2.6). A key finding however, is that all the tetragonal models elongate along the c -axis, with an axial elongation of $c/\sqrt{2}a = 1.0012(2)$. An example of one of these tetragonal structures is shown in the Appendix Fig. 2.21, with key peaks in the second row of Fig. 2.7. The quality of fit parameters, $R_{\text{wp}} = 22.4\%$, $\chi^2 = 23.5$ for ID22 and $R_{\text{wp}} = 17.0\%$, $\chi^2 = 28.1$ for HRPD are an improvement on the compression model. In particular, the (8 0 0) reflection now has the Rietveld-refined intensity matching the data, but this model still fails to capture the broad and diffuse tails of the data.

Returning to the findings at 100 K, where a distribution of lattice parameters were required to adequately describe the peak shape, it is not unreasonable to assume that this still applies following the phase transition. A double tetragonal $I4_1/amd$ refinement is shown in Fig. 2.8 and has fit parameters, $R_{\text{wp}} = 18.6\%$, $\chi^2 = 16.3$ for ID22 and $R_{\text{wp}} = 14.1\%$, $\chi^2 = 19.4$ for HRPD, a significant improvement on the previous models. For the first time, the diffuse features of the peaks are beginning to be fit (third row of Fig. 2.7). Interestingly, this model describes a portion of the sample compressing and a portion elongating simultaneously, split into a 0.4 : 0.6 ratio, respectively. The weighted average of these distortions gives a global axial elongation of $c/\sqrt{2}a = 1.0010(3)$, which is consistent with the best fit of a single phase model. A summary of the refined parameters can be found in Table 2.3. Ultimately, it is challenging to go further and definitively determine the low-temperature space group

Atom	Site	x	y	z	$B_{\text{iso}} (\text{\AA}^2)$
Zn	8a	0	0.75	0.125	0.316(9)
V	16d	0	0	0.5	0.260(8)
O	32e	0	0.02123(4)	0.25979(6)	0.43(1)

Table 2.3: Refined average chemical structure parameters for the elongated tetragonal $I4_1/amd$ model fitted to synchrotron and NPD data collected for the sintered sample at 10 K on ID22 and HRPD. Weighted average axial elongation, $c/\sqrt{2}a = 1.0010(3)$.

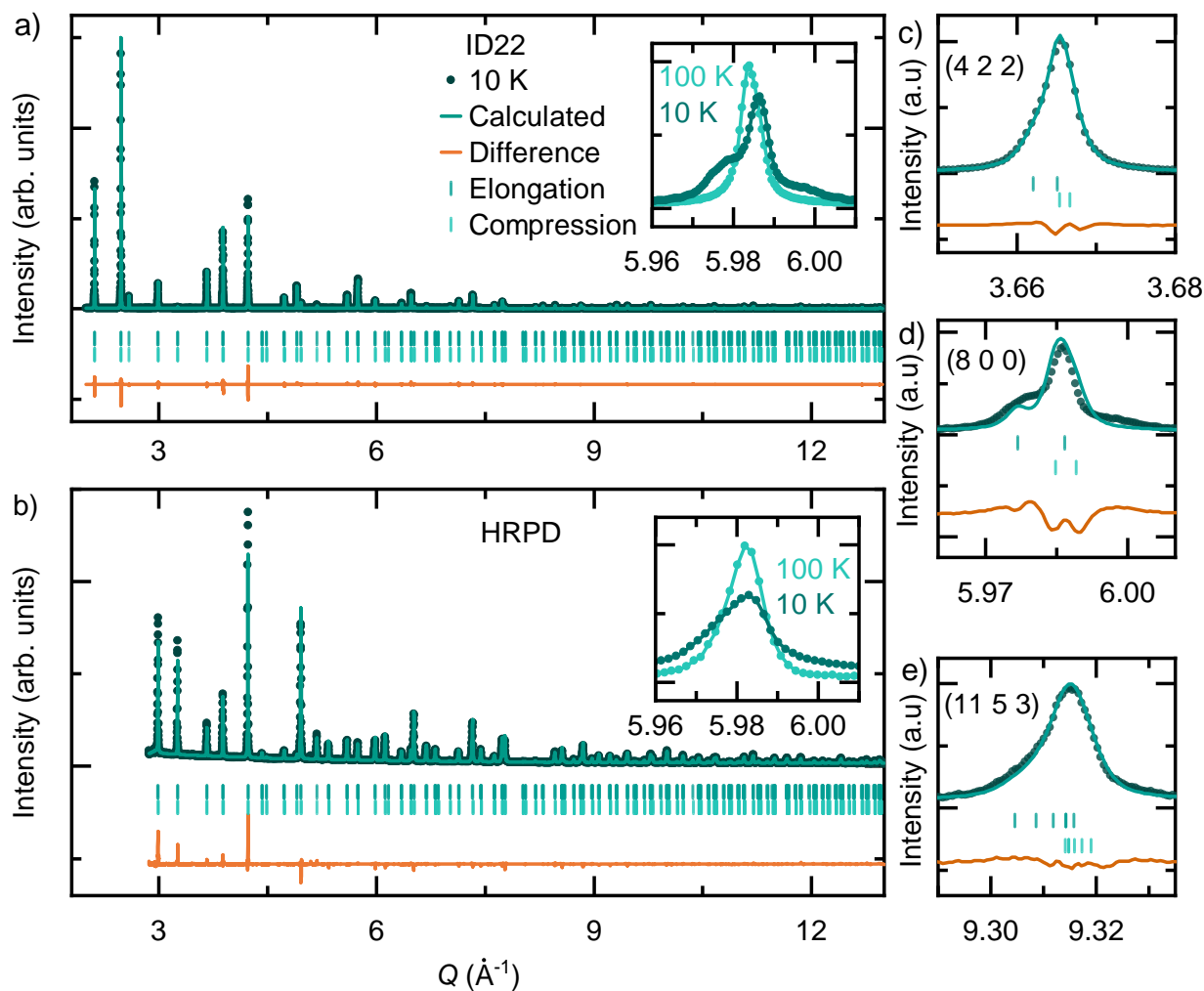


Figure 2.8: Combined Rietveld refinement of the sintered sample measured at 10 K. a) ID22, $R_{\text{wp}} = 18.6\%$, $\chi^2 = 16.3$, b) HRPD, $R_{\text{wp}} = 14.1\%$, $\chi^2 = 19.4$. The sintered sample was fit with two tetragonal $I4_1/amd$ structures (green tickmarks) with an overall global axial elongation of $c/\sqrt{2}a = 1.0010(3)$. Insets on each panel show the temperature evolution of the (800) reflection for the instrument. Rietveld fit of three key peaks from ID22, c) (4 2 2), d) (8 0 0) and e) (11 5 3).

for the sintered sample due to the subtlety of the transition, the spread in lattice parameters and the peak shapes.

2.3.1.4 Size and Strain Analysis

Size and strain of the ZnV₂O₄ samples was refined according to the Stokes and Wilson formalism [111] and described in the introduction. All size and strain parameters were highly constrained and refined isotropically. Anisotropic parameters did not increase the quality of the fit. The results are given in Table 2.4, where the sintered sample is over $2.5 \times$ more strained than the microwave sample. The presence of increased strain in the sintered sample is a key conclusion to this study. Strain is the only parameter in the structural analysis which has been found to have a positive impact on improving the quality of fit and marks a significant difference between the two samples physical composition.

Sample	Apparent size (Å)	Max-Strain ($\times 10^{-4}$)
Microwave	4575(8)	1.894(2)
Sintered	2672(5)	4.590(8)

Table 2.4: Results from size and strain analysis of the two samples from Fullprof.

2.3.1.5 Limitations of Average Structure Analysis

These comprehensive combined neutron and X-ray refinements reveal key conclusions about the average structures of the microwave and sintered ZnV₂O₄ samples. Namely, the microwave sample remains cubic down to 4 K but the sintered sample undergoes a structural distortion to an elongated tetragonal structure below 35 K. Both of these are unique conclusions about the structural behaviour for powder samples of ZnV₂O₄ in comparison to the literature. However, these refinements leave open some important questions about the

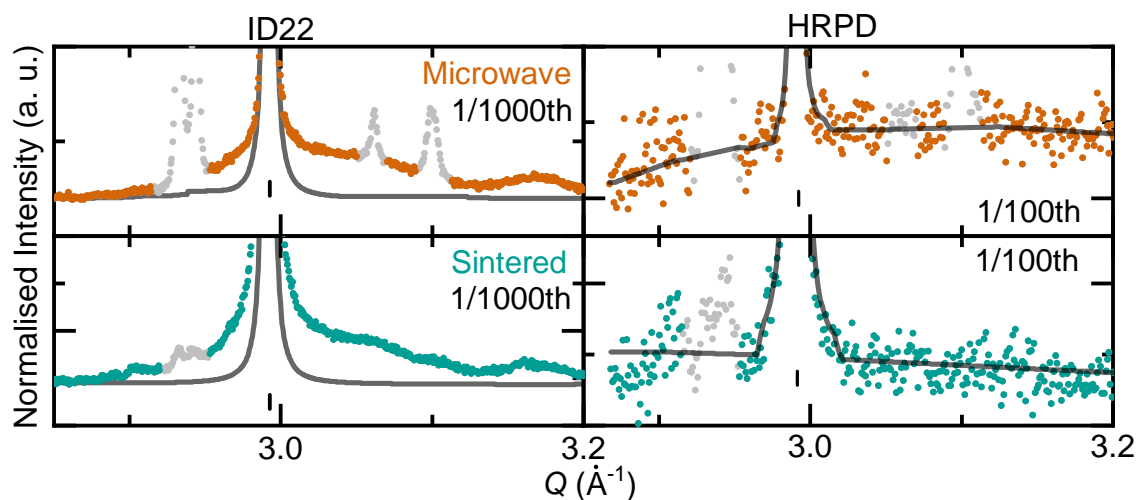


Figure 2.9: X-ray ID22 (left) and neutron HRPD (right) data at 100 K. Closer inspection of the base of the ID22 data shows diffuse scattering is present in both samples and is not captured in the average structure model. The same diffuse scattering is not present in the HRPD neutron data. In all figures data is shown by the orange and green markers for the microwave and sintered samples, respectively, grey markers are (trace) impurities, black tickmarks for ZnV_2O_4 reflections and the grey line for the fit (of ZnV_2O_4 phase only). Scale is shown as a fraction of the most intense peak.

mechanisms that drive these diverging low-temperature behaviours. It was found that the sintered sample was over $2.5 \times$ more strained than the microwave sample. Strain is an umbrella term that encompasses any deviation from the regular crystalline lattice of which, in real materials, there are many potential sources. However, common strain contributors, such as site mixing, off-stoichiometries and additional anisotropy on the thermal parameters, did not improve the quality of the fit.

Moreover, there are elements of the data in both samples that can not be explained fully by the average structure model. In the sintered sample, the low-temperature data have unusual peak shapes, which are beginning to be modelled when considering different distortions to the tetragonal structure simultaneously. Additionally, by looking very closely at the base of the peaks in Fig. 2.9, there is significant diffuse scattering in the ID22 data

for both samples which is not captured in the average structure refinement at all. More remarkably considering the distinct low-temperature structures, at 100 K the size and shape of this diffuse scattering is almost identical between the two samples. Conversely, a similar look at the HRPD data shows no sign of any diffuse scattering in either sample around the peak base, suggesting that if disorder is present it will be V-based. Together, these results indicate that to fully understand the structural behaviour of ZnV₂O₄, a detailed look into the chemical structure from a local perspective is required.

2.3.2 Local Chemical Structure

An average structure refinement over a 50 Å range of ID22 X-ray PDF data is shown in Fig. 2.10 for the a) microwave and b) sintered samples at 100 K. Both experimental PDFs were fit with the cubic $Fd\bar{3}m$ structure, which has good agreement with the data, $R_{\text{wp}} = 13.01\%$ for the microwave sample and $R_{\text{wp}} = 13.00\%$ for the sintered sample. A comparison between the difference curves can be seen in Fig. 2.10c) which reveals a distinct oscillation. Curiously, the difference curves are nearly identical between the microwave and sintered samples at 100 K. This oscillation reflects that the correlation length of both samples is the same and has a period of $r = 23$ Å, or ~ 3 crystallographic unit cells in length.

To explore if the oscillation was due to a certain type of correlated disorder, the local structure was probed via the carbox method with a 10 Å box, moved every 2 Å. All lower symmetry structures determined by ISODISTORT were fit against the data, however, for both samples, the results were overcorrelated and the lattice parameters returned to cubic each time. Then, in the $Fd\bar{3}m$ symmetry, atoms were displaced off their ideal Wyckoff position, but again, both samples returned all atoms to their ideal positions. The only parameter which was found to vary, and improve the fit, was the vanadium isothermal parameter, $V-U_{\text{iso}}$. Figure 2.11 interestingly reveals that this parameter also has an oscillatory dependence, with exactly the same periodicity (23 Å), as found in the difference curve in Fig. 2.10c).

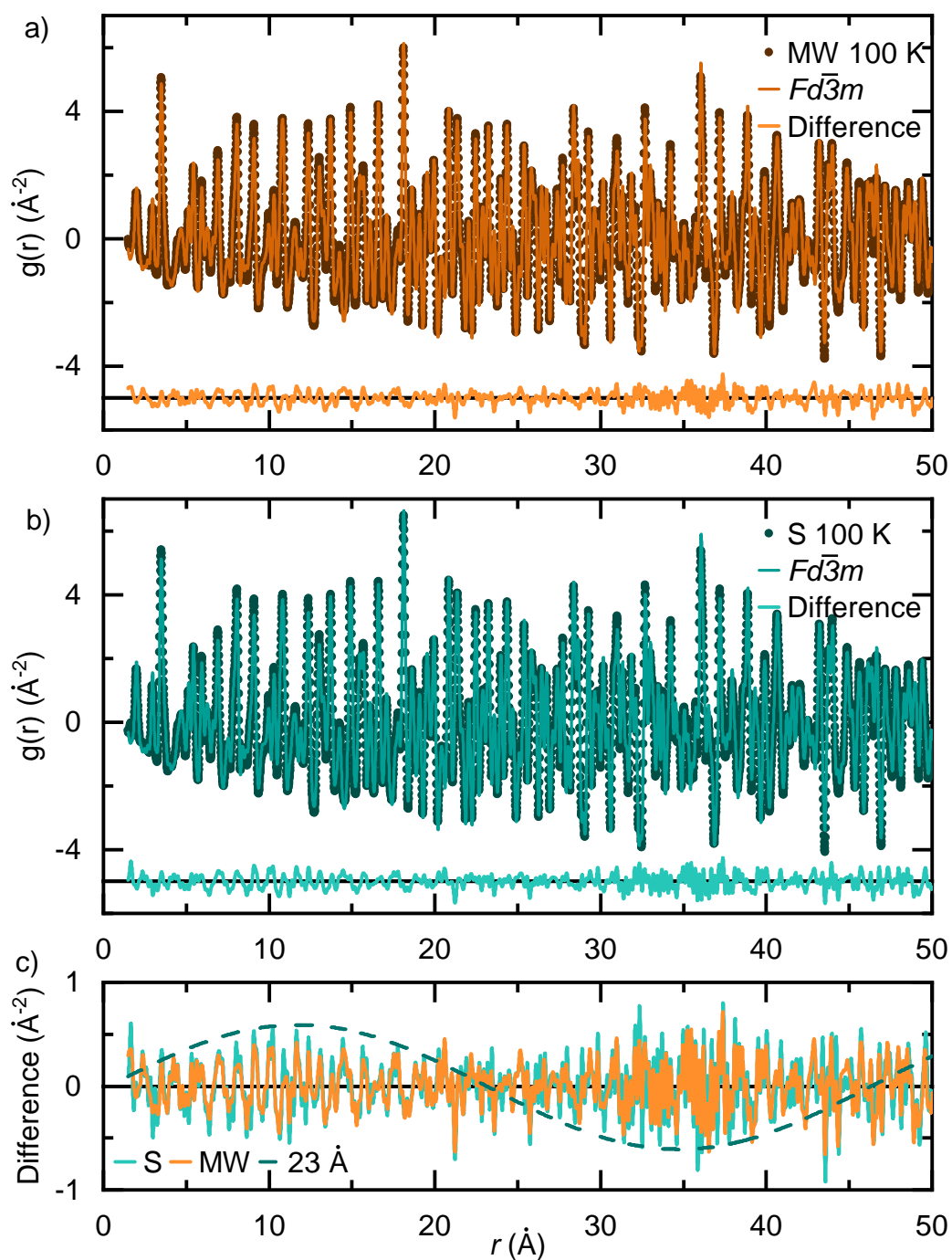


Figure 2.10: X-ray PDF fits of the average cubic $Fd\bar{3}m$ structure for the a) microwave and b) sintered samples at 100 K. c) Comparison of difference curves at 100 K are nearly identical between the samples and show a distinct oscillation with correlation length, $r = 23 \text{ \AA}$. Dashed line added as a guide to the eye.

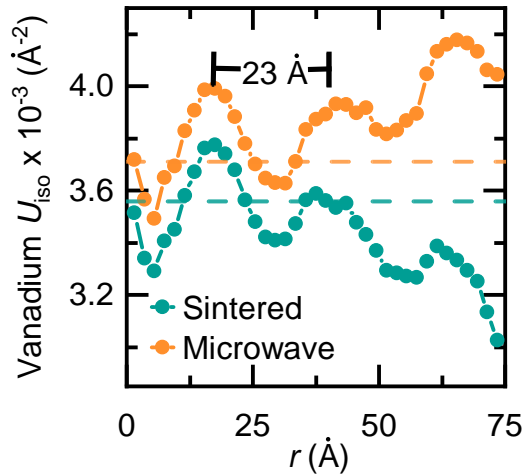


Figure 2.11: Results from refinement of only $V-U_{\text{iso}}$ via the carbox method (10 Å range, centred every 2 Å). Both samples show a distinct oscillation which has the same period as the difference curve in Fig. 2.10c). Dashed lines show the average $V-U_{\text{iso}}$ value from the fit over the 50 Å range.

Since no other lower symmetry spacegroups, with allowed vanadium disorder, improve the quality of the fit in the PDF refinement, it can be concluded that this vanadium disorder is very small, and outside the resolution of these current experiments.

Similarly, the same procedure was completed for the low-temperature data collected at 7 K. The microwave sample was best fit over the average length scale by the cubic $Fd\bar{3}m$ structure (Fig. 2.12a)), and the sintered by a tetragonal structure, such as $I4_1/amd$, with axial elongation of $c/\sqrt{2}a = 1.0038$ (Fig. 2.12b)). These results mirror the findings of the Reitveld analysis. Figure 2.12c) shows that at low-temperatures, both samples have the same correlation length (23 Å) as at high-temperatures, as the same oscillating difference curve is present. Investigations into local distortions all converged on the same results as at 100 K, with only the vanadium U_{iso} having any significant dependence.

This PDF analysis has shown that at 100 K on local, medium and average length scales the ZnV_2O_4 samples are cubic. Clearly, there is disorder present, as the difference

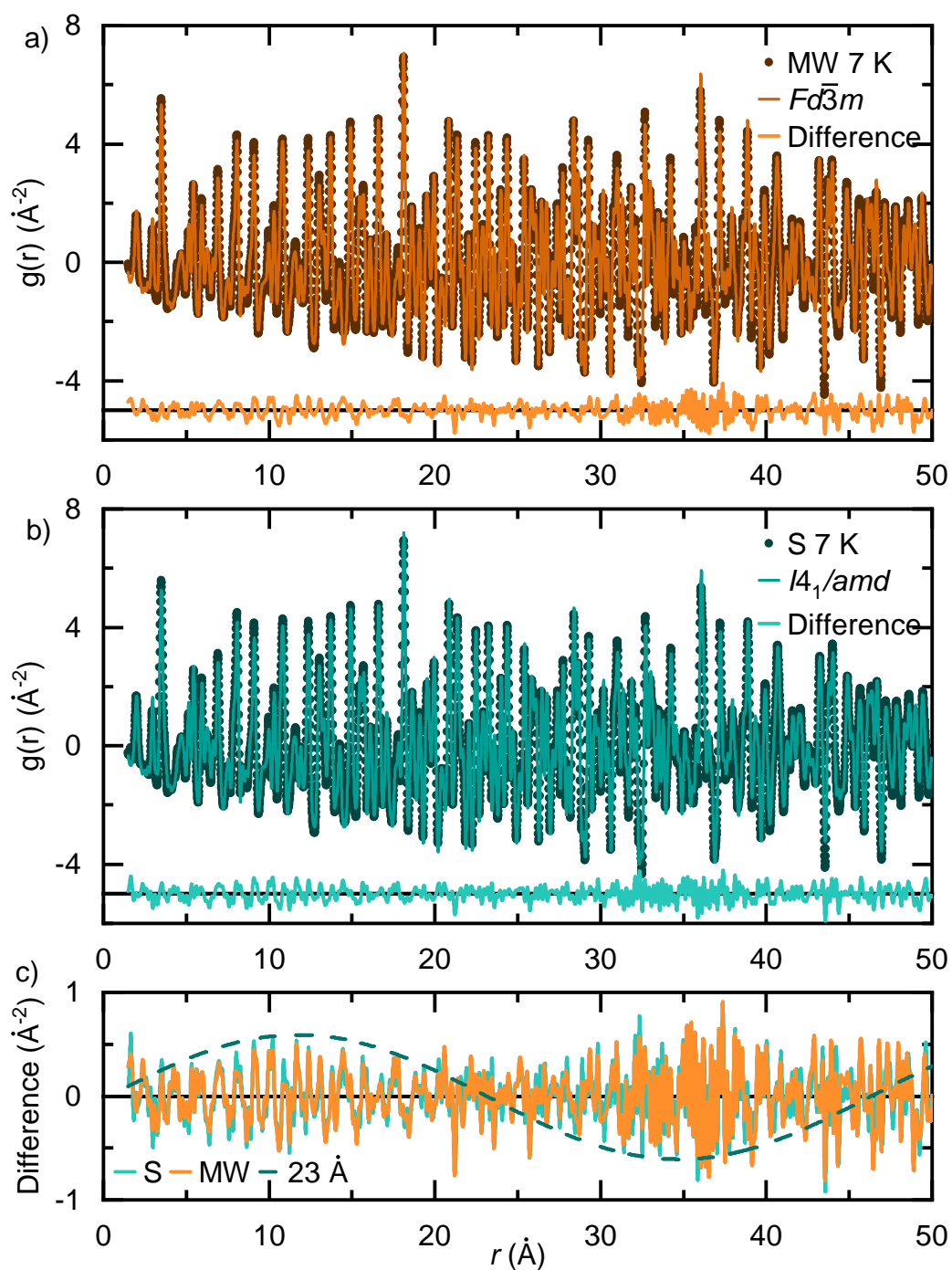


Figure 2.12: X-ray PDF fits of the average structures for the a) microwave sample with the cubic $Fd\bar{3}m$ structure and b) sintered sample with the tetragonal $I4_1/amd$ structure at 7 K. c) Comparison of difference curves at 7 K are nearly identical between the samples, and at 100 K, and show a distinct oscillation with correlation length, $r = 23 \text{ \AA}$. Dashed line added as a guide to the eye.

curves have an oscillating waveform, with a correlation length, that is unchanged between samples and temperatures, of $r = 23 \text{ \AA}$. However, this disorder is very small and most likely occurs from correlated displacement of vanadium sites as indicated by the refinement of U_{iso} in Fig. 2.11. The most important finding from these results is that because the same behaviour is seen in both samples, the disorder within ZnV_2O_4 is intrinsic to the material, and therefore synthesis independent. Thus, vanadium disorder does not drive the structural behaviour observed at low-temperatures.

It therefore remains that the key difference between the samples is the amount of strain present in the system, and this likely drives the evolution of the structure at low-temperatures. The next question to ask is: how do these distinct chemical structures affect the magnetic properties of the system? This question will be explored in the following section.

2.3.3 Magnetic Susceptibility

2.3.3.1 DC Susceptibility

Figure 2.13 shows the powder DC magnetic susceptibility data for the a) sintered and b) powder samples in a 0.01 T applied magnetic field. A first observation is that the susceptibilities are quite different between the two samples. Firstly, in the sintered sample there are two very broad features, peaked at $T_1 = 12 \text{ K}$, and $T_2 \sim 45 \text{ K}$. Though these are similar to the magnetic and structural transitions commonly observed for powdered ZnV_2O_4 samples, it should be noted that the feature at T_2 does not have the sharp discontinuity that is normally measured and associated with the structural distortion (Fig. 2.2a) [155]). On the other hand, the microwave sample has one sharp feature peaked at $T_1 = 11 \text{ K}$ which is reminiscent of the single-crystal study shown in Fig. 2.2b) [157]. The difference between ZFC and FC measurements is large in both cases, and splits at higher temperatures than

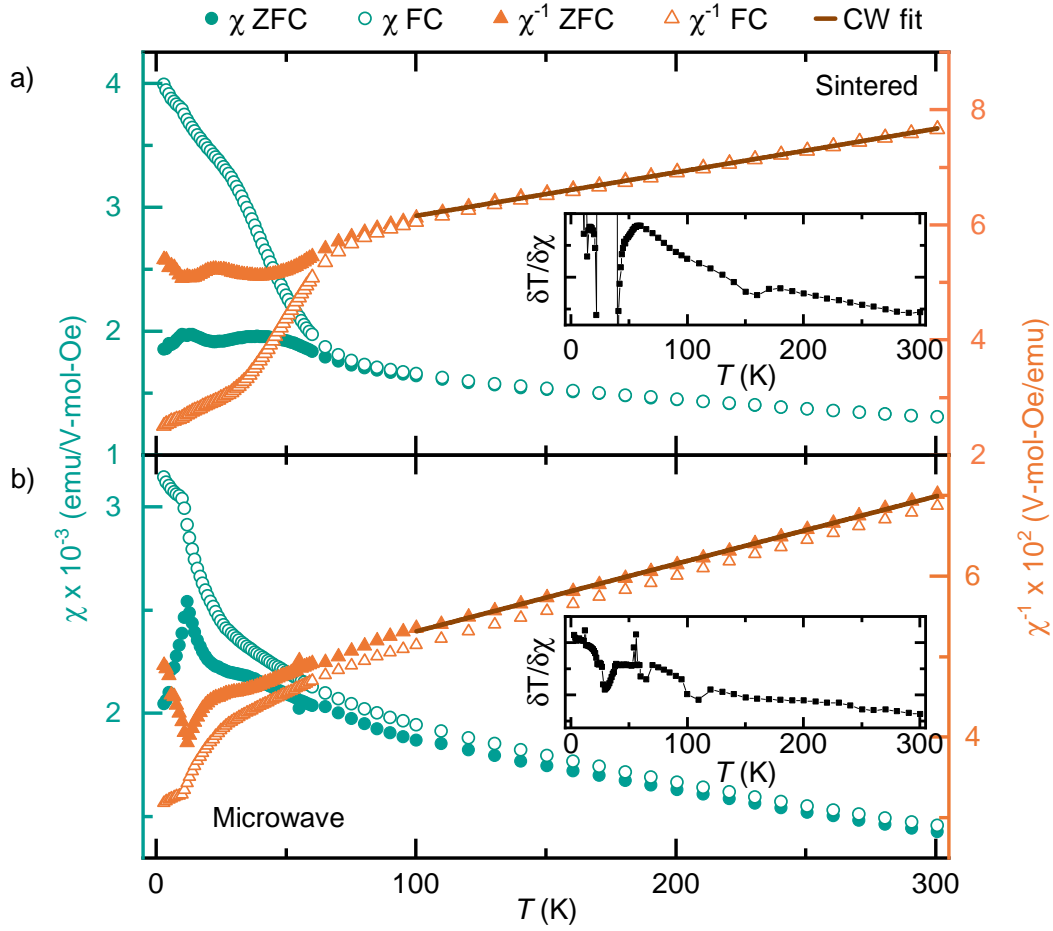


Figure 2.13: DC powder magnetic susceptibility, χ (green circles) and its inverse, χ^{-1} (orange triangles) for the a) sintered and b) microwave ZnV_2O_4 samples measured in a 0.01 T magnetic field. In both figures, closed and open markers represent ZFC and FC measurements, respectively. Curie-Weiss fits (solid brown lines) were conducted over a range of 100 to 300 K on the ZFC measurement. Inserts show the inverse of the derivative, $\frac{\delta T}{\delta \chi}$, which is not constant as a function of temperature at any point.

the observed transitions. This suggests that the T_1 features are unlikely to describe a spin glass transition [37].

The data have been fit between 100 K and 300 K with the Curie-Weiss law (Eq. 1.2). A summary of the results from a Curie-Weiss fit can be found in Table 2.5. Though the

Sample	θ_{CW} (K)	C (emu K mol ⁻¹)	μ_{eff} (μ_{B}/V)
Sintered	-714(7)	1.32(1)	3.25(1)
Microwave	-534(1)	1.19(1)	3.09(2)

Table 2.5: Results from the Curie-Weiss fit of powder ZnV₂O₄ susceptibility data for the sintered and microwave samples. θ_{CW} is the Weiss constant, C is the Curie constant and μ_{eff} is the effective magnetic moment.

results are similar to previously reported Curie-Weiss analyses of powder ZnV₂O₄ [153–156], in this study it is believed these values are likely unphysical due to the large energy scale for the extracted Weiss constant. A Curie-Weiss fit should be conducted when the sample is in its paramagnetic regime, which is identifiable when the inverse of the derivative, $\frac{\delta T}{\delta \chi}$, is constant as a function of temperature. As can be seen in the inserts of Fig. 2.13, at no point in either sample does the inverse derivative become constant below 300 K. Attempts at measuring the magnetic susceptibility to higher temperatures were unsuccessful, with the susceptibility remaining non-linear up to 1000 K (Appendix Fig. 2.22). This may be because ZnV₂O₄ lies close to the metal-insulator transition which is often not suitable for Curie-Weiss analysis due to the non-linearity of the susceptibility [180–182].

Identifying the transition temperatures is not trivial for these samples. As can be seen in Fig. 2.14a) and b), for the microwave and sintered samples respectively, a curious χ dependence with small applied magnetic fields was measured. It can be seen that over this range (2.5 mT to 25 mT), the DC susceptibility of both samples has a strong magnetic response and reveals new features. Hinted at in Fig. 2.13b), a shoulder on the microwave sample at around 25 K becomes evident at lower applied magnetic fields. This is interesting, as the broad features in ZnV₂O₄ susceptibility are generally associated with structural behaviour. However, since the microwave sample has been confirmed to remain cubic down to 4 K, this feature must describe something else. By taking the derivative of the susceptibility, further weak oscillations, representing changes in the gradient of χ , can be seen in the data,

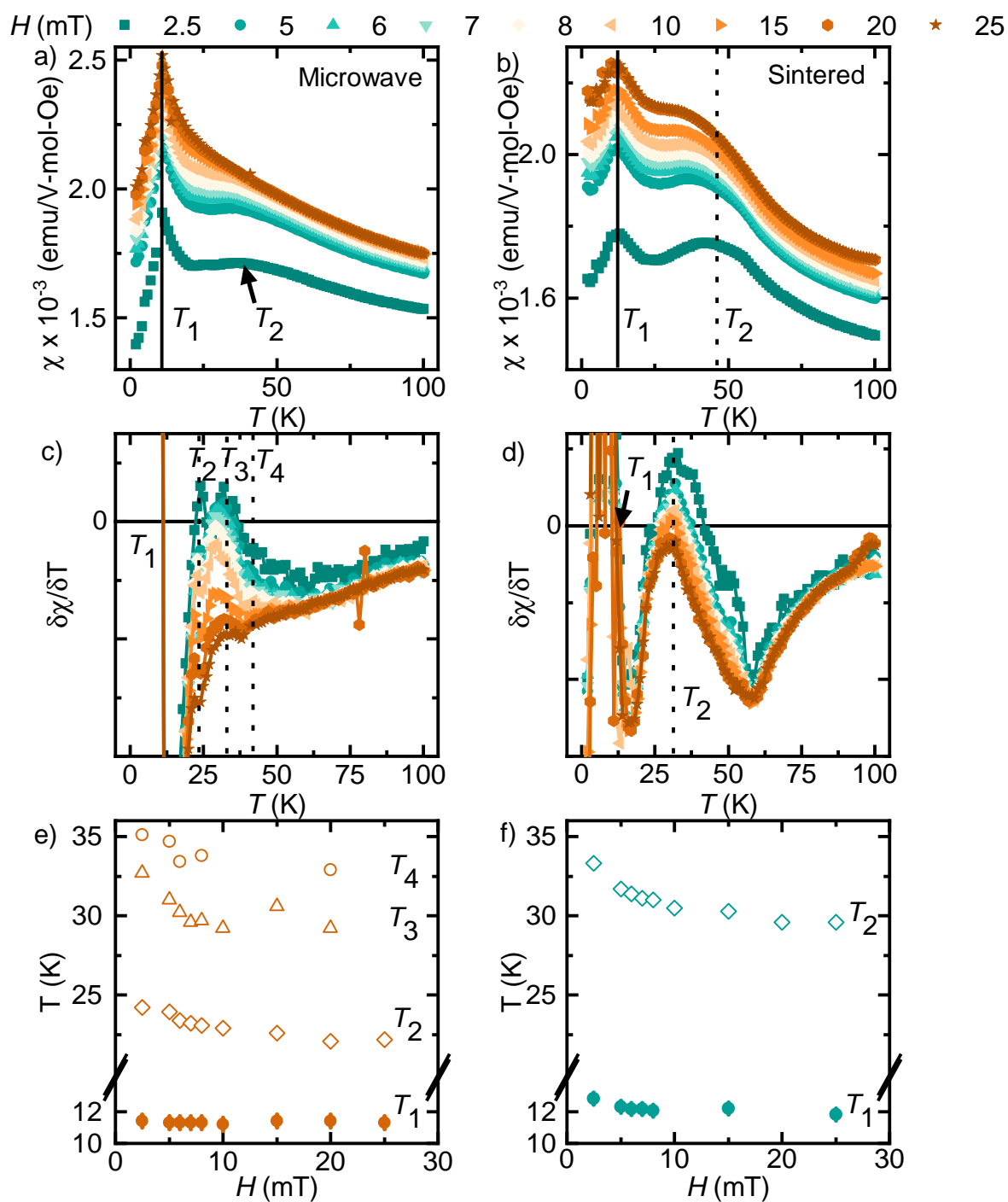


Figure 2.14: Microwave (left) and sintered (right) a) and b) DC magnetic susceptibility as a function of applied magnetic field. c) and d) The derivatives reveal oscillations which are used to extract transition temperatures in e) and f). Error bars are included but are small.

labelled $T_2 - T_4$ in Fig. 2.14c). In contrast, the sintered sample shows the two broad features, with T_2 flattening out with increasing field strengths. In the derivative, an interesting change in slope is observed at ~ 60 K, which is independent of field and indicates the onset of the T_2 feature.

The transition temperatures are summarised in Figs. 2.14e) and f) for the microwave and sintered samples respectively. T_1 was extracted when the derivative curve passed zero on the x-axis. T_1 was found to be field independent within error for the microwave sample, and slightly field dependent at low fields (< 8 mT) for the sintered sample. Since not all of the T_2 - T_4 derivatives passed zero, the $T_2 - T_4$ features were extracted by fitting a Gaussian peak to each feature in the derivative, with the peak centre defined as the transition temperature. When a Gaussian could not be well fit to the data, the transition temperature is not quoted. Despite the different transition temperatures, the transitions between the samples largely follow the same trends and appear to plateau from 10 mT onwards.

2.3.3.2 AC Susceptibility

In addition to the DC measurements, AC susceptibility data are presented in Fig. 2.15, with both the real, χ' and imaginary, χ'' , contributions viewed on a broken scale. In contrast to the DC measurements, a first observation is that the AC susceptibilities are very similar between the two samples. Firstly, there is the T_1 feature, at ~ 11 K, which in both cases, is well defined and has only slight variation as a function of frequency for the microwave sample, and no variation for the sintered sample within error (Fig. 2.15 inserts). There is also almost no dynamic response (imaginary susceptibility, χ'') at this T_1 transition, which suggests that neither sample transitions to a spin glass ground state. This observation is crucial, as it was hypothesised that since the microwave sample remained in the cubic symmetry down to 4 K the ground state would be a spin glass, like in the single-crystal [157]. However, the main experimental signatures of a spin glass—strong frequency dependence, large dynamic

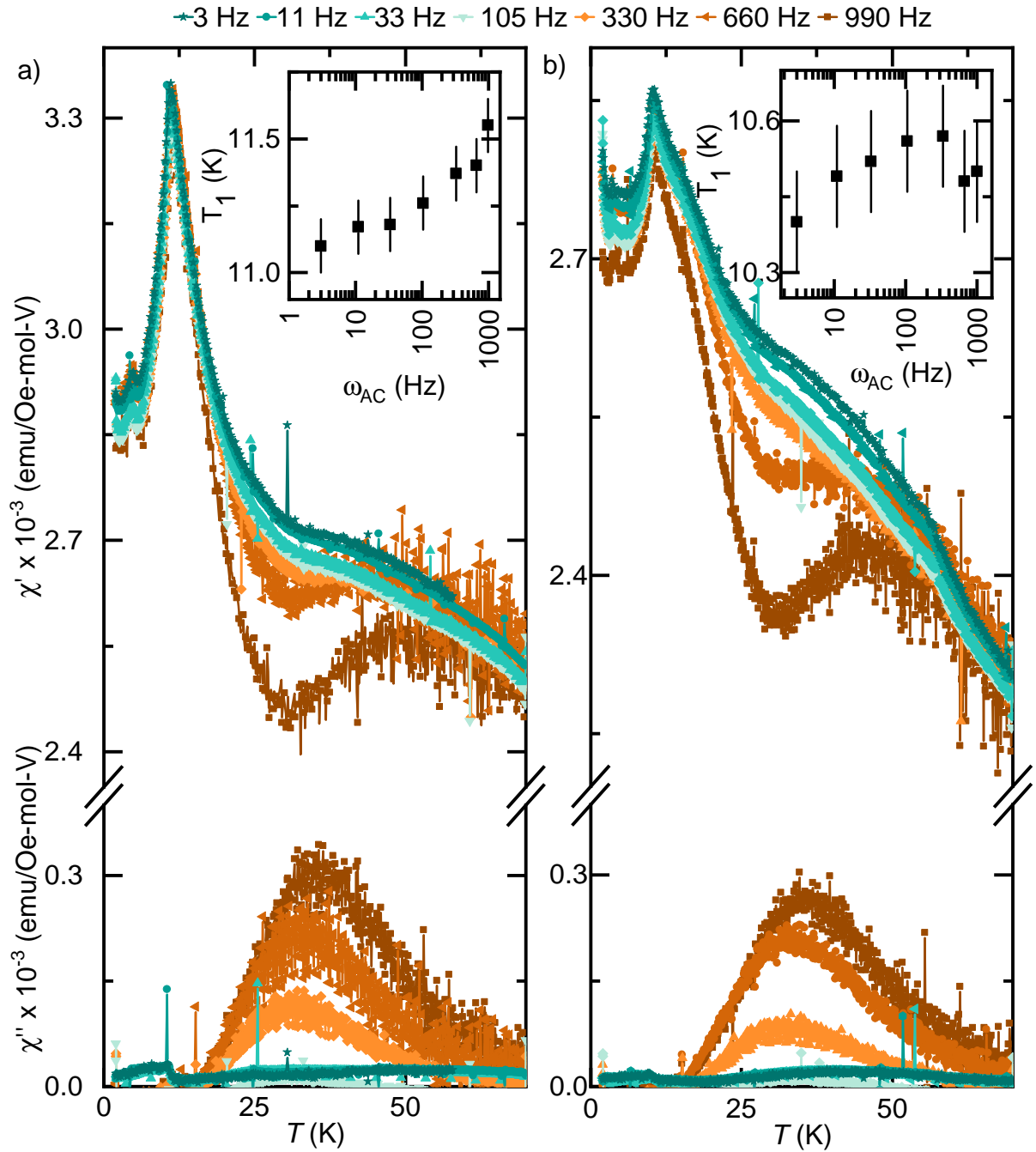


Figure 2.15: Real, χ' and imaginary, χ'' contribution to AC susceptibility for the a) microwave and b) sintered samples. Data are shown on a broken scale. Inserts show the transition temperature, T_1 , as a function of the driving frequency, ω_{AC} . There is some frequency dependence in T_1 for the microwave sample, but not in the sintered.

response, and ZFC/FC splitting at the magnetic transition [37]—are all absent from these DC and AC measurements, and suggests that neither sample has a spin glass ground state.

Despite not clarifying whether a transition towards a spin glass occurs, these AC measurements reveal some very interesting features. The region between 20 K and 60 K has, for both samples, a very strong frequency dependence and dynamic response. This is the same region where the broad T_2 feature in the sintered sample, and shoulder feature in the microwave sample were observed in the DC susceptibility data. Tracking this frequency dependence in the temperature range where χ'' is significant (20 to 55 K) is summarised in Fig. 2.16, where both samples have almost identical behaviour. It is expected in this "slow frequency" regime, that there should be a characteristic peak describing the fluctuation rate, Γ ($f = \Gamma/2\pi$, where $\Gamma = 1/\tau$). However, aside from potentially the onset of a peak at 1000 Hz at 20 K, no peak is observable. This suggests that to understand the fluctuations in ZnV_2O_4 , further AC susceptibility measurements at higher frequencies are required.

From these AC and DC magnetic susceptibility measurements, the magnetic ground state is still unknown but is unlikely in either case to be a spin glass. It is quite striking that despite all the differences in these samples, the AC behaviour is so similar, particularly in the 20 - 60 K region. A key conclusion is that this region cannot be associated with the structural evolution of the samples, and therefore the magnetic fluctuations that this behaviour is describing are inherent to ZnV_2O_4 .

2.3.4 Magnetic Diffuse Scattering

To understand the magnetic ground state further, several neutron diffraction experiments have been performed. These measurements have been complicated due to a number of factors, including:

1. ZnV_2O_4 has a small magnetic moment due to it being a spin 1 system.

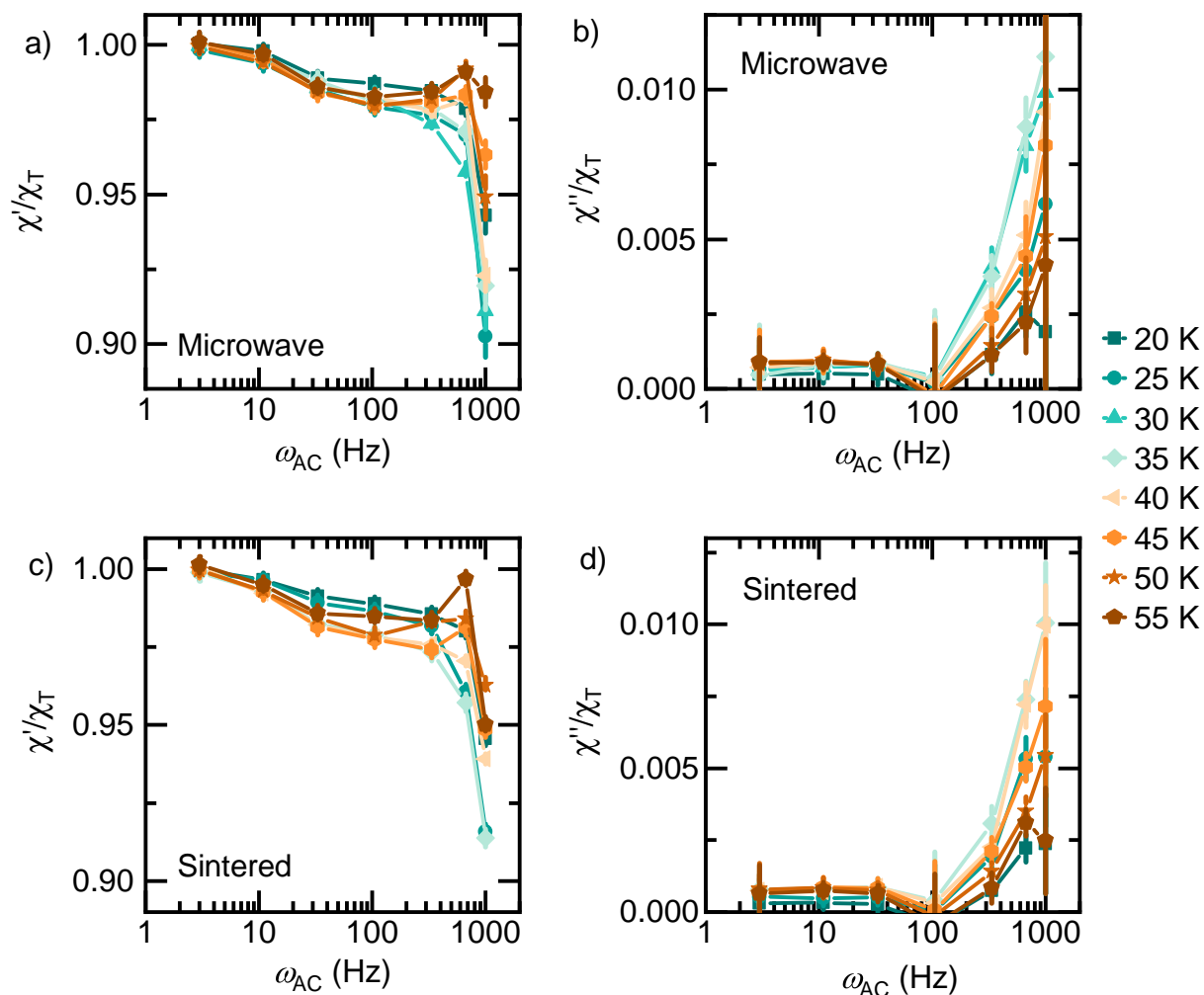


Figure 2.16: Frequency dependence of the real, χ' (left) and imaginary, χ'' (right) components of χ_{AC} in the temperature region 20 K - 55 K. Microwave sample, top and sintered sample, bottom. χ_T is the static susceptibility (χ_{AC} at low frequencies). Both show a very similar dependence, and do not show a peak indicating that the characteristic fluctuation rate has not been reached within the measured frequency range.

2. ZnV_2O_4 has large magnetic exchange interactions, as shown in previous inelastic neutron scattering measurements where a continuum of magnetic excitations were observed up to at least 30 meV [158].
3. The temperature at which the sample becomes completely paramagnetic is unknown, as highlighted in the DC magnetic susceptibility measurements.

The key conclusions about the magnetic ground states of the sintered and microwave samples are that neither undergo a transition to a long-range magnetic ordered state as only diffuse magnetic scattering is observed. The nature of the magnetic ground states in this study is not currently known, but due to the different features observed in the diffuse scattering the magnetic ground states are distinct, and likely dynamic, highly frustrated and strongly interacting. Future inelastic neutron scattering (INS) experiments will aid in the determination of the magnetic ground state for both samples.

2.3.4.1 Sintered Sample

As an example to the complexities surrounding the data collection and analysis of the magnetic ground state of ZnV_2O_4 , a summary of the experiments performed on the sintered sample is shown in Fig. 2.17.

Figure 2.17a) shows the magnetic contribution at 1.5 K from D7, where only structured diffuse scattering is observed (full data in Appendix, Fig. 2.23). The previously observed magnetic Bragg peaks from Ref. [153, 158] are positioned at $Q = 1.1 \text{ \AA}^{-1}$ and $Q = 1.7 \text{ \AA}^{-1}$, so roughly correspond with the onset of this diffuse feature. However, this diffuse scattering has quite a pronounced shape, which is not indicative of long-range magnetic order, with a very gradual reduction in magnetic intensity from $Q = 1.1 \text{ \AA}^{-1}$. SPINVERT RMC analysis was completed on this data, with a supercell size of $6 \times 6 \times 6$ cubic $Fd\bar{3}m$ unit cells, weight = 10 and moments allowed complete rotational degrees of freedom. The

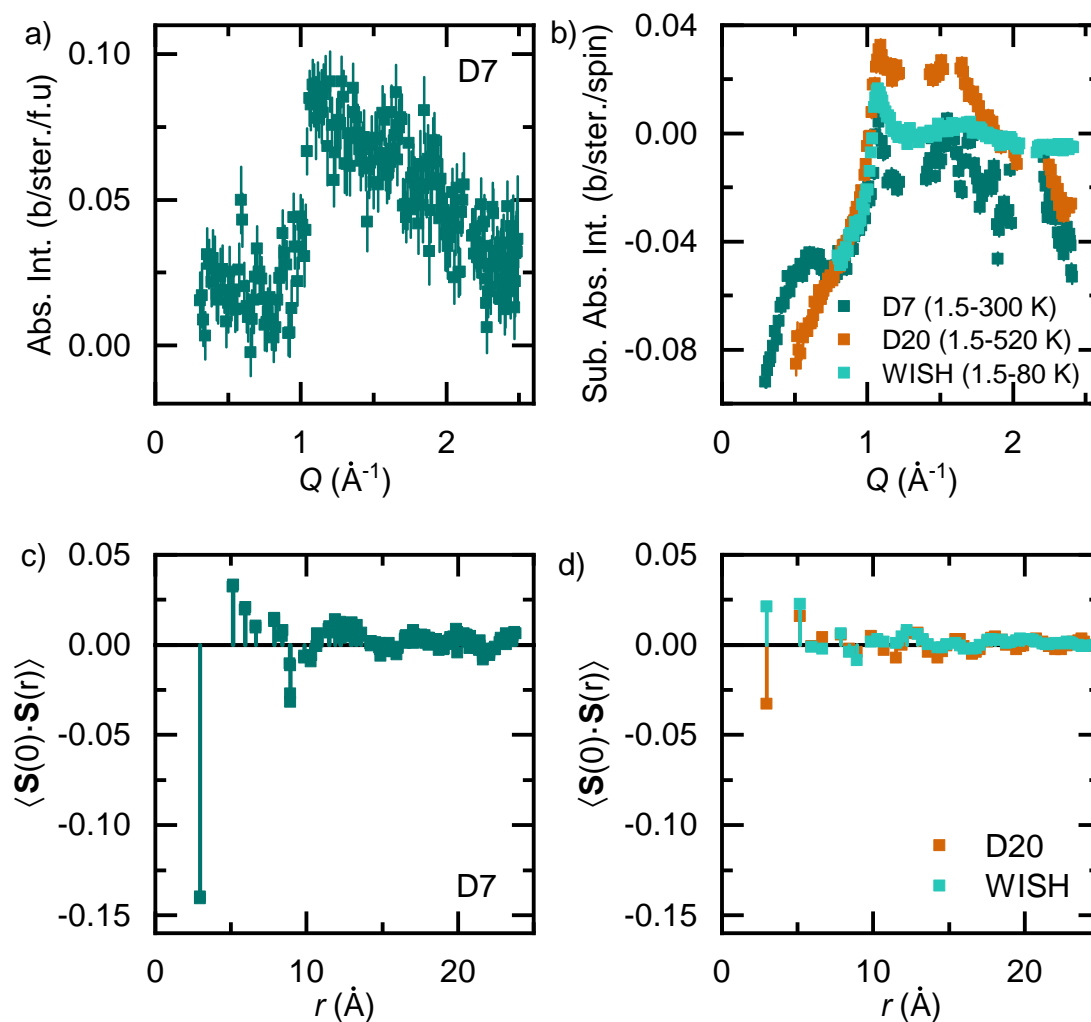


Figure 2.17: Summary of diffuse neutron scattering and correlations in the sintered sample.

a) Magnetic contribution of data from D7 at 1.5 K in b/ster./f.u. b) Subtracted total intensity in units b/ster./spin, 1.5 K - 300 K for D7 (total scattering, dark green), 1.5 - 520 K for D20 (orange) and 1.5 - 80 K for WISH (light green). Correlations from SPINCORREL analysis for c) D7 and d) D20 and WISH.

fit was in good agreement with the data, and convergence was reached within 100 moves. The corresponding correlations calculated from SPINCORREL are shown in Fig. 2.17c). As expected, it was found that an average antiferromagnetic interaction is observed for the first nearest neighbour interaction. The magnitude of correlations quickly reduces and has a slight oscillatory dependence with increasing r .

However, D7 measurements assume that the static approximation is valid over its relatively narrow integration window of $-20 \leq \Delta E \leq 3.5$ meV. Essentially, this should take a snapshot of the time-equal behaviour of the material. Previous inelastic neutron scattering measurements by Lee *et al.* [158] showed that ZnV₂O₄ has significant inelastic magnetic scattering intensity, up to at least 30 meV. This is problematic as the integration window of D7 is only able to see a limited proportion of the total magnetic scattering, which may distort the data. This is likely what has happened here, which invalidates the static approximation, and return the SPINVERT analysis.

For magnetic systems with weak magnetic features there is another route to isolating the magnetic scattering which is to perform temperature subtractions. Polarisation analysis is usually preferred as for temperature subtractions to be valid the instrument needs to be very stable, the sample should be stable enough that the non-magnetic background does not change throughout the measurement, and, most importantly, the high-temperature subtracted data set needs to be measured when the sample is fully paramagnetic. In this case, polarisation analysis is particularly useful given that the large incoherent scattering cross-section arising from the V³⁺ ions can be removed. However, as the static approximation was not valid on D7, temperature subtractions were used, with higher incident energies in an attempt to integrate over the whole magnetic scattering of ZnV₂O₄.

A summary of temperature subtractions are shown in Fig. 2.17b) for WISH (1.5 K – 80 K, light green) and D20 (1.5 K – 520 K, orange). Also included is a temperature subtraction of the total scattering of the D7 data between 1.5 K – 300 K (dark green).

Full data sets and analysis can be found in the Appendix Figs. 2.24, 2.25, 2.26. These data show roughly the same features; only magnetic diffuse scattering, a sharp feature at $Q = 1.1 \text{ \AA}^{-1}$, and a gradual reduction in magnetic intensity with increasing Q . The WISH and D20 data have been normalised to absolute units, by fitting the nuclear contribution on `Fullprof` and then using the conversion described in the introduction (Eqs. 1.18 and 1.19). Data were normalised to b/ster./spin , with $N = N_{\text{mag}} = 2$ as there are 2 V^{3+} spins per unit cell. Nuclear contributions were removed via temperature subtraction, leaving the isolated magnetic intensity to be fit using `SPINVERT`. A difference between isolating magnetic scattering data collected via polarisation analysis or by temperature subtractions is that a scale proportional to the classical moment sized squared must be specified in `SPINVERT` for the temperature subtracted data, whereas the scale is refined for data collected via polarisation analysis. This is because in the temperature subtracted case the experimental intensity oscillates around zero. A difficulty in this study is that the moment size is not known because the Curie-Weiss analysis of the DC susceptibility data was not valid. Previous investigations—in which magnetic Bragg peaks were observed [153, 158]—determined the moment size to be significantly reduced to $\mu = 0.62 \mu_{\text{B}}$, but this is not appropriate for this work as long-range magnetic order is not observed, only magnetic diffuse scattering. So, it was assumed that the moment was equal to the full expected moment of a spin 1 system, with a scale of 8 ($\mu = \sqrt{8} \mu_{\text{B}} = 2.83 \mu_{\text{B}}$) fixed during the refinement. Different fit parameters were used for each data set (summarised in the Appendix) but all converged within 100 moves and results were consistent between different runs from a new random seed.

The correlations are shown for both D20 and WISH in Fig. 2.17d), on the same scale as the correlations determined for the D7 analysis. Immediately, it is clear that there are a number of discrepancies between the three sets of correlations. Firstly, the first nearest neighbour correlation calculated for the WISH data is, on average, ferromagnetic, which is not the expected behaviour for ZnV_2O_4 . Additionally, further temperature subtractions (Appendix Figure 2.25) revealed that these correlations at 1.5 K - 80 K in general, had the weakest

magnitude. This is unexpected, because at the lowest temperatures, the system should be in its most correlated state, and with increasing temperature the correlations should decrease in magnitude as the system approaches random paramagnetic behaviour. The reason that this has occurred is likely because of the temperature used in the subtractions, 80 K. 80 K was chosen to minimise the thermal shift of the nuclear Bragg peaks which must be removed for the SPINVERT analysis. Removing any data, reduces the amount of usable information that can be used during the analysis, therefore decreasing the likelihood of getting the correct answer. This is particularly true for RMC analysis of diffuse magnetic scattering, as the number of degrees of freedom in the simulation vastly outnumbers the number of data points. However, as shown in the Curie-Weiss analysis of DC magnetic susceptibility data, 80 K is well below the θ_{CW} values (Table 2.14), and so not within the paramagnetic regime which explains why this temperature subtraction has failed.

The D20 data uses a much larger temperature subtraction as a cryofurnace was used for collecting the data. A short wavelength, of $\lambda = 1.3 \text{ \AA}$ was selected to maximise the integration window, and it can be seen that this data set has the largest overall intensity of the three, hopefully indicating that more magnetic scattering has been captured. However, whilst the first nearest neighbour is antiferromagnetic, the magnitude is significantly reduced in comparison to the D7 correlations, indicating that this temperature subtraction has also failed. The magnitude of the correlations will be determined by the scale factor, and if the scale is incorrect, such as too large, then this will squash a function with a large amplitude onto weak intensity data and ultimately reduce the magnitude of the correlations. The moment size per V³⁺ ion refined from the D7 analysis was $\mu = 0.65(2) \mu_B/V^{3+}$ which is in agreement with the moment size determined for samples which produce magnetic Bragg peaks [153, 158]. However, the temperature subtractions used to isolate these magnetic Bragg peaks was 1.5 K - 70 K [153], which from the WISH analysis, is known to not be enough to adequately isolate all of the diffuse magnetic scattering of the system. Since the moment size cannot be predicted from the Curie-Weiss analysis of DC magnetic susceptibility data,

there is no way at this stage to be able to better predict the effective moment size than to assume that ZnV_2O_4 has the expected moment from a spin 1 system.

Moving forward with the determination of the magnetic ground state using neutrons, the focus must change from diffraction to inelastic measurements. The static approximation has been found to be invalid for all of these measurements, and so the diffraction approach, which assumes no change in the neutron energy, is not appropriate for this study. Recently, time on the thermal neutron time-of-flight spectrometer, PANTHER at the ILL was awarded for this measurement, and the new data will overcome these experimental challenges to clarify the magnetic ground state of ZnV_2O_4 .

2.3.5 Discussion

The results presented in this chapter highlight the complexities of understanding the chemical and magnetic ground states of a material that is highly sensitive to the synthesis route taken, such as ZnV_2O_4 . Within the context of ZnV_2O_4 , the two powder samples studied in this chapter are anomalous. Powder ZnV_2O_4 usually undergoes a cubic-tetragonal compression along the c -axis at $T \sim 50$ K [155, 156]. Through high-resolution diffraction measurements, the sintered sample was found to undergo a cubic-tetragonal distortion below 35 K, but with an unusual global elongation along the c -axis. Conversely, the microwave sample remained cubic down to 4 K, which is the first confirmation of this behaviour in a powder sample. Strain was identified as the likely cause of this behaviour, since at high-temperatures the sintered sample was over $2.5 \times$ more strained than the microwave sample. This is a major conclusion as in the single-crystal study [157], the sample was believed to be highly strained which prevented the structural distortion from occurring. It is difficult to tell from two points a relationship that can generally describe a materials properties, particularly for a system as complex as ZnV_2O_4 . Therefore more samples prepared by different synthetic routes are required in the future. However, the structural characterisation applied to the samples

in this chapter are, to the authors knowledge, the most rigorous and standardised in the literature. An example of the complexities surrounding comparing parameters of different materials across different studies, Fig. 2.18a) in the Appendix shows the lattice parameters compiled from the literature compared against the samples from this chapter, colour coded to show the reported number of transitions. In cubic spinels, the lattice parameters are known to be highly sensitive to the sample stoichiometry, and so defects beyond the resolution of diffraction can be implied through comparing different samples. However, no relationship between the ZnV_2O_4 samples and reported number of transitions is seen, and this is likely due to the different experimental setups and instrument calibrations. Additionally, in Chapter 1 the signatures of strain in diffraction were discussed (more strained = drop in intensity and broadening of peaks), but no reference of the peak profile was included in the Ebbinghaus study to back up the hypothesis that the single-crystal was more strained than the crushed powder sample [157]. This was, however, confirmed in this chapter, as it can clearly be seen in Fig. 2.3 that the Bragg peaks in the sintered sample are much broader than those in the microwave sample at 100 K.

For the magnetic ground state, the consensus from the literature is much less established. There are typically two conclusions; long-range magnetic order develops following a structural distortion [153] or a spin glass ground state for samples that remain cubic [157]. Weak magnetic Bragg peaks describing long-range magnetic order have been observed just 3 times in ZnV_2O_4 [153, 158, 161], despite the large number of publications where a structural distortion is reported. The magnetic order these Bragg peaks describe—antiferromagnetically coupled spin chains along the a - and b -axes that are ferromagnetically coupled along c —was only inferred from the solution of the magnetic ground state of MgV_2O_4 [154, 164, 165]. This is surprising, that despite all of these measurements no better model, or more conclusive evidence that this is the right model has been put forward. In this chapter, the sintered sample was expected to form a long-range magnetic order as some of the degeneracy of the system was lifted during the structural distortion, however, no magnetic

Bragg peaks were observed in any of the diffraction measurements. Conversely, the spin glass ground state is proposed for samples which do not undergo a structural distortion, like the microwave or single-crystal samples. However, despite the frequency of this conclusion, no AC measurements of ZnV_2O_4 , or doped ZnV_2O_4 compounds, have ever been reported until now [156, 157, 161, 167, 168]. The AC measurements presented in Section 2.3.3.2 suggest that the microwave sample does not have a spin glass ground state, as the T_1 peak has very little frequency dependence and no dynamic response. Within this study the magnetic ground state of the sintered and microwave ZnV_2O_4 samples remains elusive, however, future inelastic neutron scattering measurements should solve the problems discussed earlier.

2.4 Conclusions and Outlook

Many quantum materials are found to have synthesis dependent physical properties, due to their complex, degenerate ground states. This chapter explored the effect of synthesis on the chemical and magnetic ground state selection of one such material, ZnV_2O_4 , using a combination of X-ray and neutron scattering, PDF analysis, and magnetic susceptibility measurements. The key conclusions from this chapter are summarised as follows:

- Two samples were created for this study: the sintered sample via conventional solid-state methods and the microwave sample via a novel rapid microwave assisted synthesis.
- Both samples have an average cubic $Fd\bar{3}m$ structure at high temperatures. The microwave sample remains in the cubic $Fd\bar{3}m$ structure down to 4 K, whereas the sintered sample undergoes an elongation along the c -axis to a tetragonal structure below 35 K. Both of these are unique chemical ground states for powder ZnV_2O_4 .
- At 100 K, the local and average chemical structures are cubic for both samples. Outside the resolution of current experiments, it is likely there is some vanadium based

disorder in both samples, but since the same behaviour is observed in both samples, this disorder is inherent to ZnV_2O_4 and does not drive the structural evolution seen at low temperatures.

- Strain is the most probable cause of the low temperature structural behaviour as in the parent cubic phase the sintered sample was over $2.5\times$ more strained than the microwave sample. The origin of this increased strain is currently unknown.
- Two features, $T_1 = 12$ K and $T_2 = 45$ K, are observed in DC magnetic susceptibility for the sintered sample but only one feature at $T_1 = 11$ K in the microwave sample. The microwave sample is unlikely to undergo a spin glass transition because the peak has little frequency dependence and no dynamic response in AC susceptibility measurements, and large ZFC/FC splitting above the T_1 transition in DC susceptibility. The T_2 feature in the sintered sample is usually associated with the structural distortion, however, these DC susceptibility results do not have the sharp discontinuity that is observed in other studies.
- AC susceptibility measurements revealed unusual highly frequency dependent and dynamic behaviour between 20 K and 60 K that is virtually identical between the two samples. This likely reflects collective short-range magnetic fluctuations in the samples.
- The magnetic ground state was explored in numerous neutron diffraction experiments. These measurements exclude a long-range ordered magnetic ground state for both samples, as no magnetic Bragg peaks were measured. Different magnetic diffuse scattering was measured for both samples indicating unique magnetic ground states, the nature of which is currently unknown. These measurements were complicated due to ZnV_2O_4 having a small effective moment, having large magnetic exchange interactions (outside the diffraction integration window), and the onset of the paramagnetic regime being unknown.

Despite all of these experiments there are a number of questions remaining, both

related to this study and within the wider context for the quantum materials community. A direct extension to this study is to look more deeply into the mechanisms that drive the structural behaviour. It is noteworthy that in the parent cubic phase, that no significant disorder has been resolvable in the diffraction measurements. Therefore a first approach would be to use more analytical chemistry methods that are perhaps more sensitive than diffraction, such as thermogravimetric analysis (TGA), NMR and TEM. These measurements would compliment what have already been collected, and may reveal key differences in the stoichiometry or morphology of the samples that result in the chemical structures diverging. Furthermore, density functional theory (DFT) calculations on ZnV_2O_4 were conducted many years ago, but revisiting these calculations with more modern programs could provide fruitful results into the ordering mechanisms. A first parameter to explore would be the effect of strain on the energy landscape of ZnV_2O_4 .

In terms of the magnetic ground state, the results presented in this chapter have demonstrated that the sintered and microwave samples have unique magnetic ground states, and excluded long-range order and spin glass ground states, but have not been able to determine the precise nature of the magnetic ground states. These are still important conclusions, as it is generally thought that the structural distortion allows the system to form long-range order, which has not occurred in the sintered sample, or that remaining in the cubic symmetry, like the single-crystal study, suppresses long-range order and instead forms a spin glass, but this has not occurred in the microwave sample. The problems with measuring, analysing and interpreting the data, were summarised earlier, and will hopefully be overcome with inelastic neutron scattering measurements which can capture the whole magnetic excitations of ZnV_2O_4 , with instruments such as PANTHER (ILL), MERLIN (ISIS) or SEQUOIA (Oakridge National Laboratory) being suitable candidates. Once an adequate isolation of the total magnetic scattering has been measured then the data will be analysed via reverse Monte Carlo methods on SPINVERT to determine the short-range magnetic correlations (SPINCORREL), and the average exchange interactions through a reaction mean-field

approach on SPINTERACT [183].

A further research avenue would be to make more samples of ZnV_2O_4 via different synthetic procedures and apply the same analysis that has been presented in this chapter. This would allow for definitive relationships, for example, strain and the effect of compressing/elongating the structure has on the magnetic ground state, to be made. The first two samples that I would suggest adding to the study would be a traditionally sintered powder (longer firing time, no ball milling) and a single-crystal. The single-crystal would be particularly interesting as there is only one report of ZnV_2O_4 in single-crystal form, and until the microwave sample, the results from this study are strikingly different from all other ZnV_2O_4 samples.

Additionally, this chapter has shown that microwave synthesis is a viable alternative to producing high-quality, well crystalline quantum materials. The fact that a sample with comparative physical properties to a single-crystal is producible in a microwave, in just 12 minutes, is outstanding. This opens the possibility to make more quantum materials via the microwave method, and with a drastically reduced synthesis time, allows for more focus to be put on the characterisation of the material. This also overcomes one of the biggest hurdles in quantum materials characterisation which is for more advanced characterisation single-crystals are often required, but making them large enough for neutron scattering can be very challenging. However, if the properties are reproducible by other methods, then this will significantly help with the characterisation of more materials. The one caveat, which is the central message to this chapter, is that changing the synthesis can have a profound effect on the chemical and magnetic ground states of the material. In this case, the effect was a positive one, the microwave sample was of very high quality and largely reproduced the targeted physical properties of the single-crystal, but that might not always be the case. This is one of the reasons why in the quantum materials community, we cannot take the results of one study to be definitive for that material as there are so many factors at play, as the highly degenerate nature of quantum materials means that the smallest defect can have

the biggest impact. What is perhaps more useful, is to use materials that are known to be highly synthesis and defect dependent, like ZnV_2O_4 , barlowite [87, 131] and $\text{Yb}_2\text{Ti}_2\text{O}_7$ [39], and understand which parameters have the biggest impact on the ground state selection, and then target these defects during the synthesis of other candidate materials.

2.5 Appendix

Rietveld Refinement

Refined Parameters

Figure 2.18a) shows a summary of the refined lattice parameters for the sintered (green) and microwave (orange) samples as a function of temperature. The microwave sample follows the standard cubic lattice parameter compression. Errors are included but are too small to be visible on this scale. In the sintered sample, the error is much larger which accounts for the distribution in lattice parameters. From 35 K, the divergent trend describes the phase transition to an elongated tetragonal structure.

This figure also shows the reported lattice parameters for other sample of ZnV_2O_4 , which have been categorised by if the authors reported one (blue) or two (purple) transitions in the susceptibility. In cubic spinels, the lattice parameter can be closely related to the stoichiometry, even if the level of disorder is below the detection level in Rietveld refinement. However, no relationship is seen, which is likely due to the different experimental setups and instruments used.

Figure 2.18b) shows the evolution of B_{iso} for both samples. Both show similar dependence and behave as expected.

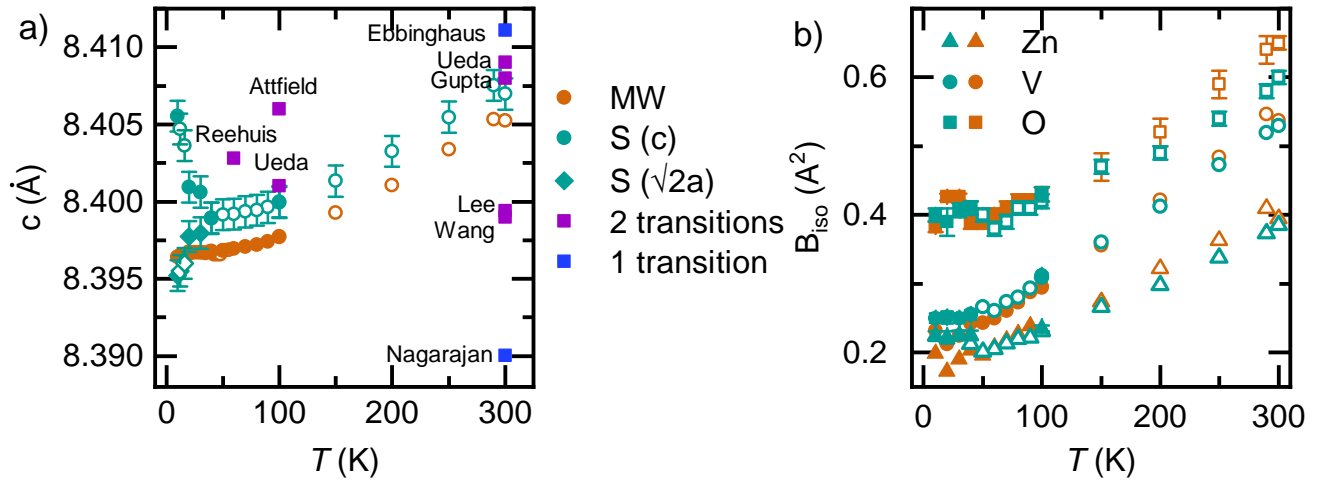


Figure 2.18: Evolution of refined parameters, a) lattice parameters and b) isotropic temperature factors as a function of temperature. In both figures, orange and green markers represent the microwave and sintered samples, respectively. Closed markers are results from a combined neutron and X-ray refinement, open markers are from an X-ray only refinement. At 100 K and 10 K, both a combined fit and X-ray only fit were completed, and extracted parameters lied well within error of each other. a) Also shown are the lattice parameters from other studies of ZnV_2O_4 , categorised by if there are one (blue) or two (purple) reported transitions in the susceptibility.

Sintered Sample: High-Temperature Cubic Phase

Figure 2.19 shows the two phase model for the sintered sample at 100 K which was used in finding the weighted average lattice parameter.

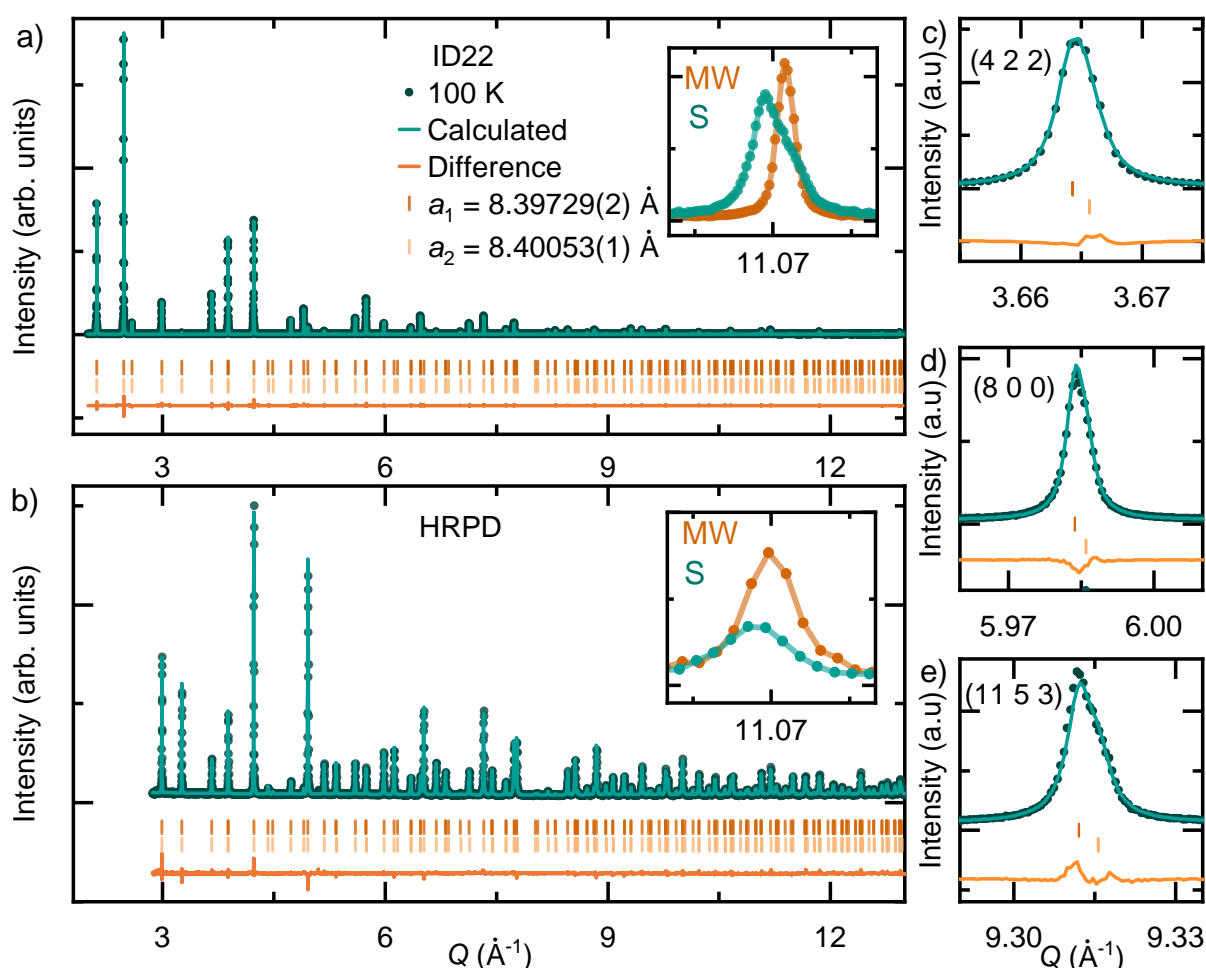


Figure 2.19: Combined Rietveld refinement of the sintered sample measured at 100 K. Two cubic phases are used in a) ID22, $R_{\text{wp}} = 10.4\%$, $\chi^2 = 20.9$, b) HRPD, $R_{\text{wp}} = 11.3\%$, $\chi^2 = 2.65$ with different lattice parameters, $a_1 = 8.39729(2)\text{ \AA}$ and $a_2 = 8.40053(1)\text{ \AA}$ which are weighted in a 0.3 : 0.7 ratio, respectively. Insets show the (13 5 5) reflection for the microwave (orange) and sintered (green) samples, where a clear shoulder can be seen in the sintered sample in a). Rietveld fit of three key peaks from ID22, c) (4 2 2), d) (8 0 0) and e) (11 5 3).

Sintered Sample: Low-Temperature Distorted Phase

Figure 2.20 shows the full refinement of the expected low temperature structure of ZnV_2O_4 , a compression along the c -axis to the tetragonal $I4_1/amd$.

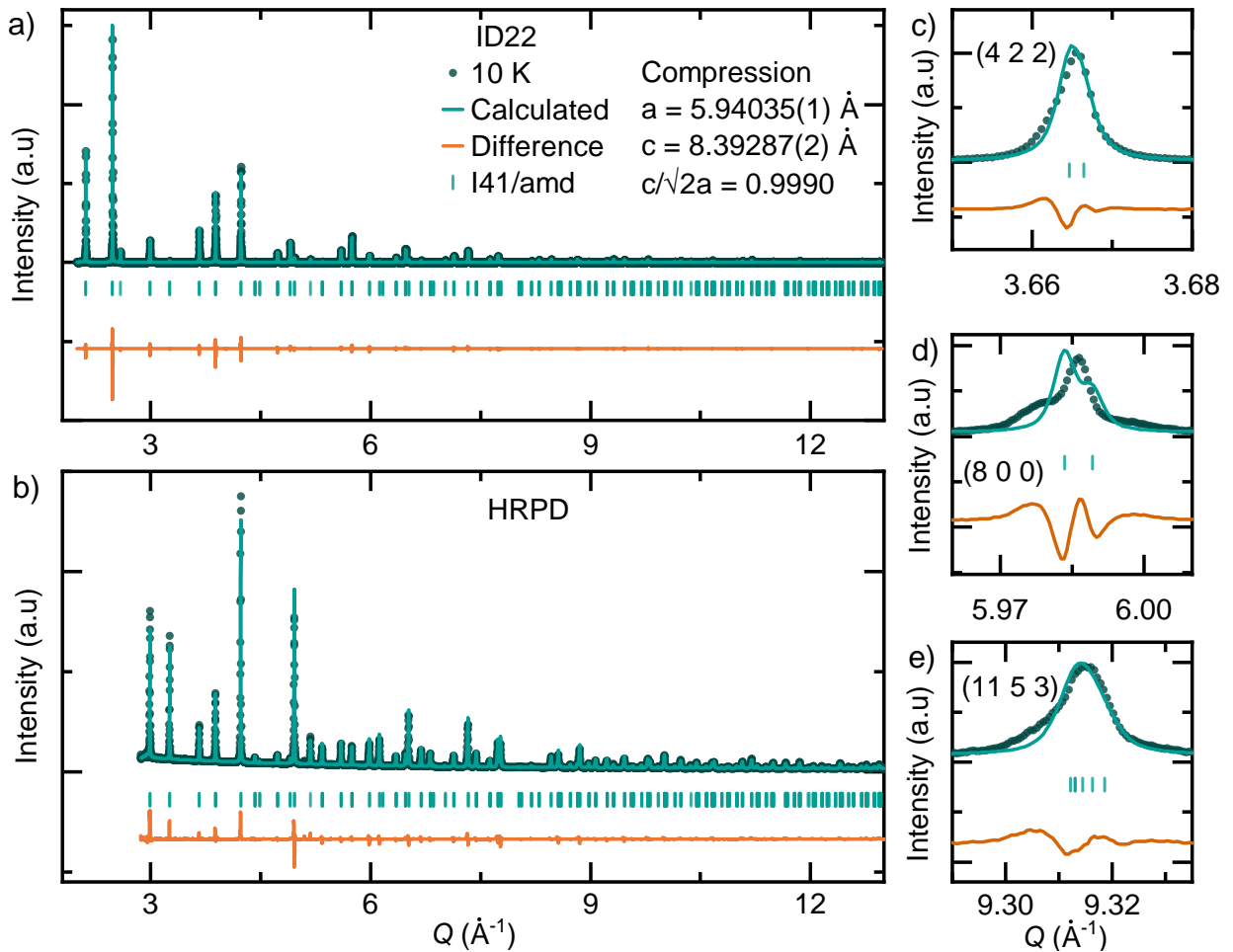


Figure 2.20: Combined Rietveld refinement of the sintered sample measured at 10 K with the compressed $I4_1/amd$ model. a) ID22, $R_{\text{wp}} = 25.5\%$, $\chi^2 = 30.3$, b) HRPD, $R_{\text{wp}} = 19.9\%$, $\chi^2 = 38.2$. Lattice parameters are $a = 5.94035(1) \text{ \AA}$, $c = 8.39287(2) \text{ \AA}$, giving an axial compression, $c/\sqrt{2}a = 0.9990$. Rietveld fit of three key peaks from ID22, c) $(4\ 2\ 2)$, d) $(8\ 0\ 0)$ and e) $(11\ 5\ 3)$.

Figure 2.21 shows the full refinement of the elongated tetragonal structure of ZnV_2O_4 .

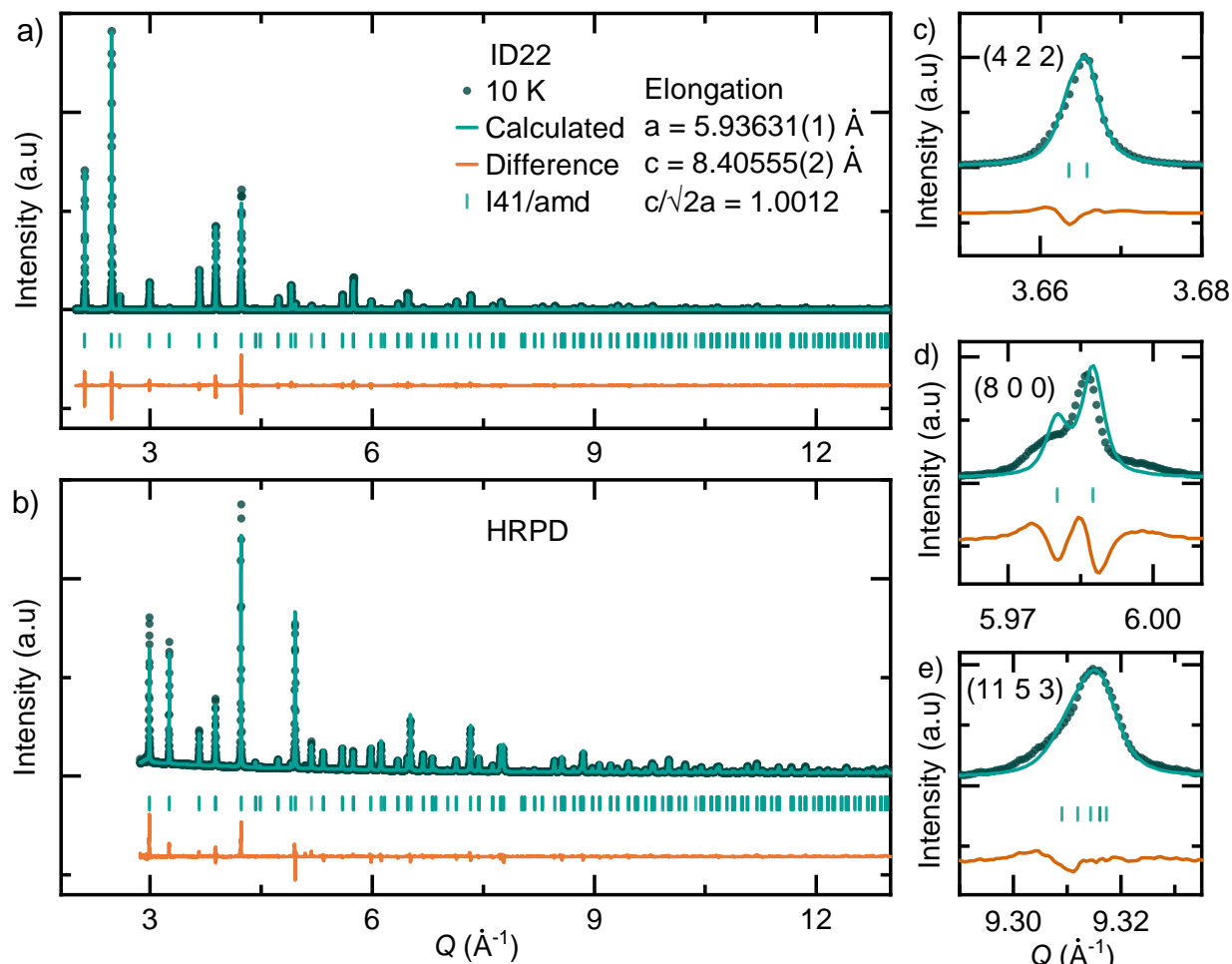


Figure 2.21: Combined Rietveld refinement of the sintered sample measured at 10 K with the elongated $I4_1/amd$ model. a) ID22, $R_{\text{wp}} = 22.4\%$, $\chi^2 = 23.5$, b) HRPD, $R_{\text{wp}} = 17.0\%$, $\chi^2 = 28.1$. Lattice parameters are $a = 5.93631(1) \text{ \AA}$, $c = 8.40555(2) \text{ \AA}$, giving an axial elongation, $c/\sqrt{2}a = 1.0012$. Rietveld fit of three key peaks from ID22, c) $(4\ 2\ 2)$, d) $(8\ 0\ 0)$ and e) $(11\ 5\ 3)$.

Table 2.6 shows all the possible lower symmetry chemical structures from ISODISTORT, and the results of fitting the ID22 data at 10 K using the Le Bail method. All the tetragonal models are indistinguishable from each other, but choose to elongate along the c -axis.

Model	Γ	a (Å)	b (Å)	c (Å)	$R_{\text{wp}}(\%)$	χ^2
$Fd\bar{3}m$	-	-	-	8.39840(1)	23.7	5.57
$I4_1/amd$	Γ_{3+}	5.93692(1)	-	8.40753(2)	19.5	3.71
$I4_1md$	Γ_{3+}	5.93689(1)	-	8.40757(2)	19.6	3.76
$I\bar{4}m2$	Γ_{3-}	5.93689(1)	-	8.40757(2)	19.6	3.73
$I4_12_2$	Γ_{3-}	5.93693(1)	-	8.40780(2)	19.5	3.70
$I4_1/a$	Γ_{4+}	5.93690(1)	-	8.40775(2)	19.6	3.73
$I\bar{4}2d$	Γ_{5-}	5.93671(1)	-	8.40704(2)	20.0	3.89
$Fddd$	Γ_{3+}	8.39739(1)	8.38493(2)	8.40977(2)	17.9	3.14
$C2/m$	Γ_{5+}	10.28384(2)	5.93834(3)	5.94619(2)	19.1	3.55
$Imma$	Γ_{5+}	5.93738(2)	5.94450(2)	8.39502(2)	20.8	4.23
$R\bar{3}m$	Γ_{5+}	5.93848(2)	-	14.54667(5)	24.0	3.71

Table 2.6: Refined average chemical structure parameters for the ISODISTORT models derived from the parent cubic $Fd\bar{3}m$ structure. Each model has been fit using the Le Bail method to the ID22 data at 10 K only.

High T Magnetic Susceptibility

An example of high temperature magnetic susceptibility for the sintered sample is shown in Fig. 2.22. The data are not linear which shows that a Curie-Weiss analysis is not an appropriate modelling system for ZnV_2O_4 . Other attempts were made in different setups but none were linear and high enough quality to draw any meaningful conclusions from.

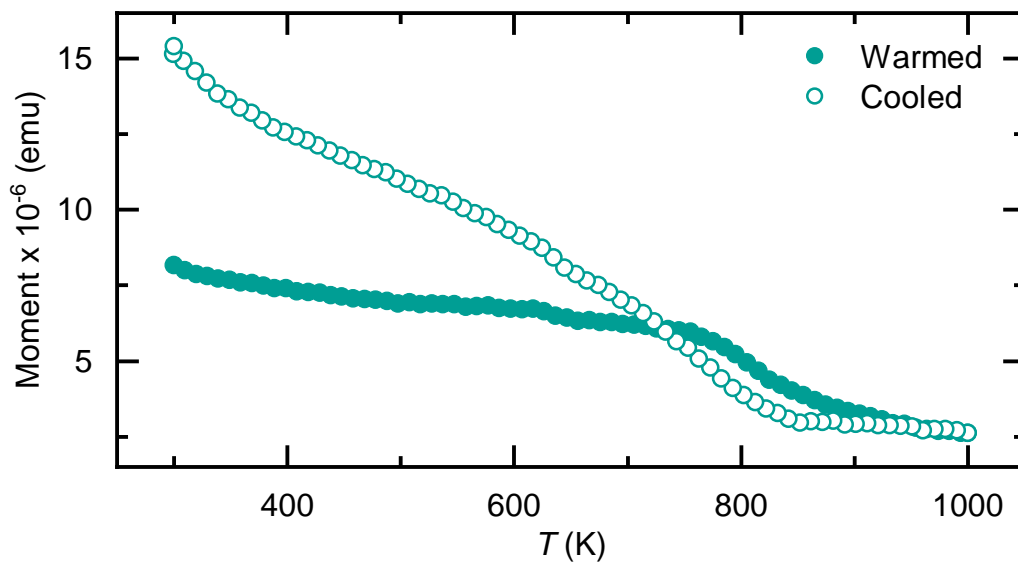


Figure 2.22: Example of high temperature magnetic susceptibility for the sintered sample. Data are measured under an applied field of 0.01 T, closed markers are measured upon warming (300-1000 K) and open markers on cooling (1000-300 K). The data are not linear which proves Curie-Weiss is not appropriate to model the data.

Magnetic Diffuse Scattering: D7

A summary of the D7 SPINVERT analysis is shown in Fig. 2.23 including spin correlations, and fit parameters in Table 2.7.

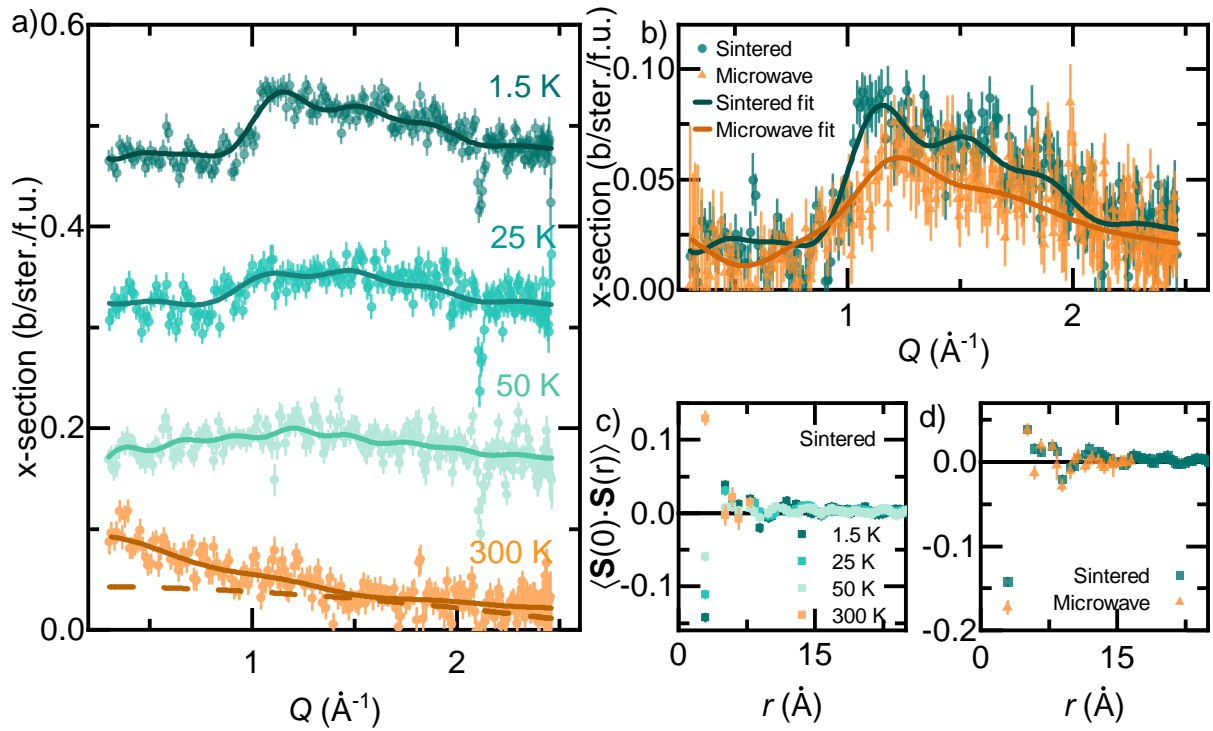


Figure 2.23: Summary of magnetic diffuse scattering on D7 for the sintered and microwave samples. a) Magnetic contribution of scattering for the sintered sample. Data have been vertically shifted by 0.15 b/ster./f.u. for clarity. Solid lines describe SPINVERT fits and the dashed line at 300 K is the expected behaviour for a V³⁺ form factor squared for a spin 1 system. b) Comparison of magnetic contribution for sintered and microwave samples at 1.5 K, SPINVERT fits are shown on top by the solid lines. The sintered sample has a more peaked feature at $Q = 1.1 \text{ \AA}^{-1}$. Spin correlations calculated by SPINCORREL for c) the sintered sample as a function of temperature and d) a comparison between the sintered and microwave samples. At 300 K, the sintered correlations have anomalous behaviour.

Sample	T (K)	Box	Weight	R-factor (%)		Acceptance (%)		μ/V^{3+} (μ_{B})
Sintered	1.5	6	10	51.7	26.2	62.7	90.3	0.62(1)
	25	6	10	51.4	35.7	84.3	95.5	0.55(1)
	50	6	10	42.9	37.2	85.1	96.5	0.51(1)
	300	2	10	29.3	27.6	53.6	82.1	0.52(2)
Microwave	1.5	4	10	57.3	33.5	73.6	94.5	0.54(1)

Table 2.7: SPINVERT parameters and output for both samples on D7. Magnetic data were isolated via polarisation analysis. All refinements had complete rotational degrees of freedom, box in the cubic, $Fd\bar{3}m$ setting, 100 moves and the calculation repeated 10 times.

WISH

A summary of the WISH analysis can be found in Figs. 2.24 and 2.25 and fit parameters in Table 2.8.

Sample	$T - 80$ (K)	Box	Weight	R-factor (%)		Acceptance (%)	
Sintered	1.5	8	10	43.2	6.1	53.5	88.0
	25	8	10	42.7	6.7	55.2	81.1
	50	4	10	31.5	22.3	45.7	13.4
Microwave	1.5	6	10	40.1	16.5	52.7	84.6
	25	6	10	49.6	18.1	60.3	87.2
	50	4	10	65.2	37.1	46.1	16.4

Table 2.8: SPINVERT parameters and output for both samples on WISH. Temperature subtractions were made with data measured at 80 K. All refinements had complete rotational degrees of freedom, box in the cubic, $Fd\bar{3}m$ setting, 100 moves and the calculation repeated 20 times.

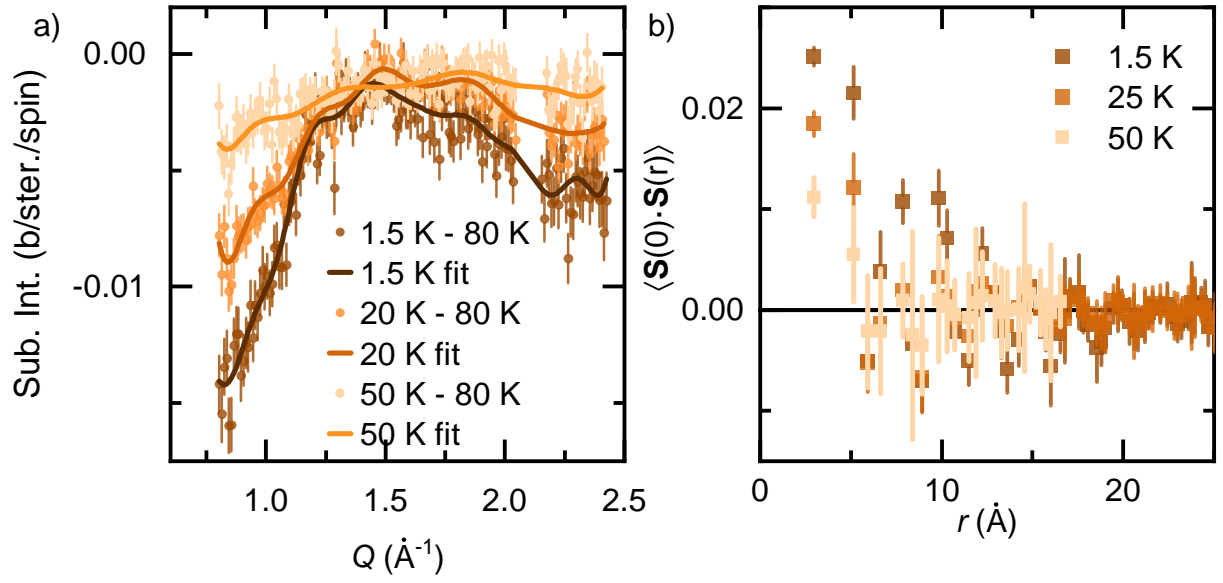


Figure 2.24: a) Subtracted magnetic intensity as a function of temperature for the microwave sample on WISH. The corresponding SPINVERT fits are shown by the solid lines. b) Spin correlations calculated by SPINCORREL as a function of increasing interatomic distance, r . Note that the first nearest neighbour is ferromagnetic.

D20

A summary of the D20 analysis can be found in Fig. 2.26 and fit parameters in Table 2.9.

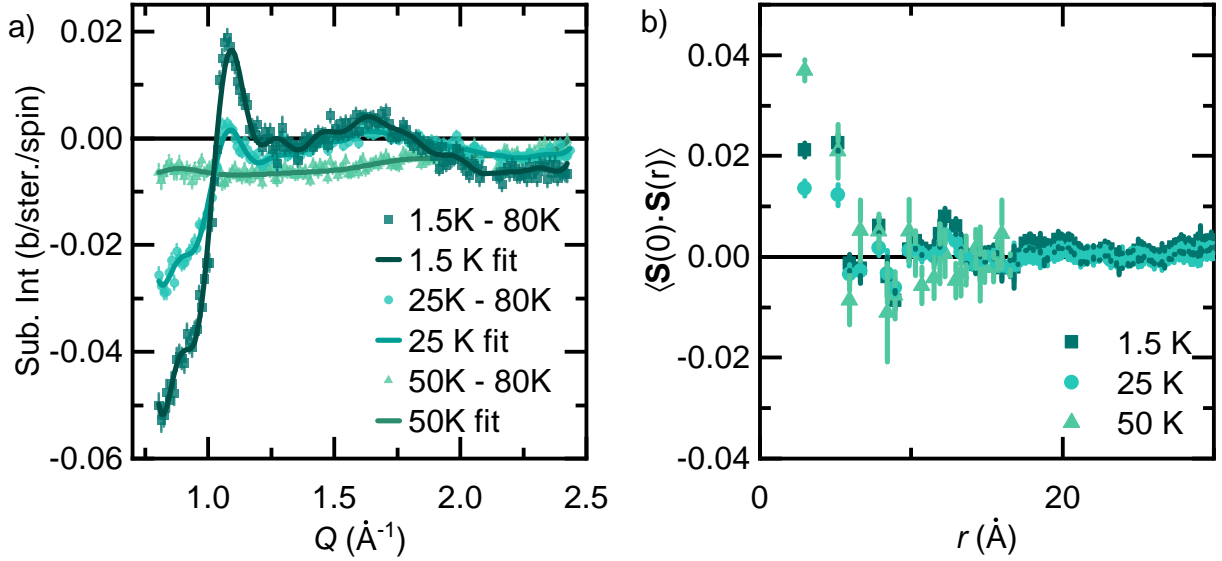


Figure 2.25: a) Subtracted magnetic intensity as a function of temperature for the sintered sample on WISH. The corresponding SPINVERT fits are shown by the solid lines. b) Spin correlations calculated by SPINCORREL as a function of increasing interatomic distance, r . Note that a number of the correlations have a non-linear temperature dependence, and the first nearest neighbour is ferromagnetic.

$T - 520$ (K)	Box	Weight	R-factor (%)		Acceptance (%)	
1.5	12	10	41.8	4.51	52.1	94.3
25	12	10	43.2	5.35	52.1	93.9
80	12	10	34.1	6.28	54.8	93.4
150	10	10	45.0	8.46	55.2	90.3
300	8	25	59.3	14.3	52.2	75.4
450	4	25	67.3	48.6	45.7	14.6

Table 2.9: SPINVERT parameters and output for the sintered sample on D20. Temperature subtractions were made with data measured at 520 K. All refinements had complete rotational degrees of freedom, box in the cubic, $Fd\bar{3}m$ setting, 100 moves and the calculation repeated 20 times except for at 450 K where the refinement was repeated 100 times.

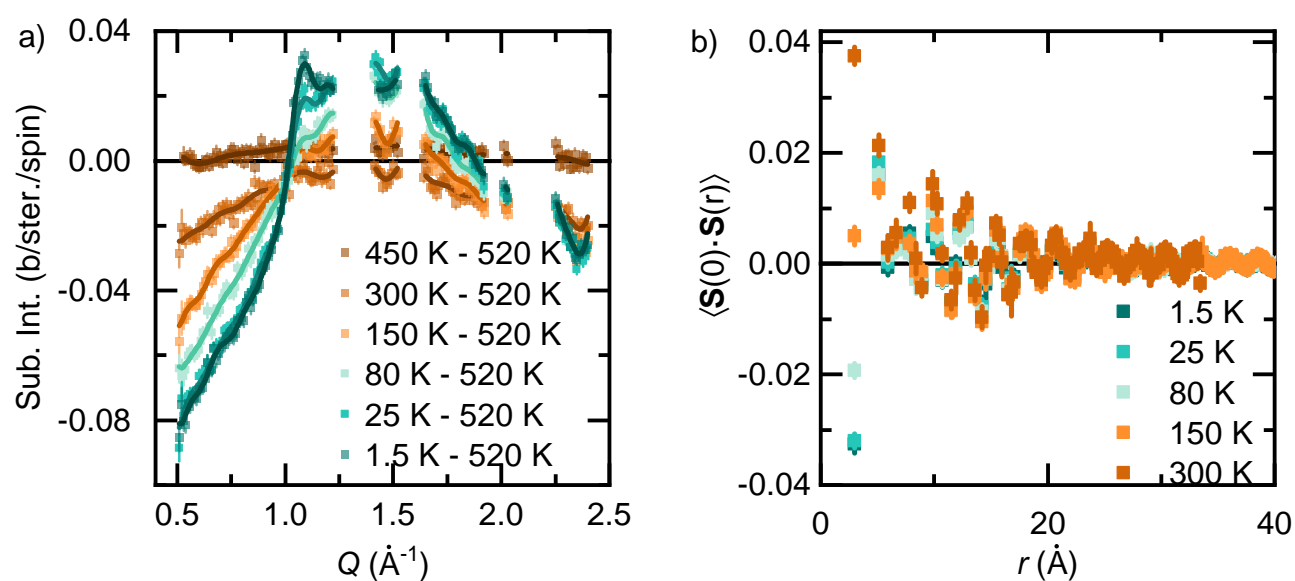


Figure 2.26: a) Subtracted magnetic intensity as a function of temperature for the sintered sample on D20. The corresponding SPINVERT fits are shown by the solid lines. b) Spin correlations calculated by SPINCORREL as a function of increasing interatomic distance, r . Note that at 150 K and 300 K, the first nearest neighbour correlations become ferromagnetic.

Chapter Three

Experimental Evidence for the Spiral

Spin Liquid in LiYbO_2

3.1 Introduction

Magnetic ground states with unusual spin textures, such as magnetic skyrmions or vortices, are hugely interesting from a fundamental perspective and for their potential applications in emerging technologies [184–187]. A less explored manifestation of unusual spin textures is the spiral spin liquid, a correlated paramagnetic state composed of a macroscopically degenerate manifold of fluctuating spin spirals that form closed contours or surfaces in reciprocal space [44, 77, 78, 188]. From a theoretical perspective, spiral spin liquids have been predicted to exist in both two- and three-dimensions within the context of the J_1 - J_2 Heisenberg model, for example, in honeycomb or diamond lattices, respectively. [44, 189, 190]. Experimentally, the search for the spiral spin liquid has largely focused on its realisation within cubic spinels, AB_2X_4 , in which the A -site forms a three-dimensional diamond lattice [28–30, 191].

The diamond lattice can be considered as two interpenetrating FCC sublattices, with nearest-neighbour (NN), J_1 and next-nearest-neighbour (NNN), J_2 exchange interactions

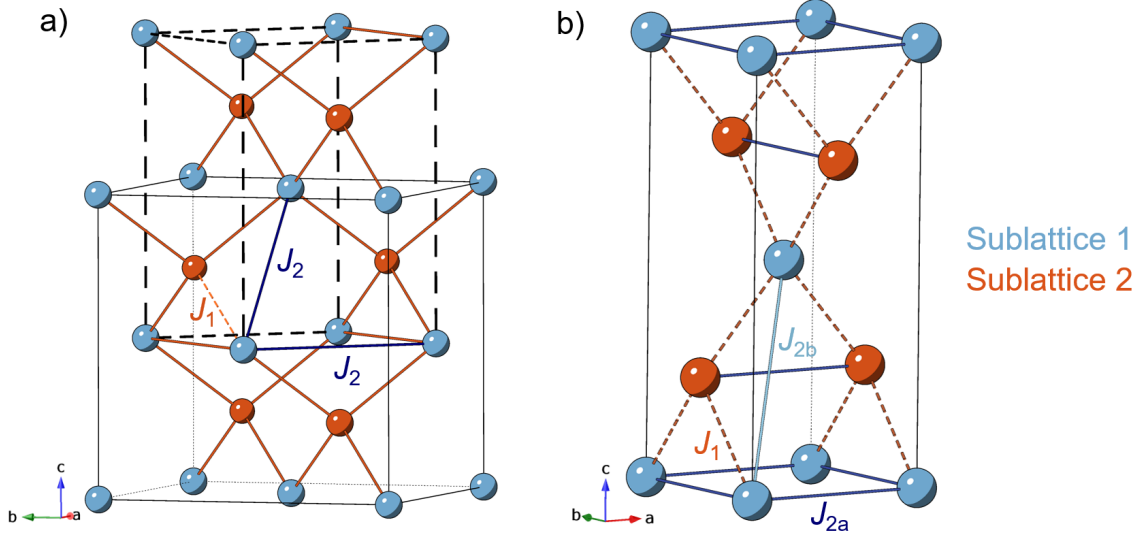


Figure 3.1: a) The undistorted diamond lattice can be considered as two interpenetrating FCC sublattices shown by the blue and orange atoms, respectively with NN J_1 (dashed orange) and NNN J_2 (solid blue) exchange interactions. The dashed box shows the definition of the unit cell used in this work. b) The elongated J_1 - J_2 Heisenberg model on a diamond lattice is stretched along the tetragonal c -axis to give the final structure. This splits J_2 into inequivalent exchanges, J_{2a} (dark blue) and the negligible J_{2b} (light blue). Frustration may be generated through competing superexchange pathways between J_1 and J_{2a} .

acting between and within sublattices, respectively (Fig. 3.1a)) [45, 77, 78]. The diamond lattice is geometrically unfrustrated, and in the case of dominant J_1 -only exchange interactions has a conventional ferromagnetic or Néel ordered magnetic ground state. However, the bipartite nature of the lattice means that the exchanges can be readily tuned, and if $J_2/|J_1| \geq 1/8$, then the system is expected to promote the spiral spin liquid ground state [45, 77, 78]. Several cubic spinels have been identified as candidates for the model including MnSc₂S₄ [192, 193], NiRh₂O₄ [78, 194, 195] and CoAl₂O₄ [196, 197]. MnSc₂S₄ is particularly exciting as it is considered the first experimental realisation of the spiral spin liquid on a perfect diamond lattice, with the observation of its spiral surface through single-crystal dif-

fuse neutron diffraction measurements and vortex state under the application of a magnetic field [192]. Yet despite this progress, a true continually fluctuating spiral spin liquid is a rare occurrence. More often, the degeneracy of the system is lifted via an order-by-disorder mechanism, which is common in cubic spinels due to their desire to alleviate their frustration by undergoing a structural distortion. In such a case, a single long-range ordered ground state is selected by the collective fluctuations in the system combined with the spontaneous breaking of symmetry following a Jahn-Teller distortion [43]. For candidate spiral spin liquid systems, the complex and degenerate fluctuating state thus collapses down into a ground state with a single long-range ordered spin helix [45, 77, 78].

It was widely accepted that structural distortions to the perfect diamond lattice trigger this order-by-disorder mechanism, and therefore, are detrimental to the realisation of the spiral spin liquid phase. However, a recent re-imagining of the theory determined that a spiral spin liquid could still be realised under a tetragonal distortion to the diamond lattice [45, 46, 77]. The key in this model is to consider the effect of superexchange pathways throughout the structure. In the ideal diamond lattice, J_2 is equivalent in length, whether acting within the ab -plane or across the diagonal (Fig. 3.1a)). But in the elongated model, J_2 is broken into two inequivalent exchanges, J_{2a} and J_{2b} , as the structure is stretched along the tetragonal c -axis (Fig. 3.1b)). Now, the superexchange pathways, J_1 and J_{2a} (J_2 acting across the unstretched axes) are nearly equivalent in length, and substantially shorter than the J_{2b} pathway (J_2 acting across the diagonal). In this case, the strength of the J_{2b} pathway is assumed negligible in comparison to J_1 and J_{2a} . It then follows that if the magnitudes of J_1 and J_{2a} are comparable, this elongated lattice is highly frustrated, and promotes a spiral spin liquid ground state, with the propagation vector of the helix being uniquely determined by the $J_{2a}/|J_1|$ ratio. In short, candidate systems for the J_1 - J_2 Heisenberg model on an elongated diamond lattice require a distortion in which the J_{2b} exchange pathway is long enough to be considered negligible in strength in comparison to J_{2a} . From now on, when discussing this model, J_{2a} will be known simply as J_2 .

One potential candidate for the J_1 - J_2 Heisenberg model on an elongated diamond lattice was NaCeO₂ [198]. NaCeO₂ adopts the tetragonal $I4_1/amd$ structure and has a stretching ratio of $c/\sqrt{2}a = 1.63$, which is enough to render J_{2b} negligible. However, neutron diffraction measurements showed NaCeO₂ formed a commensurate Néel ordered ground state below 3.18 K due to $|J_1| \gg J_2$. This is not surprising given that theory predicts that when $J_2 > 0$ (antiferromagnetic), the spiral spin liquid phase exists in a relatively narrow region between commensurate ferromagnetic ($-4 < J_1/J_2$) and antiferromagnetic ($J_1/J_2 < 4$) phases [45, 46]. This work therefore highlighted the importance of considering both the degree of the structural distortion and the magnitude of relative exchange parameters in realising the model.

Another material with an almost identical structure to NaCeO₂ is LiYbO₂ [46, 199]. Figure 3.2a) shows the structure of LiYbO₂ where magnetic Yb³⁺ ions are connected into an elongated diamond lattice via YbO₆ corner-sharing octahedra (blue octahedra). Dispersed between the diamond lattice there are almost flat planes of tetrahedrally co-ordinated Li⁺ ions (yellow polyhedra). LiYbO₂ shares the same stretching ratio as NaCeO₂, $c/\sqrt{2}a = 1.63$, but importantly the ratio of exchange parameters has been determined to be $J_1 = 1.426J_2 > 0$, placing LiYbO₂ directly within the boundary of the spiral spin liquid phase on an elongated diamond lattice [46].

The magnetic structure of LiYbO₂, previously determined from a mixture of powder neutron diffraction and magnetometry measurements, is complex with the phase diagram shown in Fig. 3.2b) [46]. Below 450 mK, in zero applied magnetic field, there is an incommensurate (IC) helical ground state with propagation vector, $\mathbf{k} = (0.384, \pm 0.384, 0)$ and ordered magnetic moment, $\mu_{\text{order}} = 1.26 \mu_B$. This is less than the expected moment, $\mu = 1.5 \mu_B$, assuming $S_{\text{eff}} = 1/2$ with $g = 3$ ($\mu = gS \mu_B$) [46]. This assumption was made from inelastic neutron scattering measurements in which the authors determined that the lowest energy CEF transition is high enough from the ground state Kramers doublet to be described as a well separated $S_{\text{eff}} = 1/2$ state at low temperatures [46]. To generate the

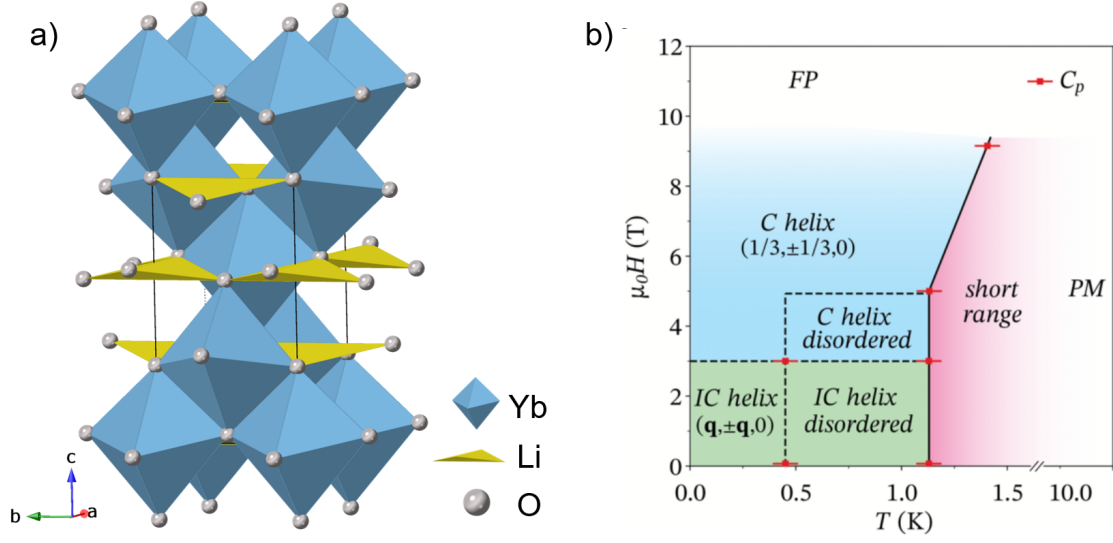


Figure 3.2: a) The Yb³⁺ ions (blue polyhedra) in LiYbO₂ are connected via an elongated diamond lattice with Li⁺ ions (yellow polyhedra) dispersed in almost flat layers between the Yb³⁺ ions. b) Magnetic phases of LiYbO₂ determined by Ref. [46], with commensurate (C), incommensurate (IC), paramagnetic (PM) and field-polarised (FP) states observed.

spiral spin liquid phase, theory allows for an incommensurate helical structure acting across the two Yb³⁺ sublattices where moments propagate along the diagonal of the tetragonal basal plane, $\mathbf{k} = (\delta, \pm\delta, 0)$. Crucially however, the moments between these sublattices must be related by a fixed phase angle of $\phi = \pi$. This allows the moments to rotate along all bonds between the sublattices equivalently which acts to minimise the energy of the system. Experimentally, this phase angle was refined to be only $\phi = 0.58 \pi$, or just over half the expected value.

Additionally, Bordelon *et al.* [46] found that between 450 mK and 1.13 K, there is an intriguing intermediary ordered phase, known as the disordered incommensurate helix. In this phase, both \mathbf{k} , and μ are fixed to the values determined below 450 mK, but the phase angle, ϕ changes. The model involved simulating the scattering of 10 arbitrary phase angles, which produces constructive and destructive interference of the magnetic Bragg peaks. The

average of these phases was then taken and reproduced the magnetic scattering data well. This model effectively described a state with a series of magnetic domains that were all well ordered with a fixed phase angle within the domain, but the domains were random and had no relationship with each other. Then between 1.13 K and 2 K, the helical magnetic order is lost and replaced with short-range magnetic correlations as indicated by broad features in specific heat measurements. A paramagnetic state was observed above 10 K. Bordelon *et al.* also conducted their neutron scattering measurements under an applied magnetic field, and found that the helical phases described earlier "lock-in" to a commensurate $\mathbf{k} = (1/3, \pm 1/3, 0)$ when the applied field is above 3 T.

Despite these promising initial results, the previous experiments concluded that LiYbO₂ is not an experimental realisation of the spiral spin liquid phase on an elongated diamond lattice [46]. The main evidence for this is the refined phase angle, $\phi = 0.58 \pi$. This reduced angle, from the expected $\phi = \pi$, led to a staggering effect of the moments, therefore requiring additional perturbations to the J_1 - J_2 Heisenberg model on an elongated diamond lattice to bring the theory into agreement with the experimental results. The possibility of disorder was hinted at as the root cause, and a potential source was two unique chemical environments around the two Yb-sublattices as indicated by weak splittings in inelastic neutron scattering measurements probing the crystal electric field. However, the origin of this chemical disorder was not resolvable in the neutron diffraction measurements presented. Furthermore, the ordered moment size, determined in powder neutron diffraction measurements, was only 84 % of the expected full ordered moment from an $S_{\text{eff}} = 1/2$ system. Lately, the possibility of a disordered magnetic ground state was introduced by Kenney *et al.* [200] through the lack of spontaneous muon precession in μ SR measurements. In combination with the disordered incommensurate helical phase between 450 mK and 1.13 K, these intriguing results indicate that the true nature of the ground state in LiYbO₂ remains elusive.

The search for a spiral spin liquid on an elongated diamond lattice therefore continues. Experimentally, there are three conditions from an average-structure perspective required to

confirm a spiral spin liquid phase: (1) the phase angle, ϕ , between magnetic sublattices is equal to π , (2) a propagation vector of the form $\mathbf{k} = (q, q, 0)$ and (3) a ratio of exchange parameters of $-4 < J_1/|J_2| < 4$ [46]. If all of these conditions are met then the smoking gun experimental signature of a spiral spin liquid is a broad continuous ring of diffuse scattering brought on by the collective fluctuations of the system [192]. In this chapter, I will re-examine LiYbO₂ as a candidate material for a spiral spin liquid in the J_1 - J_2 Heisenberg model on the elongated diamond lattice through a mixture of high-resolution neutron powder diffraction and diffuse neutron scattering measurements, and in doing so, prove that LiYbO₂ fulfils all the conditions required to realise the spiral spin liquid state in the model. This work has been published in Physical Review Letters [201].

3.2 Experimental Methods

3.2.1 Synthesis

Powder samples of LiYbO₂ were prepared via solid-state methods. Stoichiometric quantities of Yb₂O₃ (99.9%, Alfa Aesar) and Li₂CO₃ (99%, Alfa Aesar) were ground together in a mortar and pestle in a 1 : 1.5 ratio. An excess of Li₂CO₃ powder was used to counteract the volatility of lithium at high temperatures. The ground powder was pressed into a pellet and heated to 900 °C for 24 hours in air before being slowly cooled back to room temperature. On completion of the firing, individual pellets were varying shades of pink, and ground to a very fine pale pink powder. Sample quality was checked by powder X-ray diffraction using an Empyrean Malvern PANalytical diffractometer. The sample was measured to be phase pure within instrument resolution. The total mass of the sample was ~ 9 g.

3.2.2 Neutron Powder Diffraction

Constant wavelength neutron powder diffraction data were collected at 4 K and 300 K on the high-resolution D2B diffractometer [202] at the Institut Laue-Langevin. The incident wavelength was $\lambda = 1.594 \text{ \AA}$ selected by a Ge(335) monochromator, allowing the scattering to be measured over an angular range of $10 < 2\theta < 160^\circ$. 1.5 g of loose powder sample was contained in a vanadium sample can and a liquid helium cryostat was used for the temperature control. Refinements of the chemical structure were completed using the `Mag2Po1` program [106]. Raw data can be accessed via Ref [203].

Time-of-flight neutron powder diffraction data were collected on the long wavelength WISH diffractometer at the ISIS Neutron and Muon Source. 1.5 g of loose powder sample was contained in a cylindrical copper can and left open with a quartz wool plug to allow for gas exchange. Measurements were made in a dilution refrigerator in 0.1 K steps from 0.1 K to 1.2 K, with additional high-temperature measurements at 5 K and 10 K. The instrumental resolution was determined via Rietveld refinement of the Na₂Ca₃Al₂F₁₄ standard. Rietveld refinements of the chemical (Appendix Fig. 3.12) and magnetic structure were completed using the `Fullprof` program [105]. Absorption was refined and corrected for on `Fullprof` using the cylindrical sample configuration under `Iabsorb`. Instrumental contributions from the sample environment, such as copper and aluminium, were modelled using the Le Bail method. Raw data can be accessed via Ref [204].

3.2.3 Diffuse Scattering

Powder neutron scattering measurements were performed using the polarised diffuse scattering D7 diffractometer [112] at the Institut Laue-Langevin. The incident neutron wavelength was $\lambda = 4.87 \text{ \AA}$, giving a reciprocal space range of $0.15 \leq Q \leq 2.5 \text{ \AA}^{-1}$. An orange cryostat with a dilution insert was used to measure the temperatures 50 mK, 800 mK, 1.5 K, 5 K and

25 K. The technique of *xyz*-polarisation analysis was used to separate the magnetic, nuclear-coherent (NC) and nuclear-spin-incoherent (NSI) contributions to the scattering [112, 114]. Full calibration measurements were completed. Data were placed on an absolute intensity scale (with units b/ster./f.u.) by normalising to the incoherent scattering from the vanadium standard. The normalisation process was checked through Rietveld analysis of the NC cross-sections using `Mag2Po1` (Appendix Fig.3.13). Magnetic scattering data were analysed using a modified version of the program `SPINVERT` to simultaneously model magnetic Bragg and diffuse features (referred to as `SPINVERT + Bragg`) [119, 121]. `SPINVERT` calculations were repeated 100 times to average out statistical noise. The spin-spin correlation function, $\langle \mathbf{S}(0) \cdot \mathbf{S}(r) \rangle$, was calculated by `SPINCORREL` [120]. Raw data can be accessed via Ref [203].

3.3 Results and Discussion

3.3.1 Average Chemical Structure

Figure 3.3 shows the Rietveld refinement of the $I4_1/amd$ structure of LiYbO₂ against high-resolution neutron powder diffraction (NPD) data collected at 4 K on D2B. A summary of the refined parameters can be found in Table 3.1. From the results of the refinement, no site mixing or off-stoichiometries were found on any sites within the resolution of the instrument. Data were also measured at 300 K ($R_F = 2.74\%$, $\chi^2 = 7.47$), with refined lattice parameters $a = b = 4.38552(2)$ Å and $c = 10.02277(8)$ Å. No structural phase transition was observed between the temperatures. Preferred orientation was not required in the refinement.

3.3.2 Magnetic Structure

The magnetic structure of LiYbO₂ is complex and must be considered on both average and local length scales. Details of the investigations on WISH and D7 can be found in this

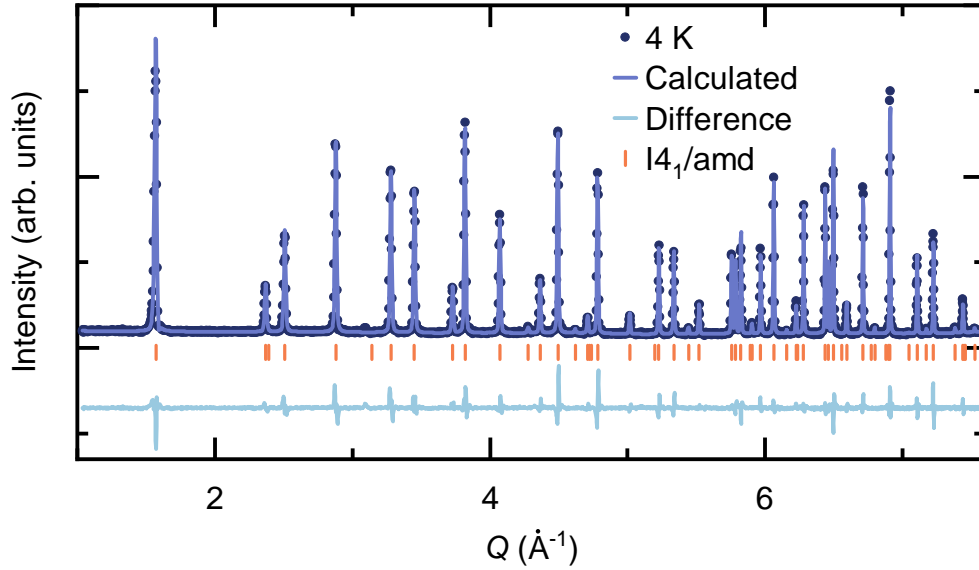


Figure 3.3: Rietveld refinement of the $I4_1/amd$ structure (origin setting 2) to high-resolution NPD data collected on D2B at 4 K ($R_F = 1.59\%$, $\chi^2 = 8.73$).

Atom	Site	x	y	z	B (\AA^2)
Yb	4a	0.0	0.75	0.125	0.06(2)
Li	4b	0.0	0.75	0.625	0.9(1)
O	8e	0.0	0.25	0.3514(1)	0.26(3)

Table 3.1: Refined structural parameters for LiYbO₂ from D2B data collected at 4 K. Atom co-ordinates are shown according to origin setting 2 of the $I4_1/amd$ structure, with refined lattice parameters, $a = b = 4.386542(3)$ \AA and $c = 10.0205(1)$ \AA .

section, but first to summarise the key findings:

1. Below 450 mK there is an incommensurate helical phase which locks into place with $\mathbf{k} = (0.3915(2), \pm 0.3915(2), 0)$, $\mu_{\text{order}} = 0.63(1)$ μ_B and relative phasing of the sublattices, $\phi = 1.15(5)$ π . The phasing confirms LiYbO₂ maps onto the J_1 - J_2 Heisenberg model on an elongated diamond lattice and $\mathbf{k} = (\delta, \pm\delta, 0)$ has the correct form needed to generate the spiral spin liquid phase.

2. Between 450 mK and 1.2 K there is an intermediary helical phase. This phase also consists of an incommensurate helical state where \mathbf{k} and μ_{order} evolve as a function of temperature but the phasing of the sublattices remains constant, $\phi = 1.15(5) \pi$.
3. Correlated short-range magnetic order exists between 50 mK and 5 K, which collect into fluctuating spin spirals as evidenced by the experimental signature of the spiral spin liquid—a continuous ring of diffuse scattering.
4. Paramagnetic behaviour is observed above 25 K.

3.3.2.1 Locked-In Incommensurate Helix, $T < 450$ mK

Below 450 mK there are several magnetic Bragg peaks that may be indexed by an incommensurate helical phase. Figure 3.4a) and b) show the Rietveld refinement of this model against the isolated magnetic scattering at 80 mK on WISH, where the propagation vector was refined to $\mathbf{k} = (0.3915(2), \pm 0.3915(2), 0)$. The corresponding ordered moment, $\mu_{\text{order}} = 0.63(1) \mu_{\text{B}}$ is only 40 % of the full expected moment size, $\mu_{\text{order}} = gS_{\text{eff}} \mu_{\text{B}} = 1.5 \mu_{\text{B}}$ assuming $S_{\text{eff}} = 1/2$ and $g = 3$ [46]. An equivalent set of helical moments exists on each sublattice, represented by the blue and orange moments in Fig. 3.4c), but are related by a fixed phase angle, $\phi = 1.15(5) \pi$. Refinements as a function of temperature have no variation below 450 mK in either \mathbf{k} or μ_{order} (Fig. 3.6b) and c), respectively) and therefore this phase is referred to as being locked-in.

Whilst the pursuit for a spiral spin liquid on a diamond lattice has been explored for many years, the extension to include elongated lattices is a relatively new one [45, 46, 198]. Previous characterisation of LiYbO₂ discounted its candidacy due to the phasing between sublattices, $\phi = 0.58 \pi$, not being in agreement with the theoretical prediction of $\phi = \pi$ [46]. However, the refinement of the phase angle in this work, $\phi = 1.15(5) \pi$, is in agreement with the prediction and therefore verifies that LiYbO₂ maps onto the J_1 -

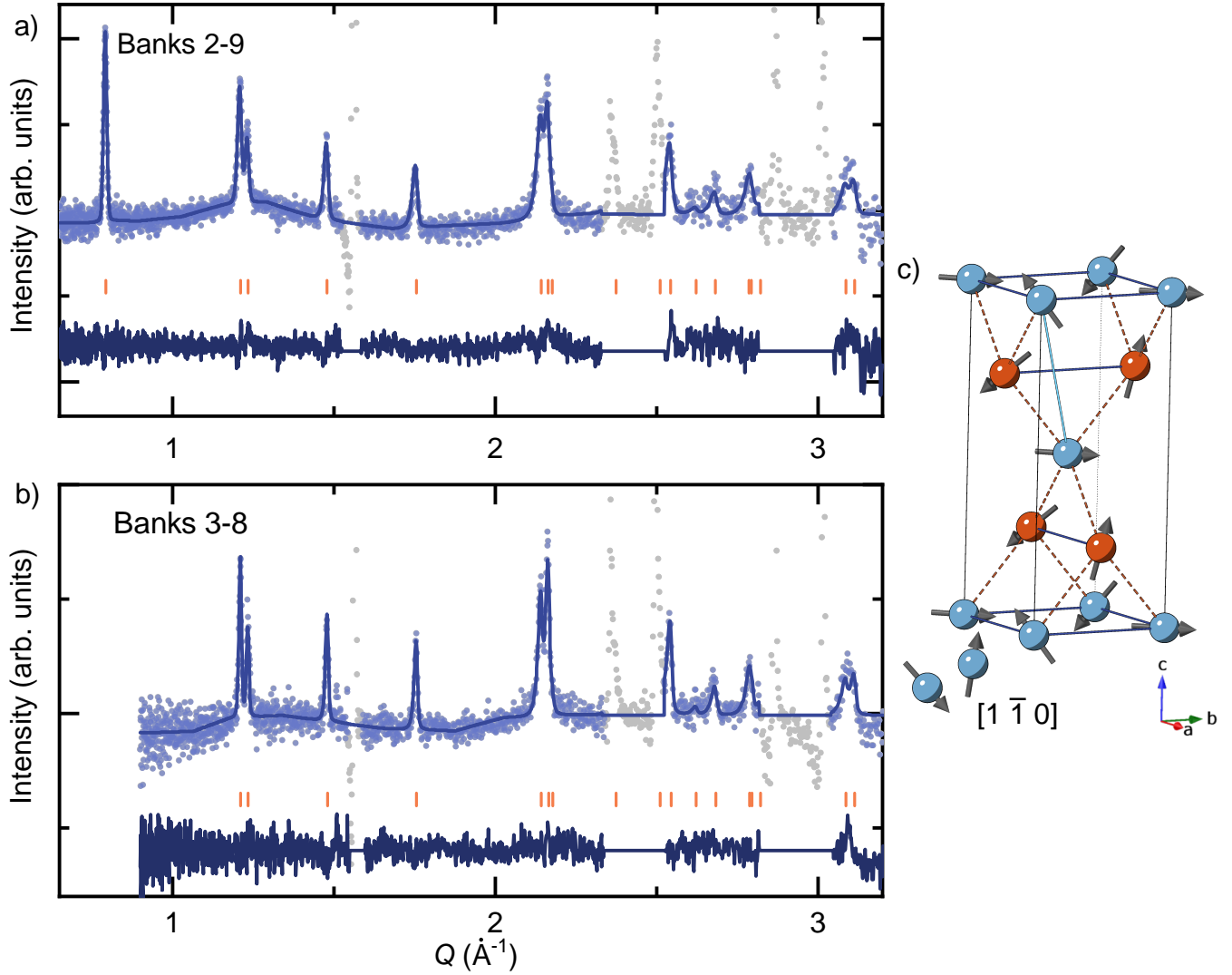


Figure 3.4: Rietveld refinement of the magnetic structure of LiYbO₂ against data collected on WISH. Magnetic only scattering at 80 mK (blue) has been isolated by subtracting the nuclear contribution at 5 K, excluded regions are shown in grey. Fit is shown by the blue line, difference curve in dark blue and magnetic Bragg peak positions by the orange tickmarks. a) Banks 2 - 9 ($R_{F,\text{mag}} = 13.1\%$, $\chi^2 = 3.06$) and b) banks 3 - 8 ($R_{F,\text{mag}} = 10.9\%$, $\chi^2 = 3.24$). c) The refinement describes a locked-in incommensurate helical magnetic structure with $\mathbf{k} = (0.3915(2), \pm 0.3915(2), 0)$ and relative phasing of the sublattices, $\phi = 1.15(5)\pi$. Trailing moments are shown propagating in the $[1 \bar{1} 0]$ direction.

J_2 Heisenberg model on an elongated diamond lattice. In previous experimental studies, this mis-assignment of ϕ was very likely due to the experimental setup as Bordelon *et al.* performed neutron scattering measurements under an applied magnetic field [46]. These measurements are notoriously difficult on a powder sample, and so it is convention to press the powder into a pellet to limit the movement of the powder particles under the applied field. Subsequently, a significant preferred orientation correction was required during the analysis of the zero field neutron scattering data, and directly impacted the refinement of the phase angle, ϕ . All measurements in this chapter were performed on loose powders, therefore, preferred orientation is not an issue. This is confirmed in Figs. 3.3 and 3.12 that a good fit of the chemical structure can be achieved without any additional preferred orientation. Additionally, the magnetic structure is best described by $\mathbf{k} = (\delta, \pm\delta, 0)$ which is the correct form of \mathbf{k} required to generate the spiral spin liquid phase. The ratio of exchange parameters determined for this helical structure, $J_1 = \pm 1.343(4)J_2 > 0$ ($J_1 = \pm 4\cos(0.391\pi)J_2$) places LiYbO₂ directly within the spiral spin liquid phase. Therefore, I propose that LiYbO₂ is the first material to fulfil experimentally all of the conditions required for the observation of the spiral spin liquid in the J_1 - J_2 Heisenberg model on an elongated diamond lattice.

3.3.2.2 Evolving Incommensurate Helix, 450 mK < T < 1.2 K

In addition to this spiral spin liquid ground state, time-of-flight neutron powder diffraction data reveal an intermediary phase exists between 450 mK and 1.2 K. This phase is very similar to the one described below 450 mK but has an evolution with temperature. An example Rietveld refinement is shown in Fig. 3.5a) and b) with data collected at 800 mK, where \mathbf{k} was refined to $\mathbf{k} = (0.3901(1), \pm 0.3901(1), 0)$ and $\mu_{\text{order}} = 0.49(1) \mu_{\text{B}}$. Figure 3.6a) highlights the evolution of this phase by the change in peak position and intensity of the $(0 + \delta, 0 \pm \delta, 0)$ magnetic Bragg peak. Refinement as a function of temperature revealed three key conclusions about the phase:

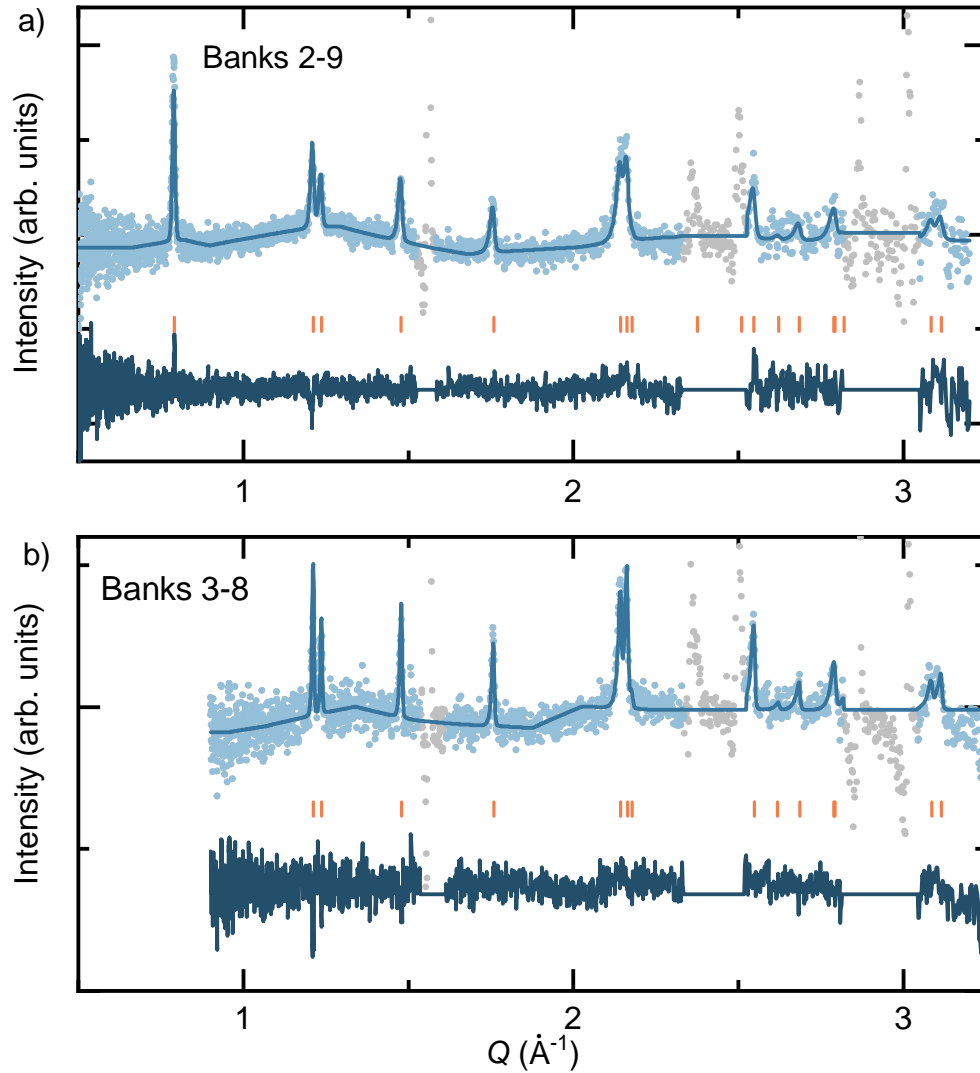


Figure 3.5: Example Rietveld refinement (800 mK) of the magnetic structure of LiYbO₂ in the intermediary ordering phase where \mathbf{k} and μ_{order} vary as a function of temperature. a) Banks 2-9 ($R_{\text{F,mag}} = 7.49\%$, $\chi^2 = 3.03$) and b) banks 3-8 ($R_{\text{F,mag}} = 10.9\%$, $\chi^2 = 2.88$). Magnetic only scattering at 80 mK (blue) has been isolated by subtracting the nuclear contribution at 5 K, excluded regions are shown in grey. Fit is shown by the blue line, difference curve in dark blue and magnetic Bragg peak positions by the orange tickmarks.

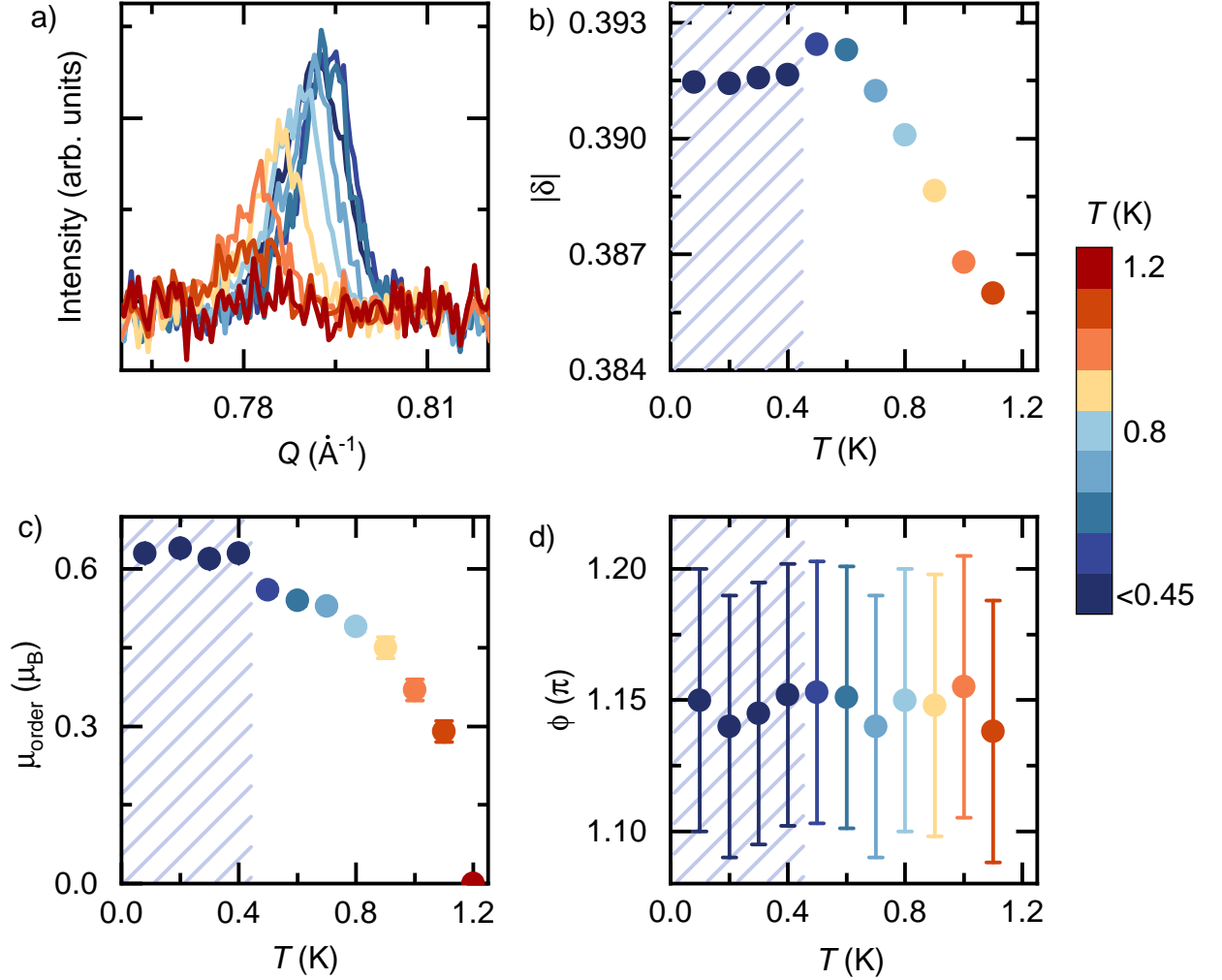


Figure 3.6: a) Evolution of the $(0 + \delta, 0 \pm \delta, 0)$ magnetic Bragg peak over the range $0.4 \leq T \leq 1.2$ K. Summary of the refined parameters, b) propagation vector \mathbf{k} varies but takes the form $\mathbf{k} = (\delta, \pm\delta, 0)$ with $|\delta|$ summarised here, c) ordered moment size, μ_{order} reduces to zero by 1.2 K and d) phasing between Yb-sublattices, ϕ (π) is constant as a function of temperature. All data points are coloured according to the colour bar on the right. Blue dashed regions, $T \leq 450$ mK represent the locked-in incommensurate region, where no change in δ or μ_{order} occurs.

1. The propagation vector varies but always takes the form $\mathbf{k} = (\delta, \pm\delta, 0)$ with $|\delta|$ being summarised in Fig. 3.6b)
2. The ordered moment size, μ_{order} , gradually reduces to zero by 1.2 K (Fig. 3.6c)).
3. The phase angle between sublattices, $\phi = 1.15(5) \pi$ remains constant as a function of temperature (Fig. 3.6d)).

Therefore, this intermediary phase still fulfils the requirements of the spiral spin liquid phase.

3.3.2.3 Short-Range Correlations, $50 \text{ mK} < T < 5 \text{ K}$

Whilst from an average-structure perspective the spiral spin liquid phase in LiYbO₂ has now been confirmed, a remaining question is to understand why the experimentally determined moment size is significantly reduced in comparison to the full ordered moment. A spiral spin liquid is by definition a correlated paramagnetic state with moments collectively fluctuating as spin spirals throughout reciprocal space. The defining experimental signature of these correlated fluctuations is a broad continuous ring of magnetic neutron scattering [192]. Thus it seemed plausible that the remaining missing moment must be contained within these spin spiral fluctuations, which will give the characteristic diffuse scattering of the spiral spin liquid.

The time-equal magnetic cross-sections measured on D7 are presented in Fig. 3.7 and have been vertically shifted by 0.3 b/ster./f.u. for clarity. Underneath the magnetic Bragg peaks at 50 mK and 800 mK, there is significant structure in the diffuse scattering. This structure describes the correlated short-range magnetic order within LiYbO₂. Most prominent is the broad bump centred around $Q = 1.1 \text{ \AA}^{-1}$ which has virtually no change in size or shape between 50 mK and 1.5 K. Structured diffuse scattering is observed up to 5 K, higher than the onset of broad features in previous specific heat measurements which are generally associated with the the formation of short-range correlations [46]. Interestingly,

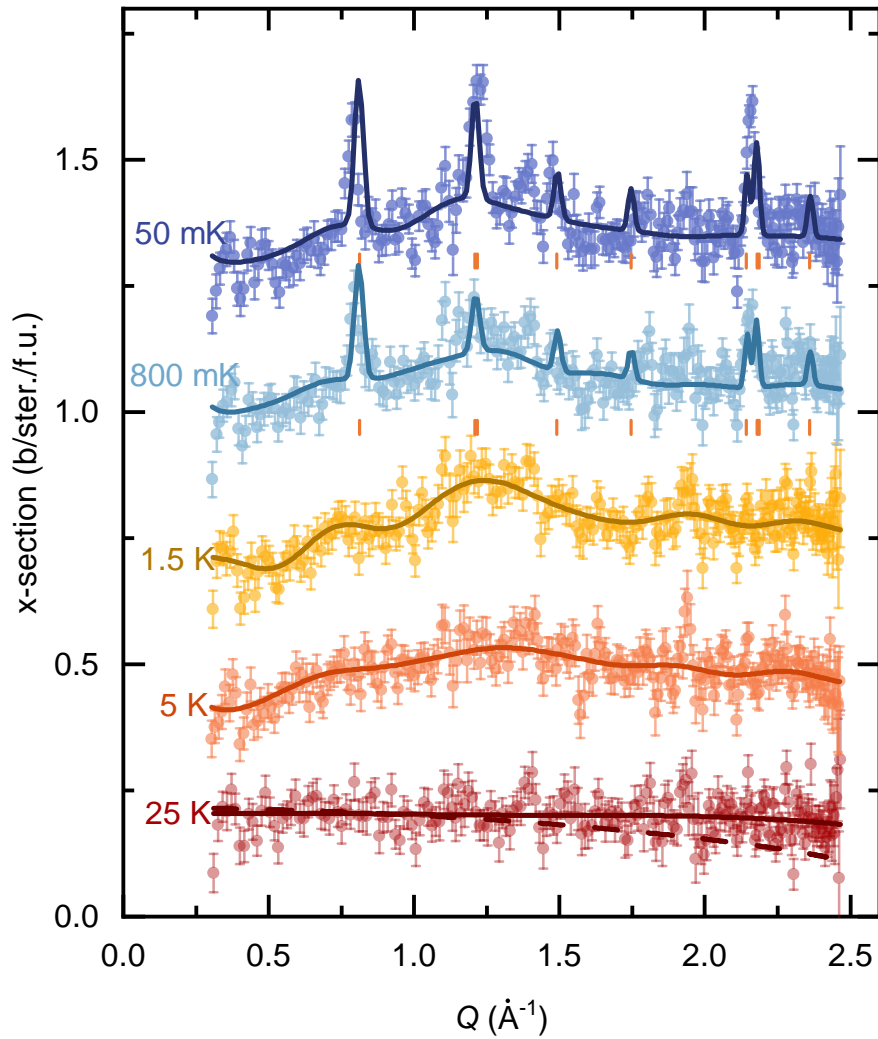


Figure 3.7: Magnetic contribution of experimental powder scattering data from D7. At 50 mK and 800 mK, there are a mixture of magnetic Bragg and structured diffuse scattering. Together these features confirm the co-existence of long- and short-range magnetic order in LiYbO₂. Fits produced from a RMC SPINVERT + Bragg calculation are shown by the solid lines at 50 mK and 800 mK, SPINVERT only between 1.5 K and 25 K, and an analytical approximation of a magnetic form factor for Yb³⁺ ions at 25 K by the dashed line. Positions of magnetic Bragg peaks assuming $\mathbf{k} = (0.4, \pm 0.4, 0)$ are shown by the orange tickmarks. Data have been vertically shifted by 0.3 b/ster./f.u. for clarity.

these broad features are also visible in the temperature subtracted data from WISH (Figs. 3.4 and 3.5), but not visible in the previous neutron scattering measurements from Ref. [46]. The reason for this is twofold; firstly the signal from the magnetic diffuse scattering is very weak and with the added background from the vertical 5 T magnet, the diffuse scattering was likely absorbed into the background. Secondly, in Ref. [46] the magnetic intensity was isolated via temperature subtraction with 1.5 K being used as the high-temperature paramagnetic data set. However, 1.5 K remains within the short-range correlations regime, and therefore is not a good approximation for isolating the whole magnetic signal. Due to the broad and weak nature of diffuse scattering, diffuse features are best isolated via polarisation analysis on an instrument such as D7, as the effects of temperature subtraction are not applicable.

Although acting across different length scales, the helical order that gives the magnetic Bragg peaks and the short-range order from the correlated fluctuations that give the diffuse features cannot be considered as independent from each other. Therefore, data at 50 mK and 800 mK were modelled using a modified version of SPINVERT in order to simultaneously fit the magnetic Bragg and diffuse features [119, 121]. SPINVERT + Bragg fundamentally runs differently to SPINVERT as the best results generally occur when starting the calculation from the fully ordered magnetic structure as opposed to a random seed (Appendix Fig. 3.14a)). Subsequently, one challenging aspect of this analysis was the incommensurate nature of the magnetic structure, as the RMC methods which underpin SPINVERT rely on periodic boundary conditions to generate a supercell. The incommensurate propagation vector, $\mathbf{k} = (0.3915(2), \pm 0.3915(2), 0)$, however, is close to two commensurate propagation vectors; $\mathbf{k} = (0.4, \pm 0.4, 0)$ meaning there are two complete rotations of the helix in $5 \times 5 \times 1$ unit cells, and $\mathbf{k} = (0.375, \pm 0.375, 0)$ with three complete rotations of the helix in $8 \times 8 \times 1$ unit cells. A pseudo-magnetic unit cell was constructed with commensurate boundary conditions in MATLAB by calculating the helical moment distribution with Eq. 3.1 [205]

$$\mathbf{m}_l = m_0 \sum [\cos(\mathbf{k} \cdot \mathbf{R}_l + \phi) \cdot \hat{\mathbf{u}}_k + \sin(\mathbf{k} \cdot \mathbf{R}_l + \phi) \cdot \hat{\mathbf{v}}_k] \quad (3.1)$$

which describes the vectors for the orientation of each moment, \mathbf{m}_l , that are rotating within the $(\hat{\mathbf{u}}_k, \hat{\mathbf{v}}_k)$ plane by an angle of $\mathbf{k} \cdot (\mathbf{R}_l - \mathbf{R}_{l'})$ when moving from unit cell l' to l . The atomic co-ordinates of the magnetic Yb³⁺ ions are given by \mathbf{R} , the periodicity by the propagation vector, \mathbf{k} , m_0 is an arbitrary scaling factor and ϕ is the phase shift. The best configuration was found to be a $10 \times 10 \times 4$ supercell constructed from the $\mathbf{k} = (0.4, \pm 0.4, 0)$ approximation as this prevented overfitting the data and was an adequate range to calculate spin correlations over (Appendix Fig. 3.14b)). Moments were allowed complete rotational degrees of freedom as constraining the spin dimensionality to only allow for conical motion did not improve the quality of the fit. In **SPINVERT + Bragg** there are separate cost functions associated with the ordered (order) and diffuse (weight) calculations, and it was found that the cost function associated with the ordered structure needed to be strongly constrained in order to fit the data. Although strongly constrained, the long-range ordered magnetic structure is not fixed because otherwise there would be no diffuse contribution to the calculation. In total the supercell contained 6400 Yb³⁺ spin vectors with empirical weighting factors, weight = 10 and order = 4000. The resolution function of D7 was fixed at $U = 2.2$, $V = -4.07$ and $W = 3.93$, as determined for the wavelength, $\lambda = 4.8$ [113]. All refinements used single-spin flip dynamics and the χ^2 converged within 100 proposed flips per spin. Refinements starting from a random seed (order = 0) were not able to fit all the Bragg peaks in the 50 mK and 800 mK data (Appendix Fig. 3.14a)).

Data at 1.5 K and 5 K were fit using **SPINVERT**. The main difference to the fit was a lowering in the supercell size to $6 \times 6 \times 3$, which is a natural decision as there are fewer features within the data. The other parameters associated with the diffuse calculation, such as weight and anisotropy, were kept constant from before.

The resultant fits are shown in Fig. 3.7 and emulate the main features of the data extremely well. The scale factor from **SPINVERT** is classically related to the moment size from Eq. 1.21. Through the **SPINVERT + Bragg** analysis the moment was separated into the proportion arising from the helical order and short-range order, and these values are

T (K)	WISH	D7		
	$\mu_{\text{order}} (\mu_{\text{B}})$	$\mu_{\text{order}} (\mu_{\text{B}})$	$\mu_{\text{disorder}} (\mu_{\text{B}})$	$\mu_{\text{total}} (\mu_{\text{B}})$
base	0.63(1)	0.80(1)	1.80(1)	2.60(1)
0.8	0.49(1)	0.67(2)	1.92(2)	2.59(2)
1.5	-	-	2.73(2)	2.73(2)
5	-	-	2.74(2)	2.74(2)
25	-	-	2.76(2)	2.76(2)

Table 3.2: Summary of experimental magnetic moments, μ_{order} from Rietveld analysis on WISH and μ split into long-range helical ordered, μ_{order} and correlated short-range ordered, μ_{disorder} components from SPINVERT + Bragg analysis on D7.

summarised in Table 3.2. Thus, it can be shown that the full expected moment of LiYbO₂ can be obtained through the simultaneous refinement of magnetic Bragg and diffuse scattering. It should be noted, that the moment sizes from the analysis of the WISH and D7 data are not directly comparable due to the definition used, Rietveld: $\mu^2 = g^2 S_{\text{eff}}^2 \mu_{\text{B}}^2$ and SPINVERT + Bragg: $\mu^2 = \text{scale} = g^2 S_{\text{eff}} (S_{\text{eff}} + 1) \mu_{\text{B}}^2$. Assuming both have an effective spin, $S_{\text{eff}} = 1/2$ and $g = 3$ [46], a full moment size of $\mu = 1.5\mu_{\text{B}}$ for WISH and $\mu = 2.6\mu_{\text{B}}$ for D7 is expected. At base temperature, μ_{order} accounts for 40% and 30% of μ_{eff} for the WISH and D7 analyses, respectively. The differences between the two methods is likely due to the incommensurate-commensurate approximation in the SPINVERT + Bragg analysis. For example, the \mathbf{k} -approximation results in peak shifting at $Q = 0.8 \text{ \AA}^{-1}$ and peak splitting at $Q = 2.2 \text{ \AA}^{-1}$, causing a slight underfit of some of the magnetic Bragg reflections. This is a limitation of the RMC analysis at this time, but given the complexity of the magnetic structure, and the agreement with the WISH results, the moment sizes presented here are likely an accurate description of the system.

3.3.2.4 Paramagnetic, $T > 25$ K

Further increasing the temperature to 25 K leads to a collapse of the diffuse structure within the magnetic scattering, indicating the transition to a paramagnetic state. The 25 K data have been fit two ways; firstly using an analytical approximation of Yb³⁺ ions (Eq. 1.13) [206], and secondly by SPINVERT, shown by the dashed and solid lines, respectively in Fig. 3.7. For the analytical approximation it was assumed that the system was in an effective $S_{\text{eff}} = 1/2$ state with $g = 3$. The $S_{\text{eff}} = 1/2$ assumption is valid due to the integration window of D7 ($-20 \leq \Delta E < 3.5$ meV) being well below the previously observed CEF excitations [46]. The fit has reasonable agreement with the data but the data do not have a true magnetic form factor dependence since the scattering is very flat. Here, it is assumed that this is due to the additional orbital contributions to the total angular momentum [46]. Furthermore, in many rare-earth systems it can be necessary to calculate the magnetic form factor to higher orders (j_2 and j_4) however this did not give a significant improvement to the fit. Data were also fit using SPINVERT with a relaxed supercell of $2 \times 2 \times 1$ unit cells. This yielded an effective moment, $\mu_{\text{eff}} = 2.76(2) \mu_{\text{B}}$ which is in agreement with previously reported susceptibility results [46] and the associated paramagnetic moment at $Q = 0 \text{ \AA}^{-1}$ of $\mu_{\text{eff}} = 2.6(1) \mu_{\text{B}}$. Analysis of the scale factor from SPINVERT with $S_{\text{eff}} = 1/2$ gave $g = 3.20(5)$, verifying the assumption used in the analytical approximation.

3.3.3 Single-Crystal Simulations

Reconstructions of single-crystal magnetic neutron diffraction patterns were calculated by SCATTY from fits to the experimental powder data at 50 mK. Figure 3.8a) shows the $(h k 0)$ plane and reveals strong magnetic intensity at the expected incommensurate magnetic Bragg positions. Due to the calculation method of the single-crystal scattering plane, the magnetic Bragg peaks appear to be artificially broadened in the simulation. The $(h h l)$ plane, a slice diagonally through the $(h k 0)$ plane, is shown in Fig. 3.8b), where a faint ring of diffuse

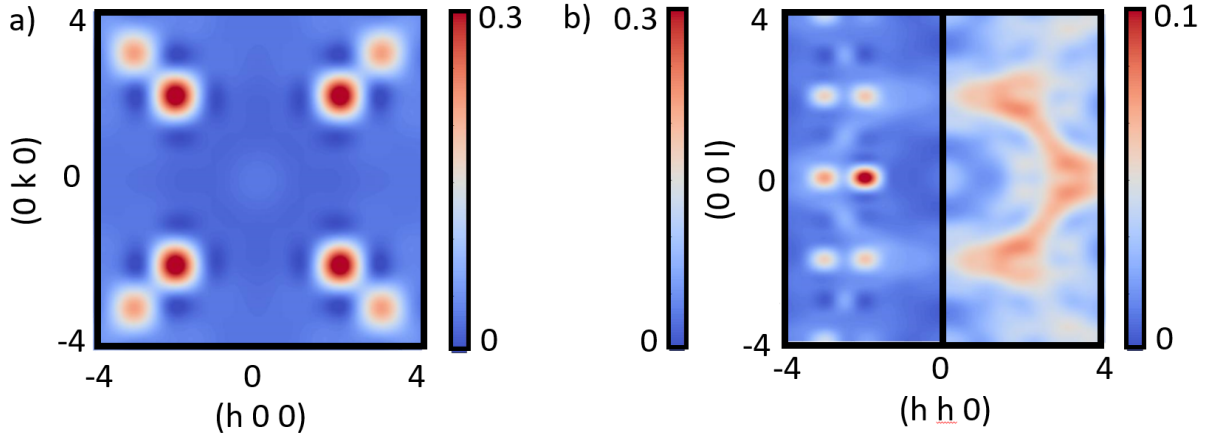


Figure 3.8: Reconstructions of single-crystal magnetic scattering from analysis of the powder data using SPINVERT + Bragg and SCATTY at 50 mK. In the a) $(h k 0)$ plane, strong magnetic Bragg peaks are observed at incommensurate Bragg positions and b) the $(h h l)$ plane reveals the signature of the spiral spin liquid, a continuous diffuse ring of scattering. Left: total scattering calculation and right: magnetic Bragg peaks have been excluded to show the diffuse ring more clearly. Intensities have been normalised to absolute units according to the colour bars.

scattering, representing the contoured spiral surface, can be seen. Since the intensity of the magnetic Bragg peaks dominates, on the right, the satellites have been removed from the calculation leaving the diffuse ring clearly visible. This is the expected manifestation of the spiral spin liquid in single-crystal diffuse neutron scattering measurements [192], and therefore, further confirms that the analysis and interpretation of the magnetic ground state of LiYbO₂ is that of a spiral spin liquid.

3.3.4 Spin Correlations

Figure 3.9a) shows the radial spin-spin correlation function, $\langle \mathbf{S}(0) \cdot \mathbf{S}(r) \rangle$, calculated by SPINCORREL at 50 mK for LiYbO₂. Correlations have been split to show those that act

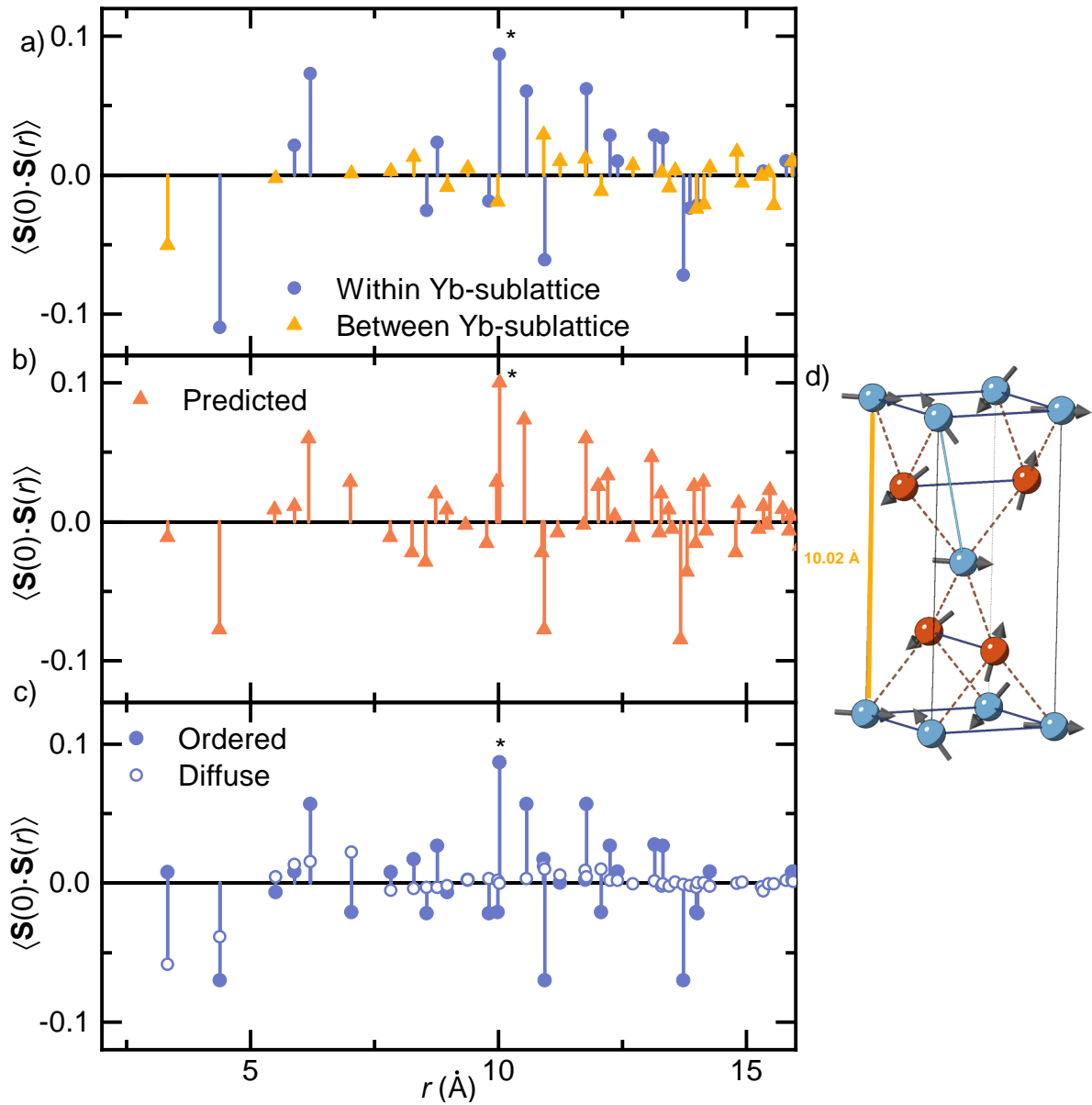


Figure 3.9: a) Radial spin-spin correlations, $\langle \mathbf{S}(0) \cdot \mathbf{S}(r) \rangle$ as a function on interatomic distance, r , calculated by SPINCORREL at 50 mK. Blue circular and yellow triangular markers are correlations within and between Yb-sublattices, respectively. b) Predicted correlations from a long-range helical structure. c) Spin correlations can be separated into the proportion of the correlation from the ordered (closed) and diffuse (open) structure. d) Schematic of magnetic structure, where a key FM correlation along the c -axis (starred in a), b) and c)).

within and between Yb-sublattices with the blue circular and yellow triangular markers, respectively. The correlations at 50 mK have, in general, good agreement with the predicted correlations from a long-ranged ordered helical state as shown in Fig. 3.9b). This suggests that a helical structure is an appropriate description of the ordered magnetic structure in LiYbO₂. Additionally, by considering the expected behaviour of correlations, the correlations output from SPINCORREL can be checked to make sure they make physical sense. For example, the first nearest neighbour correlation acting directly along the tetragonal c -axis, $r = 10.02 \text{ \AA}$ is shown in Fig. 3.9d) and should be completely ferromagnetically coupled. Figure 3.9a) and b) show that this is one of the most strongly ferromagnetically coupled correlations within the set, verifying the expected behaviour.

Figure 3.9a) shows the total correlation at 50 mK, but each correlation can be broken down further to show the proportion originating from the long-range ordered and short-range diffuse structures by the closed and open markers in Fig. 3.9c), respectively. In most cases at 50 mK, the ordered magnetic structure dominates and has excellent agreement with the predicted correlations from a fully ordered helical structure. However, there are some exceptions. The first correlation, $r = 3.33 \text{ \AA}$, has a significant diffuse component and as this describes the first nearest-neighbour interaction between sublattices (J_1 in Fig. 3.1b)) may be related to the phasing of the sublattices. Additionally, the correlation at 7.5 \AA has equal and opposite magnitudes of ordered and diffuse components, giving the impression the total correlation has no magnitude.

Examining the ordered and diffuse contributions to the correlation as a function of temperature reveals that they have different behaviours, specifically that the diffuse component is largely temperature-independent but the ordered component is temperature-dependent. This is demonstrated in Fig. 3.10a) with correlations that have a dominant diffuse contribution (reds) and dominant ordered contribution (blues). The diffuse and ordered contributions are shown by the open and closed markers, respectively. As illustrated here, the behaviour is the same regardless of which ordering term dominates, the diffuse

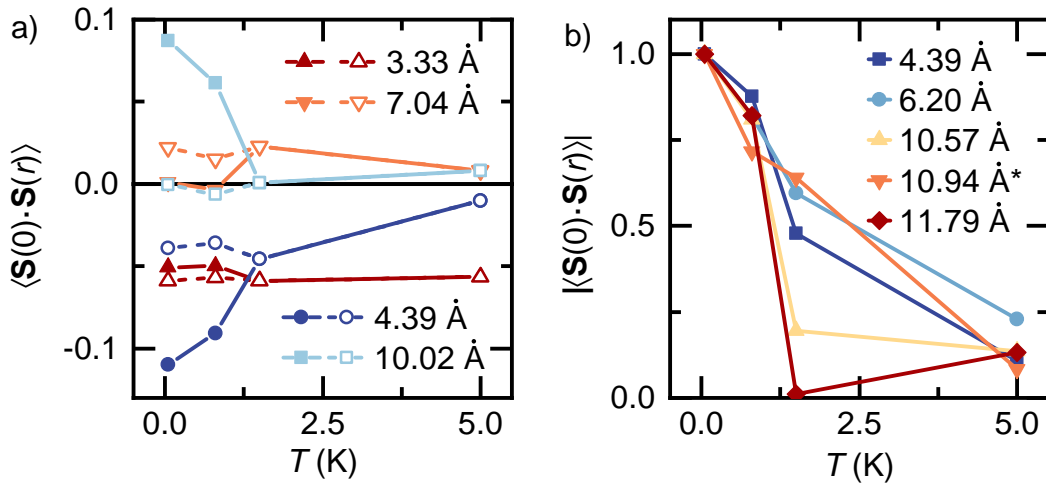


Figure 3.10: a) Correlations as a function of temperature where ordered and diffuse contributions are represented by closed and open markers, respectively. Diffuse contributions are largely temperature-independent whereas ordered contributions are temperature-dependent. b) Normalised intensity of total correlations to their value at 50 mK as a function of temperature, which highlights how the correlation strength and length develop. Correlations have been selected as they have a strong ordered contribution. $r = 10.94 \text{ \AA}$ is starred as it is the only correlation in this group that changes from predominantly antiferromagnetic to ferromagnetic at 1.5 K. In both figures, lines are added as a guide to the eye.

stays roughly constant between 50 mK and 1.5 K, but the ordered component has a large temperature dependence. This quantifies the observations in the D7 powder scattering data, as the diffuse scattering remains relatively unchanged between 50 mK and 1.5 K, but helical magnetic order develops below 1.5 K.

To understand this temperature dependence better, a number of correlations with a strong ordered contribution have been normalised to their maximum value at 50 mK in Fig. 3.10b). At 800 mK, the strength of most correlations has dropped to 80 % of their nominal value, which is similar to the ratio by which the ordered moment diminishes in the Fullprof and SPINVERT + Bragg analysis. At 1.5 K however, the rate of decay varies significantly

with longer correlations generally dying off faster than shorter correlations. An exception is the correlation at $r = 10.94 \text{ \AA}$ (orange triangle) but this is the only correlation in this group that switches from dominant antiferromagnetic to ferromagnetic exchanges at 1.5 K. These results prove that not only does the correlation strength weaken as a function of temperature but also the correlation length shortens. Generally this can be associated with the transition from long- to short-range magnetic order.

3.3.5 Discussion

The results in this chapter are significant as I have shown for the first time that the elongated diamond lattice is an experimentally accessible route to achieving a spiral spin liquid ground state. To date, only LiYbO₂ [46, 200] and NaCeO₂ [198] have been explored within the context of the J_1 - J_2 Heisenberg model on an elongated diamond lattice, but their differing ratios of exchange parameters led to the formation of distinct magnetic ground states. LiYbO₂ candidacy as a spiral spin liquid was previously discounted, the reasons for which I will explain in comparison with this work now [46, 200].

3.3.5.1 Realising the Model: The Power of Preferred Orientation

There are three conditions required to confirm a spiral spin liquid phase: (1) the phase angle, ϕ , between magnetic sublattices is equal to π , (2) a propagation vector of the form $\mathbf{k} = (q, q, 0)$ and (3) a ratio of exchange parameters of $-4 < J_1/|J_2| < 4$ [46]. Previous analysis confirmed conditions (2) and (3) through neutron scattering measurements, but found the phase angle in condition (1) to be only $\phi = 0.58 \pi$ [46]. However, the refinement of $\phi = 1.15(5) \pi$ in this work is consistent with condition (1) and therefore verifies that LiYbO₂ can map onto the J_1 - J_2 Heisenberg model on an elongated diamond lattice [45, 46, 77]. As discussed earlier, this mis-assignment of ϕ very likely came from the need to pelletise

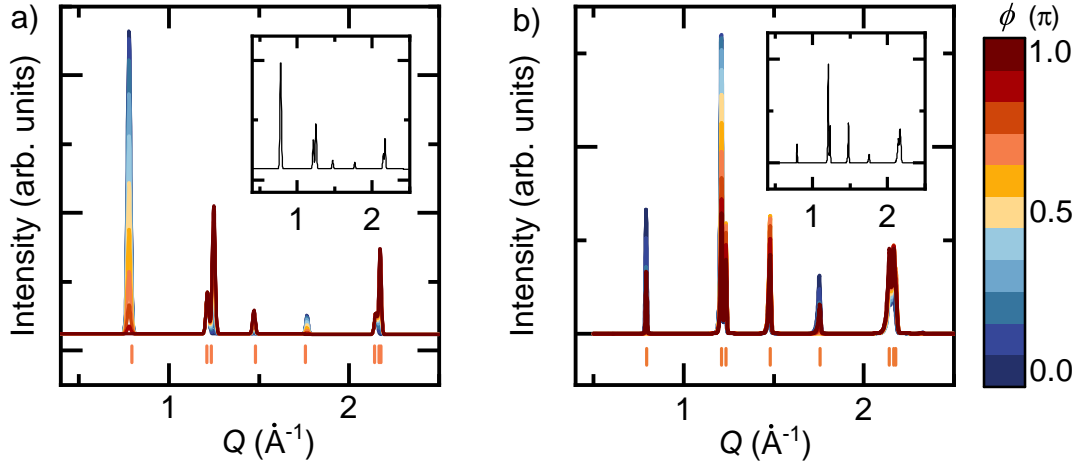


Figure 3.11: Effect of changing the phase angle, ϕ between sublattices. a) Reproduction of results from Ref. [46] which includes a significant preferred orientation correction and b) without preferred orientation. In both figures, ϕ is given by the colour bar on the right and the insert shows the average phase model.

the sample for in-field neutron scattering measurements. Subsequently the refinement of the chemical structure required a significant preferred orientation correction that unknowingly redistributed the intensity of the magnetic Bragg peaks.

A key example of this effect is seen in the intermediary ordered phase between 450 mK and 1.2 K. Previously, the intermediary phase was described by a complex and unusual disordered incommensurate helical state. In this model both \mathbf{k} and μ_{order} had been fixed to their values determined below 450 mK, but the phasing of the sublattices, ϕ was changed. This produces various constructive and destructive interference of the peaks. The scattering was simulated over 10 of these arbitrary phase angles and the average was used to fit the data. A reproduction of this analysis is shown in Fig. 3.11a) with the effect of changing the phase angle in the main figure and the insert showing the average used to fit the data. However, it is not possible to reproduce this analysis without preferred orientation. The same simulations with no preferred orientation gives the results shown in Fig. 3.11b), where the average in the insert is clearly very different to the originally proposed model and does

not have good agreement with the data.

In light of this analysis, the intermediary phase between 450 mK and 1.2 K has been re-evaluated so as to remove the need for preferred orientation by measuring all samples on a loose powder. WISH data from Fig. 3.6a) shows a clear evolution in the position and intensity of the $(0 + \delta, 0 \pm \delta, 0)$ magnetic Bragg peak as a function of temperature. This suggested that it was the propagation vector, \mathbf{k} and ordered moment size, μ_{order} that were changing, not the phase angle. Rietveld refinement confirmed this hypothesis, with the much simpler model proposed during this chapter having very good agreement with the experimental data. The preferred orientation also affected the refinement below 450 mK, which is why, when the need for preferred orientation is removed by measuring loose powders, ϕ is now in agreement with the theoretical prediction.

3.3.5.2 The Lifetime of a Spiral Spin Liquid and their Relationship to Experimental Probes

Very few examples of spiral spin liquids on any lattice have been confirmed [189, 190, 192]. As such, there are many fundamental questions about this exotic magnetic ground state that still need answers, for example, why do the moments choose to fluctuate in this manner and how long do the fluctuations exist for? In order to understand the true nature of the spiral spin liquid, a combination of experimental probes are therefore required. LiYbO₂ has been studied with high resolution and diffuse neutron scattering in this work, magnetometry and inelastic neutron scattering [46] and muon spin relaxation (μ SR) [200] by others. These results are all connected but some differences are observed which are related to the timescales of the fluctuations versus the experimental probes.

Specific heat measurements in zero field observed three features, a broad peak indicative of short-range correlations below 2 K, and two sharp peaks at 1.13 K and 450 mK [46]. The peak at 1.13 K corresponds to a rapid increase in the zero-field muon depolarisation

rate in the μ SR measurements [200], and the onset of magnetic Bragg peaks in the WISH data. This can be interpreted as the formation of the spiral spin liquid phase. The second transition in the specific heat, at 450 mK [46] corresponds to the point in the neutron diffraction data where the propagation vector, \mathbf{k} , and ordered moment size, μ_{order} , change from evolving as a function of temperature to being constant. This is described as a locking-in of the phase, but the fluctuations that form the spiral spin liquid are still persistent, which is shown in the diffuse scattering data in Fig. 3.7. However, no such transition is observable in the μ SR results [200]. The transition in the μ SR data is interesting, as it is characteristic of a freezing system. This is likely an effect of the continual fluctuations of the spiral spin liquid phase coupled with the disorder in the system, which will interfere with the muon precession. Here, disorder is defined by the uncertainty in the propagation direction on the doubly degenerate tetragonal axes, which is unresolvable on a powder sample. The μ SR data also show that the depolarisation rate is very fast ($< \mu\text{s}$) and so at the very limit of what can be detected in this type of experiment. Interpreting this μ SR data is complicated as the muon depolarisation rate depends not only on the fluctuation rate of the sample's internal magnetic field, but also on its magnitude and distribution, which in turn will depend on the muon stopping sites within the sample, which are not identified in Ref. [200]. Conversely, the interaction time for a neutron with the sample is of the order of ps, which allows for the assumption that the fluctuations are existing for long enough for the scattering to be considered as elastic. This therefore suggests that the lifetime of the spiral spin liquid of LiYbO₂ exists on a timescale between ~ 10 ps and < 1 μs , and although μ SR can measure the onset of this phase, the fluctuations are moving too quickly to capture the details of the lock-in.

3.4 Conclusions and Outlook

The J_1 - J_2 Heisenberg model on an elongated diamond lattice predicts an intriguing spiral spin liquid ground state that had not yet been experimentally realised. This chapter explored the candidacy of LiYbO₂ using high-resolution neutron powder diffraction and diffuse neutron scattering measurements. The key conclusions from this chapter are summarised as follows:

- The phasing between Yb-sublattices, $\phi = 1.15(5) \pi$ is consistent with the prediction from theory, $\phi = \pi$ [46]. This verifies that LiYbO₂ maps onto the J_1 - J_2 Heisenberg model on an elongated diamond lattice.
- Helical magnetic order develops below 1.2 K with the propagation vector, $\mathbf{k} = (\delta, \pm\delta, 0)$. This is the correct form of \mathbf{k} needed to generate the spiral spin liquid phase.
- The ratio of exchange parameters, $J_1 = 1.343(4)J_2 > 0$, in the ground state is directly within the spiral spin liquid regime ($-4 < J_1/|J_2| < 4$).
- The helical order undergoes a twostep ordering process. Firstly below 1.2 K, evolving helical order is observed with varying $|\delta|$ in $\mathbf{k} = (\delta, \pm\delta, 0)$ and gradually increasing ordered moment size, μ_{order} . Then, below 450 mK, \mathbf{k} ($= (0.3915(2), \pm 0.3915(2), 0)$) and μ_{order} ($= 0.63(1) \mu_B$) lock into place. At all times below 1.2 K, the phase angle is constant, $\phi = 1.15(5) \pi$.
- Significant structure in diffuse scattering persists down to 50 mK. Reconstructions of single-crystal diffraction patterns from the D7 powder analysis reveal the characteristic ring of diffuse scattering in the $(h h l)$ plane, confirming the spiral spin liquid ground state in LiYbO₂.
- The expected full magnetic moment was recovered by considering both magnetic Bragg and diffuse scattering simultaneously in LiYbO₂. This was determined through state-of-the-art RMC spin simulations.

- Analysis of spin correlations quantified observations in diffuse powder scattering data. Temperature-dependent correlations were responsible for the helical order and temperature-independent correlations contribute to the short-range diffuse structure.

The next direction for LiYbO₂ is to confirm these experimental findings with measurements on a single-crystal sample. The results presented in this chapter are at the very forefront of analysis for powder magnetic diffuse scattering and showcase the capabilities of RMC modelling in a partially ordered system. Conclusive evidence for the spiral spin liquid however, is only achievable within a single-crystal diffuse neutron scattering study through the direct observation of the continuous spiral contours in the $(h\ h\ l)$ plane. Another experimental aim would be to directly measure the exchange parameters in a single-crystal inelastic neutron scattering measurement, to verify the ratio of $J_1/|J_2|$ lies within the spiral spin liquid boundary ($-4 < J_1/|J_2| < 4$). Powder inelastic neutron scattering has been attempted before [46], however, this analysis was complicated by a number of factors including the low magnetic signal from the $S_{\text{eff}} = 1/2 \text{ Yb}^{3+}$ moments, the need for phonon subtraction and the complexity of the magnetic ground state. Single-crystal measurements on the other hand, should be able to resolve these issues and accurately establish the exchange parameters. In addition, single-crystal neutron diffraction would be able to distinguish if the ordering plane lies along the $[1\ 1\ 0]$ or $[1\ \bar{1}\ 0]$ plane. This is currently unsolvable due to powder averaging effects and the doubly degenerate tetragonal axes. If the ordering plane was found to be changing and disordered, then this may explain the appearance of the freezing transition in the μSR measurements [200].

Beyond LiYbO₂ this work has shown that a new geometry, the elongated diamond lattice, is experimentally able to host a spiral spin liquid ground state. The importance of this cannot be underestimated. It has long been thought that structural distortions away from the ideal diamond lattice were detrimental to the observance of the spiral spin liquid. However, after the re-imagining of the J_1 - J_2 Heisenberg model, and this experimental work,

distorted diamond structures are now proven to be able to host this elusive phase. Other candidate systems with similar stretching ratios include CeLiBi₂ [207], NaNdO₂ and NdGdO₂ [208]. A currently unexplored theoretical question is the importance of the superexchange pathway in attaining the spiral-spin liquid state. For example, KRuO₄ [209] and KOsO₄ [210], share a similar stretching ratio to LiYbO₂ but have Néel ordered ground states. This was thought to be due to their $I4_1/a$ structure prohibiting the superexchange pathway across the diagonal (J_{2b} in Fig. 3.1a)), but this is considered a negligible interaction within the model, so its lack of presence should not affect the final ground state. Additionally, given the recent introduction of the elongated diamond lattice to the list of candidate systems, a further research avenue would be to explore the robustness of the model in realising the spiral spin liquid phase. For example, the only two materials which have been investigated as candidates for the model, LiYbO₂ and NaCeO₂, both share the same $I4_1/amd$ structure and have an extreme elongation along the c -axis, $c/\sqrt{2}a = 1.63$, which is important as it renders J_{2b} negligible in strength. An interesting research question would be to explore the tolerance in the stretch, and the relative importance of exchange interactions when selecting new candidate systems.

3.5 Appendix

WISH

The refinement of the chemical structure of LiYbO₂ at 5 K from WISH is shown in Fig. 3.12. A very good refinement is achieved across all banks without preferred orientation, verifying on a loose powder the assumptions in the main text are valid.

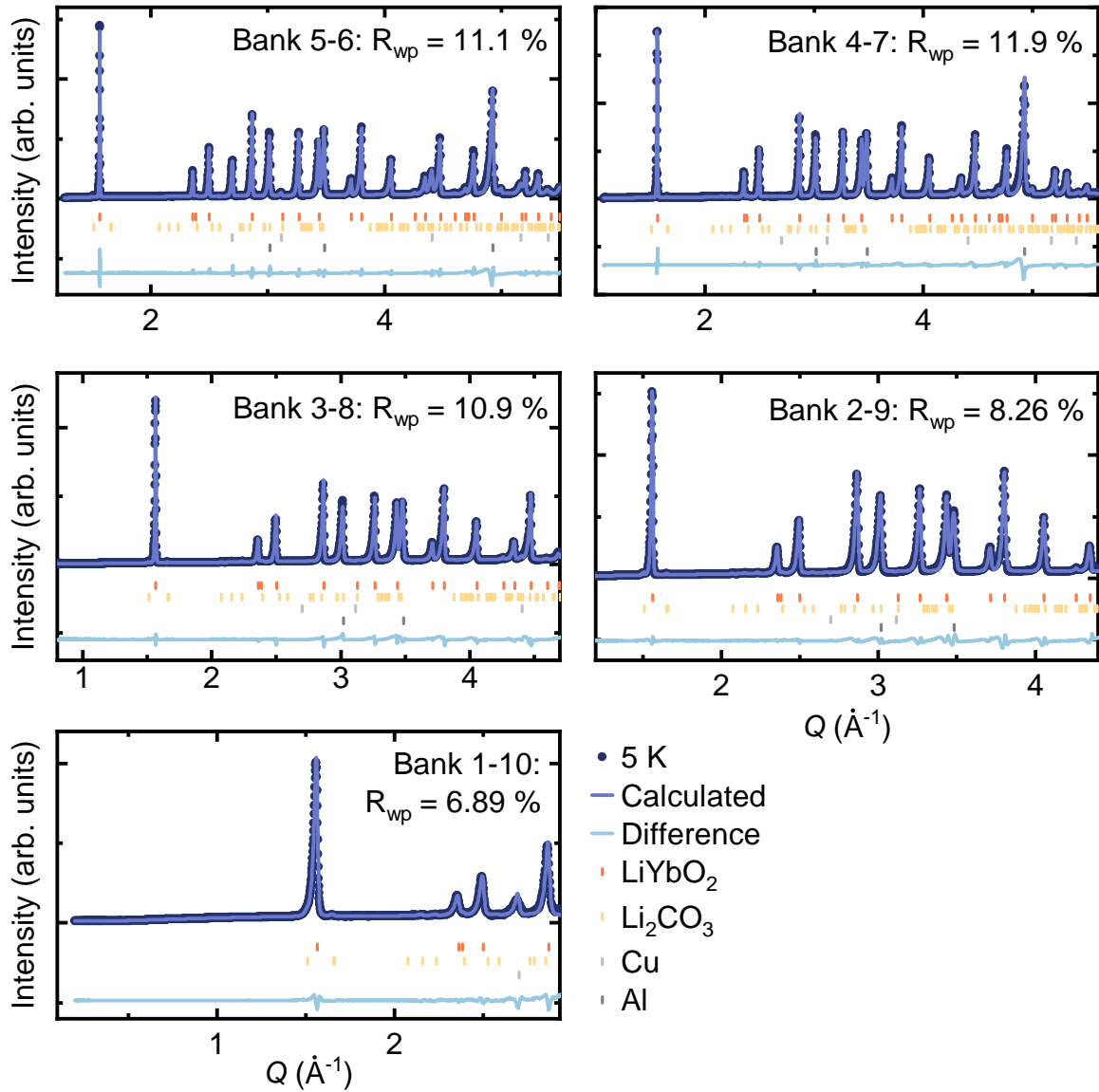


Figure 3.12: Multi-bank refinement of the chemical structure of LiYbO₂ on WISH at 5 K. LiYbO₂ (orange) and the Li₂CO₃ impurity (yellow, 2.2 %) were refined via the Rietveld method, instrumental contributions from copper (light grey) and aluminium (dark grey) were refined using the Le Bail method. The results from this structural refinement were used in the subtraction to isolate the magnetic scattering.

D7 Calibration

Since there was no change in the NC scattering between 5 K and 50 mK, the structural information obtained through the D2B refinement of the average chemical structure at 4 K could be used as a precise normalisation for all the D7 refinements. The absolute normalisation was checked through Rietveld refinement (Fig. 3.13) where the only parameters refined were the scale factor and zero-shift of the instrument. The absolute normalisation was found to be a little low, ~ 0.66 following the conversion of the arbitrary scale factor, 0.229(3) from Mag2Po1. Ideally, this value should be within 10 % of 1 if the absolute normalisation is correct. This underestimation is most likely due to a change in the flux during calibration measurements which dropped the flux by around 1/3. Consequently, the data and derived parameters presented in this work are scaled according to the value found from Rietveld refinement of the data, 0.66.

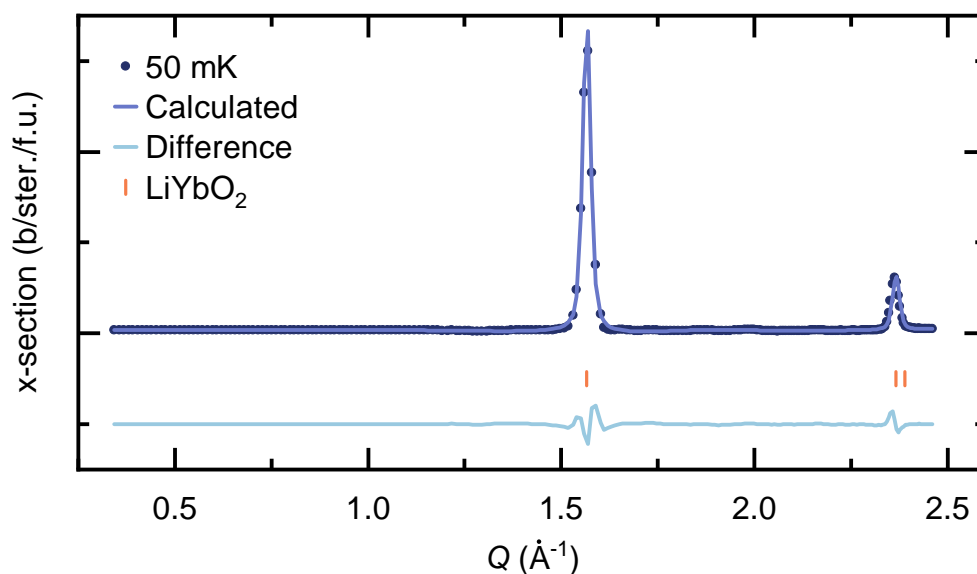


Figure 3.13: Rietveld refinement of NC cross-section from D7 at 50 mK ($R_F = 1.01 \%$, $\chi^2 = 284.18$).

SPINVERT + Bragg

The choice of the starting configuration in SPINVERT + Bragg is important for getting a good fit of the data. Figure 3.14a) shows the difference between calculations starting from the helical ordered structure (dark blue) and a random seed (orange). The calculation

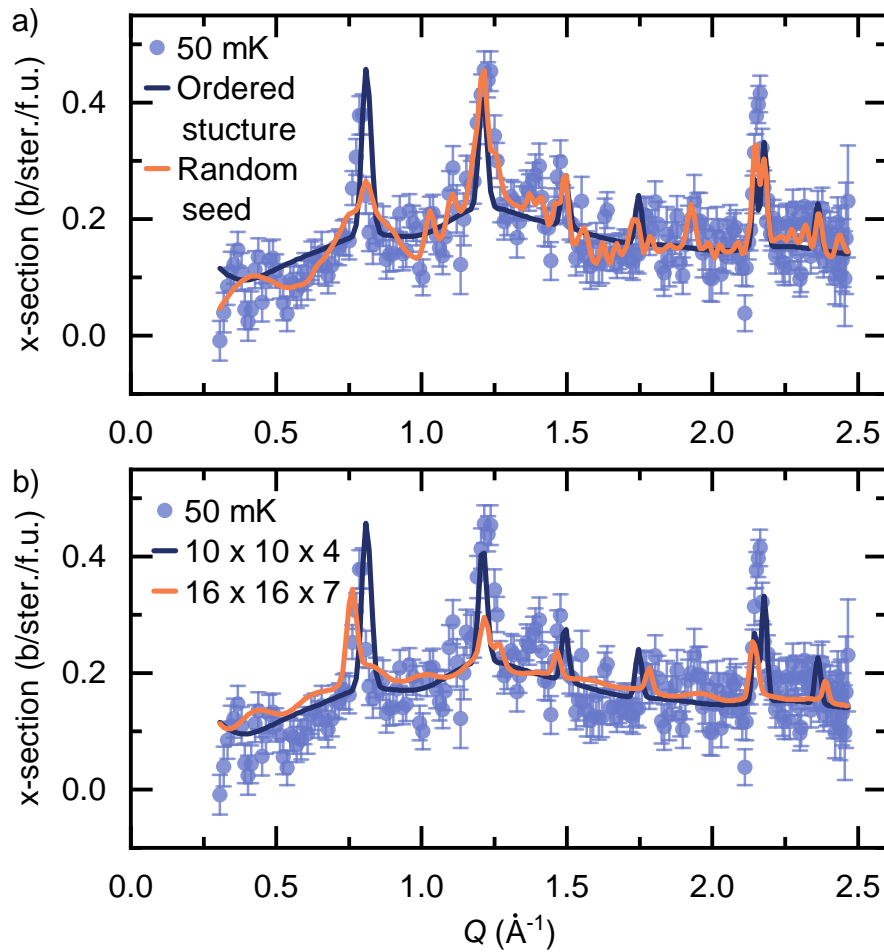


Figure 3.14: SPINVERT + Bragg fits with different conditions. a) Comparison of starting from the long-ranged ordered magnetic structure (dark blue) and a random configuration of moments (orange). b) Comparison of different commensurate \mathbf{k} approximations, $10 \times 10 \times 4$ for $\mathbf{k} = (0.4, \pm 0.4, 0)$ (dark blue) and $16 \times 16 \times 7$ for $\mathbf{k} = (0.375, \pm 0.375, 0)$ (orange).

starting from a random seed particularly fails to pick up the first magnetic Bragg peak at $Q = 0.8 \text{ \AA}^{-1}$. Furthermore, the fit is very noisy around the diffuse regions, this is likely due to removing the cost function associated with the long-ranged structure, leaving the fit less constrained and therefore accepting more bad moves. Few examples of **SPINVERT + Bragg** analysis exist so the fact that it fails to converge on the correct long-range magnetic structure may be due to the complexity of the helix.

Additionally, the choice of commensurate approximation is also an important consideration as highlighted in Fig. 3.14b). Changing the propagation vector, even slightly, can cause a large shift in the peak positions and relative intensities. The $16 \times 16 \times 7$ supercell is constructed from the $\mathbf{k} = (0.375, \pm 0.375, 0)$ approximation and the intensity of the peaks is worse in all cases, particularly around the central peak at $Q = 1.2 \text{ \AA}^{-1}$ which has almost complete destructive interference. This is not too dissimilar from a Rietveld simulation of this propagation vector against the data. Reducing the supercell to $8 \times 8 \times 3$ unit cells, only gives $\sim 10 \text{ \AA}$ radial range for calculating correlations which is not sufficient to get a reliable estimate of how the correlations behave.

Chapter Four

Local Chemical and Magnetic Order in the Two-Dimensional Spin Glass,

$\text{Mn}_{0.5}\text{Fe}_{0.5}\text{PS}_3$

4.1 Introduction

The pursuit of two-dimensional materials continues to fascinate the scientific community due to the wide range of potential applications lower dimensional structures open up, from nanocatalysis to spintronics [211–215]. The discovery of the most famous low-dimensional material, graphene, was particularly captivating as upon exfoliation an astonishing amount of new physics existed on its two-dimensional honeycomb layers [216–220]. Subsequent explorations into other materials that may be exfoliated down to a monolayer followed [221]. Whilst many researchers extensively studied their materials chemical and electronic properties, examples of two-dimensional magnetic materials remained relatively scarce [222, 223]. This may be due to the fact that until very recently, the Mermin-Wagner theorem suggested that magnetism could not exist in two-dimensional systems in a conventional sense [48–51]. However, this appears to be a missed opportunity, as there is now evidence that a huge array

of exotic magnetism can exist in low-dimensional compounds [221]. In certain cases, combining these low-dimensional materials with external stimuli, for example the application of pressure, has the potential to form unconventional magnetic states of matter that are rarely encountered in their bulk counterparts [57, 224, 225]. One particularly interesting family of materials with a chemical structure similar to graphene, that may also be magnetic, are the layered metal thiophosphates, MPS_3 .

The MPS_3 compounds adopt a monoclinic $C2/m$ structure in which the transition-metal ions (M) are arranged in honeycomb networks within the ab -plane (Fig. 4.1a)) [226, 227]. The transition-metal ions are octahedrally co-ordinated by sulphur atoms with a pair of phosphorous atoms found at the centre of each honeycomb ring. Figure 4.1b) shows that these layers are weakly held together by van der Waals interactions and stacked in an ABC sequence, similar to the CdCl_2 structure [227]. Most MPS_3 compounds have well separated layers, with no cations occupying sites in the van der Waals gap, and for first row transition-metal ions a characteristic gap of 3.24 Å between the layers [226]. One of the most compelling reasons to study the MPS_3 family is the flexibility of the chemical structure, and in turn

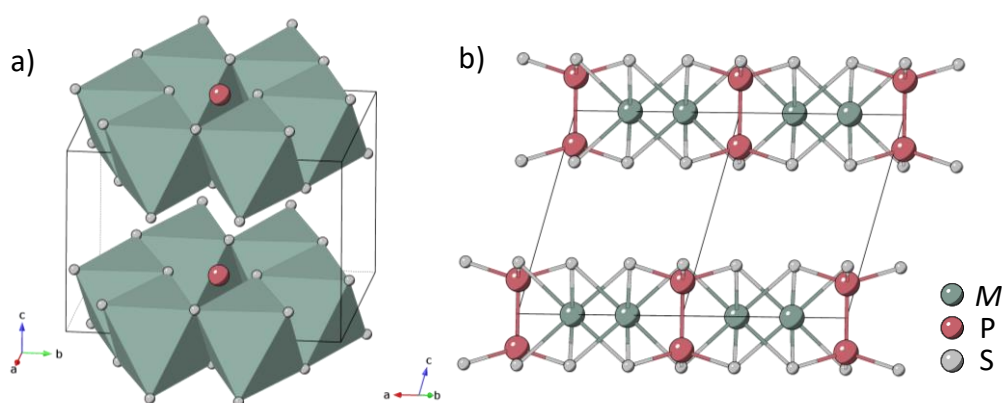


Figure 4.1: The MPS_3 compounds adopt a monoclinic $C2/m$ structure. a) Edge sharing octahedra of transition-metal ions form honeycomb rings in the ab -planes and are b) weakly bound by van der Waals interactions along the c -axis.

manipulation of their physical characteristics. Any transition-metal with a charge of +2 can be substituted into the honeycomb and the sulphur can be switched for other elements like selenium [55]. Substitution of various magnetic transition-metals have been shown to produce magnetic structures with very different ordering types and anisotropies [59, 228–230]. Additionally, since the layers are held together only by van der Waals interactions, there have been studies where the layers have been intercalated with Li for possible battery use [231, 232], or delaminated down to a single monolayer [233–235]. Because of this, the family has been likened to graphene, but with the additional benefit of retaining its magnetisation after delamination. Conversely, with the application of pressure, the structure undergoes an insulator-metal transition which has been found, in some instances, to produce high-temperature superconducting states. [57, 236, 237].

The magnetic character of two members of the MPS_3 family, MnPS_3 and FePS_3 , have been well studied previously [59, 229, 238, 239]. Both are quasi-two-dimensional antiferromagnets, with relatively high magnetic ordering temperatures ($\text{MnPS}_3, T_N = 78$ K, $\text{FePS}_3, T_N = 120$ K), but this is where the similarities stop. In MnPS_3 , all the nearest-neighbours are coupled antiferromagnetically within the ab -plane and ferromagnetically along the c -axis (Fig. 4.2a)). Whereas in FePS_3 , there are two ferromagnetic neighbours and one antiferromagnetic neighbour for every Fe^{2+} ion creating zigzag chains in the ab -plane, and the layers are coupled antiferromagnetically along the c -axis (Fig. 4.2b)). Therefore, MnPS_3 has a $\mathbf{k} = 0$ magnetic propagation vector, whereas FePS_3 has $\mathbf{k} = (0 \ 1 \ \frac{1}{2})$. Additionally, MnPS_3 is well modelled by a Heisenberg Hamiltonian with isotropic moments, whilst the moments in FePS_3 are more appropriately described as Ising-like and highly anisotropic.

Creating a solid-solution of MnPS_3 and FePS_3 , which have these distinct long-range ordered magnetic structures, therefore has the potential to generate a highly frustrated system. Specifically, the Hamiltonian determined from inelastic neutron scattering shows that assuming $J > 0$ is ferromagnetic, the first nearest-neighbour exchange interaction in MnPS_3 is antiferromagnetic, $J_1 = -0.77$ meV [56], and ferromagnetic in FePS_3 , $J_1 = 1.46$ meV [59]

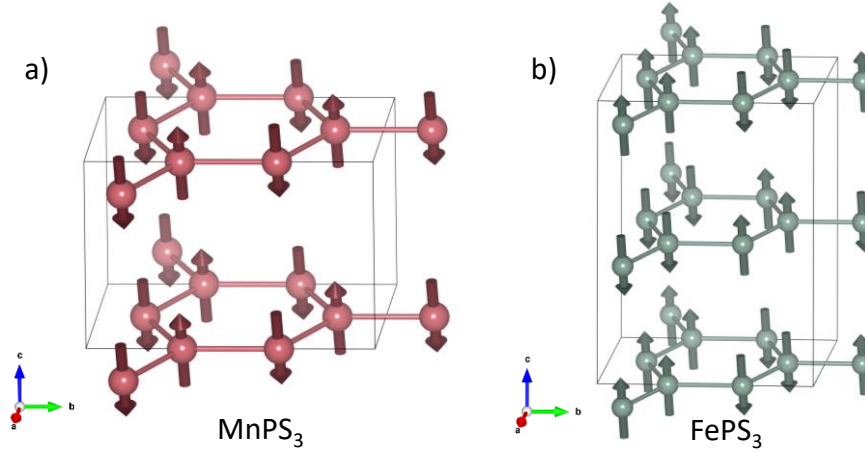


Figure 4.2: Long-range ordered magnetic structures of a) MnPS_3 where all nearest-neighbours are coupled antiferromagnetically in the ab -plane and ferromagnetically between the layers [229], and b) FePS_3 where each Fe^{2+} ion has two ferromagnetic neighbours and one antiferromagnetic neighbour in the ab -plane, but the moments are coupled antiferromagnetically between the planes [59]. In both cases, coupling between the planes is very weak compared to the direct and superexchange intraplanar interactions.

(Fig. 4.3a) and b)). The frustration may then be further compounded by the competition between spin and exchange anisotropies that exist between the two end members. Moreover, since the ionic charge and radius of Mn^{2+} and Fe^{2+} ions are similar, maximal compositional disorder between the two ions is expected to induce a spin glass phase [37]. Previous magnetisation and specific heat capacity measurements determined the phase diagram of the $\text{Mn}_{0.5}\text{Fe}_{0.5}\text{PS}_3$ series as shown in Fig. 4.3c) [240]. At either end of the series are the long-range ordered antiferromagnetic (AF) states as described earlier. Between $0.2 < x < 0.45$ and $0.6 < x < 0.8$ there is an intriguing re-entrant spin glass (RSG) phase. In conventional magnetic materials a paramagnetic state is usually observed at high temperatures, but in an RSG instead of being in a paramagnetic state these compounds have an ordered antiferromagnetic state at high temperatures, which upon cooling freeze into a disordered magnetic state akin to a spin glass. The spin glass (SG) phase exists between $0.45 < x < 0.6$, when the differences in the spin and exchange anisotropies are in greatest conflict. Through

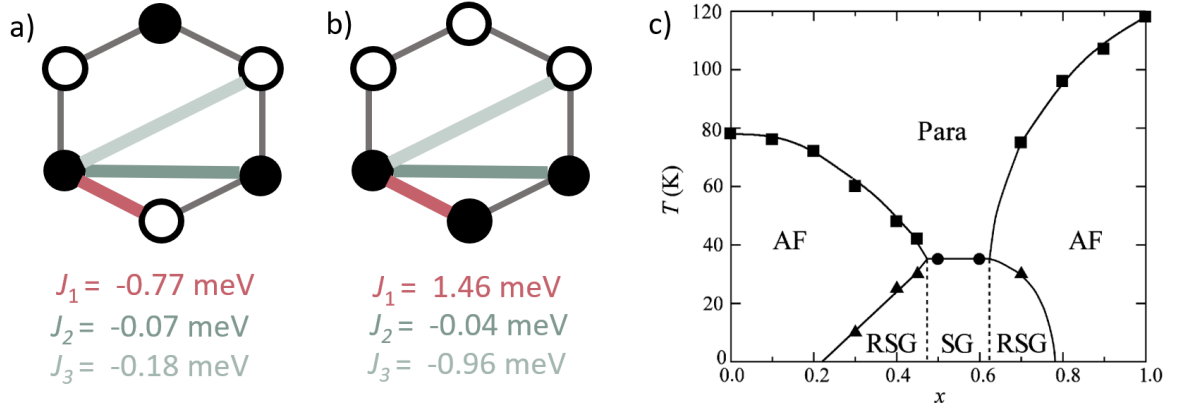


Figure 4.3: Nearest-neighbour exchange interactions making up the Hamiltonian for a) MnPS_3 and b) FePS_3 ($J > 0$ is ferromagnetic). c) Magnetic phase diagram for $\text{Mn}_x\text{Fe}_{1-x}\text{PS}_3$ where antiferromagnetic (AF), re-entrant spin glass (RSG), spin glass (SG) and paramagnetic (Para) phases have been determined [240].

these magnetisation measurements, the spin glass transition was confirmed at $T_g = 35 \text{ K}$. The other key ingredient in the spin glass—compositional disorder—has been verified using Mössbauer spectroscopy [241].

Concerning $\text{Mn}_{0.5}\text{Fe}_{0.5}\text{PS}_3$ however, there is still a lot to be understood about the proposed spin glass phase. For example, are the Mn^{2+} and Fe^{2+} ions completely randomly mixed within the honeycomb layers, or do they form a correlated short-range chemical order that impacts the magnetism? Furthermore, do the different ordering types of the parent compounds, MnPS_3 and FePS_3 , influence the magnetic behaviour of the mixed, $\text{Mn}_{0.5}\text{Fe}_{0.5}\text{PS}_3$ compound? These questions will be explored in this chapter through the combination of high-resolution neutron powder diffraction, magnetic susceptibility and diffuse neutron scattering studies. This work has been published in *Physical Review Materials* [242].

4.2 Experimental Methods

4.2.1 Synthesis

Samples of $\text{Mn}_{0.5}\text{Fe}_{0.5}\text{PS}_3$ were prepared by Dr. Suhan Son at the Centre for Quantum Materials at Seoul National University, Republic of Korea. Single crystals of $\text{Mn}_{0.5}\text{Fe}_{0.5}\text{PS}_3$ were grown via a three-step process to maximise the homogeneous mixing of manganese and iron constituents. Stoichiometric quantities of elemental powders - Fe (99.998 %, Alfa Aesar), Mn (99.95 %, Alfa Aesar), P (red phosphorous, 99.99 %, Sigma Aldrich) and S (99.998 %, Alfa Aesar) were ground under an argon atmosphere and sealed in quartz tubes, which were filled with a 10 mbar Ar gas pressure. Quartz tubes used in each step had an 18 mm inner diameter and were 100 mm in length. The sealed tubes were annealed at 500 °C for 2 days. The powder from this initial heating stage was then reground in an Ar glove box. The ground powder was sealed in a quartz tube as per the first synthesis step, and annealed at 600 °C for a further 2 days. Single crystals were grown from the powder via chemical vapour transport. The powder was reground and loaded into quartz tubes with an iodine powder flux agent (50 mg of I_2 per 1 g of reactants). The tubes were filled to $\sim 10^{-3}$ mbar vacuum using a molecular diffusion pump and sealed. The sealed tubes were placed in a two-zone furnace and heated to 730 °C/630 °C over 12 hours and held for 7 days before cooling to room temperature over 24 hours. The grown crystals formed shiny black flakes with typical dimensions, 1 cm \times 1 cm \times 50 μm .

The sample stoichiometry and quality was confirmed with energy dispersive X-ray (EDX) spectroscopy on a Bruker QUANTAX system combined with a scanning electron microscope (COXEM, EM-30) and powder X-ray diffraction. EDX results revealed the sample stoichiometry was 47(1) % and 53(2) % for Mn^{2+} and Fe^{2+} respectively. The quality of single-crystals was verified via X-ray Laue diffraction, using an Imaging Plate X-ray Diffraction (IP-XRD) Laue Camera (IPX Co. Ltd) which showed the high crystallinity

of the crystals and that they adopted the expected $C2/m$ structure.

4.2.2 Neutron Powder Diffraction

Constant wavelength neutron powder diffraction data were collected at room temperature on the high-resolution D2B [202] diffractometer at the Institut Laue-Langevin. The incident wavelength was $\lambda = 1.594 \text{ \AA}$, allowing the scattering to be measured over an angular range of $10 < 2\theta < 160^\circ$. Refinements of the chemical structure were completed using the **GSAS** [107] package. The powder used in these measurements was the powder produced from step two of the growth process. Raw data can be accessed via Ref [243].

4.2.3 Magnetometry

Magnetisation measurements of single crystal samples were conducted in MPMS3 and MPMS SQUID magnetometers, Quantum Design by Dr. Matthew Coak at Seoul National University. DC measurements were carried out in a 0.1 T applied magnetic field, in a ZFC and FC cycle over a temperature range of 2 K to 300 K. To avoid strain, the sample was not held in any epoxy or grease, and was instead held between sheets of plastic film. Raw data can be accessed via Ref [244].

4.2.4 Diffuse Scattering

Single-crystal samples of $\text{Mn}_{0.5}\text{Fe}_{0.5}\text{PS}_3$ were aligned in orientations parallel and perpendicular to the c^* -axis on the three-axis spectrometer IN3 at the Institut Laue-Langevin. Diffuse neutron scattering measurements were performed on powder and single-crystal samples using the polarised diffuse scattering diffractometer D7 [112] at the Institut Laue-Langevin. The incident neutron wavelength was $\lambda = 4.87 \text{ \AA}$, giving access to a reciprocal space range of

$0.15 < Q < 2.5 \text{ \AA}^{-1}$. Powder data were measured at the temperatures 1.5 K, 24 K, 35 K, 50 K, 150 K and 300 K. Single-crystal data were measured as a function of the sample rotation about the normal to the scattering plane at 1.5 K and 300 K. The samples were rotated over a total range of 210° . The technique of *xyz*-polarisation analysis was used to separate out the nuclear-coherent (NC), magnetic and nuclear-spin-incoherent(NSI) components of the scattering. Full calibration measurements were completed. Data were placed on an absolute intensity scale with units b/ster./f.u. The normalisation process was checked through Rietveld refinement of the NC cross-sections using Fullprof [105] and yielded an absolute scaling factor, $s = 0.877$. Magnetic diffuse scattering data were analysed using the programs SPINVERT, SPINCORREL and SCATTY [119, 120]. SPINVERT calculations were repeated 10 times to average out statistical noise. Raw data can be accessed via Ref [245].

4.3 Results and Discussion

4.3.1 Average Chemical Structure

Figure 4.4 shows the Rietveld refinement of the monoclinic $C2/m$ structure against high-resolution neutron powder diffraction (NPD) data of $\text{Mn}_{0.5}\text{Fe}_{0.5}\text{PS}_3$ collected at 300 K on the D2B instrument at the ILL. A summary of the refined parameters can be found in Table 4.1. A preferred orientation correction was included via the spherical harmonics method applied to the $(0\ 0\ l)$ plane. This is necessary as the layers are only weakly bound by van der Waals interactions and have a tendency to slide over each other which therefore makes producing an isotropic powder difficult. Refinement of the transition-metal site occupancies confirmed that the sample has the expected stoichiometry whereby the honeycomb network is comprised of an approximately equal amount of Mn^{2+} and Fe^{2+} ions. If a short-range chemical structure exists, diffuse scattering in the background of the NPD data will be present and will be clearly visible due to the excellent contrast of the neutron scattering lengths of Mn^{2+} and

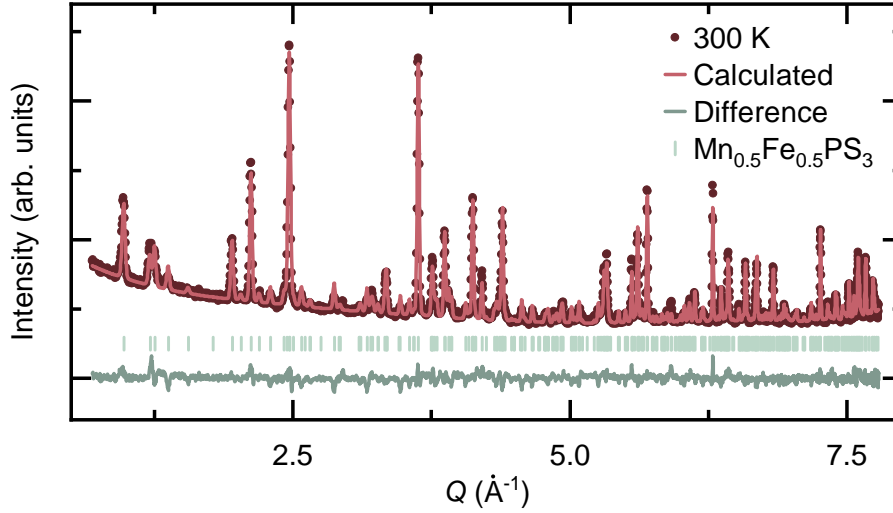


Figure 4.4: Rietveld refinement of the $C2/m$ structure to high-resolution NPD data collected on D2B at 300 K ($R_{\text{wp}} = 4.54\%$, $\chi^2 = 5.273$).

Atom	Site	x	y	z	Occupancy	U_{iso} (\AA^2)
Mn	$4g$	0	0.3354(9)	0	0.520(4)	0.022(2)
Fe	$4g$	0	0.3354(9)	0	0.480(4)	0.022(2)
P	$4i$	0.0542(8)	0	0.1619(5)	1.0	0.0188(7)
S1	$4i$	0.738(1)	0	0.2442(8)	1.0	0.0051(5)
S2	$8j$	0.2358(7)	0.1661(4)	0.2503(6)	1.0	0.0051(5)

Table 4.1: Refined chemical structure parameters for the $C2/m$ model fitted to NPD data collected at 300 K on D2B. Refined lattice parameters are $a = 6.0137(2)$ \AA , $b = 10.4174(2)$ \AA , $c = 6.7591(2)$ \AA and $\beta = 107.129(2)$ $^\circ$.

Fe^{2+} , $b_{\text{Mn}} = -3.73$ fm and $b_{\text{Fe}} = +9.45$ fm, respectively. But the background of the data is relatively flat and absent of any diffuse structure, which indicates there is a lack of short-range chemical ordering between the Mn^{2+} and Fe^{2+} ions, and therefore implies a completely random distribution of the magnetic ions throughout the magnetic structure.

Additionally, powder neutron scattering data were measured on D7 and are shown in

Fig. 4.6. The NC and NSI contributions to the scattering had no variation with temperature, an example is shown in Fig. 4.6a) which was collected at 1.5 K. The NSI is mostly flat, aside from at $Q = 1.25 \text{ \AA}^{-1}$ where there is a large nuclear Bragg peak, indicating that the separation has worked well. Similarly to the D2B data, the background of the NC contribution is flat which confirms the absence of any short-range chemical order of Mn^{2+} and Fe^{2+} ions within the honeycomb layers.

4.3.2 Magnetic Susceptibility

Figure 4.5 shows the single-crystal magnetic susceptibility data and reveals features indicative of spin glass behaviour [37]. Firstly, the measurement parallel to the c^* -axis shows a sharp cusp at 35 K, which corresponds with previous reports of the glass transition temperature, T_g [240, 246]. Secondly, below T_g there is splitting between the ZFC and FC measurements, which is a signature of spin glasses due to their irreversibility [37]. The data have been fit between 75 K and 300 K with the Curie-Weiss law, modified to include a temperature independent background term due to the inherent diamagnetic contribution of $\text{Mn}_{0.5}\text{Fe}_{0.5}\text{PS}_3$, $\chi_0 = -1.0631 \times 10^{-9} \text{ m}^3 \text{ mol}^{-1}$ [33]. A summary of the results from the Curie-Weiss fit can be found in Table 4.2. In both orientations, the Weiss constants, θ_{CW} , are large and negative indicating dominating antiferromagnetic interactions.

The effective moments, μ_{eff} , derived from the Curie constant, C , are slightly larger than the expected spin-only effective moment, $\mu_{\text{eff}} = 5.43 \mu_{\text{B}}$, assuming an average $S = 2.25$

Orientation	θ_{CW} (K)	$C \times 10^{-5}$ ($\text{m}^3 \text{ K mol}^{-1}$)	μ_{eff} ($\mu_{\text{B}}/\text{f.u.}$)
Parallel	-105(4)	6.5(1)	6.43(1)
Perpendicular	-267(4)	5.29(5)	5.80(3)

Table 4.2: Results from the Curie-Weiss fit of single-crystal $\text{Mn}_{0.5}\text{Fe}_{0.5}\text{PS}_3$ susceptibility data in orientations parallel and perpendicular to the c^* -axis.

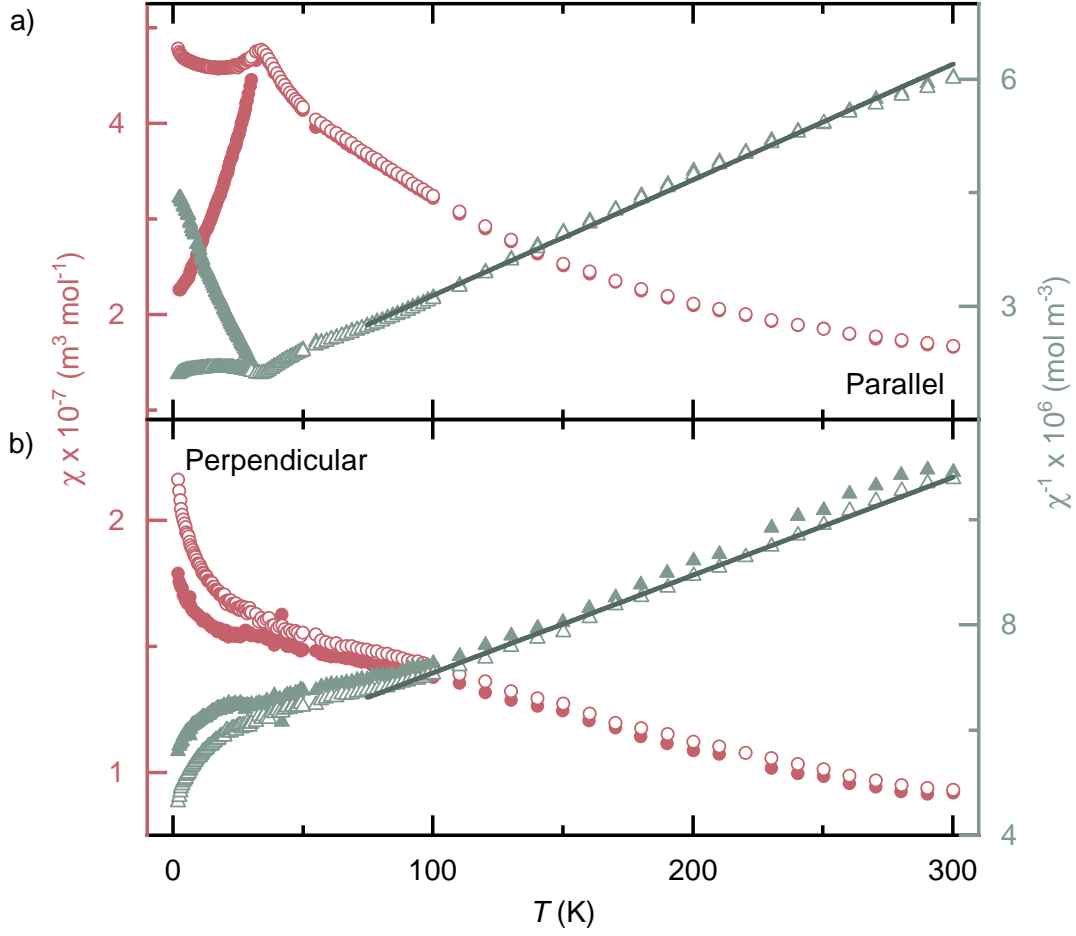


Figure 4.5: DC single-crystal magnetic susceptibility, χ (pink circles) and its inverse, χ^{-1} (green triangles) for $\text{Mn}_{0.5}\text{Fe}_{0.5}\text{PS}_3$ measured in a 0.1 T magnetic field. Single-crystals were aligned with respect to the applied field a) parallel and b) perpendicular to the c^* -axis. In both figures, closed and open markers represent ZFC and FC measurements, respectively. Curie-Weiss fits (solid green line) were conducted over a range of 75 to 300 K on the ZFC measurement.

from the mixture of Mn^{2+} and Fe^{2+} ions. Although previous magnetic susceptibility studies of MnPS_3 have been well modelled by an effective spin-only moment, the high-spin state of Fe^{2+} ions results in a sizeable spin-orbit contribution, seen in both magnetisation [247] and neutron [59] studies of FePS_3 . The large difference in the measured susceptibility when the field is applied in different orientations indicates that $\text{Mn}_{0.5}\text{Fe}_{0.5}\text{PS}_3$ is highly anisotropic, similar

to the measured magnetic susceptibility of FePS_3 , which has pronounced Ising anisotropy parallel to the c^* -axis.

4.3.3 Magnetic Diffuse Scattering

4.3.3.1 Powder Data Analysis

The time-equal magnetic contributions to the scattering measured on D7 are shown in Fig. 4.6b) and have been vertically shifted by 1.25 b/ster./f.u. for clarity. Below 50 K, there are a mixture of broad and sharp features which are reminiscent of the parent compounds, MnPS_3 and FePS_3 . For instance, the broad feature centred around $Q = 0.6 \text{ \AA}^{-1}$ is similar to powder neutron diffraction measurements observed in FePS_3 [58, 248]. The magnitude of this feature has little variation below 50 K, and therefore suggests that FePS_3 -type correlations are more or less fully developed above T_g . In contrast, the sharp peak at $Q = 1.2 \text{ \AA}^{-1}$ is continually evolving with temperature and most similar to studies of MnPS_3 [249]. This suggests that MnPS_3 -type correlations are still developing below T_g . The diffuse structure is lost at high-temperatures, $\geq 150 \text{ K}$, above which point the data follow a magnetic form factor squared Q -dependence.

Data above 150 K have been fit with an analytical approximation of a magnetic form factor (Eq. 1.13) [206]. Since the magnetic form factors of Mn^{2+} and Fe^{2+} are roughly equivalent, only the Mn^{2+} form factor has been used in this analysis. This function compares with the data reasonably well, however, the associated paramagnetic moment at $Q = 0 \text{ \AA}^{-1}$, $\mu_{\text{eff}} = 4.45 \mu_B$, is a little low when compared with the expected $\mu_{\text{eff}} = 5.43 \mu_B$. This can occur when some of the magnetic scattering is outside the integration window of D7, which in this case, could be attributed to persistent critical fluctuations that extend beyond 20 meV, similar to those found in FePS_3 [250]. From the Curie-Weiss analysis on the single crystal, and subsequent determination of the Weiss constants, θ_{CW} , it is expected that the sample

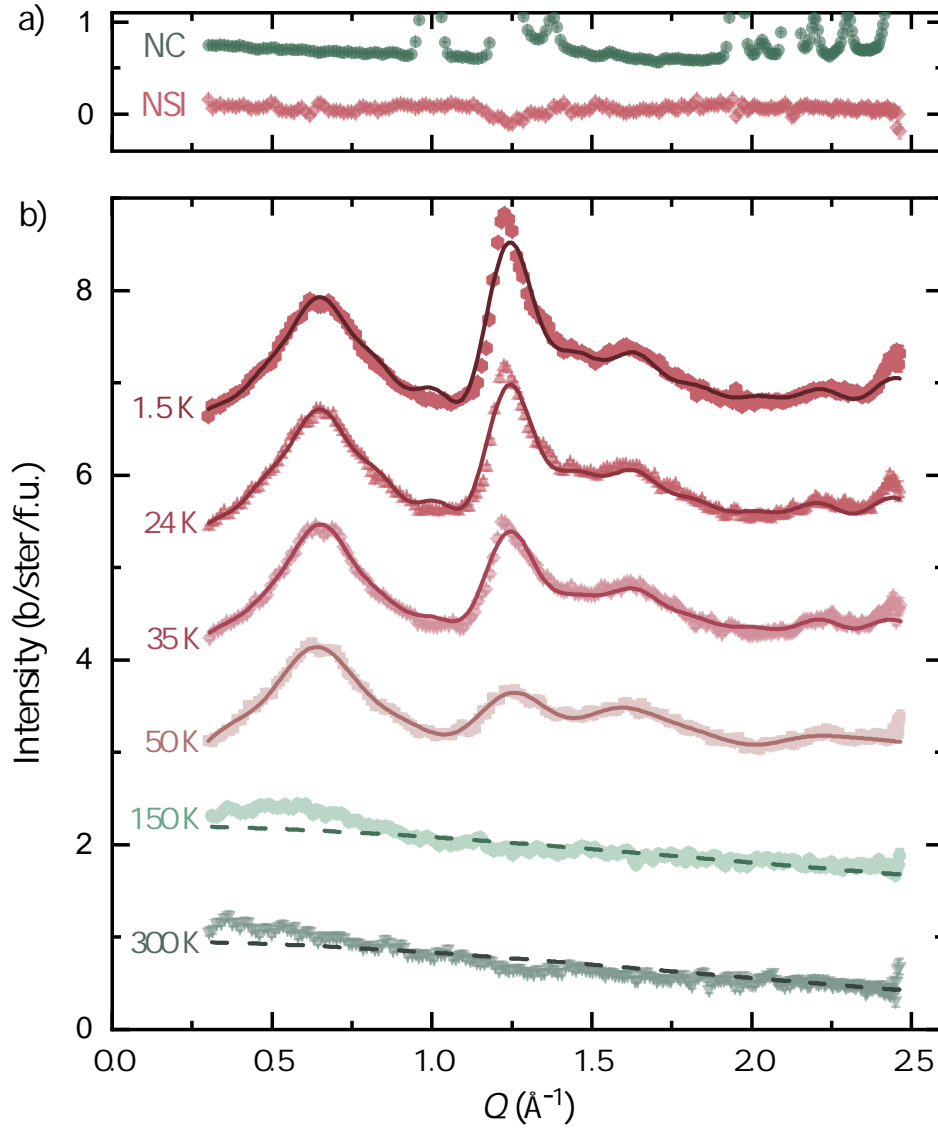


Figure 4.6: Experimental powder neutron scattering data from D7. a) NC and NSI contributions measured at 1.5 K. b) Magnetic diffuse scattering contributions. Fits produced from a RMC SPINVERT calculation assuming moments lie along the c^* -axis are shown by the solid lines and a calculation of the paramagnetic form factor of Mn^{2+} ions is shown by the dashed line. Magnetic data have been vertically shifted by 1.25 b/ster./f.u. for clarity.

be in its paramagnetic regime at 300 K. However, it is apparent that the data at low Q do not exclusively have a form factor squared Q -dependence. This reflects that there are still short-range correlations present within the system at 300 K.

Data below 50 K were fit using SPINVERT and are shown in Fig. 4.6b) by the solid lines. A supercell of $12 \times 12 \times 12$ unit cells was constructed with the moments constrained to lie either parallel or antiparallel to the c^* -axis. The assumption that moments lie along the c^* -axis is supported by the anisotropy in the paramagnetic susceptibility and the fact that the orientation of ordered moments in the parent compounds align approximately along the c^* -axis. Specifically in MnPS_3 the moments are canted 7° from the c^* -axis, whereas in FePS_3 ordered moments lie directly along the c^* -axis [229, 251]. The SPINVERT fits have good agreement with the data and capture the features well. The simplicity of this model is particularly appealing, as allowing moments more rotational degrees of freedom did not reproduce the data as well and larger boxes began to fit the statistical noise (Chapter 1, Fig. 1.11). There are some small anomalies to the fit, such as the small peak emerging at $Q = 0.9 \text{ \AA}^{-1}$, and that the intensity of the sharp peak at $Q = 1.2 \text{ \AA}^{-1}$ is lower than the measured value. However the derived effective moment from SPINVERT, $\mu_{\text{eff}} = 5.23(8) \mu_{\text{B}}$, with $S = 2.15(4)$ is in good agreement with the expected moment, $\mu_{\text{eff}} = 5.43 \mu_{\text{B}}$ from $S = 2.25$ (Eq. 1.21). Most convincingly, the quality of the later reconstruction of single-crystal data indicates that this model is representative of the magnetic diffuse structure of $\text{Mn}_{0.5}\text{Fe}_{0.5}\text{PS}_3$.

The feature at $Q = 1.2 \text{ \AA}^{-1}$ is particularly interesting, in part because it has a very defined and asymmetric line shape. Such a feature is often observed in two-dimensional materials because the two-dimensional layers in real space would extend out in reciprocal space as Bragg rods, but disorder, originating from stacking faults causes a diffuse tail on the other side. The same principle can be applied to magnetic structures, and a characteristic

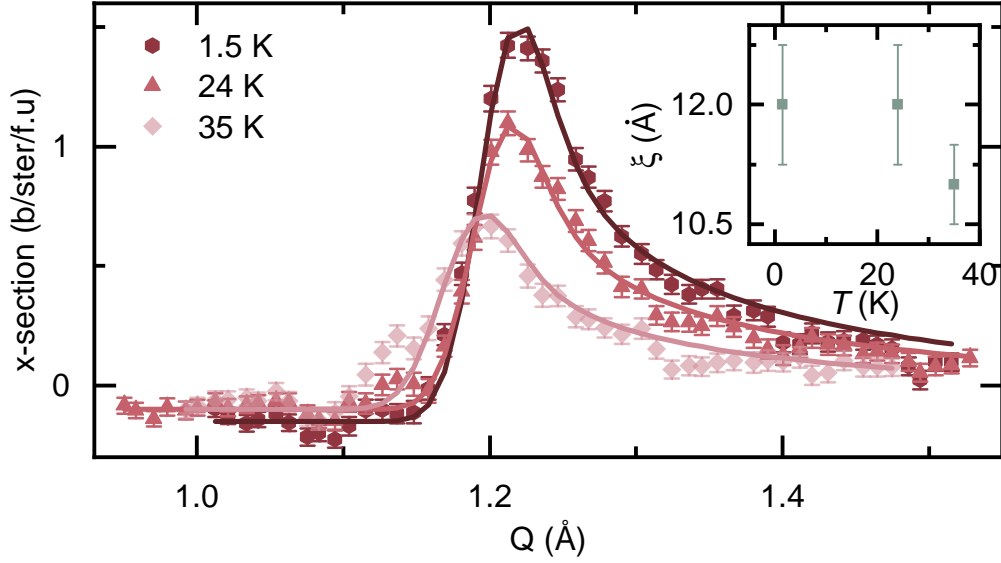


Figure 4.7: Warren function analysis for $T \leq 35$ K, where the peak has been isolated by subtracting the diffuse scattering at 50 K from each temperature. This asymmetric lineshape is synonymous with two-dimensional correlations. The inset summarises the two-dimensional correlation length, ξ , which is temperature-independent within error.

lineshape for modelling these asymmetric features is a Warren function (Eq. 4.1) [103].

$$P(Q) = k_{\text{W}} m \frac{F_{hk}^2 \left[1 - 2 \left(\frac{\lambda Q}{4\pi} \right)^2 + 2 \left(\frac{\lambda Q}{4\pi} \right)^4 \right]}{\left(\frac{\lambda Q}{4\pi} \right)^{3/2}} \times \left(\frac{\xi}{\lambda \sqrt{2}} \right)^{1/2} F(a) [f(Q)]^2 \quad (4.1)$$

$$\text{where} \quad F(a) = \int_0^{10} \exp[-(x^2 - a)^2] dx \quad a = \frac{\xi \sqrt{\pi}}{2\pi} (Q - Q_0)$$

where k_{W} is a scaling constant, m is the multiplicity of the reflection, F_{hk}^2 is the two-dimensional structure factor for the array ($kmF_{hk}^2 = \text{Amplitude}$), λ is the neutron wavelength, ξ is the spin correlation length, $f(Q)$ is the magnetic form factor for Mn^{2+} and Q_0 is the peak centre. Figure 4.6b) reveals that the underlying diffuse scattering has little variation between 50 K and 1.5 K. Therefore, to isolate the asymmetric feature, the 50 K data were subtracted from each temperature, and the data fit with a Warren Function in MATLAB. Fits are shown in Fig. 4.7 for 1.5 K, 24 K and 35 K, which have excellent agreement with

Temperature (K)	ξ (Å)	Q_0 (Å ⁻¹)	Amplitude	Background
1.5	12(1)	1.205(2)	0.0125(2)	-0.15(2)
24	12(1)	1.200(3)	0.009(1)	-0.10(1)
35	11(1)	1.180(2)	0.006(1)	-0.10(1)

Table 4.3: Fitted parameters from Warren function analysis of the sharp peak. Amplitude = kmF_{hk}^2 and the background was assumed to be flat.

the data. This suggests that the magnetic structure is two-dimensional, but also contains prominent compositional and positional disorder, which is expected due to the glassy nature of $\text{Mn}_{0.5}\text{Fe}_{0.5}\text{PS}_3$. A summary of the fit parameters can be found in Table 4.3. The most important result from the fit is the correlation length, ξ , as this can be physically related to the distance over which correlated short-range order acts between moments in the system. Calculated ξ values are summarised in the inset of Fig. 4.7, and are temperature independent within error below T_g .

4.3.3.2 Single-Crystal Data Analysis

Figure 4.8 shows the magnetic components of single-crystal data from D7 at 1.5 K in two orientations. Figure 4.8a) reveals rod-like scattering when the moments are parallel to the c^* -axis, which corresponds to the M_y component of the data. These observations coincide with the main feature in the low-temperature powder data, the sharp peak at $Q = 1.2 \text{ \AA}^{-1}$. Both of these features are synonymous with two-dimensional structures and thus reflect the two-dimensional nature of the magnetic structure of $\text{Mn}_{0.5}\text{Fe}_{0.5}\text{PS}_3$. When the c^* -axis is normal to the scattering plane (M_z component, moments are normal to the scattering plane), as in Fig. 4.8b), there is strong magnetic intensity, approximately 60° apart, which correspond to the expected magnetic Bragg peak positions of ordered MnPS_3 [229]. Additional magnetic Bragg peaks are observed at low temperatures, with the same sixfold rotation but their intensity is weaker. Reconstructions of single-crystal diffraction patterns were calculated via fast Fourier

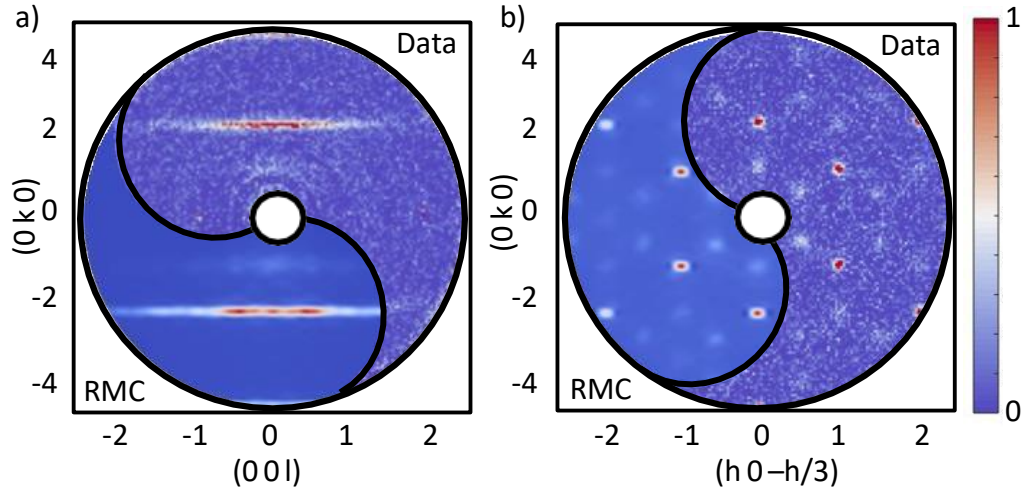


Figure 4.8: Magnetic component of single-crystal neutron scattering data measured at 1.5 K compared against the RMC SPINVERT model. a) M_y component show data in the $(0 k l)$ plane and reveal rod-like structures that reflect the two-dimensionality of $\text{Mn}_{0.5}\text{Fe}_{0.5}\text{PS}_3$. b) M_z component show data in the $(h k \frac{-h}{3})$ plane, which is orthogonal to the plane in part a), where strong magnetic intensity is observed at expected magnetic Bragg positions for MnPS_3 . The intensity of these data have been normalised to comparable intensities as given by the colour bar.

transforms from fits of the experimental powder data using SCATTY. A comparison between the experimental data and the scattering predicted from the RMC SPINVERT analysis is shown in Fig. 4.8. The excellent agreement confirms the model used in fitting the powder data will provide a reliable estimate of the spin correlations for $\text{Mn}_{0.5}\text{Fe}_{0.5}\text{PS}_3$.

4.3.4 Spin Correlations

Figure 4.9 shows the radial spin-spin correlation function, $\langle \mathbf{S}(0) \cdot \mathbf{S}(r) \rangle$, calculated by SPIN-CORREL at 1.5 K for $\text{Mn}_{0.5}\text{Fe}_{0.5}\text{PS}_3$. Correlations have been split to show those that act within and between the honeycomb planes by the closed and open markers, respectively. As is expected for a two-dimensional system, the intraplanar correlations are much stronger

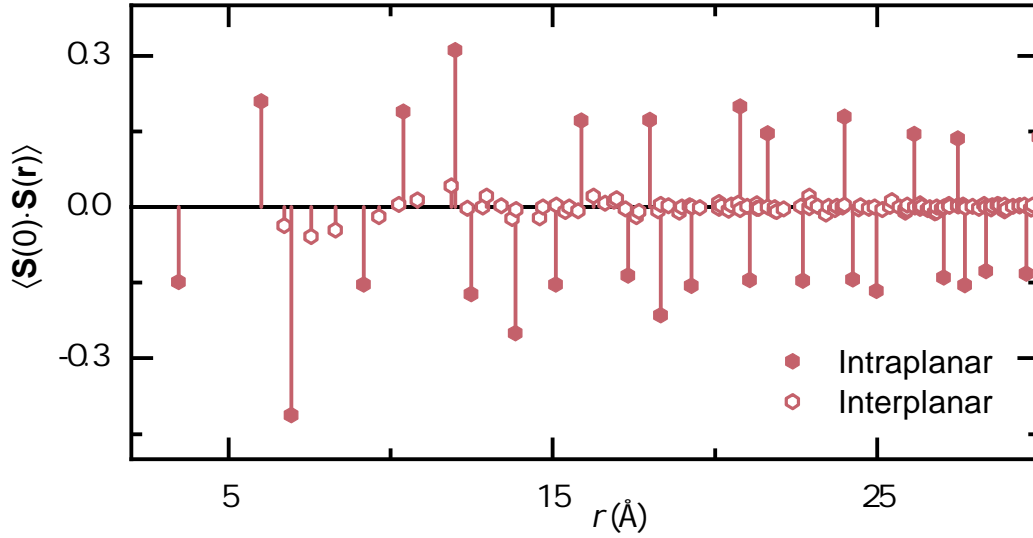


Figure 4.9: Radial spin-spin correlations, $\langle \mathbf{S}(0) \cdot \mathbf{S}(r) \rangle$ as a function on interatomic distance, r , calculated by SPINCORREL at 1.5 K. Closed and open markers represent correlations within and between honeycomb planes, respectively.

than the interplanar correlations. However, Fig. 4.10a) reveals that by taking the magnitude, $|\langle \mathbf{S}(0) \cdot \mathbf{S}(r) \rangle|$, of the intraplanar correlations there are two distinct trends. Firstly, the correlations shown by the pink hexagonal markers, decrease in magnitude as a function of interatomic distance, r . Secondly, the correlations shown by the green triangular markers, are roughly constant as a function of increasing r . These two groups of correlations were therefore modelled independently. The green points were averaged out to give a constant, $|\langle \mathbf{S}(0) \cdot \mathbf{S}(r) \rangle| = A$, and the pink markers were fit with an exponential function, $|\langle \mathbf{S}(0) \cdot \mathbf{S}(r) \rangle| = \exp(-\frac{r}{\xi}) + A$, where ξ is the spin correlation length and A was fixed from analysis of the green points. An example fit of these models are shown in Fig. 4.10a) at 1.5 K. Intraplanar correlations are temperature-dependent, and the fit values of ξ and A are shown as a function of temperature in Figs. 4.10b) and c), respectively.

In contrast, interplanar correlations were found to be temperature-independent and very weak in magnitude. Figure 4.10d) shows the magnitude of the correlations lying

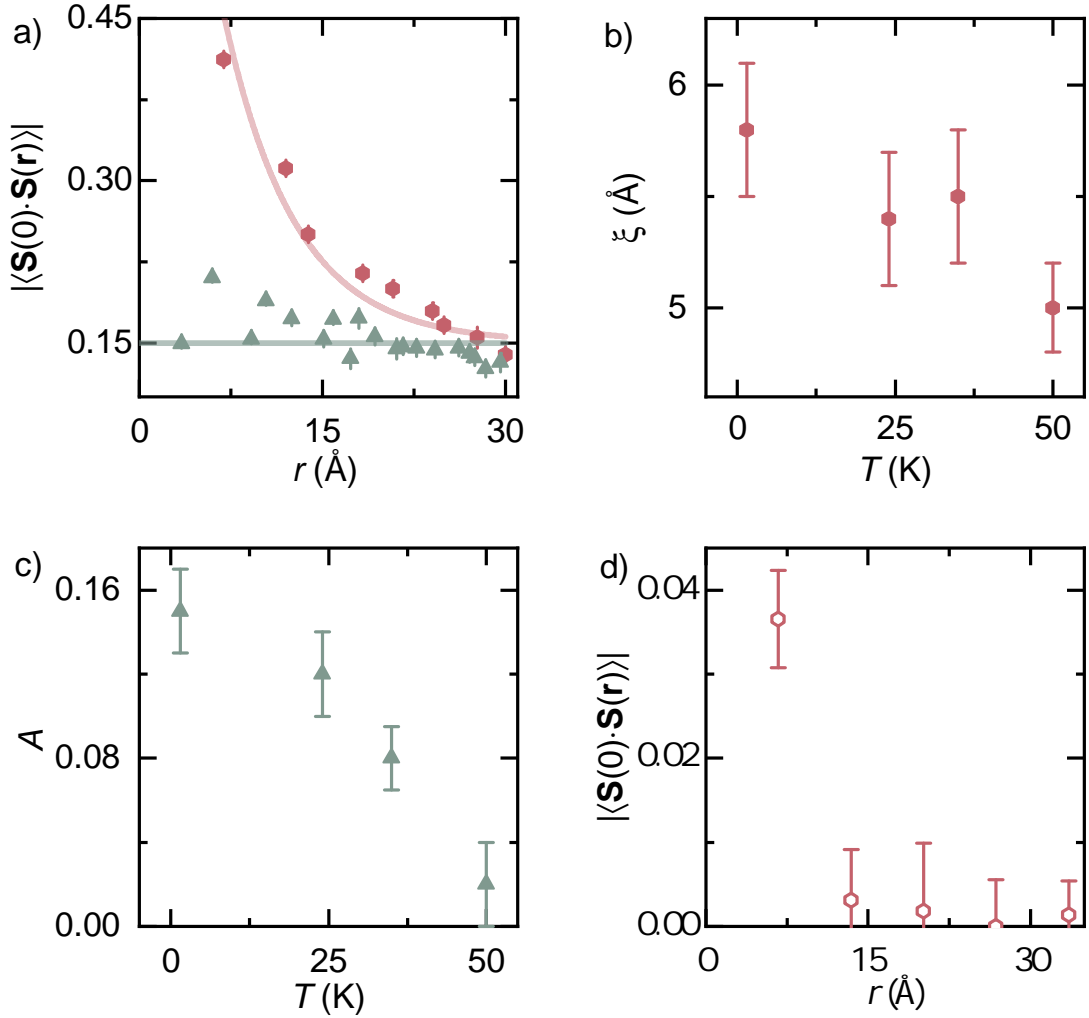


Figure 4.10: a) Magnitude of intraplanar correlations, $|\langle \mathbf{S}(0) \cdot \mathbf{S}(r) \rangle|$, at 1.5 K. Pink hexagon markers are correlations that have a decreasing exponential dependence with increasing r , whilst green triangle markers have linear behaviour over the calculated range. b) Correlation length, ξ , from the exponential fit is independent of temperature within error below T_g . c) Linear fits, where $|\langle \mathbf{S}(0) \cdot \mathbf{S}(r) \rangle| = A$, as a function of temperature fall to zero after T_g . d) Magnitude of interplanar correlations, $|\langle \mathbf{S}(0) \cdot \mathbf{S}(r) \rangle|$, lying closest to the c^* -axis at 1.5 K. Measurable intensity is only observed between the first set of adjacent planes.

closest to the c^* -axis, that is, the nearest-neighbour correlations acting between adjacent planes. Only the first correlation has any significant magnitude, and that is very weak at $|\langle \mathbf{S}(0) \cdot \mathbf{S}(r) \rangle| = 0.035(2)$. This weak interaction between the planes reflects the two-dimensional nature of $\text{Mn}_{0.5}\text{Fe}_{0.5}\text{PS}_3$.

4.3.5 Discussion

A physical explanation as to why there are two trends within the intraplanar correlations can be understood by considering the magnetic structures of the parent compounds, MnPS_3 and FePS_3 . In MnPS_3 , all nearest-neighbour exchange interactions within the ab -planes are antiferromagnetic [229], whereas in FePS_3 there are two ferromagnetic and one antiferromagnetic neighbour creating zigzag chains[59]. This is illustrated in Fig. 4.11a) and b), where open and closed circles represent spin up and spin down moment orientations, respectively. Despite the different magnetic structures there are some moment orientations that are common between the two structures, in which it can be assumed that the underlying correlation between the moments must be similar. These correlations will be known as satisfied. The other moment orientations are competing, and these moments therefore act as the source of frustration within the mixed $\text{Mn}_{0.5}\text{Fe}_{0.5}\text{PS}_3$ compound. Uncommon moment correlations will be known as unsatisfied, because their behaviour cannot be predicted over a long length scale. Figure 4.11c) and d) shows the commonly orientated moments with the open and closed pink circles and the uncommon, frustrated moments with the striped green circles.

Each correlation outputted by SPINCORREL represents an average of all the correlations between the different moment pairs at one particular distance. For example, the nearest neighbour correlation at $r = 3.46 \text{ \AA}$, has three neighbours at an equivalent distance. Figure 4.11c) shows that from an arbitrary point, one is between a pair of moments that are common between the parent structures and two are between common and frustrated moments. These interactions can be described as satisfied (green) and unsatisfied (red). If any neighbour

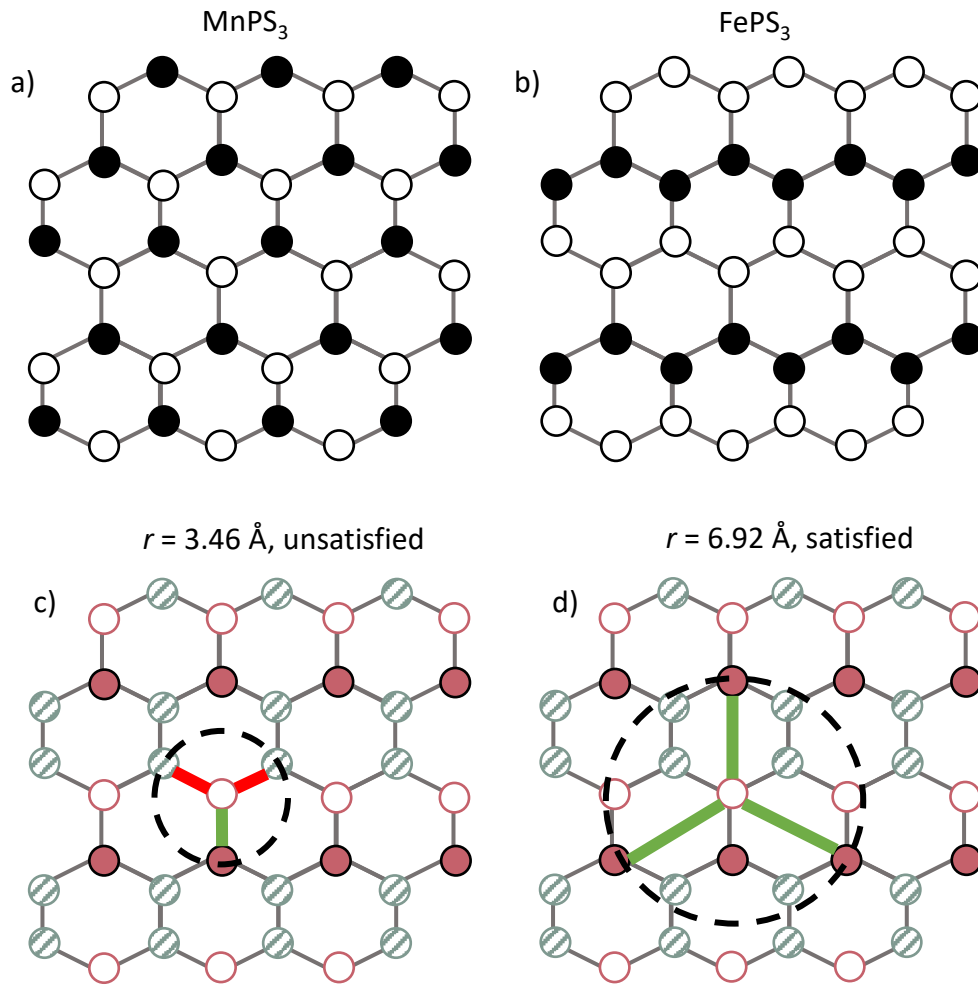


Figure 4.11: Intraplanar magnetic structures of a) MnPS_3 and b) FePS_3 which have conventional long-ranged antiferromagnetic structures. Spin up and spin down moments are shown by open and closed circles, respectively. c) and d) Common and uncommon moment orientations between the parent structures are shown by solid pink and striped green circles, respectively. Red and green lines represent interactions between a pair of moment correlations that are unsatisfied and satisfied, respectively. A correlation is in the unsatisfied group if it has at least one red interaction. c) The first nearest-neighbour correlation at $r = 3.46 \text{ \AA}$ has one satisfied interaction and two unsatisfied interactions, therefore, $r = 3.46 \text{ \AA}$ is an unsatisfied correlation. d) The third nearest-neighbour correlation at $r = 6.92 \text{ \AA}$ acts between moment pairs that are all satisfied, therefore $r = 6.92 \text{ \AA}$ is a satisfied correlation.

at an equivalent distance has an unsatisfied interaction then it has been assigned to the unsatisfied correlation group, regardless of the number of satisfied interactions that distance may have. Therefore, the correlation at $r = 3.46 \text{ \AA}$ has been assigned to the unsatisfied group. In contrast, Fig. 4.11d) shows the third nearest-neighbour correlation, $r = 6.92 \text{ \AA}$ which also acts between three moment pairs. However, all of these interactions are satisfied and therefore, forms the second group of correlations. All correlations can be considered like this, and have been divided into the two groups. Quite remarkably the groups have perfect agreement with the trends observed in Fig. 4.10a), and thus gives a physical interpretation to the fits.

Figure 4.10b) reveals that the average correlation length, ξ , between satisfied correlations is constant within error below T_g . This is perhaps not surprising given that the magnetic ordering temperatures of the parent compounds are much higher than T_g . This is also in agreement with the Warren function analysis in Fig. 4.7, though the magnitude of the correlation length is slightly different. The average correlation length from the SPINCORREL analysis is relatively small, $\xi = 5.5(6) \text{ \AA}$, stretching not even one unit cell across in the honeycomb. This means that ordered correlations can only be considered between the closest neighbouring ions, and no longer-range magnetic order goes onto develop across the honeycomb. Whereas, in Fig. 4.10c) the dropoff of A is more pronounced with increasing temperature, reducing to zero above T_g . Therefore, the unsatisfied correlations give rise to the glassy behaviour of $\text{Mn}_{0.5}\text{Fe}_{0.5}\text{PS}_3$.

To summarise, correlations can be divided into three groups:

1. Interplanar correlations are very weak, which verifies the two-dimensional character of $\text{Mn}_{0.5}\text{Fe}_{0.5}\text{PS}_3$.
2. Satisfied intraplanar correlations act between moments that have a common moment orientation between the parent compounds. These correlations decrease exponentially

with increasing interatomic distance, which allows for the extraction of the correlation length, ξ which is temperature-independent and persists below the glass temperature.

3. Unsatisfied intraplanar correlations act between moments that have a different moment orientation between the parent compounds. These correlations are approximately constant with interatomic distance and are temperature-dependent. These correlations can be interpreted as being responsible for the glassy behaviour in $\text{Mn}_{0.5}\text{Fe}_{0.5}\text{PS}_3$.

4.4 Conclusions and Outlook

The MPS_3 compounds are an exciting family of two-dimensional materials, which have great chemical and physical flexibility. This chapter explored the chemical and magnetic short-range correlations of one member, the spin glass $\text{Mn}_{0.5}\text{Fe}_{0.5}\text{PS}_3$, using high-resolution neutron powder diffraction, diffuse neutron scattering and magnetometry measurements. The key conclusions from this chapter are summarised as follows:

- There is no short- or long-range chemical order present within the honeycomb. It was expected that the Mn^{2+} and Fe^{2+} ions would mix due to the similarity in their ionic charge and radius. The excellent contrast in their neutron scattering lengths proved site mixing was completely randomised through the absence of any structured diffuse nuclear scattering that would otherwise indicate a short-ranged chemical structure.
- $\text{Mn}_{0.5}\text{Fe}_{0.5}\text{PS}_3$ has a spin glass ground state as confirmed through a characteristic cusp in magnetic susceptibility measurements at $T_g = 35$ K. Measurements parallel and perpendicular to the planes revealed that the moments are highly anisotropic.
- In the ground state there are short-range correlations that relate to the magnetic exchange interactions between moments in the parent compounds, MnPS_3 and FePS_3 .

- Single-crystal diffraction patterns were reconstructed from analysis of the powder data and excellently matched the measured single-crystal, confirming the Ising model was correct.
- $\text{Mn}_{0.5}\text{Fe}_{0.5}\text{PS}_3$ is a near-ideal example of a two-dimensional magnetic material through the observation of rod-like features in the single-crystal data, and very weak interplanar correlations.

Future work can target the determination of the exchange parameters and Hamiltonian for $\text{Mn}_{0.5}\text{Fe}_{0.5}\text{PS}_3$. A possible route to determine the exchange parameters is through a new open access software, **SPINTERACT**, which uses reaction-field approach methods to fit powder and single-crystal data [183]. This method would not produce an exact solution of the exchange parameters, but rather a mean, similar in principle to the calculation of the spin correlations presented earlier in this chapter. One potential drawback is that for now, **SPINTERACT** can only compute stoichiometric compounds with a single magnetic ion. $\text{Mn}_{0.5}\text{Fe}_{0.5}\text{PS}_3$ not only has two magnetic ions, but also, as verified in neutron diffraction measurements, the magnetic structure is completely absent of short-ranged chemical order which would make setting up a simulation difficult. An alternate route would be direct Monte Carlo simulations, where a supercell with a random distribution of magnetic ions could be created and the exact solution of exchange parameters found [252]. This is, however, computationally expensive. Despite these challenges, $\text{Mn}_{0.5}\text{Fe}_{0.5}\text{PS}_3$ could be an excellent test-bed for software development, and given the recent revival in interest for spin glass materials with the Nobel Prize in 2021 awarded to Parisi for his modelling of complex systems [253, 254], $\text{Mn}_{0.5}\text{Fe}_{0.5}\text{PS}_3$ could be a model system to compare these different computational approaches in a topical spin glass material.

Due to the distinct magnetic structures of the MPS_3 compounds, a direct extension to this work would be to explore other solid-solutions within the family [255–258]. $\text{Mn}_{0.5}\text{Fe}_{0.5}\text{PS}_3$ is unique in this sense, as it is the only member that has a clear spin glass phase, brought

on from the contrasting exchange anisotropies of the two end members. $\text{Fe}_{1-x}\text{Co}_x\text{PS}_3$ would be an interesting mix as this solid-solution would be anisotropically frustrated— FePS_3 has Ising moments pointing directly along the c -axis [59] whereas the moments in CoPS_3 predominantly point along the a -axis [230]—and therefore could create an interesting magnetic ground state.

The wider interest in the MPS_3 family is rooted in the similarity of the chemical structure to graphene [211, 213, 223]. Multiple studies have shown its possible to intercalate the layers, but unfortunately not enough Li can be contained for applications in batteries, for example [259, 260]. Additionally, joining an ever growing list of materials [221, 251], the layers of MPS_3 compounds can be delaminated, which can significantly change the physical properties compared to the bulk. However, this would not be a direct extension to this work as it would not be possible to perform neutron scattering studies on single monolayers. Finally, the ongoing pursuit of heterostructures, built from layers of graphene, delaminated MPS_3 and other van der Waals materials is an exciting opportunity to tune optical, electronic and magnetic properties for a variety of uses [213, 221, 251].

Chapter Five

Conclusions and Outlook

The aim of this thesis was to understand the interplay of correlated disorder on the ground state selection of quantum materials. This was achieved through synthesising inorganic materials, and performing detailed structural and magnetic characterisations from both an average and local perspective. In particular, I highlighted the technique of diffuse neutron scattering and the analysis of data through RMC refinements to achieve this aim.

All materials have some degree of disorder, whether that be chemical or magnetic in nature. When thinking about disorder, most people assume a completely random distribution of objects, with no particular relationship between them. Remarkably however, disorder in materials is rarely random but rather correlated on a local length scale. As has been shown in this thesis, the effect this correlated disorder has on quantum materials can be profound. This was particularly evident in the exploration of two powder samples of ZnV_2O_4 prepared via different methods in Chapter 2. Due to the complexities induced by the competing exchange interactions between magnetic moments, many quantum materials have very narrow energy landscapes of distinct phases that make them highly susceptible to the effects of disorder. ZnV_2O_4 is a prime example of such an effect, and learning to harness disorder via the synthetic route is going to be essential if quantum materials are to become functional. In the first instance, materials like ZnV_2O_4 which are highly synthesis dependent should be studied

across a series of individual samples to find out what sort of disorder is present, its origin, and whether or not this is the right sort of disorder for the desired function. If certain types of disorder can be linked to aspects in synthesis, then physical properties could be predicted from the laboratory, which would be a very powerful tool. In ZnV_2O_4 , I identified strain in the sintered sample as the likely factor that drives the structural distortion, and therefore, the evolution of the magnetic ground state. In other materials, like $\text{Yb}_2\text{Ti}_2\text{O}_7$, the energy landscape was most influenced by the sample stoichiometry, that could be targeted through tuning the firing atmosphere or starting reactants [39, 137, 138].

Each of these chapters included the analysis of diffuse powder neutron scattering data via RMC refinements. This is an important technique for understanding how short-range correlations behave, and subsequently, how disorder has influenced these local interactions. The exploration into the partially ordered, spiral spin liquid state of LiYbO_2 in Chapter 3 is at the very forefront of the analysis that can be performed on powder samples. I was able to simultaneously refine the magnetic Bragg peaks and diffuse scattering to recover the expected manifestation of the diffuse scattering in a spiral spin liquid. This is not just significant because it was the first experimental realisation of the spiral spin liquid in a distorted diamond structure, but also for the showcasing the possibilities of the method, with a complex incommensurate helical model. This is important, as materials with partial magnetic order, in which this analysis is necessary, are becoming more and more prevalent in the quantum materials field [261–263]. I hope through presenting this research that more examples will be published and the limits of these research methodologies will be pushed further.

Despite the progress on powder samples, I have also highlighted the importance of using single-crystals to confirm the results presented. In Chapter 4, measurements of a single-crystal of $\text{Mn}_{0.5}\text{Fe}_{0.5}\text{PS}_3$ confirmed the RMC simulations produced from powder samples, a model that may have been missed without the single-crystal. In the case of LiYbO_2 , a single-crystal would be hugely exciting, as the experimental hallmark of the spiral spin liquid—the

continuous diffuse ring of magnetic scattering—could be directly observed in the $(h\ h\ l)$ plane, and verify the powder simulations. Furthermore, the exchange interactions could be measured in inelastic neutron scattering, and the ordering plane of the helix in single-crystal diffraction. The ZnV_2O_4 study also requires a single-crystal, but here the case is more complex since the physical properties are so reliant on the individual synthesis and form of the material. Prior to the microwave sample, the only single-crystal of ZnV_2O_4 had strikingly different physical properties to all other samples [157]. With the microwave synthesis proving to be a viable alternative to produce high-quality and crystalline powder samples, the single-crystal study can be revisited and some of the measurements that were not clearly presented before can be repeated. This is an example of a material where the results of the powder studies may not be verified by a single-crystal, because the effects of correlated disorder are so fundamental to the physics, but by using a single-crystal the mechanisms that drive the physical behaviour could be elucidated.

In conclusion, this thesis has shown that the inevitable disorder that exists in real materials is not to be dismissed but rather celebrated. The search for quantum magnetic materials is often on the lookout for the perfect material, such as the perfect evasion of long-range magnetic order in the elusive quantum spin liquid model. But life is not perfect and made to fit a model. By embracing the disorder that is present in the real world, an abundance of information about materials can be understood, which is essential if these quantum magnetic materials are to become functional in the future.

Bibliography

- ¹W. L. Roth, “Magnetic Structures of MnO, FeO, CoO, and NiO”, [Physical Review](#) **110**, 1333–1341 (1958).
- ²S. V. Grigoriev, V. A. Dyadkin, E. V. Moskvina, D. Lamago, T. Wolf, H. Eckerlebe, and S. V. Maleyev, “Helical spin structure of $\text{Mn}_{1-y}\text{Fe}_y\text{Si}$ under a magnetic field: Small angle neutron diffraction study”, [Physical Review B](#) **79**, 144417 (2009).
- ³K. R. A. Ziebeck and P. J. Webster, “Helical magnetic order in Ni_2MnAl ”, [Journal of Physics F: Metal Physics](#) **5**, 1756 (1975).
- ⁴M. Ślaski, J. Leciejewicz, and A. Szytuła, “Magnetic ordering in HoRu_2Si_2 , HoRh_2Si_2 , TbRh_2Si_2 and TbIr_2Si_2 by neutron diffraction”, [Journal of Magnetism and Magnetic Materials](#) **39**, 268–274 (1983).
- ⁵M. M. Bordelon, C. Girod, F. Ronning, K. Rubi, N. Harrison, J. D. Thompson, C. dela Cruz, S. M. Thomas, E. D. Bauer, and P. F. S. Rosa, “Interwoven atypical quantum states in CeLiBi_2 ”, [Physical Review B](#) **106**, 214433 (2022).
- ⁶P. G. Radaelli and L. C. Chapon, “A neutron diffraction study of RMn_2O_5 multiferroics”, [Journal of Physics: Condensed Matter](#) **20**, 434213 (2008).
- ⁷S. J. R. Holt, C. Ritter, M. R. Lees, and G. Balakrishnan, “Investigation of the magnetic ground state of GaV_4S_8 using powder neutron diffraction”, [Journal of Physics: Condensed Matter](#) **33**, 255802 (2021).

- ⁸C. Broholm, R. J. Cava, S. A. Kivelson, D. G. Nocera, M. R. Norman, and T. Senthil, “Quantum spin liquids”, *Science* **367**, 6475 (2020).
- ⁹L. Balents, “Spin liquids in frustrated magnets”, *Nature* **464**, 199–200 (2010).
- ¹⁰B. J. Powell and R. H. McKenzie, “Quantum frustration in organic mott insulators: from spin liquids to unconventional superconductors”, *Reports on Progress in Physics* **74**, 056501 (2011).
- ¹¹J. K. Glasbrenner, I. I. Mazin, H. O. Jeschke, P. J. Hirschfeld, R. M. Fernandes, and R. Valenti, “Effect of magnetic frustration on nematicity and superconductivity in iron chalcogenides”, *Nature Physics* **11**, 953–958 (2015).
- ¹²T. Neupert, M. M. Denner, J.-X. Yin, R. Thomale, and M. Z. Hasas, “Charge order and superconductivity in kagome materials”, *Nature Physics* **18**, 137–143 (2022).
- ¹³W. G. Zheng, V. Balédent, E. Ressouche, V. Petricek, D. Bounoua, P. Bourges, Y. Sidis, A. Forget, D. Colson, and P. Foury-Leylekan, “Chiral magnetic structure of spin-ladder multiferroic BaFe_2Se_3 ”, *Physical Review B* **106**, 134429 (2022).
- ¹⁴G. Gong, J. Zhou, Y. Duan, H. Hu, Y. Wang, X. Cheng, and Y. Su, “Relaxor ferroelectric nature and magnetoelectric coupling of the one dimensional frustrated $\text{Ca}_3\text{CoMnO}_6$ ”, *Journal of Alloys and Compounds* **908**, 164587 (2022).
- ¹⁵A. Sahoo, D. Bhattacharya, M. Das, and P. Mandal, “Shape dependent multiferroic behavior in $\text{Bi}_2\text{Fe}_4\text{O}_9$ nanoparticles”, *Nanotechnology* **33**, 305702 (2022).
- ¹⁶E. Moreno-Pineda and W. Wernsdorfer, “Measuring molecular magnets for quantum technologies”, *Nature Reviews Physics* **3**, 654–659 (2021).
- ¹⁷R. Cava, N. de Leon, and W. Xie, “Introduction: Quantum Materials”, *Chemical Reviews* **121**, 2777–2779 (2021).
- ¹⁸C. Psaroudaki and C. Panagopoulos, “Skyrmion qubits: a new class of quantum logic elements based on nanoscale magnetization”, *Physical Review Letters* **127**, 067201 (2021).

-
- ¹⁹L. Clark and A. H. Abdeldaim, “Quantum Spin Liquids from a Materials Perspective”, [Annual Review of Materials Research](#) **51**, 495–519 (2021).
- ²⁰J. A. Paddison, M. Daum, Z. Dun, G. Ehlers, Y. Liu, M. B. Stone, H. Zhou, and M. Mourigal, “Continuous excitations of the triangular-lattice quantum spin liquid YbMgGaO_4 ”, [Nature Physics](#) **13**, 117–122 (2017).
- ²¹M. Baenitz, M. M. Piva, S. Luther, J. Sichelschmidt, K. M. Ranjith, H. Dawczak-Dębicki, M. O. Ajeesh, S.-J. Kim, G. Siemann, C. Bigi, P. Manuel, D. Khalyavin, D. A. Sokolov, P. Mokhtari, H. Zhang, H. Yasuoka, P. D. C. King, G. Vinai, V. Polewczyk, P. Torelli, J. Wosnitza, U. Burkhardt, B. Schmidt, H. Rosner, S. Wirth, H. Kühne, M. Nicklas, and M. Schmidt, “Planar triangular $S = \frac{3}{2}$ magnet AgCrSe_2 : magnetic frustration, short range correlations, and field-tuned anisotropic cycloidal magnetic order”, [Physical Review B](#) **104**, 134410 (2021).
- ²²T. Kurumaji, T. Nakajima, M. Hirschberger, A. Kikkawa, Y. Yamasaki, H. Sagayama, H. Nakao, Y. Taguchi, T.-H. Arima, and Y. Tokura, “Skyrmion lattice with a giant topological hall effect in a frustrated triangular-lattice magnet”, [Science](#) **365**, 914–918 (2019).
- ²³M. A. de Vries, J. R. Stewart, P. P. Deen, J. O. Piatek, G. J. Nilsen, H. M. Rønnow, and A. Harrison, “Scale-free antiferromagnetic fluctuations in the $s = 1/2$ kagome antiferromagnet herbertsmithite”, [Physical Review Letters](#) **103**, 237201 (2009).
- ²⁴K. Tustain, G. J. Nilsen, C. Ritter, I. da Silva, and L. Clark, “Nuclear and magnetic structures of the frustrated quantum antiferromagnet barlowite, $\text{Cu}_4(\text{OH})_6\text{FBr}$ ”, [Physical Review Materials](#) **2**, 111405 (2018).
- ²⁵S. A. Ivko, K. Tustain, T. Dolling, A. Abdeldaim, O. H. J. Mustonen, P. Manuel, C. Wang, H. Luetkens, and L. Clark, “Uncovering the $S = \frac{1}{2}$ kagome ferromagnet within a family of metal–organic frameworks”, [Chemistry of Materials](#) **34**, 5409–5421 (2022).

- ²⁶K. Wierschem, S. S. Sunku, T. Kong, T. Ito, P. C. Canfield, C. Panagopoulos, and P. Sengupta, “Origin of modulated phases and magnetic hysteresis in TmB_4 ”, [Physical Review B](#) **92**, 214433 (2015).
- ²⁷H. Chen, A. S. Manvell, M. Kubus, M. A. Dunstan, G. Lorusso, D. Gracia, M. S. B. Jørgensen, S. Kegnæs, F. Wilhelm, A. Rogalev, M. Evangelisti, and K. S. Pedersen, “Towards frustration in Eu(II) Archimedean tessellations”, [Chemical Communications](#) **59**, 1609–1612 (2023).
- ²⁸N. Tristan, J. Hemberger, A. Krimmel, H.-A. Krug von Nidda, V. Tsurkan, and A. Loidl, “Geometric frustration in the cubic spinels $M\text{Al}_2\text{O}_4$ ($M = \text{Co}, \text{Fe}, \text{and Mn}$)”, [Physical Review B](#) **72**, 174404 (2005).
- ²⁹L. Ge, J. Flynn, J. A. M. Paddison, M. B. Stone, S. Calder, M. A. Subramanian, A. P. Ramirez, and M. Mourigal, “Spin order and dynamics in the diamond-lattice heisenberg antiferromagnets CuRh_2O_4 and CoRh_2O_4 ”, [Physical Review B](#) **96**, 064413 (2017).
- ³⁰G. J. MacDougall, D. Gout, J. L. Zarestky, G. Ehlers, A. Podlesnyak, M. A. McGuire, D. Mandrus, and S. E. Nagler, “Kinetically inhibited order in a diamond-lattice antiferromagnet”, [Proceedings of the National Academy of Sciences](#) **108**, 15693–15698 (2011).
- ³¹S. Blundell, *Magnetism in Condensed Matter*, Oxford Master Series in Condensed Matter Physics (Oxford University Press, Oxford, 2001).
- ³²S. Mugiraneza and A. M. Hallas, “Tutorial: a beginner’s guide to interpreting magnetic susceptibility data with the Curie-Weiss law.”, [Communications Physics](#) **5**, 95 (2022).
- ³³G. A. Bain and J. F. Berry, “Diamagnetic Corrections and Pascal’s Constants”, [Journal of Chemical Education](#) **85**, 532 (2008).
- ³⁴P. Anderson, “Resonating valence bonds: a new kind of insulator?”, [Materials Research Bulletin](#) **8**, 153–160 (1973).

-
- ³⁵L. C. Pauling, “A resonating-valence-bond theory of metals and intermetallic compounds”, *Proceedings of the Royal Society of London. Series A. Mathematical and Physical Sciences* **196**, 343–362 (1949).
- ³⁶P. W. Anderson, “The Resonating Valence Bond State in La_2CuO_4 and Superconductivity”, *Science* **235**, 1196–1198 (1987).
- ³⁷J. A. Mydosh, “Spin glasses: redux: an updated experimental/materials survey”, *Reports on Progress in Physics* **78**, 052501 (2015).
- ³⁸S. T. Bramwell and M. J. Harris, “The history of spin ice”, *Journal of Physics: Condensed Matter* **32**, 374010 (2020).
- ³⁹D. Bowman, E Cemal, T Lehner, A. Wildes, L Mangin-Thro, G. Nilsen, M. Gutmann, D. Voneshen, D Prabhakaran, A. Boothroyd, et al., “Role of defects in determining the magnetic ground state of ytterbium titanate”, *Nature Communications* **10**, 637 (2019).
- ⁴⁰D. J. P. Morris, D. A. Tennant, S. A. Grigera, B. Klemke, C. Castelnovo, R. Moessner, C. Czternasty, M. Meissner, K. C. Rule, J. Hoffmann, K. Kiefer, S. Gerischer, D. Slobinsky, and R. S. Perry, “Dirac Strings and Magnetic Monopoles in the Spin Ice $\text{Dy}_2\text{Ti}_2\text{O}_7$ ”, *Science* **326**, 411–415 (2009).
- ⁴¹J. Binney and D. Skinner, *The Physics of Quantum Mechanics* (Oxford University Press, 2014).
- ⁴²F. Mandl, *Quantum Mechanics* (John Wiley and Sons, 2013).
- ⁴³J. Villain, R Bidaux, J.-P. Carton, and R Conte, “Order as an effect of disorder”, *Journal de Physique* **41**, 1263–1272 (1980).
- ⁴⁴X. P. Yao, J. Q. Liu, C.-J. Huang, X. Wang, and G. Chen, “Generic spiral spin liquids”, *Frontiers in Physics* **16**, 53303 (2021).
- ⁴⁵D. Bergman, J. Alicea, E. Gull, S. Trebst, and L. Balents, “Order-by-disorder and spiral spin-liquid in frustrated diamond-lattice antiferromagnets.”, *Nature Physics* **3**, 487–491 (2007).

- ⁴⁶M. M. Bordelon, C. Liu, L. Posthuma, E. Kenney, M. J. Graf, N. P. Butch, A. Banerjee, S. Calder, L. Balents, and S. D. Wilson, “Frustrated Heisenberg $J_1 - J_2$ model within the stretched diamond lattice of LiYbO_2 ”, [Physical Review B](#) **103**, 014420 (2021).
- ⁴⁷H. A. Kramers, “Théorie générale de la rotation paramagnétique dans les cristaux”, Proceedings of the Royal Netherlands Academy of Art and Sciences (French) **3**, 959–972 (1930).
- ⁴⁸S. Jenkins, L. Rózsa, U. Atxitia, R. F. L. Evans, K. S. Novoselov, and E. J. G. Santos, “Breaking through the Mermin-Wagner limit in 2D van der Waals magnets”, [Nature Communications](#) **13**, 6917 (2022).
- ⁴⁹G. Palle and D. K. Sunko, “Physical limitations of the Hohenberg–Mermin–Wagner theorem”, [Journal of Physics A: Mathematical and Theoretical](#) **54**, 315001 (2021).
- ⁵⁰M. Pomerantz, “Experiments on literally two-dimensional magnets”, [Surface Science](#) **142**, 556–570 (1984).
- ⁵¹N. D. Mermin and H. Wagner, “Absence of ferromagnetism or antiferromagnetism in one-or two-dimensional isotropic Heisenberg models”, [Physical Review Letters](#) **17**, 1133 (1966).
- ⁵²A. Kitaev, “Anyons in an exactly solved model and beyond”, [Annals of Physics](#) **321**, 2–111 (2006).
- ⁵³M. Hermanns, I. Kimchi, and J. Knolle, “Physics of the Kitaev model: fractionalization, dynamical correlations, and material connections”, [Annual Reviews of Condensed Matter Physics](#) **9**, 1 (2018).
- ⁵⁴S. Yang, T. Zhang, and C. Jiang, “van der Waals Magnets: Material Family, Detection and Modulation of Magnetism, and Perspective in Spintronics”, [Advanced Science](#) **8**, 2002488.
- ⁵⁵F. Wang, T. A. Shifa, P. Yu, P. He, Y. Liu, F. Wang, Z. Wang, X. Zhan, X. Lou, F. Xia, and J. He, “New Frontiers on van der Waals Layered Metal Phosphorous Trichalcogenides”, [Advanced Functional Materials](#) **28**, 1802151 (2018).

-
- ⁵⁶A. R. Wildes, B. Roessli, B. Lebech, and K. W. Godfrey, “Spin waves and the critical behaviour of the magnetization in MnPS_3 ”, *Journal of Physics: Condensed Matter* **10**, 6417 (1998).
- ⁵⁷M. J. Coak, D. M. Jarvis, H. Hamidov, C. R. S. Haines, P. L. Alireza, C. Liu, S. Son, I. Hwang, G. I. Lampronti, D. Daisenberger, P. Nahai-Williamson, A. R. Wildes, S. S. Saxena, and J.-G. Park, “Tuning dimensionality in van-der-Waals antiferromagnetic Mott insulators TMPS_3 ”, *Journal of Physics: Condensed Matter* **32**, 124003 (2020).
- ⁵⁸K. C. Rule, S. J. Kennedy, D. J. Goossens, A. M. Mulders, and T. J. Hicks, “Contrasting antiferromagnetic order between FePS_3 and MnPS_3 ”, *Applied Physics A* **74**, s811–s813 (2002).
- ⁵⁹D. Lançon, H. C. Walker, E. Ressouche, B. Ouladdiaf, K. C. Rule, G. J. McIntyre, T. J. Hicks, H. M. Rønnow, and A. R. Wildes, “Magnetic structure and magnon dynamics of the quasi-two-dimensional antiferromagnet FePS_3 ”, *Physical Review B* **94**, 214407 (2016).
- ⁶⁰Z. Wu, J. Yu, and S. Yuan, “Strain-tunable magnetic and electronic properties of monolayer CrI_3 ”, *Physical Chemistry Chemical Physics* **21**, 7750–7755 (2019).
- ⁶¹B. Huang, G. Clark, D. R. Klein, D. MacNeill, E. Navarro-Moratalla, K. L. Seyler, N. Wilson, M. A. McGuire, D. H. Cobden, D. Xiao, W. Yao, P. Jarillo-Herrero, and X. Xu, “Electrical control of 2D magnetism in bilayer CrI_3 ”, *Nature Nanotechnology* **13**, 544–548 (2018).
- ⁶²D. Staros, G. Hu, J. Tiihonen, R. Nanguneri, J. Krogel, M. C. Bennett, O. Heinonen, P. Ganesh, and B. Rubenstein, “A combined first principles study of the structural, magnetic, and phonon properties of monolayer CrI_3 ”, *The Journal of Chemical Physics* **156**, 014707 (2022).
- ⁶³Y. Deng, Y. Yu, Y. Song, J. Zhang, N. Z. Wang, Z. Sun, Y. Yi, Y. Z. Wu, S. Wu, J. Zhu, J. Wang, X. H. Chen, and Y. Zhang, “Gate-tunable room-temperature ferromagnetism in two-dimensional Fe_3GeTe_2 ”, *Nature* **563**, 94–99 (2018).

- ⁶⁴Z. Fei, B. Huang, P. Malinowski, W. Wang, T. Song, J. Sanchez, W. Yao, D. Xiao, X. Zhu, A. F. May, W. Wu, D. H. Cobden, J.-H. Chu, and X. Xu, “Two-dimensional itinerant ferromagnetism in atomically thin Fe_3GeTe_2 ”, *Nature Materials* **17**, 778–782 (2018).
- ⁶⁵X. Hu, Y. Zhao, X. Shen, A. V. Krashenninnikov, Z. Chen, and L. Sun, “Enhanced Ferromagnetism and Tunable Magnetism in Fe_3GeTe_2 Monolayer by Strain Engineering”, *ACS Applied Materials & Interfaces* **12**, 26367–26373 (2020).
- ⁶⁶S. W. Jang, H. Yoon, M. Y. Jeong, S. Ryee, H.-S. Kim, and M. J. Han, “Origin of ferromagnetism and the effect of doping on Fe_3GeTe_2 ”, *Nanoscale* **12**, 13501–13506 (2020).
- ⁶⁷Z. Ma, J. Wang, Z. Y. Dong, J. Zhang, S. Li, S. H. Zheng, Y. Yu, W. Wang, L. Che, K. Ran, S. Bao, Z. Cai, P. Čermák, A. Schneidewind, S. Yano, J. S. Gardner, X. Lu, S. L. Yu, J. M. Liu, S. Li, J. X. Li, and J. Wen, “Spin-Glass Ground State in a Triangular-Lattice Compound YbZnGaO_4 ”, *Physical Review Letters* **120**, 087201 (2018).
- ⁶⁸Y. Li, G. Chen, W. Tong, L. Pi, J. Liu, Z. Yang, X. Wang, and Q. Zhang, “Rare-Earth Triangular Lattice Spin Liquid: A Single-Crystal Study of YbMgGaO_4 ”, *Physical Review Letters* **115**, 167203 (2015).
- ⁶⁹E. A. Nytko, J. S. Helton, P. Müller, and D. G. Nocera, “A Structurally Perfect $S = \frac{1}{2}$ Metal–Organic Hybrid Kagomé Antiferromagnet”, *Journal of the American Chemical Society* **130**, 2922–2923 (2008).
- ⁷⁰W.-Z. Shen, X.-Y. Chen, P. Cheng, S.-P. Yan, B. Zhai, D.-Z. Liao, and Z.-H. Jiang, “A Structural and Magnetic Investigation of Ferromagnetically Coupled Copper(II) Isophthalates”, *European Journal of Inorganic Chemistry* **2005**, 2297–2305.
- ⁷¹O. Mustonen, S. Vasala, E. Sadrollahi, K. P. Schmidt, C. Baines, H. C. Walker, I. Terasaki, F. J. Litterst, E. Baggio-Saitovitch, and M. Karppinen, “Spin-liquid-like state in a spin- $\frac{1}{2}$ square-lattice antiferromagnet perovskite induced by d^{10} - d^0 cation mixing”, *Nature Communications* **9**, 0–7 (2018).

-
- ⁷²A. A. Tsirlin, R. Nath, A. M. Abakumov, Y. Furukawa, D. C. Johnston, M. Hemmida, H.-A. Krug von Nidda, A. Loidl, C. Geibel, and H. Rosner, “Phase separation and frustrated square lattice magnetism of $\text{Na}_{1.5}\text{VOPO}_4\text{F}_{0.5}$ ”, [Physical Review B **84**, 014429 \(2011\)](#).
- ⁷³E. Fogh, O. Mustonen, P. Babkevich, V. M. Katukuri, H. C. Walker, L. Mangin-Thro, M. Karppinen, S. Ward, B. Normand, and H. M. Rønnow, “Randomness and frustration in a $S = \frac{1}{2}$ square-lattice heisenberg antiferromagnet”, [Physical Review B **105**, 184410 \(2022\)](#).
- ⁷⁴Y. Tan and D.-X. Yao, “Spin waves and phase transition on a magnetically frustrated square lattice with long-range interactions”, [Frontiers in Physics **18**, 33309 \(2023\)](#).
- ⁷⁵H. Kramers, “L’interaction entre les atomes magnétogènes dans un cristal paramagnétique”, [Physica **1**, 182–192 \(1934\)](#).
- ⁷⁶P. W. Anderson, “Antiferromagnetism. Theory of Superexchange Interaction”, [Physical Review **79**, 350–356 \(1950\)](#).
- ⁷⁷S. Lee and L. Balents, “Theory of the ordered phase in *A*-site antiferromagnetic spinels”, [Physical Review B **78**, 144417 \(2008\)](#).
- ⁷⁸F. L. Buessen, M. Hering, J. Reuther, and S. Trebst, “Quantum spin liquids in frustrated spin-1 diamond antiferromagnets”, [Physical Review Letters **120**, 057201 \(2018\)](#).
- ⁷⁹R. D. Johnson, S. C. Williams, A. A. Haghighirad, J. Singleton, V. Zapf, P. Manuel, I. I. Mazin, Y. Li, H. O. Jeschke, R. Valentí, and R. Coldea, “Monoclinic crystal structure of $\alpha - \text{RuCl}_3$ and the zigzag antiferromagnetic ground state”, [Physical Review B **92**, 235119 \(2015\)](#).
- ⁸⁰H.-C. Yang, B.-C. Gong, K. Liu, and Z.-Y. Lu, “Quasi-degenerate magnetic states in $\alpha\text{-RuCl}_3$ ”, [Journal of Physics: Condensed Matter **31**, 025803 \(2019\)](#).
- ⁸¹M. Roslova, J. Hunger, G. Bastien, D. Pohl, H. M. Haghighi, A. U. B. Wolter, A. Isaeva, U. Schwarz, B. Rellinghaus, K. Nielsch, B. Büchner, and T. Doert, “Detuning the Honeycomb

- of the α - RuCl_3 Kitaev Lattice: A Case of Cr^{3+} Dopant”, *Inorganic Chemistry* **58**, 6659–6668 (2019).
- ⁸²H. Kobayashi, M. Tabuchi, M. Shikano, H. Kageyama, and R. Kanno, “Structure, and magnetic and electrochemical properties of layered oxides, Li_2IrO_3 ”, *Journal of Materials Chemistry* **4**, 957–962 (2003).
- ⁸³S. C. Williams, R. D. Johnson, F. Freund, S. Choi, A. Jesche, I. Kimchi, S. Manni, A. Bombardi, P. Manuel, P. Gegenwart, and R. Coldea, “Incommensurate counterrotating magnetic order stabilized by kitaev interactions in the layered honeycomb α - Li_2IrO_3 ”, *Physical Review B* **93**, 195158 (2016).
- ⁸⁴Y. Singh and P. Gegenwart, “Antiferromagnetic mott insulating state in single crystals of the honeycomb lattice material Na_2IrO_3 ”, *Physical Review B* **82**, 064412 (2010).
- ⁸⁵Y. Sizyuk *et al.*, “Importance of anisotropic exchange interactions in honeycomb iridates: minimal model for zigzag antiferromagnetic order in Na_2IrO_3 ”, *Physical Review B* **90**, 155126 (2014).
- ⁸⁶Y. Singh, S. Manni, J. Reuther, T. Berlijn, R. Thomale, W. Ku, S. Trebst, and P. Gegenwart, “Relevance of the heisenberg-kitaev model for the honeycomb lattice iridates A_2IrO_3 ”, *Physical Review Letters* **108**, 127203 (2012).
- ⁸⁷R. W. Smaha, W. He, J. M. Jiang, J. Wen, Y.-F. Jiang, J. P. Sheckelton, C. J. Titus, S. G. Wang, Y.-S. Chen, S. J. Teat, A. A. Aczel, Y. Zhao, G. Xu, J. W. Lynn, H.-C. Jiang, and Y. S. Lee, “Materializing rival ground states in the barlowite family of kagome magnets: quantum spin liquid, spin ordered, and valence bond crystal states”, *npj Quantum Materials* **5**, 23 (2020).
- ⁸⁸Z. Ma, J. Wang, Z.-Y. Dong, J. Zhang, S. Li, S.-H. Zheng, Y. Yu, W. Wang, L. Che, K. Ran, S. Bao, Z. Cai, P. Çermk, A. Schneidewind, S. Yano, J. S. Gardner, X. Lu, S.-L. Yu, J.-M. Liu, S. Li, J.-X. Li, and J. Wen, “Spin-glass ground state in a triangular-lattice compound YbZnGaO_4 ”, *Physical Review Letters* **120**, 087201 (2018).

-
- ⁸⁹Z. Ma, K. Ran, J. Wang, S. Bao, Z. Cai, S. Li, and J. Wen, “Recent progress on magnetic-field studies on quantum-spin-liquid candidates”, *Chinese Physics B* **27**, 106101 (2018).
- ⁹⁰J.-P. Colinge and C. A. Colinge, *Physics of semiconductor devices* (Springer Science & Business Media, 2005).
- ⁹¹M. Tampier and D. Johrendt, “Structural evidence for ferroelectricity in Eu_2GeS_4 ”, *Journal of Solid State Chemistry* **158**, 343–348 (2001).
- ⁹²N. Lampis, P. Sciau, and A. G. Lehmann, “Rietveld refinements of the paraelectric and ferroelectric structures of $\text{PbFe}_{0.5}\text{Nb}_{0.5}\text{O}_3$ ”, *Journal of Physics: Condensed Matter* **11**, 3489 (1999).
- ⁹³C. S. Coates, M. Baise, A. Schmutzler, A. Simonov, J. W. Makepeace, A. G. Seel, R. I. Smith, H. Y. Playford, D. A. Keen, R. Siegel, et al., “Spin-ice physics in cadmium cyanide”, *Nature Communications* **12**, 2272 (2021).
- ⁹⁴D. P. Shoemaker, R. Seshadri, A. L. Hector, A. Llobet, T. Proffen, and C. J. Fennie, “Atomic displacements in the charge ice pyrochlore $\text{Bi}_2\text{Ti}_2\text{O}_6\text{O}$ studied by neutron total scattering”, *Physical Review B* **81**, 144113 (2010).
- ⁹⁵C. Ahn, A. Cavalleri, A. Georges, S. Ismail-Beigi, A. J. Millis, and J.-M. Triscone, “Designing and controlling the properties of transition metal oxide quantum materials”, *Nature Materials* **20**, 1462–1468 (2021).
- ⁹⁶J. M. Kim, M. F. Haque, E. Y. Hsieh, S. M. Nahid, I. Zarin, K.-Y. Jeong, J.-P. So, H.-G. Park, and S. Nam, “Strain engineering of low-dimensional materials for emerging quantum phenomena and functionalities”, *Advanced Materials*, 2107362 (2022).
- ⁹⁷E. G. Meekel, E. M. Schmidt, L. J. Cameron, A. D. Dharma, H. J. Windsor, S. G. Duyker, A. Minelli, T. Pope, G. O. Lepore, B. Slater, C. J. Kepert, and A. L. Goodwin, “Truchet-tile structure of a topologically aperiodic metal organic framework”, *Science* **379**, 357–361 (2023).

- ⁹⁸P. Boulet, M.-C. de Weerd, M. Krnel, S. Vrtnik, Z. Jagličić, and J. Dolinšek, “Structural Model and Spin-Glass Magnetism of the $\text{Ce}_3\text{Au}_{13}\text{Ge}_4$ Quasicrystalline Approximant”, *Inorganic Chemistry* **60**, 2526–2532 (2021).
- ⁹⁹A. T. Boothroyd, *Principles of Neutron Scattering from Condensed Matter* (Oxford University Press, 2020).
- ¹⁰⁰G. L. Squires, *Introduction to the theory of thermal neutron scattering* (Cambridge University Press, 1996).
- ¹⁰¹D. S. Sivia, *Elementary scattering theory: for X-ray and neutron users* (Oxford University Press, 2011).
- ¹⁰²P. J. Brown, A. G. Fox, E. N. Maslen, M. A. O’Keefe, and B. T. M. Willis, *International Tables for Crystallography, Volume C*, Vol. C (2006) Chap. 6.1, pp. 554–595.
- ¹⁰³D. Visser, J. Frunzke, A. Harrison, A. S. Wills, G. S. Oakley, and K. H. Andersen, “Short-range order in the topological spin glass $(\text{D}_3\text{O})\text{Fe}_3(\text{SO}_4)_2(\text{OD}_6)$ using *xyz* polarized neutron diffraction”, *Physical Review B* **64**, 21–24 (2001).
- ¹⁰⁴H. M. Rietveld, “A profile refinement method for nuclear and magnetic structures”, *Journal of Applied Crystallography* **2**, 65–71 (1969).
- ¹⁰⁵J. Rodriguez-Carvajal, “Recent advances in magnetic structure determination by neutron powder diffraction”, *Physica B*. **192**, 55–69 (1993).
- ¹⁰⁶N. Qureshi, “Mag2Pol: a program for the analysis of spherical neutron polarimetry, flipping ratio and integrated intensity data”, *Journal of Applied Crystallography* **52**, 175–185 (2019).
- ¹⁰⁷A. C. Larson and R. B. Von Dreele, “General Structure Analysis System (GSAS)”, Los Alamos National Laboratory Report (LAUR) **86** (1994).
- ¹⁰⁸P. Thompson, D. Cox, and J. Hastings, “Rietveld refinement of Debye–Scherrer synchrotron X-ray data from Al_2O_3 ”, *Journal of Applied Crystallography* **20**, 79–83 (1987).

-
- ¹⁰⁹L. Finger, “PROFVAL: functions to calculate powder-pattern peak profiles with axial-divergence asymmetry”, *Journal of Applied Crystallography* **31**, 111–111 (1998).
- ¹¹⁰W. David, “Powder diffraction peak shapes. Parameterization of the pseudo-Voigt as a Voigt function”, *Journal of Applied Crystallography* **19**, 63–64 (1986).
- ¹¹¹D. Snyder, R. Snyder, J. Fiala, H. Bunge, H. Bunge, and I. U. of Crystallography, *Defect and Microstructure Analysis by Diffraction*, IUCr monographs on crystallography (Oxford University Press, 1999).
- ¹¹²J. R. Stewart, P. P. Deen, K. H. Andersen, H. Schober, J.-F. Barthélémy, J. M. Hillier, A. P. Murani, T. Hayes, and B. Lindenau, “Disordered materials studied using neutron polarization analysis on the multi-detector spectrometer, D7”, *Journal of Applied Crystallography* **42**, 69–84 (2009).
- ¹¹³T. Fennell, L. Mangin-Thro, H. Mutka, G. Nilsen, and A. Wildes, “Wavevector and energy resolution of the polarized diffuse scattering spectrometer D7”, *Nuclear Instruments and Methods in Physics Research Section A: Accelerators, Spectrometers, Detectors and Associated Equipment* **857**, 24–30 (2017).
- ¹¹⁴W. Schweika, “XYZ-polarisation analysis of diffuse magnetic neutron scattering from single crystals”, *Journal of Physics: Conference Series* **211**, 012026 (2010).
- ¹¹⁵G. Ehlers, J. R. Stewart, A. R. Wildes, P. P. Deen, and K. H. Andersen, “Generalization of the classical xyz-polarization analysis technique to out-of-plane and inelastic scattering”, *Scientific Instruments* **84**, 093901 (2013).
- ¹¹⁶O. Schärpf and H. Capellmann, “The XYZ-Difference Method with Polarized Neutrons and the Separation of Coherent, Spin Incoherent, and Magnetic Scattering Cross Sections in a Multidetector”, *Physica Status Solidi (a)* **135**, 359–379 (1993).
- ¹¹⁷F. Mezei, “Novel polarized neutron devices: supermirror and spin component amplifier”, *Communications on Physics (London)* **1**, 81–85 (1976).

- ¹¹⁸D. Richard, M. Ferrand, and G. J. Kearley, “Analysis and Visualisation of Neutron-Scattering Data”, [Journal of Neutron Research](#) **4**, 33–39 (1996).
- ¹¹⁹J. A. M. Paddison and A. L. Goodwin, “Empirical Magnetic Structure Solution of Frustrated Spin Systems”, [Physical Review Letters](#) **108**, 017204 (2012).
- ¹²⁰J. A. M. Paddison, J. R. Stewart, and A. L. Goodwin, “SPINVERT: a program for refinement of paramagnetic diffuse scattering data”, [Journal of Condensed Matter Physics](#) **25**, 454220 (2013).
- ¹²¹J. A. M. Paddison, H. S. Ong, J. O. Hamp, P. Mukherjee, X. Bai, M. G. Tucker, N. P. Butch, C. Castelnovo, M. Mourigal, and S. E. Dutton, “Emergent order in the kagome Ising magnet $\text{Dy}_3\text{Mg}_2\text{Sb}_3\text{O}_{14}$ ”, [Nature Communications](#) **7**, 13842 (2016).
- ¹²²J. A. M. Paddison, “Ultrafast calculation of diffuse scattering from atomistic models”, [Acta Crystallographica Section A](#) **75**, 14–24 (2019).
- ¹²³T. Egami and S. J. L. Billinge, *Underneath the Bragg peaks: structural analysis of complex materials*, 2nd edn (Elsevier, Amsterdam, The Netherlands, 2012).
- ¹²⁴S. J. L. Billinge, “The rise of the X-ray atomic pair distribution function method: a series of fortunate events”, [Philosophical Transactions of the Royal Society A: Mathematical, Physical and Engineering Sciences](#) **377**, 20180413 (2019).
- ¹²⁵B. H. Toby and T. Egami, “Accuracy of pair distribution function analysis applied to crystalline and non-crystalline materials”, [Acta Crystallographica Section A](#) **48**, 336–346 (1992).
- ¹²⁶M. G. Tucker, D. A. Keen, M. T. Dove, A. L. Goodwin, and Q. Hui, “RMCPProfile: reverse Monte Carlo for polycrystalline materials”, [Journal of Physics: Condensed Matter](#) **19**, 335218 (2007).
- ¹²⁷C. L. Farrow, P. Juhas, J. W. Liu, D. Bryndin, E. S. Božin, J. Bloch, T. Proffen, and S. J. L. Billinge, “PDFfit2 and PDFgui: computer programs for studying nanostructure in crystals”, [Journal of Physics: Condensed Matter](#) **19**, 335219 (2007).

-
- ¹²⁸Y. Uemura, A. Keren, L. Le, G. Luke, B. Sternlieb, and W. Wu, “Muon spin relaxation studies in frustrated and/or low-dimensional spin systems”, [Hyperfine Interactions](#) **85**, 133–144 (1994).
- ¹²⁹G. Misguich, *Introduction to Frustrated Magnetism: Materials, Experiments, Theory*, edited by C. Lacroix, P. Mendels, and F. Mila (Springer Berlin Heidelberg, 2011) Chap. 8.
- ¹³⁰T.-H. Han, J. S. Helton, S. Chu, D. G. Nocera, J. A. Rodriguez-Rivera, C. Broholm, and Y. S. Lee, “Fractionalized excitations in the spin-liquid state of a kagome-lattice antiferromagnet”, [Nature](#) **492**, 406–410 (2012).
- ¹³¹C. M. Pasco, B. A. Trump, T. T. Tran, Z. A. Kelly, C. Hoffmann, I. Heinmaa, R. Stern, and T. M. McQueen, “Single-crystal growth of $\text{Cu}_4(\text{OH})_6\text{BrF}$ and universal behavior in quantum spin liquid candidates synthetic barlowite and herbertsmithite”, [Physical Review Materials](#) **2**, 044406 (2018).
- ¹³²K. Tustain, E. E. McCabe, A. M. Arevalo-Lopez, A. S. Gibbs, S. P. Thompson, C. A. Murray, C. Ritter, and L. Clark, “Disorder-Induced Structural Complexity in the Barlowite Family of $s = \frac{1}{2}$ Kagomé Magnets”, [Chemistry of Materials](#) **33**, 9638–9651 (2021).
- ¹³³P. Cheng, W. Sun, Y. Fang, B. Kang, W. Lv, Q. Xiao, J. Zhang, and F. Chen, “The evolution of spin-glass behavior in hexagonal $\text{Lu}_{1-x}\text{Ca}_x\text{MnO}_3$ single crystals”, [Ceramics International](#) **46**, 15958–15962 (2020).
- ¹³⁴P. Yadav, S. Sharma, P. J. Baker, P. K. Biswas, I. da Silva, R. Raghunathan, U. Deshpande, R. J. Choudhary, N. P. Lalla, and A. Banerjee, “ μSR And neutron diffraction studies on the tuning of spin-glass phases in the partially ordered double perovskites $\text{SrMn}_{1-x}\text{W}_x\text{O}_3$ ”, [Physical Review B](#) **99**, 214421 (2019).
- ¹³⁵A. Nath, S. S. Islam, P. K. Mukharjee, R. Nath, and S. Mandal, “Reentrant Spin-Glass Behavior in Cobalt(II) Based Coordination Polymers”, [Crystal Growth & Design](#) **19**, 6463–6471 (2019).

- ¹³⁶T. Fennell, P. P. Deen, A. R. Wildes, K. Schmalzl, D. Prabhakaran, A. T. Boothroyd, R. J. Aldus, D. F. McMorrow, and S. T. Bramwell, “Magnetic Coulomb Phase in the Spin Ice $\text{Ho}_2\text{Ti}_2\text{O}_7$ ”, *Science* **326**, 415–417 (2009).
- ¹³⁷K. E. Arpino, B. A. Trump, A. O. Scheie, T. M. McQueen, and S. M. Koohpayeh, “Impact of stoichiometry of $\text{Yb}_2\text{Ti}_2\text{O}_7$ on its physical properties”, *Physical Review B* **95**, 094407 (2017).
- ¹³⁸E. Kermarrec, J. Gaudet, K. Fritsch, R. Khasanov, Z. Guguchia, C. Ritter, K. A. Ross, H. A. Dabkowska, and B. D. Gaulin, “Ground state selection under pressure in the quantum pyrochlore magnet $\text{Yb}_2\text{Ti}_2\text{O}_7$ ”, *Nature Communications* **8**, 14810 (2017).
- ¹³⁹A. R. West, *Solid state chemistry and its applications* (Wiley, 2013) Chap. 4.
- ¹⁴⁰A. Nandy, C. Duan, M. G. Taylor, F. Liu, A. H. Steeves, and H. J. Kulik, “Computational Discovery of Transition-metal Complexes: From High-throughput Screening to Machine Learning”, *Chemical Reviews* **121**, 9927–10000 (2021).
- ¹⁴¹J. P. Janet, F. Liu, A. Nandy, C. Duan, T. Yang, S. Lin, and H. J. Kulik, “Designing in the Face of Uncertainty: Exploiting Electronic Structure and Machine Learning Models for Discovery in Inorganic Chemistry”, *Inorganic Chemistry* **58**, 10592–10606 (2019).
- ¹⁴²E. E. Levin, J. H. Grebenkemper, T. M. Pollock, and R. Seshadri, “Protocols for High Temperature Assisted-Microwave Preparation of Inorganic Compounds”, *Chemistry of Materials* **31**, 7151–7159 (2019).
- ¹⁴³J. A. Kurzman, X. Ouyang, W. B. Im, J. Li, J. Hu, S. L. Scott, and R. Seshadri, “ $\text{La}_4\text{LiAuO}_8$ and $\text{La}_2\text{BaPdO}_5$: Comparing two highly stable d8 square-planar oxides”, *Inorganic chemistry* **49**, 4670–4680 (2010).
- ¹⁴⁴M. Bhattacharya and T. Basak, “A review on the susceptor assisted microwave processing of materials”, *Energy* **97**, 306–338 (2016).
- ¹⁴⁵K. J. Rao, B. Vaidhyanathan, M. Ganguli, and P. A. Ramakrishnan, “Synthesis of Inorganic Solids Using Microwaves”, *Chemistry of Materials* **11**, 882–895 (1999).

-
- ¹⁴⁶H. J. Kitchen, S. R. Vallance, J. L. Kennedy, N. Tapia-Ruiz, L. Carassiti, A. Harrison, A. G. Whittaker, T. D. Drysdale, S. W. Kingman, and D. H. Gregory, “Modern Microwave Methods in Solid-State Inorganic Materials Chemistry: From Fundamentals to Manufacturing”, [Chemical Reviews](#) **114**, 1170–1206 (2014).
- ¹⁴⁷S. W. Muir, O. D. Rachdi, and M. Subramanian, “Rapid microwave synthesis of the iron arsenides NdFeAsO and NdFe_{0.9}Co_{0.1}AsO”, [Materials Research Bulletin](#) **47**, 798–800 (2012).
- ¹⁴⁸K. Biswas, S. Muir, and M. A. Subramanian, “Rapid microwave synthesis of indium filled skutterudites: an energy efficient route to high performance thermoelectric materials”, [Materials Research Bulletin](#) **46**, 2288–2290 (2011).
- ¹⁴⁹J. W. Lekse, T. J. Stagger, and J. A. Aitken, “Microwave metallurgy: synthesis of intermetallic compounds via microwave irradiation”, [Chemistry of Materials](#) **19**, 3601–3603 (2007).
- ¹⁵⁰C. Mastrovito, J. W. Lekse, and J. A. Aitken, “Rapid solid-state synthesis of binary group 15 chalcogenides using microwave irradiation”, [Journal of Solid State Chemistry](#) **180**, 3262–3270 (2007).
- ¹⁵¹J. W. Lekse, A. M. Pischera, and J. A. Aitken, “Understanding solid-state microwave synthesis using the diamond-like semiconductor, AgInSe₂, as a case study”, [Materials Research Bulletin](#) **42**, 395–403 (2007).
- ¹⁵²P. Priece and J. A. Lopez-Sanchez, “Advantages and limitations of microwave reactors: from chemical synthesis to the catalytic valorization of biobased chemicals”, [ACS Sustainable Chemistry & Engineering](#) **7**, 3–21 (2019).
- ¹⁵³M. Reehuis, A. Krimmel, N. Büttgen, A. Loidl, and A. Prokofiev, “Crystallographic and magnetic structure of ZnV₂O₄: Structural phase transition due to spin-driven Jahn-Teller distortions”, [The European Physical Journal B-Condensed Matter and Complex Systems](#) **35**, 311–316 (2003).

- ¹⁵⁴P. G. Radaelli, “Orbital ordering in transition-metal spinels”, [New Journal of Physics](#) **7**, [53](#) (2005).
- ¹⁵⁵Y. Ueda, N. Fujiwara, and H. Yasuoka, “Magnetic and Structural Transitions in $(\text{Li}_x\text{Zn}_{1-x})\text{V}_2\text{O}_4$ with the Spinel Structure”, [Journal of the Physical Society of Japan](#) **66**, 778–783 (1997).
- ¹⁵⁶A. J. Browne and J. P. Attfield, “Orbital molecules in vanadium oxide spinels”, [Physical Review B](#) **101**, 024112 (2020).
- ¹⁵⁷S. Ebbinghaus, J. Hanss, M. Klemm, and S. Horn, “Crystal structure and magnetic properties of ZnV_2O_4 ”, [Journal of Alloys and Compounds](#) **370**, 75–79 (2004).
- ¹⁵⁸S.-H. Lee, D Louca, H Ueda, S Park, T. Sato, M Isobe, Y Ueda, S Rosenkranz, P Zschack, J Íñiguez, et al., “Orbital and Spin Chains in ZnV_2O_4 ”, [Physical Review Letters](#) **93**, 156407 (2004).
- ¹⁵⁹T. Maitra and R. Valenti, “Orbital order in ZnV_2O_4 ”, [Physical Review Letters](#) **99**, 126401 (2007).
- ¹⁶⁰H. Tsunetsugu and Y. Motome, “Magnetic transition and orbital degrees of freedom in vanadium spinels”, [Physical Review B](#) **68**, 3–6 (2003).
- ¹⁶¹S. Nizioł, “Investigation of magnetic properties of ZnV_2O_4 spinel”, [Physica Status Solidi \(a\)](#) **18**, K11–K13 (1973).
- ¹⁶²A. Vasiliev, M. Markina, M. Isobe, and Y. Ueda, “Specific heat and magnetic susceptibility of spinel compounds CdV_2O_4 , ZnV_2O_4 and MgTi_2O_4 ”, [Journal of Magnetism and Magnetic Materials](#) **300**, e375–e377 (2006).
- ¹⁶³M. Singha and R. Gupta, “Structural and magnetic studies on polycrystalline Ni doped ZnV_2O_4 ”, [Physica B: Condensed Matter](#) **563**, 101–106 (2019).
- ¹⁶⁴R. Plumier, “Contribution a l’étude des interactions magnetiques dans quelques spinelles ferri-et antiferromagnetiques normaux etudies par diffraction des neutrons”, PhD thesis (Centre d’Etudes Nucleaires de Saclay, Paris, 1968).

-
- ¹⁶⁵H. Mamiya, M. Onoda, T. Furubayashi, J. Tang, and I. Nakatani, “Structural and magnetic studies on vanadium spinel MgV_2O_4 ”, [Journal of Applied Physics](#) **81**, 5289–5291 (1997).
- ¹⁶⁶S. Kondo, D. Johnston, C. Swenson, F Borsa, A. Mahajan, L. Miller, T Gu, A. Goldman, M. Maple, D. Gajewski, et al., “ LiV_2O_4 : A heavy fermion transition metal oxide”, [Physical Review Letters](#) **78**, 3729 (1997).
- ¹⁶⁷D. Johnston, “Heavy fermion behaviors in LiV_2O_4 ”, [Physica B: Condensed Matter](#) **281**, 21–25 (2000).
- ¹⁶⁸P Fulde, A. Yaresko, A. Zvyagin, and Y Grin, “On the origin of heavy quasiparticles in LiV_2O_4 ”, [Europhysics Letters](#) **54**, 779 (2001).
- ¹⁶⁹R. M. Ibberson, “Design and performance of the new supermirror guide on HRPD at ISIS”, [Nuclear Instruments and Methods in Physics Research Section A: Accelerators, Spectrometers, Detectors and Associated Equipment](#) **600**, 47–49 (2009).
- ¹⁷⁰L. Clark, A. D. Fortes, J. N. Graham, and J. R. Stewart, *Unravelling Structural, Orbital and Magnetic Complexity in the Frustrated Spinel ZnV_2O_4* , ISIS Neutron and Muon Source, doi:10.5286/ISIS.E.RB2090049, 2020.
- ¹⁷¹J. N. Graham, P. Manuel, A. Abdeldaim, S. A. Ivko, T. N. Dolling, and L. Clark, *Understanding Complex Synthesis-Structure-Property Relationships in the Frustrated $S = 1$ Spinel Antiferromagnet, ZnV_2O_4* , ISIS Neutron and Muon Source, doi:10.5286/ISIS.E.RB2200355, 2020.
- ¹⁷²T. C. Hansen, P. F. Henry, H. E. Fischer, J. Torregrossa, and P. Convert, “The D20 instrument at the ILL: a versatile high-intensity two-axis neutron diffractometer”, [Measurement Science and Technology](#) **19**, 034001 (2008).
- ¹⁷³L. Clark, J. N. Graham, C. Ritter, J. R. Stewart, and A. R. Wildes, *Understanding Complex Synthesis-Structure-Property Relationships in the Frustrated $S = 1$ Spinel An-*

- tiferromagnet*, ZnV_2O_4 , Institut Laue-Langevin (ILL), doi:10.5291/ILL-DATA.5-31-2929, 2023.
- ¹⁷⁴J. N. Graham, J. R. Stewart, L. Clark, and A. R. Wildes, *Unravelling Structural, Orbital and Magnetic Complexity in the Frustrated Spinel ZnV_2O_4* , Institut Laue-Langevin, doi:10.5291/ILL-DATA.5-32-897, 2020.
- ¹⁷⁵J. N. Graham and A. R. Wildes, *Structural, Magnetic and Orbital Complexities in the Frustrated Spinel, ZnV_2O_4* , Institut Laue-Langevin, doi:doi:10.5291/ILL-DATA.EASY-926, 2020.
- ¹⁷⁶J. N. Graham, A. R. Wildes, and G. Confalonieri, *Exploring structural, magnetic and orbital orderings in ZnV_2O_4 [Data set]*. European Synchrotron Radiation Facility, doi.org/0.15151/ESRF-ES-473795570, 2021.
- ¹⁷⁷A. R. Wildes, G. Beckett, J. N. Graham, L. Clark, J. R. Stewart, and G. Confalonieri, *ZnV_2O_4 : On the Border of Disorder [Data set]*. European Synchrotron Radiation Facility, doi.org/10.15151/ESRF-ES-652448489, 2022.
- ¹⁷⁸H. T. Stokes, D. M. Hatch, and B. J. Campbell, *ISODISTORT, ISOTROPY Software Suite*, iso.byu.edu.
- ¹⁷⁹B. J. Campbell, H. T. Stokes, D. E. Tannes, and D. M. Hatch, “ISODISPLACE: An Internet Tool for Exploring Structural Distortions.”, *Journal of Applied Crystallography* **39**, 607–614 (2006).
- ¹⁸⁰E. Helgren, F. Hellman, L. Zeng, N. Sinenian, R. Islam, and D. J. Smith, “Magnetic and transport properties of amorphous Gd_xGe_{1-x} alloys near the metal-insulator transition”, *Physical Review B* **76**, 184440 (2007).
- ¹⁸¹H. Taguchi and M. Shimada, “Metal-insulator transition in the system $(Ca_{1-x}La_x)MnO_{2.97}$ ($0.05 \leq x \leq 0.4$)”, *Journal of Solid State Chemistry* **63**, 290–294 (1986).

-
- ¹⁸²P. Lemmens, T. Suzuki, H. Goshima, T. Fujita, B. Beschoten, and C. Quitmann, “Specific heat measurements across the metal-insulator transition in $\text{Bi}_2\text{Sr}_2(\text{Ca}_z\text{RE}_{1-z})\text{Cu}_2\text{O}_8$ with $\text{RE}=\text{Y,Pr,Nd}$ and Gd ”, *Physica B: Condensed Matter* **194-196**, 467–468 (1994).
- ¹⁸³J. A. M. Paddison, “Spinteract: a program to refine magnetic interactions to diffuse scattering data”, [10.48550/ARXIV.2210.09016](https://arxiv.org/abs/10.48550/ARXIV.2210.09016) (2022).
- ¹⁸⁴W. Kang, Y. Huang, X. Zhang, Y. Zhou, and W. Zhao, “Skyrmion-electronics: an overview and outlook”, *Proceedings of the IEEE* **104**, 2040–2061 (2016).
- ¹⁸⁵G. Finocchio, F. Büttner, R. Tomasello, M. Carpentieri, and M. Kläui, “Magnetic skyrmions: from fundamental to applications”, *Journal of Physics D: Applied Physics* **49**, 423001 (2016).
- ¹⁸⁶Y. Tokura and N. Kanazawa, “Magnetic Skyrmion Materials”, *Chemical Reviews* **121**, 2857–2897 (2021).
- ¹⁸⁷B. Göbel, I. Mertig, and O. A. Tretiakov, “Beyond skyrmions: Review and perspectives of alternative magnetic quasiparticles”, *Physics Reports* **895**, 1–28 (2021).
- ¹⁸⁸N. Niggemann, M. Hering, and J. Reuther, “Classical spiral spin liquids as a possible route to quantum spin liquids”, *Journal of Physics: Condensed Matter* **32**, 024001 (2019).
- ¹⁸⁹S. Gao, M. A. McGuire, Y. Liu, D. L. Abernathy, C. d. Cruz, M. Frontzek, M. B. Stone, and A. D. Christianson, “Spiral Spin Liquid on a Honeycomb Lattice”, *Physical Review Letters* **128**, 227201 (2022).
- ¹⁹⁰S. Lee, J.-S. Jeong, K. Hwang, and Y. B. Kim, “Emergent quantum phases in a frustrated J_1-J_2 heisenberg model on the hyperhoneycomb lattice”, *Physical Review B* **90**, 134425 (2014).
- ¹⁹¹X. Bai, J. A. M. Paddison, E. Kapit, S. M. Koohpayeh, J.-J. Wen, S. E. Dutton, A. T. Savici, A. I. Kolesnikov, G. E. Granroth, C. L. Broholm, J. T. Chalker, and M. Mourigal, “Magnetic excitations of the classical spin liquid MgCr_2O_4 ”, *Physical Review Letters* **122**, 097201 (2019).

- ¹⁹²S. Gao, O. Zaharko, V. Tsurkan, Y. Su, J. S. White, G. S. Tucker, B. Roessli, F. Bourdarot, R. Sibille, D. Chernyshov, T. Fennell, A. Loidl, and C. Rüegg, “Spiral spin-liquid and the emergence of a vortex-like state in MnSc_2S_4 .”, [Nature Physics](#) **13**, 157–161 (2017).
- ¹⁹³Y. Iqbal, T. Müller, H. O. Jeschke, R. Thomale, and J. Reuther, “Stability of the spiral spin liquid in MnSc_2S_4 ”, [Physical Review B](#) **98**, 064427 (2018).
- ¹⁹⁴J. R. Chamorro, L. Ge, J. Flynn, M. A. Subramanian, M. Mourigal, and T. M. McQueen, “Frustrated spin one on a diamond lattice in NiRh_2O_4 ”, [Physical Review Materials](#) **2**, 034404 (2018).
- ¹⁹⁵S. Das, D. Nafday, T. Saha-Dasgupta, and A. Paramakanti, “ NiRh_2O_4 : A spin-orbit entangled diamond-lattice paramagnet”, [Physical Review B](#) **100**, 140408 (2019).
- ¹⁹⁶S. Ghara, N. V. Ter-Oganessian, and A. Sundaresan, “Linear magnetoelectric effect as a signature of long-range collinear antiferromagnetic ordering in the frustrated spinel CoAl_2O_4 ”, [Physical Review B](#) **95**, 094404 (2017).
- ¹⁹⁷G. J. MacDougall, D. Gout, J. L. Zarestky, G. Ehlers, A. Podlesnyak, M. A. McGuire, D. Mandrus, and S. E. Nagler, “Kinetically inhibited order in a diamond-lattice antiferromagnet”, [Proceedings of the National Academy of Sciences](#) **108**, 15693–15698 (2011).
- ¹⁹⁸M. M. Bordelon, J. D. Bocarsly, L. Posthuma, A. Banerjee, Q. Zhang, and S. D. Wilson, “Antiferromagnetism and crystalline electric field excitations in tetragonal NaCeO_2 ”, [Physical Review B](#) **103**, 024430 (2021).
- ¹⁹⁹Y. Hashimoto, M. Wakeshima, K. Matsuhira, Y. Hinatsu, and Y. Ishii, “Structures and Magnetic Properties of Ternary Lithium Oxides LiRO_2 ($R = \text{Rare Earths}$)”, [Chemistry of Materials](#) **14**, 3245–3251 (2002).
- ²⁰⁰E. M. Kenney, M. M. Bordelon, C. Wang, H. Luetkens, S. D. Wilson, and M. J. Graf, “Novel magnetic ordering in LiYbO_2 probed by muon spin relaxation”, [Physical Review B](#) **106**, 144401 (2022).

-
- ²⁰¹J. N. Graham, N. Qureshi, C. Ritter, P. Manuel, A. R. Wildes, and L. Clark, “Experimental Evidence for the Spiral Spin Liquid in LiYbO_2 ”, [Physical Review Letters](#) **130**, 166703 (2023).
- ²⁰²A. W. Hewat, “A New High Resolution Neutron Powder Diffractometer at Ill Grenoble.”, [Materials Science Forum](#) **9**, 69–80 (1986).
- ²⁰³J. N. Graham, C. Ritter, L. Clark, and A. R. Wildes, *Exploring Chemical and Magnetic Disorders in the Triangular Antiferromagnet $\text{Yb}(\text{Mg}/\text{Zn})\text{GaO}_4$* , Institut Laue-Langevin, doi:10.5291/ILL-DATA.5-32-921, 2021.
- ²⁰⁴J. N. Graham, P. Manuel, A. R. Wildes, and L. Clark, *Determining Magnetic Order in the Intermediate Phase of LiYbO_2* , ISIS Neutron and Muon Source, doi:10.5286/ISIS.E.R-B2200001-1, 2022.
- ²⁰⁵J. Rossat-Mignod, *Methods of Experimental Physics*, Vol. 23.C (Academic Press Inc., 1987) Chap. Magnetic Structures.
- ²⁰⁶P. J. Brown, *Electron and Magnetisation Densities in Molecules and Crystals* (Plenum Press New York, 1979) Chap. Magnetic Neutron Scattering.
- ²⁰⁷M. M. Bordelon, C. Girod, F. Ronning, K. Rubi, N. Harrison, J. D. Thompson, C. dela Cruz, S. M. Thomas, E. D. Bauer, and P. F. S. Rosa, “Interwoven atypical quantum states in CeLiBi_2 ”, [Physical Review B](#) **106**, 214433 (2022).
- ²⁰⁸Y. Hashimoto, M. Wakeshima, and Y. Hinatsu, “Magnetic properties of ternary sodium oxides NaLnO_2 (Ln =rare earths)”, [Journal of Solid State Chemistry](#) **176**, 266–272 (2003).
- ²⁰⁹C. A. Marjerrison, C. Mauws, A. Z. Sharma, C. R. Wiebe, S. Derakhshan, C. Boyer, B. D. Gaulin, and J. E. Greedan, “Structure and Magnetic Properties of KRuO_4 ”, [Inorganic Chemistry](#) **55**, 12897–12903 (2016).
- ²¹⁰S. Injac, A. K. L. Yuen, M. Avdeev, F. Orlandi, and B. J. Kennedy, “Structural and magnetic studies of KOsO_4 , a $5d^1$ quantum magnet oxide”, [Physical Chemistry Chemical Physics](#) **21**, 7261–7264 (2019).

- ²¹¹Q. Tang and Z. Zhou, “Graphene-analogous low-dimensional materials”, *Progress in Materials Science* **58**, 1244–1315 (2013).
- ²¹²K. F. Mak and J. Shan, “Photonics and optoelectronics of 2D semiconductor transition metal dichalcogenides”, *Nature Photonics* **10**, 216–226 (2016).
- ²¹³J. S. Ponraj, Z.-Q. Xu, S. C. Dhanabalan, H. Mu, Y. Wang, J. Yuan, P. Li, S. Thakur, M. Ashrafi, K. Mccoubrey, Y. Zhang, S. Li, H. Zhang, and Q. Bao, “Photonics and optoelectronics of two-dimensional materials beyond graphene”, *Nanotechnology* **27**, 462001 (2016).
- ²¹⁴A. Kumar and Q. Xu, “Two-Dimensional Layered Materials as Catalyst Supports”, *ChemNanoMat.* **4**, 28–40 (2018).
- ²¹⁵M. Hossain, B. Qin, B. Li, and X. Duan, “Synthesis, characterization, properties and applications of two-dimensional magnetic materials”, *Nano Today* **42**, 101338 (2022).
- ²¹⁶A. K. Geim and K. S. Novoselov, “The rise of graphene”, *Nature Materials* **6**, 183–191 (2007).
- ²¹⁷A. K. Geim, “Graphene: Status and Prospects”, *Science* **324**, 1530–1534 (2009).
- ²¹⁸C. N. R. Rao, K. Biswas, K. S. Subrahmanyam, and A. Govindaraj, “Graphene, the new nanocarbon”, *Journal of Materials Chemistry* **19**, 2457–2469 (2009).
- ²¹⁹F. Zhang, K. Yang, G. Liu, Y. Chen, M. Wang, S. Li, and R. Li, “Recent advances on graphene: Synthesis, properties and applications”, *Composites Part A: Applied Science and Manufacturing* **160**, 107051 (2022).
- ²²⁰I. Colmiais, V. Silva, J. Borme, P. Alpuim, and P. M. Mendes, “Towards RF graphene devices: A review”, *FlatChem* **35**, 100409 (2022).
- ²²¹Q. H. Wang, A. Bedoya-Pinto, M. Blei, A. H. Dismukes, A. Hamo, S. Jenkins, M. Koperski, Y. Liu, Q.-C. Sun, E. J. Telford, H. H. Kim, M. Augustin, U. Vool, J.-X. Yin, L. H. Li, A. Falin, C. R. Dean, F. Casanova, R. F. L. Evans, M. Chshiev, A. Mishchenko, C. Petrovic, R. He, L. Zhao, A. W. Tsen, B. D. Gerardot, M. Brotons-Gisbert, Z. Guguchia,

- X. Roy, S. Tongay, Z. Wang, M. Z. Hasan, J. Wrachtrup, A. Yacoby, A. Fert, S. Parkin, K. S. Novoselov, P. Dai, L. Balicas, and E. J. G. Santos, “The Magnetic Genome of Two-Dimensional van der Waals Materials”, *ACS Nano* **16**, 6960–7079 (2022).
- ²²²K. S. Burch, D. Mandrus, and J.-G. Park, “Magnetism in two-dimensional van der Waals materials”, *Nature* **563**, 47–52 (2018).
- ²²³J.-G. Park, “Opportunities and challenges of 2D magnetic van der Waals materials: Magnetic graphene?”, *Journal of Physics: Condensed Matter* **28**, 301001 (2016).
- ²²⁴D. A. Dikin, M. Mehta, C. W. Bark, C. M. Folkman, C. B. Eom, and V. Chandrasekhar, “Coexistence of Superconductivity and Ferromagnetism in Two Dimensions”, *Physical Review Letters* **107**, 056802 (2011).
- ²²⁵B. Huang, G. Clark, D. R. Klein, D. MacNeill, E. Navarro-Moratalla, K. L. Seyler, N. Wilson, M. A. McGuire, D. H. Cobden, D. Xiao, W. Yao, P. Jarillo-Herrero, and X. Xu, “Electrical control of 2D magnetism in bilayer CrI_3 ”, *Nature Nanotechnology* **13**, 544–548 (2018).
- ²²⁶R. Brec, D. M. Schleich, G. Ouvrard, A. Louisy, and J. Rouxel, “Physical Properties of Lithium Intercalation Compounds of the Layered Transition Chalcogenophosphates”, *Inorganic Chemistry* **18**, 1814–1818 (1979).
- ²²⁷G. Ouvrard, R. Brec, and J. Rouxel, “Structural determination of some MPS_3 layered phases ($M = \text{Mn, Fe, Co, Ni}$ and Cd)”, *Materials Research Bulletin* **20**, 1181–1189 (1985).
- ²²⁸A. R. Wildes, V. Simonet, E. Ressouche, G. J. McIntyre, M. Avdeev, E. Suard, S. A. J. Kimber, D. Lançon, G. Pepe, B. Moubaraki, and T. J. Hicks, “Magnetic structure of the quasi-two-dimensional antiferromagnet NiPS_3 ”, *Physical Review B* **92**, 224408 (2015).
- ²²⁹E. Ressouche, M. Loire, V. Simonet, R. Ballou, A. Stunault, and A. Wildes, “Magnetoelectric MnPS_3 as a candidate for ferrotoroidicity”, *Physical Review B* **82**, 100408(R) (2010).

- ²³⁰A. R. Wildes, V Simonet, E Ressouche, R Ballou, and G. J. McIntyre, “The magnetic properties and structure of the quasi-two-dimensional antiferromagnet CoPS_3 ”, [Journal of Physics: Condensed Matter](#) **29**, 455801 (2017).
- ²³¹X. Liu, T. Najam, G. Yasin, M. Kumar, and M. Wang, “Facile Synthesis of $M\text{PS}_3/\text{C}$ ($M = \text{Ni}$ and Sn) Hybrid Materials and Their Application in Lithium-Ion Batteries”, [ACS Omega](#) **6**, 17247–17254 (2021).
- ²³²W. Klingen, G. Eulenberger, and H. Hahn, “Über die Kristallstrukturen von $\text{Fe}_2\text{P}_2\text{Se}_6$ und $\text{Fe}_2\text{P}_2\text{S}_6$ ”, [Zeitschrift für anorganische und allgemeine Chemie](#) **401**, 97–112 (1973).
- ²³³J.-U. Lee, S. Lee, J. H. Ryoo, S. Kang, T. Y. Kim, P. Kim, C.-H. Park, J.-G. Park, and H. Cheong, “Ising-Type Magnetic Ordering in Atomically Thin FePS_3 ”, [Nano Letters](#) **16**, 7433–7438 (2016).
- ²³⁴X. Wang, K. Du, Y. Y. F. Liu, P. Hu, J. Zhang, Q. Zhang, M. H. S. Owen, X. Lu, C. K. Gan, P. Sengupta, C. Kloc, and Q. Xiong, “Raman spectroscopy of atomically thin two-dimensional magnetic iron phosphorus trisulfide (FePS_3) crystals”, [2D Materials](#) **3**, 031009 (2016).
- ²³⁵C. T. Kuo, M. Neumann, K. Balamurugan, H. J. Park, S. Kang, H. W. Shiu, J. H. Kang, B. H. Hong, M. Han, T. W. Noh, and J.-G. Park, “Exfoliation and Raman Spectroscopic Fingerprint of Few-Layer NiPS_3 Van der Waals Crystals”, [Scientific Reports](#) **6**, 20904 (2016).
- ²³⁶C. R. S. Haines, M. J. Coak, A. R. Wildes, G. I. Lampronti, C. Liu, P. Nahai-Williamson, H. Hamidov, D. Daisenberger, and S. S. Saxena, “Pressure-Induced Electronic and Structural Phase Evolution in the van der Waals Compound FePS_3 ”, [Physical Review Letters](#) **121**, 266801 (2018).
- ²³⁷D. M. Jarvis, M. J. Coak, H. Hamidov, C. R. S. Haines, G. I. Lampronti, C. Liu, S. Deng, D. Daisenberger, D. R. Allan, M. R. Warren, A. R. Wildes, and S. S. Saxena,

- “Comparative structural evolution under pressure of powder and single crystals of the layered antiferromagnet FePS_3 ”, *Physical Review B* **107**, 054106 (2023).
- ²³⁸K. Kurosawa, S. Saito, and Y. Yamaguchi, “Neutron Diffraction Study on MnPS_3 and FePS_3 ”, *Journal of the Physical Society of Japan* **52**, 3919–3926 (1983).
- ²³⁹C. Murayama, M. Okabe, D. Urushihara, T. Asaka, K. Fukuda, M. Isobe, K. Yamamoto, and Y. Matsushita, “Crystallographic features related to a van der Waals coupling in the layered chalcogenide FePS_3 ”, *Journal of Applied Physics* **120**, 142114 (2016).
- ²⁴⁰T. Masubuchi, H. Hoya, T. Watanabe, Y. Takahashi, S. Ban, N. Ohkubo, K. Takase, and Y. Takano, “Phase diagram, magnetic properties and specific heat of $\text{Mn}_{1-x}\text{Fe}_x\text{PS}_3$ ”, *Journal of Alloys and Compounds* **460**, 668–674 (2008).
- ²⁴¹Y. He, Y. D. Dai, H. Huang, J. Lin, and Y. Hsia, “The ordering distribution of the metal ions in the layered cation-mixed phosphorus trisulfides $\text{Mn}_x\text{Fe}_{1-x}\text{PS}_3$ ”, *Journal of Alloys and Compounds* **359**, 41–45 (2003).
- ²⁴²J. N. Graham, M. J. Coak, S. Son, E. Suard, J.-G. Park, L. Clark, and A. R. Wildes, “Local nuclear and magnetic order in the two-dimensional spin glass $\text{Mn}_{0.5}\text{Fe}_{0.5}\text{PS}_3$ ”, *Physical Review Materials* **4**, 084401 (2020).
- ²⁴³E. Suard and A. R. Wildes, *The Spin Glass Phase of $\text{Mn}_{0.5}\text{Fe}_{0.5}\text{PS}_3$* , Institut Laue-Langevin, doi:10.5291/ILL-DATA.EASY-541, 2019.
- ²⁴⁴M. J. Coak, *Open access magnetic susceptibility data for $\text{Mn}_{0.5}\text{Fe}_{0.5}\text{PS}_3$* , University of Warwick, <https://wrap.warwick.ac.uk/139402/>, 2020.
- ²⁴⁵A. R. Wildes, M. J. Coak, J. N. Graham, and S. S. Saxena, *The Spin Glass Phase of $\text{Mn}_{0.5}\text{Fe}_{0.5}\text{PS}_3$* , Institut Laue-Langevin, doi.ill.fr/10.5291/ILL-DATA.5-32-870, 2019.
- ²⁴⁶Y. Takano, A. Arai, Y. Takahashi, K. Takase, and K. Sekizawa, “Magnetic properties and specific heat of new spin glass $\text{Mn}_{0.5}\text{Fe}_{0.5}\text{PS}_3$ ”, *Journal of Applied Physics* **93**, 8197–8199 (2003).

- ²⁴⁷P. A. Joy and S. Vasudevan, “Optical-absorption spectra of the layered transition-metal thiophosphates MPS_3 ($M=Mn, Fe, \text{ and } Ni$)”, [Physical Review B](#) **46**, 5134–5141 (1992).
- ²⁴⁸K. C. Rule, T. Ersez, S. J. Kennedy, and T. J. Hicks, “Identification of features in the powder pattern of the antiferromagnet $FePS_3$ using polarization analysis with energy analysis”, [Physica B Condensed Matter](#) **335**, 6–10 (2003).
- ²⁴⁹A. R. Wildes, S. J. Kennedy, and T. J. Hicks, “True two-dimensional magnetic ordering in $MnPS_3$ ”, [Journal of Physics: Condensed Matter](#) **6**, L335 (1994).
- ²⁵⁰A. R. Wildes, K. C. Rule, R. I. Bewley, M. Enderle, and T. J. Hicks, “The magnon dynamics and spin exchange parameters of $FePS_3$ ”, [Journal of Physics: Condensed Matter](#) **24**, 416004 (2012).
- ²⁵¹M. A. Susner, M. Chyasnachyus, M. A. McGuire, P. Ganesh, and P. Maksymovych, “Metal Thio- and Selenophosphates as Multifunctional van der Waals Layered Materials”, [Advanced Materials](#) **29**, 1602852 (2017).
- ²⁵²O. El Rhazouani, Y. Ziat, and A. Benyoussef, “Monte Carlo simulation for calculating the exchange couplings in Ca_2CrNO_6 ($N = Mo, Re$) double perovskites”, [Modern Electronic Materials](#) **3**, 99–103 (2017).
- ²⁵³G. Parisi, “Order parameter for spin-glasses”, [Physical Review Letters](#) **50**, 1946–1948 (1983).
- ²⁵⁴M. Mezard, G. Parisi, and M. Virasoro, *Spin Glass Theory And Beyond: An Introduction To The Replica Method And Its Applications*, World Scientific Lecture Notes In Physics (World Scientific Publishing Company, 1987).
- ²⁵⁵R. Basnet, K. M. Kotur, M. Rybak, C. Stephenson, S. Bishop, C. Autieri, M. Birowska, and J. Hu, “Controlling magnetic exchange and anisotropy by non-magnetic ligand substitution in layered MPX_3 ($M = Ni, Mn; X = S, Se$)”, [Physical Review Research](#) **4**, 023256 (2022).

- ²⁵⁶Z. Lu, X. Yang, L. Huang, X. Chen, M. Liu, J. Peng, S. Dong, and J.-M. Liu, “Evolution of magnetic phase in two-dimensional van der Waals $\text{Mn}_{1-x}\text{Ni}_x\text{PS}_3$ single crystals”, [Journal of Physics: Condensed Matter](#) **34**, 354005 (2022).
- ²⁵⁷M. Cheng, Y.-S. Lee, R. dos Reis, A. Iyer, D. Chica, M. Kanatzidis, and V. Dravid, “Structural and chemical analysis of mixed cation antiferromagnetic layered metal chalcophosphate FeCoP_2S_6 ”, [Microscopy and Microanalysis](#) **27**, 140–143 (2021).
- ²⁵⁸C. Autieri, G. Cuono, C. Noce, M. Rybak, K. M. Kotur, C. E. Agrapidis, K. Wohlfeld, and M. Birowska, “Limited Ferromagnetic Interactions in Monolayers of MPS_3 ($M = \text{Mn}$ and Ni)”, [The Journal of Physical Chemistry C](#) **126**, 6791–6802 (2022).
- ²⁵⁹M Barj, C Sourisseau, G Ouvrard, and R Brec, “Infrared studies of lithium intercalation in the FePS_3 and NiPS_3 layer-type compounds”, [Solid State Ionics](#) **11**, 179–183 (1983).
- ²⁶⁰Q. Liang, Y. Zheng, C. Du, Y. Luo, J. Zhang, B. Li, Y. Zong, and Q. Yan, “General and scalable solid-state synthesis of 2D MPS_3 ($M = \text{Fe}, \text{Co}, \text{Ni}$) nanosheets and tuning their Li/Na storage properties”, [Small Methods](#) **1**, 1700304 (2017).
- ²⁶¹J. A. M. Paddison, G. Ehlers, A. B. Cairns, J. S. Gardner, O. A. Petrenko, N. P. Butch, D. D. Khalyavin, P. Manuel, H. E. Fischer, H. Zhou, A. L. Goodwin, and J. R. Stewart, “Suppressed-moment 2- \mathbf{k} order in the canonical frustrated antiferromagnet $\text{Gd}_2\text{Ti}_2\text{O}_7$ ”, [npj Quantum Materials](#) **6**, 99 (2021).
- ²⁶²F. Giustino, J. H. Lee, F. Trier, M. Bibes, S. M. Winter, R. Valentí, Y.-W. Son, L. Taillefer, C. Heil, A. I. Figueroa, B. Plaçais, Q. Wu, O. V. Yazyev, E. P. A. M. Bakkers, J. Nygård, P. Forn-Díaz, S. D. Franceschi, J. W. McIver, L. E. F. F. Torres, T. Low, A. Kumar, R. Galceran, S. O. Valenzuela, M. V. Costache, A. Manchon, E.-A. Kim, G. R. Schleder, A. Fazzio, and S. Roche, “The 2021 quantum materials roadmap”, [Journal of Physics: Materials](#) **3**, 042006 (2021).

Bibliography

- ²⁶³C. L. Sarkis, M. J. Tarne, J. R. Neilson, H. B. Cao, E. Coldren, M. P. Gelfand, and K. A. Ross, “Partial antiferromagnetic helical order in single-crystal $\text{Fe}_3\text{PO}_4\text{O}_3$ ”, [Physical Review B](#) **101**, 184417 (2020).